Electro-reforming of glycerol over Ni for hydrogen production in alkaline media

Author: Frédéric Murphy

A thesis submitted in conformity with the requirements for the degree of

Master of Applied Science

Department of Chemical and Biological Engineering

University of Ottawa

Supervised by: Dr. Elena A. Baranova

“We’ve arranged a global civilisation in which most crucial elements profoundly depend on science and technology. We have also arranged things so that almost no one understands science and technology. This is a prescription for disaster. We might get away with it for a while, but sooner or later this combustible mixture of ignorance and power is going to blow up in our faces. Who is running the science and technology in a democracy if a people don’t know anything about it ? The second I am worried about this is that science is more than a body of knowledge. It is a way of thinking. **It is a way of skeptically interrogating the universe with a fine understanding of human fallibility. If we are not able to ask skeptical questions and interrogate those who tell us that something is true, to be skeptical of those in authority, then we are up for grabs.**“

- Carl Sagan

Statement of Contributions of Co-Authors

I Hereby declare that I am the sole writer of this thesis and the work presented is of my own effort. I have performed the experiments and analyses independently but also under the scientific supervision of Dr. Elena A. Baranova. I have acknowledged the assistance in experimentation by co-authors where applicable.

In chapter 3, Dr. Elena A. Baranova is a co-author for the assistance in the data interpretation as it relates to the argument of catalyst loading.

For all chapters, Asma Shubair played a key role in assisting to synthesize the nanoparticles of my thesis and Dr. Emily Cossar played a key role in assisting on how to assemble electrolysers and perform appropriate electrochemical testing procedures.

Abstract

The commercialising of green H_2 from water electrolysis is expected to play an important role in the decarbonisation of the global economy. While its commerciality has steadily been improved over the decades from breakthroughs in electrocatalyst, separator and cell design, it still is uncompetitive against other forms of energy storage such as natural gas. This challenge is primarily related with the intrinsic equilibrium potential needed to initiate the coupled half-cell reactions of water electrolysis in similar pH which represents the majority of it's electricity consumption. To contour this, coupling the half cell hydrogen evolution reaction (HER) responsible for producing H_2 with a more thermodynamically favourable anodic electrochemical reaction has shown promise.

Among the possible oxidation reactions, glycerol electrooxidation (GEOR) has shown a great deal of attention due to its surplus, high functionality allowing for a large window of potential products, significantly low onset potential, reduced risk both in terms of handling and competitive inhibition of O_2 production. Most scientific research in GEOR has been focused on its selectivity, reactivity, and resistance to poisonous species due to its significant revenue generation from its value-added products as opposed to H_2. Much has been achieved in terms of designing both reactive and selective platinum group and Ni based catalysts. However, the focus on selectivity and general electrochemical tests within small 3-electrode cells has created an under reporting of relevant electrochemical tests within industrially relevant zero-gap electrolysers. This is of particular importance since reporting the advantage of GEOR without its required coupled cathodic reaction to complete the circuit doesn't provide information to its advantages or limitations from an engineering perspective.

In this thesis, previous electrocatalysts developed by Houache et al. 2020 and Asma Shubair et al. 2022 were examined in a relevant 25 cm^2 zero-gap electrochemical cell where polarization curves are produced. Additionally, electrolyser parameters such as temperature, catalyst loading, and concentrations are varied due to the lack of studies investigating the influence of external parameters on GEOR in literature. Due to the absence of O_2 production, all electrolyser tests were performed with a filter paper to demonstrate the further possibility to reduce the CAPEX significantly as opposed to an anion exchange membrane water electrolysers. The application of a

membrane-free electrolyser also requires an investigation of the influence of glycerol on the hydrogen evolution reaction.

Unexpected discoveries were made along the electrolyser tests which did require further investigation. Scaling GEOR to a larger cell not only demonstrated challenges and opportunity to GEOR in terms of energy consumption for H_2 production, but it also detected novel GEOR reactions which have not previously been discovered due to difficulties of measuring such phenomena within small 3-electrode cells. Additionally, upscaled polarization curves also demonstrated the detection of a novel GEOR related deactivation mechanism which differs from literature and suggests that catalyst designs for GEOR should consider downstream electrolyte compositional changes to resist deactivation or changes in GEOR mechanism. Finally, investigation of glycerol on the hydrogen evolution reaction has led to a contradiction to the hypothesis in literature. Electrochemical results suggest glycerol acts as both an inhibitor and promoter for HER depending on the catalyst material and the specific HER mechanism in question. DFT and AIMD simulations are recommended to further investigate. However, the differences in catalyst sensitivities to glycerol suggest catalyst designs can mitigate the inhibitory effects of glycerol on HER or even promote HER. Additionally, impedance spectroscopy measurements strongly correlate glycerol interferes with the Nafion® binder microphase structures, significantly inhibiting electrolyte conduction and H_2O replenishment which are critical for the hydrogen evolution reaction, highlighting the need for the GEOR field to investigate other ionomers as suitable binders. Furthermore, evidence points to the influence of glycerol on OH^- conduction in liquid phase is nulled due to the novel Grothuss conduction mechanism of OH^-, presenting a significant advantage for membrane-free electrolysers. Overall, no symmetrical/asymmetrical Ni cell in this work met the D.O.E. target, with the lowest operating at 42.1 $kWh.kg_{H2}^{-1}$, due to the required metal oxidation state for GEOR to initiate over Ni is intrinsically elevated. Nonetheless, Pd phase GEOR-HER did manage to operate at 37 $kWh.kg_{H2}^{-1}$, meeting the D.O.E.. This is due to its lower required potential to oxidise potential to an active GEOR state.

Acknowledgments

I would like to begin this thesis by expressing my appreciation to my thesis supervisor Dr. Elena A. Baranova for allowing me the opportunity to explore the electrochemistry field.

I would like to also thank Dr. Emily Cossar for her mentorship, guiding me through this field with still so much mystery and unknowns, and inviting me to participate in her work during both my undergraduate studies and the pandemic. Without this invaluable hands-on experience, it would have been more of a challenge to enter this field.

I wish to thank the technical officers Gerard Nina and Franco Ziroldo for assisting with multiple technical issues and repairs that were needed during my time at the laboratory of Electrochemical Engineering in the Department of Chemical and Biological Engineering.

I would also like to thank members of my family and close friend: Dr. Julie Roy, Peter Murphy, Pierre-Michel Murphy, Jean-Louis Murphy, Karen Kmeid and Céleste Bouchaud for their unconditional support, especially Dr. Julie Roy in relation to the technical nature of gasket fitting.

I would like to state my immeasurable gratitude to the mentors in my life who have assisted me in my intellectual development, especially Dr. Géraldine Robache Wickert for critically aiding me in developing my speech and communication abilities when I was a child and teenager, Charles Romero and Jaquie Lepaint for introducing me to mathematics and singing, and Shawne Elizabeth as my vocal instructor.

Table of content

List of figures

List of diagrams

List of Tables

Chapter 1: Introduction

1.1 Background and Problem statement

Achieving a low-cost green hydrogen (H_2) production method is recognised as a necessary step for the decarbonisation of economies across the world [1–3]. Green hydrogen is a termed used to describe the production of hydrogen gas that originates from the electrolysis of water from renewably sourced electricity [4, 5]. Water electrolysis produces H_2 from the reduction of water at a cathode and an electron via the hydrogen evolution reaction (HER) [4, 5]. An electron is supplied from the oxidation reaction of water originating from the connected anode which co-produces O_2 [4, 5]. Over the course of several decades, several technological advancements have increased the efficiency of this process to nearly 100% with the goal of making green H_2 economically competitive to other forms of energy storage [1, 2, 4, 5]. While there are no strict targets globally, a recognised target is one proposed by the Department of Energy of the United States at 40 $kWh.kg_{H2}^{-1}$ [1, 2]. Despite the significant improvements in both electrochemical cell, electrode and catalysts designs, the nature of water electrolysis is in of itself its largest barrier to achieve this goal at STP [4, 5]. The reason is water electrolysis ideally requires 1.23V to occur at room temperature, this ignores the heating requirements of the reaction which pushes it up to 1.48V if ignored [4, 5]. Assuming a cell operates at 1.23V with 100% efficiency in all regards, the cell would need to consume a minimum of 33 $kWh.kg_{H2}^{-1}$. However, multiple intrinsic inefficiencies are to be found in water electrolysis when scaled up. These include three phase boundary layers from the formation of bubbles, electrolyte resistance, catalyst degradation overtime, stack and cell assembly related inefficiencies, etc. [4, 5]. While this may be optimized, little room for error can be allowed to achieve the D.O.E. target, which still has not been achieved after 70 years since the innovative design the efficient zero-gap cell [4, 5].

To contour this issue, it has been explored for multiple decades the coupling of HER with less potential demanding oxidative reaction of waste chemicals [6]. Among these chemicals is glycerol, a major by-product of the growing biofuel industry with an increasingly accumulating surplus [7]. Over the two-decade long investigation of glycerol electrooxidation, significant advancements have been made to develop electrocatalysts which can achieve high selectivity to value added products such as Formate, Oxalate, Mesooxoalte, Glycolate Hydroxupyruvate,

tartronate and glycerate to name a few [8]. While the primary focus on glycerol is selectivity is justified by the important revenue generation of the value-added products, few papers have reported the hydrogen production efficacy of their glycerol electrooxidation reaction (GEOR) catalysts when coupled to HER [6, 8–10]. Furthermore, most studies which do report their hydrogen production and energy consumption, do so in H-cells and few perform them in relevant zero-gap cells [11–15]. In addition, most studies only investigate the GEOR-HER coupled cells under constant potential conditions to control selectivity while not performing other critical standard electrochemical tests such as polarization curves, single pass conversion of the catalyst, the effect of concentration on their catalysts, the influence of mass diffusion limitations on GEOR, the nature of the poisoning species, etc [6, 16]. In turn, the catalytic behavioural profile of a GEOR-HER coupled electrolyser is poorly understood when these systems are scaled up and the little practical information for upscaling these systems render it difficult to justify their practicality.

1.2 Scope of this work

The main thesis is to observe the performance of the multiple Ni based GEOR catalysts developed by previous members of this group over a large and relevant zero-gap cell, and to perform relevant electrolyser experimentation, particularly polarization curves while reporting it's H_2 efficacy. Since there is little literature with such reporting for GEOR, the expectations are unknown and thus objectives for this thesis were developed during its development and discovery of novel related catalysis behaviours. The objectives which were achieved were: 1) Perform standard water electrolyser testing on a $Ni_{90}Bi_{10}$ and Ni anode GEOR-HER coupled electrolyser with Pt/C as the cathode catalyst; 2) Understand the influence of glycerol on HER, catalyst binder and OH^- conduction; 3) Perform standard water electrolyser testing on an asymmetrical Ni/C, $Ni_{95}Bi_5$/C, $Ni_{80}Au_{20}$/C and $Ni_{80}Pd_{20}$/C anode, with a $Ni_{80}Pd_{20}$/C cathode to measure the efficacy of coupling HER with GEOR over a Ni cell.

1.3 Thesis structure

This thesis contains 6 chapters and appendices. Chapter 1 introduces the thesis problem statement and objectives. Chapter 2 presents a literature review of water electrolysis, the thermodynamic barriers responsible for limiting its commerciality, the plausibility for glycerol electro-reforming to address this barrier and the engineering research gaps that haven't been addressed to justify this claim. Chapter 3 is an investigation of the electrolyser performance of

$Ni_{90}Bi_{10}$ and Ni catalysts while varying different cell parameters. Due to the membrane free design of the cell, chapter 4 investigates the influence of glycerol on HER over Ni based catalyst. Chapter 5 investigates and discusses the relevance of upscaled electrochemical testing for GEOR related systems to identify unknown engineering problems related to these systems and catalysts. Finally, chapter 6 presents the overall conclusions summarising the discoveries of the thesis and future recommendations to address remaining research gaps.

1.4 References

[1] The Honourable Galvez, R.; The Honourable Verner, J. Hydrogen: A Viable Option for a Net-Zero Canada in 2050? *The Standing Senate committee on Energy, Natural Resources and Environment Canada*, **2023**.

[2] Tlili, O.; De Rivaz, S.; Lucchese, P. *TASK 38 FINAL REPORT POWER-TO-HYDROGEN AND HYDROGEN-TO-X: SYSTEM ANALYSIS OF THE TECHNO-ECONOMIC, LEGAL AND REGULATORY CONDITIONS Report Coordinated by POWER-TO-HYDROGEN AND HYDROGEN-TO-X: SYSTEM ANALYSIS OF THE TECHNO-ECONOMIC, LEGAL AND REGULATORY CONDITIONS Task Force: Power-to-Hydrogen and Hydrogen-to-X Pathways: Clearing the Definitions from Ambiguities 31*; 2020.

[3] Tsotridis, G.; Pilenga, A. EU Harmonised Protocols for Testing of Low Temperature Water Electrolysers; 2021. https://doi.org/10.2760/58880.

[4] Shiva Kumar, S.; Himabindu, V. Hydrogen Production by PEM Water Electrolysis – A Review. *Materials Science for Energy Technologies*. KeAi Communications Co. December 1, 2019, pp 442–454. https://doi.org/10.1016/j.mset.2019.03.002.

[5] Phillips, R.; Dunnill, C. W. Zero Gap Alkaline Electrolysis Cell Design for Renewable Energy Storage as Hydrogen Gas. *RSC Advances*. Royal Society of Chemistry 2016, pp 100643–100651. https://doi.org/10.1039/c6ra22242k.

[6] Simões, M.; Baranton, S.; Coutanceau, C. Electrochemical Valorisation of Glycerol. *ChemSusChem*. November 2012, pp 2106–2124. https://doi.org/10.1002/cssc.201200335.

[7] Pirzadi, Z.; Meshkani, F. From Glycerol Production to Its Value-Added Uses: A Critical Review. *Fuel*. Elsevier Ltd December 1, 2022. https://doi.org/10.1016/j.fuel.2022.125044.

[8] Fan, L.; Liu, B.; Liu, X.; Senthilkumar, N.; Wang, G.; Wen, Z. Recent Progress in Electrocatalytic Glycerol Oxidation. *Energy Technology*. Wiley-VCH Verlag February 1, 2021. https://doi.org/10.1002/ente.202000804.

[9] Kim, H. J.; Kim, Y.; Lee, D.; Kim, J. R.; Chae, H. J.; Jeong, S. Y.; Kim, B. S.; Lee, J.; Huber, G. W.; Byun, J.; et al. Coproducing Value-Added Chemicals and Hydrogen with

Electrocatalytic Glycerol Oxidation Technology: Experimental and Techno-Economic Investigations. *ACS Sustain Chem Eng*, **2017**, *5* (8), 6626–6634. https://doi.org/10.1021/acssuschemeng.7b00868.

[10] Khan, M. A.; Al-Attas, T. A.; Yasri, N. G.; Zhao, H.; Larter, S.; Hu, J.; Kibria, M. G. Techno-Economic Analysis of a Solar-Powered Biomass Electrolysis Pathway for Coproduction of Hydrogen and Value-Added Chemicals. *Sustain Energy Fuels*, **2020**, *4* (11), 5568–5577. https://doi.org/10.1039/d0se01149e.

[11] Morales, D. M.; Jambrec, D.; Kazakova, M. A.; Braun, M.; Sikdar, N.; Koul, A.; Brix, A. C.; Seisel, S.; Andronescu, C.; Schuhmann, W. Electrocatalytic Conversion of Glycerol to Oxalate on Ni Oxide Nanoparticles-Modified Oxidized Multiwalled Carbon Nanotubes. *ACS Catal*, **2022**, *12* (2), 982–992. https://doi.org/10.1021/acscatal.1c04150.

[12] Dong, L.; Chang, G.-R.; Feng, Y.; Yao, X.-Z.; Yu, X.-Y. Regulating Ni Site in NiV LDH for Efficient Electrocatalytic Production of Formate and Hydrogen by Glycerol Electrolysis. *Rare Metals*, *41*. https://doi.org/10.1007/s12598.

[13] Bagchi, J.; Bhattacharya, S. K. Studies of the Electrocatalytic Activity of Binary Palladium Ruthenium Anode Catalyst on Ni Support for Ethanol Alkaline Fuel Cells. *Transition Metal Chemistry*, **2008**, *33* (1), 113–120. https://doi.org/10.1007/s11243-007-9021-3.

[14] Habibi, B.; Delnavaz, N. Electrooxidation of Glycerol on Nickel and Nickel Alloy (Ni-Cu and Ni-Co) Nanoparticles in Alkaline Media. *RSC Adv*, **2016**, *6* (38), 31797–31806. https://doi.org/10.1039/c5ra26006j.

[15] Luo, H.; Yukuhiro, V. Y.; Fernández, P. S.; Feng, J.; Thompson, P.; Rao, R. R.; Cai, R.; Favero, S.; Haigh, S. J.; Durrant, J. R.; et al. Role of Ni in PtNi Bimetallic Electrocatalysts for Hydrogen and Value-Added Chemicals Coproduction via Glycerol Electrooxidation. *ACS Catal*, **2022**, *12* (23), 14492–14506. https://doi.org/10.1021/acscatal.2c03907.

[16] Li, T.; Harrington, D. A. An Overview of Glycerol Electrooxidation Mechanisms on Pt, Pd and Au. *ChemSusChem*. John Wiley and Sons Inc March 22, 2021, pp 1472–1495. https://doi.org/10.1002/cssc.202002669.

Chapter 2: Literature review

2.1 Overview of water electrolysis

Water electrolysis (WE) is a considered as a promising renewable production method of H_2. As an electrochemical process, WE is composed of two independent half cell reactions termed the hydrogen evolution reaction (HER) and oxygen evolution reaction (OER) [1, 2].

$$H_2O(liquid) + Energy = H_2(g) + \frac{1}{2}O_2(g)$$

Historically, WE has been performed in alkaline conditions since the elevated pH inhibited the corrosion or dissolution of abundant earth metals that could be used for the electrodes. In neutral or alkaline conditions, HER (equation 2.1) produces H_2 and OH^- from the reduction of water by an electron at the cathode interface [2]. Since the cathode requires a supply of electrons to drive HER, an oxidation reaction needs to be electrically coupled from an anode. In an aqueous alkaline electrolyte, OER (equation 2.2) occurs at the anode where OH^- is the reactant which produces O_2, water and an electron [2]. Since both the oxidation of OH^- and reduction of H_2O is not thermodynamically ideal, a potential (i.e. voltage) is needed to overcome the activation barrier needed to initiate both reactions independently. Since both reactions need to be coupled for there to be a flow of electrons, the cell potential is the difference of the anodic reaction potential to the cathodic potential. Because OH^- is involved in both reactions, there exists a pH sensitivity with the Nernstian equation of WE [2]. Hence coupling both half-cell reactions together will require a minimum potential equal to 1.23V to initiate the decomposition of water at STP if both reactions occur at similar pH [2]. This minimum potential is termed the equilibrium potential. This potential ignores the heat requirements which would push the required voltage up to 1.48V if not supplied [1, 2].

HER (equation 2.1): $2\ H_2O + 2e^- \rightarrow H_{2\,(g)} + 2\ OH^-$ (0 V vs RHE or -0.826 V vs SHE)

OER (equation 2.2): $4\ OH^- \rightarrow O_{2\,(g)} + 2\ H_2O$ (1.23V vs RHE or 0.401 V vs SHE)

This voltage is critical in engineering terms since the commercialisation of WE is primarily dependent on the required electricity consumption which represents the largest OPEX costs of the electrolyser since $P_{ele} = I_{cell} * V_{cell}$ [3]. Since the production rate of H_2 is proportional to the current, the cell potential represents the operational parameter that must be decreased in an electrolyser

(equation 2.3) [3, 4]. According to the department of energy (D.O.E.) of the United States, WE needs to achieve an electrical energy consumption of 40 kWh.kg_{H2}^{-1} in order to be competitive against other forms of energy storage such as natural gas [5, 6]. Although a century's worth of development and milestones has brought WE closer to this target, this target has still not been met by engineering challenges and the intrinsic properties of WE [5, 6]. To explain these limitations and the strategies applied to mitigated them, a small revision of the advancements in WE will also be explored which has relevance for this thesis.

Power consumption (equation 2.3): $$W_e(kWh \cdot kg_{H2}^{-1}) = \frac{n\,F}{3600 * M_{H_2}} * V_{cell}$$

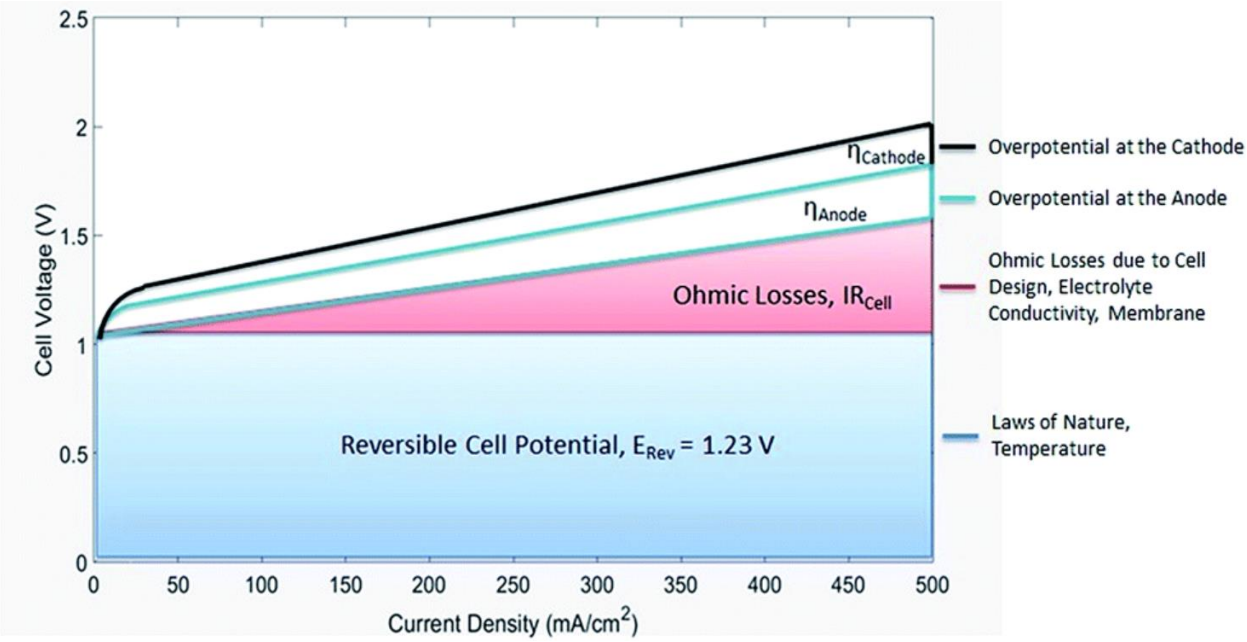

Figure 2.1) An illustration of the individual contributions to a WE electrolyser voltage [1].

Since OH^- is both a product and reactant on the cathode and anode, the conductivity of OH^- in solution presents an important source of ohmic resistance which increases the required voltage to achieve a desired current [1, 2]. This additional potential in comparison to the equilibrium potential is termed the overpotential [1, 2]. For a cell, the overpotential originating from the OH^- conduction resistance is represented by the ohmic loss in the polarization curve of Figure 2.1 [1, 2]. While the ohmic resistance from OH^- conduction is not the only source of overpotential for the cell's overall ohmic resistance, it does contribute as an important source of it [1, 2]. Initially, supporting electrolytes were used to minimise this ohmic polarization [1, 2]. However, ohmic

polarizations are proportionally amplified by the distance the ion must travel (i.e. the distance between electrodes) as shown in Figure 2.2 [1, 2]. In turn, reducing the distance between electrodes is a straightforward design to reduce the ohmic polarization significantly [1, 2]. However, reducing the distance between electrodes also increases the risk of gas cross-over between H_2 and O_2, which can produce an explosive mixture [1, 2]. In turn, the traditional porous separator (for example: zirconia or PPS) that were traditionally used were replaced by ion conductive membranes with small gas cross-over properties [1–3, 7]. The first generation was the proton exchange membranes (PEM). This allowed for both electrodes to be separated by less than a millimeter, significantly reducing the ohmic resistance [1, 2]. Furthermore, PEM electrolysers operated in acidic environments. This led to an intrinsic advantage when compared to alkaline WE since H^+ was the conductive ion which boast a smaller intrinsic ohmic resistance than OH^-, further reducing the ohmic polarization [1, 2].

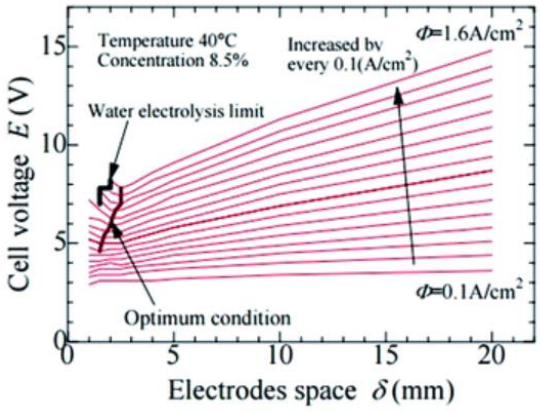

Figure 2.2) Plot of cell voltage against the gap between electrodes at increasing current densities [1].

Still, PEM electrolysers could not achieve the D.O.E. target and presented an additional challenge which is the increased CAPEX due to the acidity, requiring the use of expensive and scarce platinum group metals (PGMs) [1, 2, 5, 6]. In turn, a derivative of PEM was developed termed anion exchange membranes (AEM) to allow the use of earth abundant metals in alkaline conditions (figure 2.3A) [3]. While AEM still intrinsically conducts inferior OH^-, recent AEM electrolyser performances demonstrates AEM can be comparable to PEM in performance, with the benefit of a reduced CAPEX and use of abundant materials [3, 8, 9]. Due to the reduced conductive resistance

of OH^- from the ionomers and the zero-gap cell designs, most membrane studies are focused on stability [8, 9]. Still, the D.O.E. target is not met [5, 6].

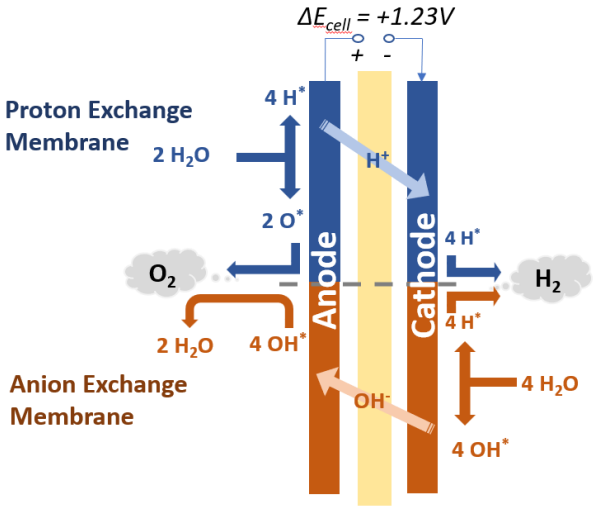

Figure 2.3) A general diagram of an AEM and PEM reaction kinetics on each electrodes and their conductive ions.

To further reduce the cell operating potential for WE, reducing other overpotentials presents a major focus of WE research. Among these is the presence of three-phase boundary layers and reaction overpotentials. In the case of three phase boundary layer overpotentials, it relates to the unideal electrolyte environment for reactants replenishment or removal of products from the turbulent formation of H_2 and O_2 [1, 10, 11]. This participates in the ohmic losses of the cell seen in Figure 2.1. In the past decade, this overpotential has been addressed through improved electrode design and assembly where bubble removal is favoured early on [1]. There is also the experimental concepts of sonication to remove bubbles with signs of success as well [12]. However, the main focus of most WE research is related to reducing the reaction overpotentials which are represented by as η_{anode} and $\eta_{cathode}$ in figure 2.1, which relates to the experimental potential needed to initiate the half-cell reactions in comparison to it's theoretical minimum [1, 8, 10, 11, 13–15]. To discuss this, a review related to alkaline HER will be done since it has relevance for chapter 4 and how electrocatalysis design is a main solution to address this issue.

2.2 Alkaline hydrogen evolution reaction

To understand the reaction overpotential and why it exists, a basic revision of HER needs to be made in relation to catalyst design and why much remains to be improved and understood

for HER. Despite the various debates over the exact mechanism [16, 17], HER in alkaline conditions is agreed to be a two-step reaction process. The first step is the dissociative adsorption of H_2O into H^* and OH^* or the breaking of O-H bond to form only H^* onto the cathode, where an electron is transferred to OH^*/OH^-. This is termed the Volmer mechanism (equation 2.4) and it is associated as a proton coupled electron transfer (PCET) reaction [16, 17]. Following the dissociation, two different reaction mechanisms can occur, Heyrovsky (equation 2.5) and Tafel (equation 2.6) reactions [16, 17]. The Heyrovsky mechanism is the desorptive recombination of H^* to a local hydrogen atom from a nearby H_2O molecule near the catalyst interface. The Tafel reaction mechanism is the recombination of two neighboring H^*. Both reactions produce $H_{2(g)}$ and only the Heyrovsky step accepts an electron between the two.

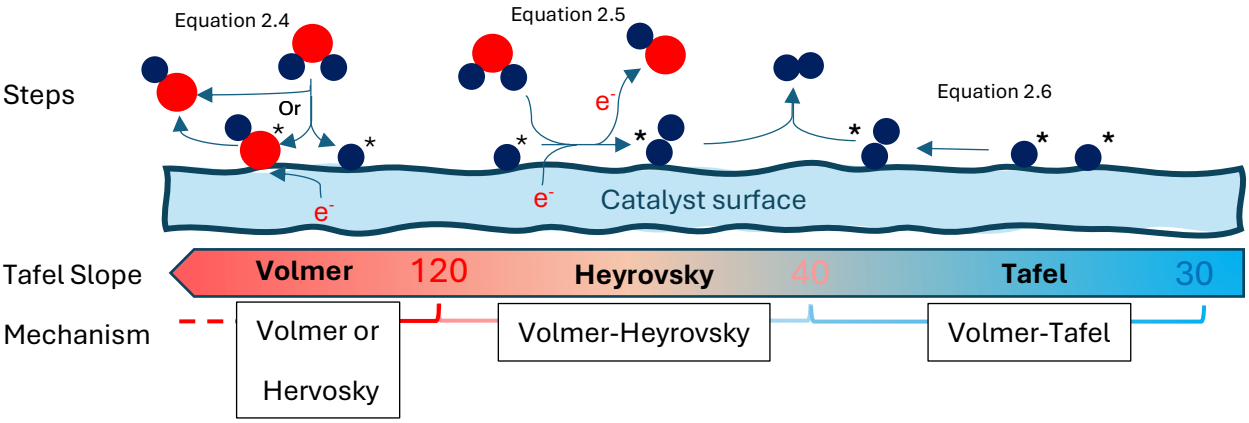

Figure 2.4) A representation of the HER mechanism in alkaline conditions and the associated minimal Tafel slope values.

Knowing the fundamentals, two primary trains of thoughts exist on the dictating HER factors and have dictated the design of catalyst materials over the past decade with a focus on how geometry and surface composition can improve HER but also provide a blueprint in understanding HER and how the reaction overpotential can be reduced. The most practiced mechanistic theory of HER is highlighting the importance of the hydrogen binding energy (HBE) for each reaction step of HER [11, 18–20], as is seen for the Volmer step where hydrogen adsorption is a critical step. In theory, not utilising materials with ideal HBE will lead to a catalyst with high reaction overpotentials. This theory has been tested and proven over multitudes of works across the past decade for being a critical factor in the design of highly active catalyst materials when applying Sabatier's principle to HBE [10, 11, 13, 14, 18]. Assuming only H^* dissociatively adsorbs onto the

catalyst surface, balancing its binding energy will optimize the overall adsorption, recombination, and desorption steps of HER (Scheme 1: eq 3, 5 and 6). This strategy has been successful in predicting the performances of various catalysts, particularly for Pt group metals, substantiating HBE as a key parameter [11, 18–20]. However, it fails to explain the relevance of the possible co-adsorption of OH* which is the second most practiced mechanistic theory for improving HER [11, 14, 18, 21]. In recent years, consideration for the OH binding energy (OHBE) has been extensively investigated to improve HER for non-Pt group metal (NPG) bimetallic catalysts and has been successful in producing highly active and stable state of the art NPG electrocatalysts which can out compete commercially available Pt catalyst at elevated currents, significantly reducing the reaction overpotential [14, 22]. The optimization of OHBE and HBE by combining ideal OHBE elements in an optimal geometric configuration with ideal HBE elements have significantly improved HER when compared to following just the HBE doctrine as shown in figure 2.5, showing the relevance of HBE and OHBE and the relevance of each adsorbate for alkaline HER [11, 14, 18].

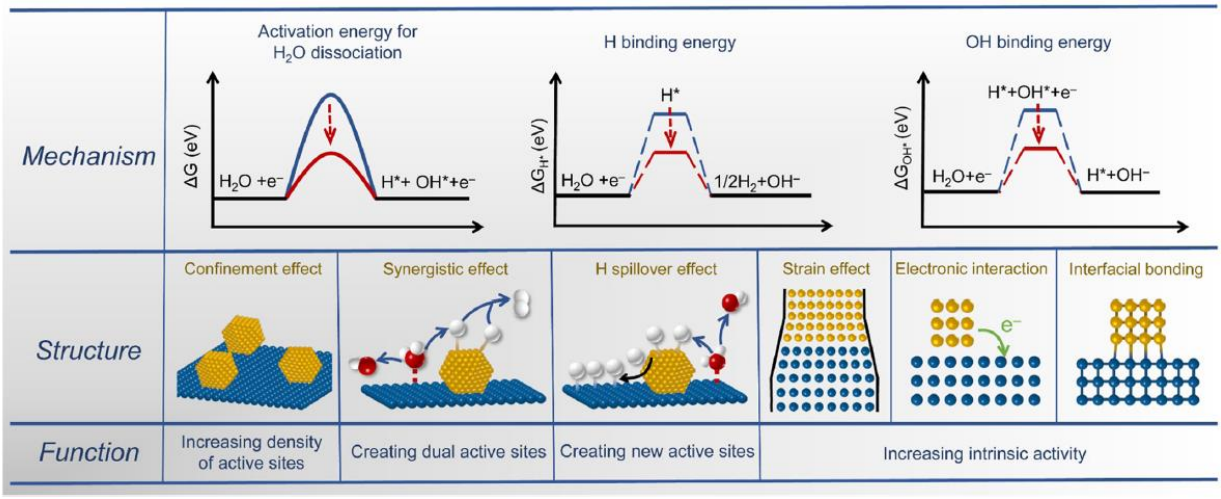

Figure 2.5) Illustration of the electrocatalyst design strategies towards alkaline HER. Figure from Lao et al. 2022 [18].

Due to these major developments in HER theory, Ni has been explored as a promising catalyst material of choice for HER due to it's near ideal and tunable HBE and OHBE in relation to its abundance [19, 23], and significantly improved reactivity from the design of bimetallic catalysts which intrinsically improved its desirable HER properties or aid in the HER process [17, 24]. Other materials also show promise such as Mo, Fe, Co, etc [16, 17, 20, 24–39]. Recent novel Ni catalyst materials can achieve low overpotentials and Tafel slopes which outperform Pt/C, considered as

one of the most active catalysts for HER [39]. Like HER, OER catalyst design have followed their own design principles which have also led to the development of highly efficient and reactive earth abundant electrocatalysts [10].

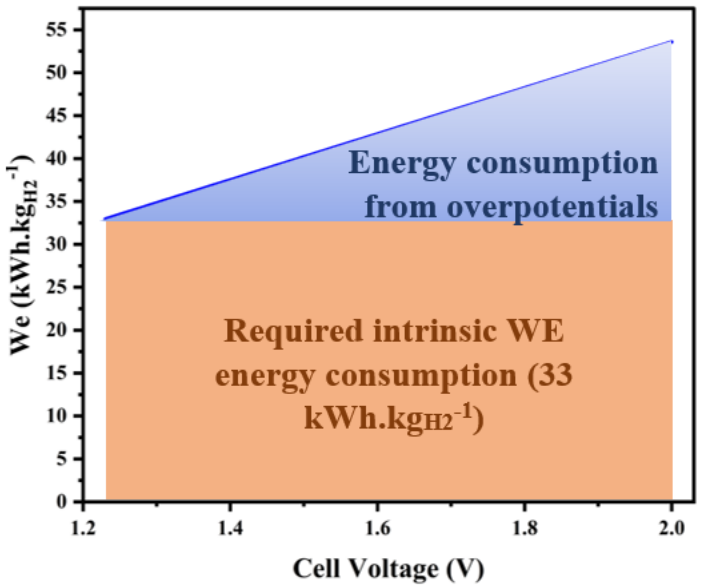

Figure 2.6) Energy consumption of an electrolyser at room temperature at various operating potentials with the contribution of the intrinsic WE equilibrium potential in red assuming 100% faradaic efficiency.

Even though several decades have been dedicated to the improvement of HER and OER, the D.O.E. target still has not been met. To this day, the most efficient WE electrolyser known by the author is HySTAT PEM electrolyser with an electrolyser stack efficiency of 95% which achieved an impressive 41.5 kWh.kg$_{H2}^{-1}$ [5, 6]. Then what presents the largest barrier to achieving this 40 kWh.kg$_{H2}^{-1}$? The answer is found in the intrinsic thermodynamics of the reaction itself as shown in Figure 2.6. Assuming ideal conditions with no overpotentials and ignoring the heat requirements at STP, an electrolyser operating at 1.23V at any current would require a minimum of 33 kWh.kg$_{H2}^{-1}$. While this meets the D.O.E. target, it does place into perspective that the largest contribution to the required operating potential of cells today is mostly contributed by the equilibrium potential required to theoretically initiate the reaction itself at similar pH. Furthermore, if the D.O.E. target was overcome, the window to further improve the cell is thermodynamically limited and maybe questioned if worth while as shown in Figure 2.7 [3]. The work by Yang et al. 2022 demonstrated that even if significant reduction in key WE overpotentials were achieved with current state of the art materials, these would result in marginal OPEX reductions unless significant

subsidies are in place [3]. In turn, WE intrinsically presents its own largest barrier to commercialisation.

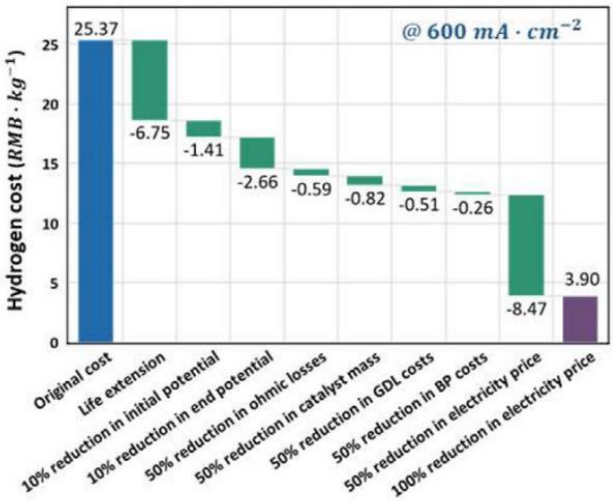

Figure 2.7) AEM's cost reduction spatial analysis waterfall chart [3].

2.3 Glycerol electrooxidation reaction

While WE intrinsically represent its own largest limitation with today's current understanding of the reaction, there are promising alternative approaches to address this issue. Firstly, the reaction is endothermic at room temperature, hence, increasing the temperature decreases this energy barrier [2]. Due to the ion conductivity and high thermal stability of solid oxides, solid oxide electrochemical cells permit the operation of WE at elevated temperatures, which has shown to be commercially viable when coupled with high heat generating processes such as nuclear power plants [2]. Another alternative is to substitute OER for another oxidative half-cell reaction with a decreased minimal potential to operate since a cell's potential is the difference between the cathodic and anodic half cell potentials [40]. Of the various reactants, glycerol electrooxidation shows particular promise [40]. Similar to other alcohols, the minimal electrooxidation of glycerol is significantly more desirable at 0.003V, as opposed to OER at 1.23V at 0 pH [40]. This significant reduction in required potential when coupled with HER should significantly reduce the operating cell potential and has been demonstrated at lab scale where <30 $kWh.kg_{H2}^{-1}$ has been achieved by PGM catalysts [40, 41]. Furthermore, GEOR is competitive against OER which further reduces the risk of explosive mixtures occurring which can allow for novel cell designs without a membrane [40].

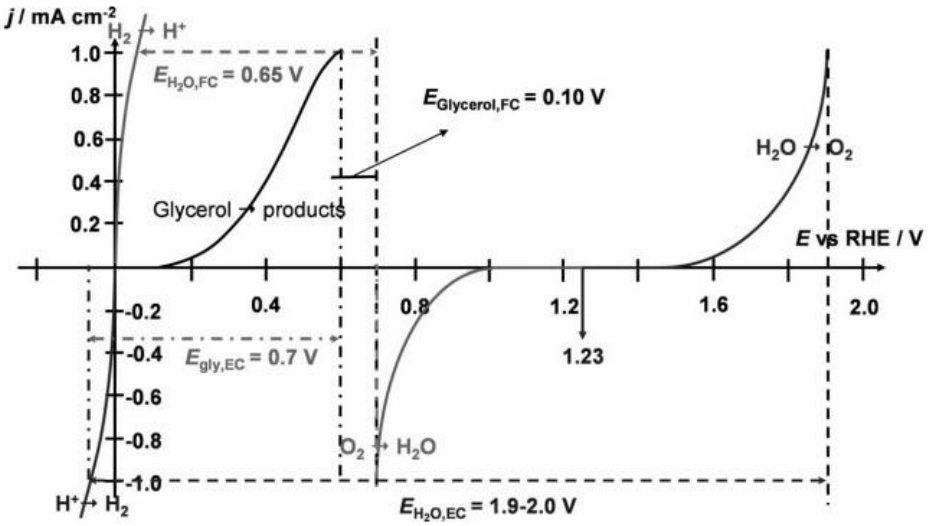

Figure 2.8) Comparison of the theoretical E(j) electric characteristics representative of the Butter-Volmer kinetics law for water oxidation, glycerol oxidation, oxygen reduction and proton reduction. Figure adapted from Simoes et al. 2012 [40].

Unlike most alcohols, there is also a large economic incentive for glycerol electro-oxidation reaction (GEOR) to be coupled with a multitude of energy intensive cathodic reactions since glycerol is a surplus chemical in the global markets [42]. Glycerol primarily originates as a side-product of the biofuel industry where 1 kg of glycerol is produced for every 10 kg of biofuel produced [42]. Even though the demand for glycerol in the food, pharmaceutical, polyether polyol, beverages, alkyd resin and cosmetic industry is growing, it has not kept up with the increase in biofuel demand, leading to an accelerated surplus of glycerol for the coming years [42]. Due to this, glycerol is 6 times cheaper than the value of H_2 [43], opening an opportunity for profitability which has driven the direction of the research in this field. Additionally, the risks of handling glycerol as opposed to other alcohols is more desirable [44]. Furthermore, the high chemical functionality of glycerol from it's three hydroxide functional groups allows for the production of a multitude of high value-added chemicals [42]. According to Pirzadi, et al. 2022, glycerol presents a larger possible list of value-added chemicals than hydrocarbons [42]. Additionally, it's electrooxidation pathway is competitive to other pathways to valorize glycerol [45]. In turn, the increasing surplus, decreasing raw material cost, large potential product window, reduced OPEX via electrooxidation, decreased toxicity and hazards makes glycerol an attractive alcohol to couple with HER.

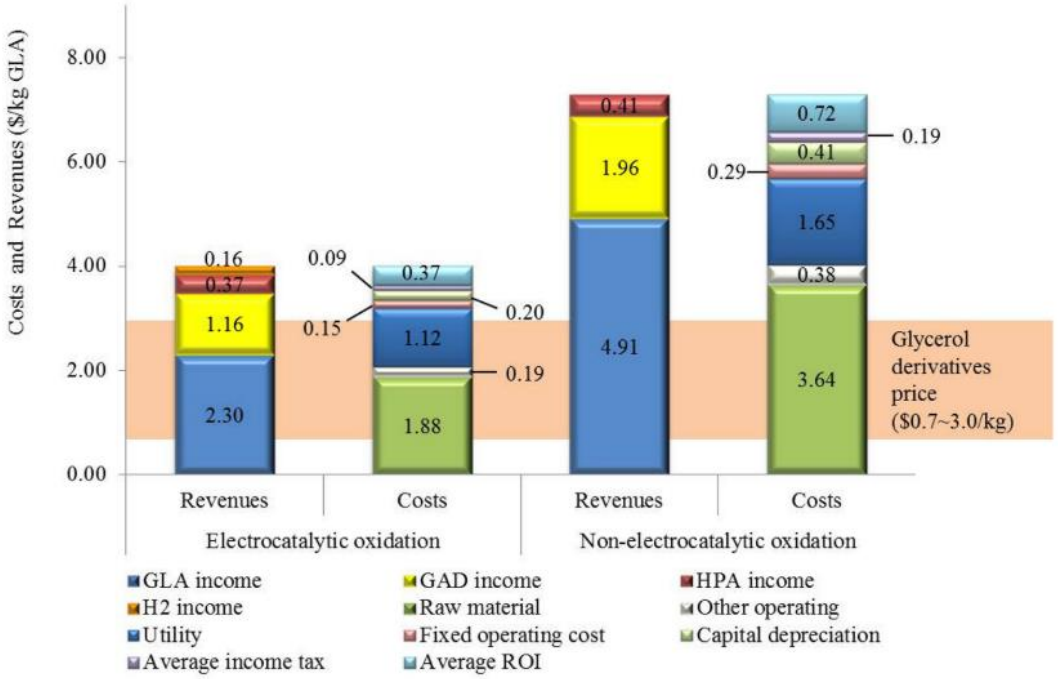

Figure 2.9) Comparison of the costs and revenues of the electrocatalytic and non-electrocatalytic glycerol oxidation strategies. Figure from Kim et al. 2017 [45].

That said, the value-added products caused an interesting dynamic where the revenue generation from H_2 and the value-added products is heavily skewed towards the latter as shown in figure 2.9 [46]. Furthermore, the recovery of the value-added products is a dominant source of the required OPEX and CAPEX, as seen in figure 2.10 [46]. In turn, the important capital commitment and revenue generation of GEOR has focused most of its research on selectivity of its catalysts since a more selective catalysts will reduce the operational complexity and OPEX of this type of plant and improve profitability. In turn, the engineering priorities for alcohol-HER coupled electrolysers deviate from those of WE electrolysers where selectivity is paramount [47].

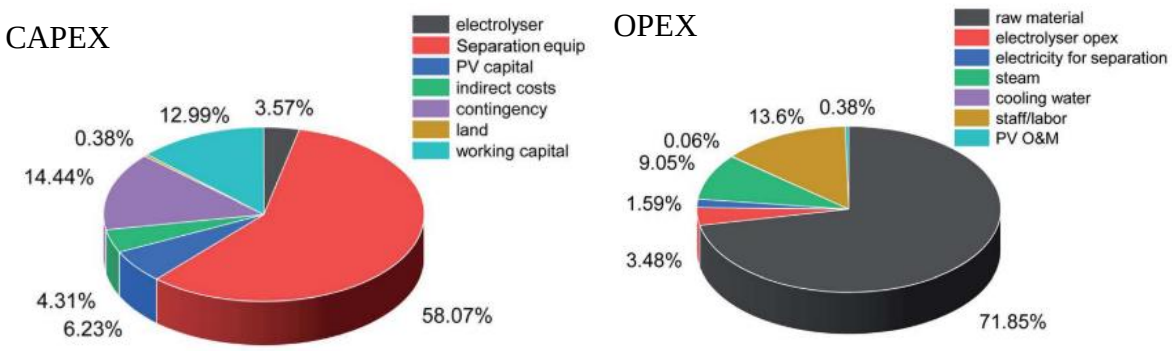

Figure 2.10) Breakdown of the optimistic CAPEX and annual OPEX for a solar-powered glucose electrolysis process. Figure from Khan et al. 2020 [46].

Over the past decade, significant strides have been made in developing selective GEOR catalyst. However, controlling selectivity is a challenge for GEOR due to the wide functionality of glycerol [42]. To understand this and explore other advantages of GEOR, a short review of GEOR will be performed with a focus on the relevant catalysts materials for this thesis which were developed by Houache et al 2020-2021 and Shubair et al. 2024 for Pd, Au and Ni [43, 48, 49]. For any material, the first step of GEOR is the adsorption of glycerol over a free site. While not strictly understood, it is agreed that the adsorption of glycerol occurs from one of it's carbon atom [50]. The adsorption of either the primary or secondary carbon can be favoured depending on the plane of the adsorption site and the bimetallic design [50]. However, the adsorption of glycerol is independent of potential since it doesn't transfer an electron with the electrode [50]. In turn, its adsorption is primarily driven by standard adsorption parameters such as temperature and concentration [51]. This is an important difference from WE where the adsorption of H_2O, OH^- or H^+ requires an electron transfer step with the electrode, which makes it potential dependent [15]. Thus, most GEOR studies which perform FTIR spectras of the catalyst at open circuit potential (no applied potential/current – rest state) will detect glycerol adsorbed over its surface [50].

Following its adsorption, the mechanism can either pass through two pathways which were proposed by Li et al. 2021 who performed a comprehensive review and meta-analysis of GEOR studies over PGMs such as Pd and Au [50]. One pathway is the acidic pathway where neighboring free sites can proceed with the oxidation of glycerol by adsorbing other carbon atoms from the same glycerol molecule and inducing C-C cleaving or dehydrogenate the carbon atoms through a proton coupled electron transfer step (PCET) [50]. Since electron transfers are involved with the electrode surface, this pathway requires a potential, which contributes to the cell power

consumption. The acidic pathway can achieve a high yield of 3 carbon atoms products (C_3) [50]. However, the acidic pathway has an elevated tendency to completely oxidise glycerol to CO which is a known poisonous species for PGMs such as Pt at low overpotentials [50]. Furthermore, the acidic pathway is a slow reaction which is undesirable. To address both the reactivity and reduce the poisoning tendency, the OH_{ads}-present pathway is desired [50]. This pathway can be achieved at elevated potentials in acidic media or at lower overpotentials in alkaline conditions [50]. Since a low overpotential reduces the operating cell potential, most studies investigate GEOR in alkaline conditions [50]. When surface OH^* is present, it catalytically desorbs CO^* through the Langmuir-Hinschelwood mechanism which regenerates the surface and increases the catalyst reactivity [50]. In addition, OH^* favourably oxidises and dehydrogenates glycerol as opposed to neighbouring free sites, which further increases the reactivity of the electrocatalysts [50]. However, OH^* also favours the cleavage of C-C bonds which increases the yield of C_2/C_1 products which can be desirable depending on the desired product. This can be avoided through bimetallic designs such as the addition of Bi or Sn [50]. Still, this does require the adsorption of OH^-, which is a potential dependent step that is higher than the oxidation of glycerol in acidic conditions. In turn, the operating cell potential via the alkaline pathway is dependent on the capacity of the electrode to oxidise the surface to form OH^*.

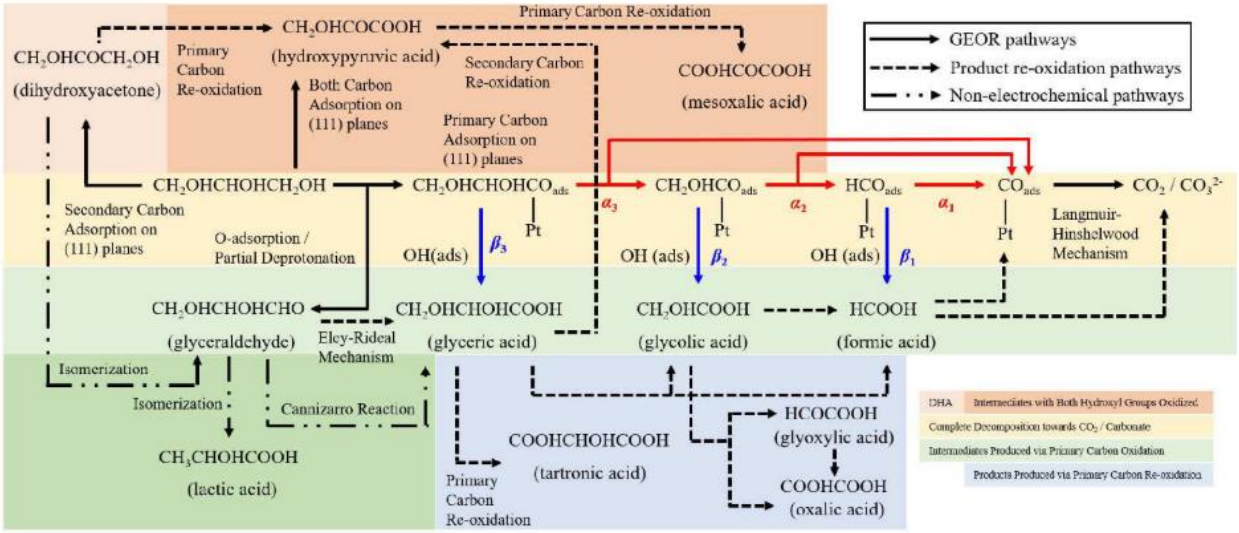

Figure 2.11) Li et al. 2021 proposed reaction mechanism of glycerol on Pt, Pd and Au. Figure from Li et al. 2021 [50].

While reducing the operational potential is paramount, the reactivity of the catalyst (i.e. the current) it can sustain at a given potential is equally relevant. In the case of Pd, it has a relatively low GEOR reactivity as opposed to most metals due to its relatively elevated d-band (-1.83 eV) center which isn't ideal for deprotonation [50]. As for Au, it's d-band is filled, hindering the adsorption of free radicals of alcohols which renders its reactivity in acidic conditions poor and explains why the OH^* pathway is more reactive when compared to Pd [50]. In fact, nearly all Au based GEOR studies are performed in alkaline conditions [50]. However, Au has a remarkable degree of GEOR reactivity primarily attributed to the difficulty to poison the surface from the filled d-band center and the promotional role of CO^* has on OH^- adsorption over Au [50]. Additionally, the reactive species over Au is the deprotonated form of glycerol (glycerate – the alkoxide of glycerol) where the negatively charged O^- is the atom that is adsorbed onto Au from the alkoxide [52]. Although Au has a higher degree of poison resistance, it still deactivates from the formation of poisonous species which deactivates its surface. This is also true of Pd which limits the maximum current and potential that can be achieved [50, 52]. Furthermore, WE where electrocatalysts will lose their reactivity due to mass transport limitations which creates a concentration polarization in polarization curves [1], the deactivation of PGMs catalysts in GEOR is caused by the formation of CO or unknown intermediates whose desorption by OH^* is rate limiting [50]. But the deactivation is sudden and drops the current to nearly to 0 mA and is caused by the eventual preferred oxidation of OH^* to inactive O^* which is potential dependent [50]. In turn, increasing the potential (i.e. current) not only increases the risk of unknown intermediates slowing GEOR, but OH^* oxidation to O^* increasingly becomes favourable which is further promoted by the presence of rate limiting poisonous intermediates [50]. Thus, a need for poison resistant materials is desired. chapter 5 will discuss this deactivation further in its discussion.

To address this, Ni presents a promising non-PGM for GEOR due to it's anti-poisoning properties from glycerol intermediates [53]. Furthermore, experiments have repeatedly shown Ni has a high reactivity for GEOR that is comparable to PGMs [50, 53]. Nonetheless, Ni has a tendency to be selective to C_1 products although recent bimetallic designs have achieved increased C_2 selectivity, unlike PGMs [49]. However, glycerol adsorption over Ni doesn't occur over metallic Ni but over it's oxide states such as NiOOH or NiO_2. Achieving these oxidation states requires a potential higher than Pd-OH^* or Au-OH^* [50]. Due to this, the overpotential of Ni based GEOR is undesirably elevated. In turn, much research in Ni GEOR is focused on reducing the onset-

potential of β-$Ni(OH)_2$/β-NiOOH by means of various bimetallic design principles in order to reduce the power consumption [43, 48]. To this day, Ni based catalysts still cannot achieve the D.O.E. target at 41 $kWh.kg_{H2}^{-1}$ unlike Pd and Au based catalysts which can achieve 22 $kWh.kg_{H2}^{-1}$ due to this difference in the required oxidation of the electrode [54–57].

2.4 GEOR research gaps

Due to the economics of GEOR-coupled electrolysers, the primary focus of GEOR coupled systems is on the development of selective and reactive anodic electrocatalysts with few reporting the power consumption of the cell, and fewer reporting the cathodic power consumption, like HER [58]. This has led to a research gap of under-reporting the practical operating potential of Ni based cells and observing the behaviours of electrolysers under relevant operational conditions. Instead, the GEOR literature produces estimates of what the operating potential should be based on voltammograms. Voltammograms are produced where a potential is applied and swept within a potential range to measure the current either originating from a faradaic (GEOR, HER, OER, electrode oxidation) or non-faradaic (capacitance) process [59, 60]. Of these methods, cyclic voltammetry (CV) is the most common in GEOR related publications.

CVs are the most practiced electrochemical method to determine the needed potential to drive an electrochemical reaction [59, 60]. It also provides information on the reactivity of a catalyst for a wide potential range. For example, the production of Bi core Ni shell electrocatalysts by Houache et al. 2020 ($Ni_{90}Bi_{10}$) produced a higher GEOR current density peak for a given potential as opposed to Ni alone, implying the reactivity of GEOR was improved as shown in Figure 2.12 b [49]. Furthermore, the onset potential needed to initiate GEOR on a CV was reduced over $Ni_{90}Bi_{10}$, implying the apparent activation energy of GEOR was reduced as well from a reduced activation barrier for the oxidation of inactive β-$Ni(OH)_2$ to active β-NiOOH [49]. The cyclicity of CVs also allow the reversal of the scan rate for the detection of reversible and irreversible reactions which originated from the previous scan direction [59, 60]. From this reversed scan, information on a reactions' reversibility can readily be determined [61]. In the case of the β-$Ni(OH)_2$/β-NiOOH redox reactions, the potential value of the reduction peak relative to it's oxidation reaction can determine the reversibility of said reaction. In the case of $Ni_{90}Bi_{10}$ reported by Houache et al. 2021, CV results demonstrated a more ideal reversibility by the presence of Bi in the absence of glycerol [49]. Based

on the reduced onset potential and more favourable reversibility, an electrolyser should operate at a reduced potential.

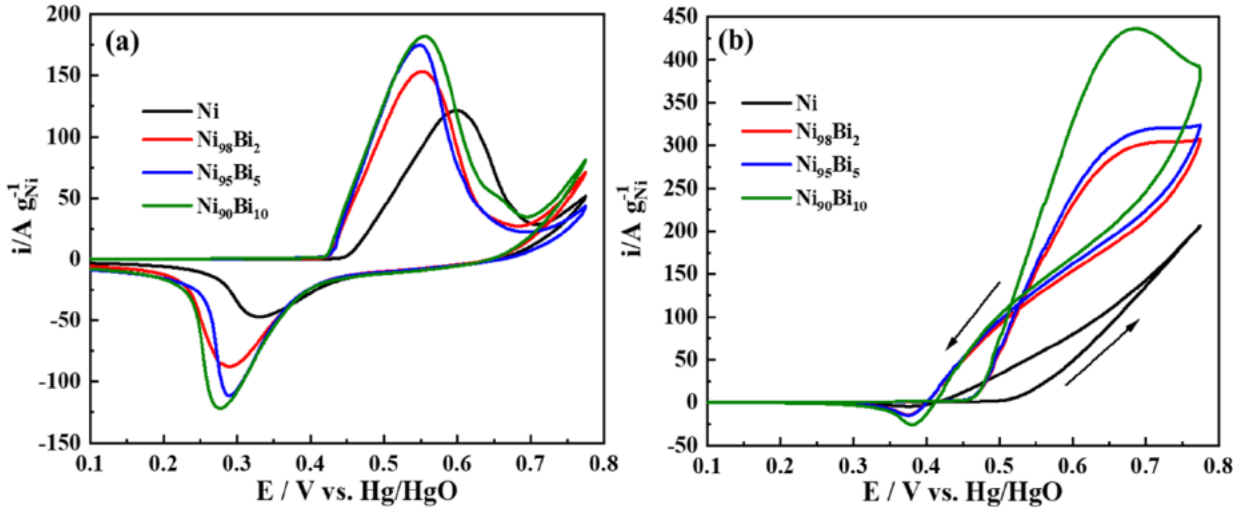

Figure 2.12) CVs of Ni-based catalysts N_xBi_{1-x} performed in (a) 1M KOH solution and (b) 1M KOH + 0.1M glycerol solution at a scan rate of 50 $mV.s^{-1}$. Figures from Houache et al. 2020 [49].

That said, the challenge related to CVs are that it doesn't necessarily reflect the reactive conditions in which the catalyst will be in a relevant system at-scale [62]. An important factor in this difference is the sweep rate and its nature (figure 2.13) [59, 60]. Assuming a simple heterogeneous reaction where reactant A is converted to B and B is desorbed into the electrolyte, the concentration of A near the catalyst interface and bulk electrolyte is similar when the potential is below the onset potential since the reaction cannot initiate. As this reaction begins at a sufficiently elevated potential, a required amount of time is needed for the concentration gradients of reactant and products to reach equilibrium [59, 60, 63]. In other words, the diffusion layer of the heterogenous reaction requires time to reach steady state (figure 2.13 A & B) [60, 63]. In that time interval, the catalyst reactivity decreases since the diffusion layer extends further into the electrolyte over time near the interface. This phenomenon is observed in all GEOR studies where chronoamperometry (CA) is performed (figure 2.15) (this method will be explained later) [43, 49, 64, 65]. But in the case of CVs, the potential is swept at a rate. This has an unintentional consequence since the potential driving force of the reaction increases overtime since it is dependent on the potential, while the diffusion layer near the interface has not reached steady state for the previous applied potential. In turn, the scan rates of CVs always produce a more ideal reactive environment for the catalyst since the persistently thinner diffusion layer for the respective driving force

increases the catalyst reactivity. This increased reactivity is often negligeable or is not accounted for in straightforward reactions like HER or OER.

However, in the case of more complex reactions where A is additionally converted to C and C is a poisonous molecule blocking active sites and competing against A adsorption, not permitting equilibrium or steady state to be achieved due to a high scan rate may artificially increase a catalyst performance or hide key electrochemical properties. In the case of poisonous deactivation, the concentration of species C or A near the interface may not have sufficient time to increase or decrease appropriately for a given potential or current, respectively. This has important relevance for GEOR since several FTIR spectrums have identified unknown carboxylate products near and after the deactivation on multiple catalysts as is seen for PGMs [49, 50]. To address this, a slower scan rate can be applied which is often done in GEOR studies when linear sweep voltammetry (LSV) is performed. LSVs are like CVs but the potential is swept only in one direction. While CVs may not be representative, the manipulation of the scan rate can provide vital kinetic and diffusion information since one can manipulate the boundary layer thickness [59, 60, 63]. However, these in-depth kinetic investigations are rarely performed in GEOR [66, 67].

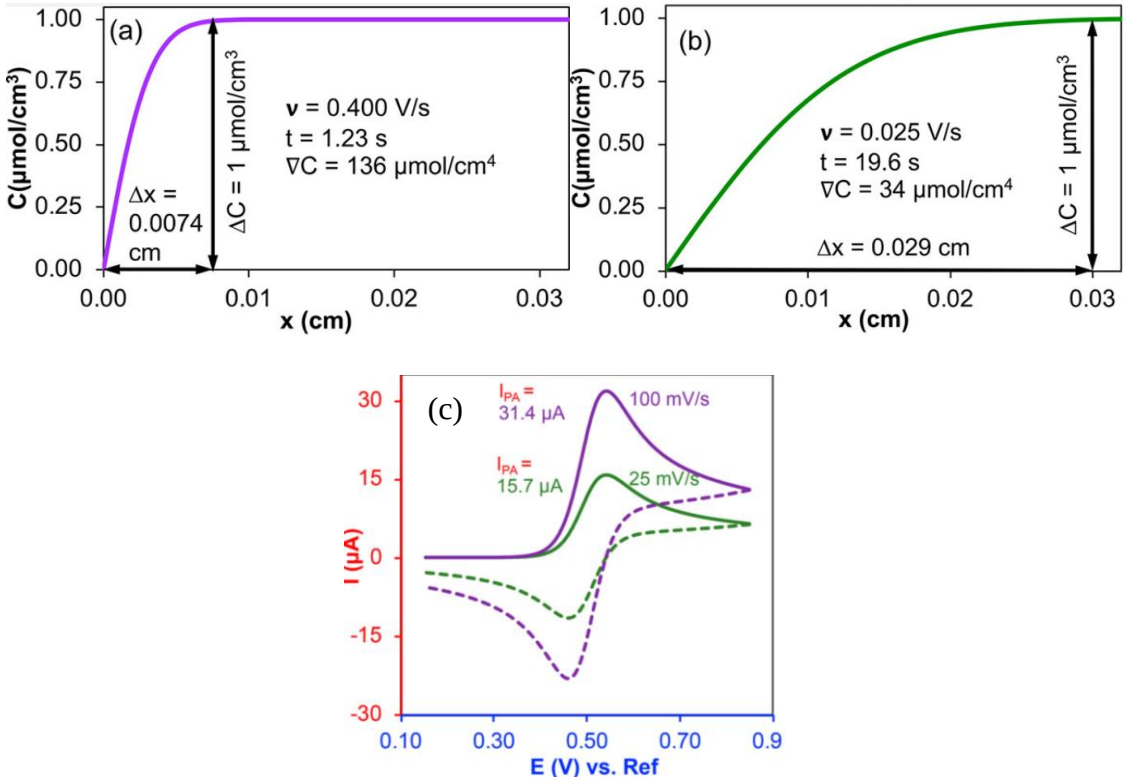

Figure 2.13) (A and B) Concentration profiles near the electrode surface at different scan rates. (c) CV of a generic redox process at two separate scan rates. Figures from Khalafi et al. 2021 [63].

For example, only recently has it been shown through a slow scan rate (which is seldom performed in this field) that a second oxidation peak is detectable for alcohol oxidation [53]. This separate oxidation peak is different from Fleischman mechanism and represents an indirect potential dependent GEOR mechanism where NiO_2 is an important reactive phase which reduces down to $Ni(OH)_2$ during its GEOR as shown in Figure 2.14 and is responsible for a large window of products recorded in Ni based GEOR studies [53]. In turn, a simple experimental parameter such as the scan rate can mask multiple oxidation peaks which are close to one another and conceal vital kinetic information about the catalyst [63]. In turn, multiple scan rate investigations should be performed for given electrocatalyst.

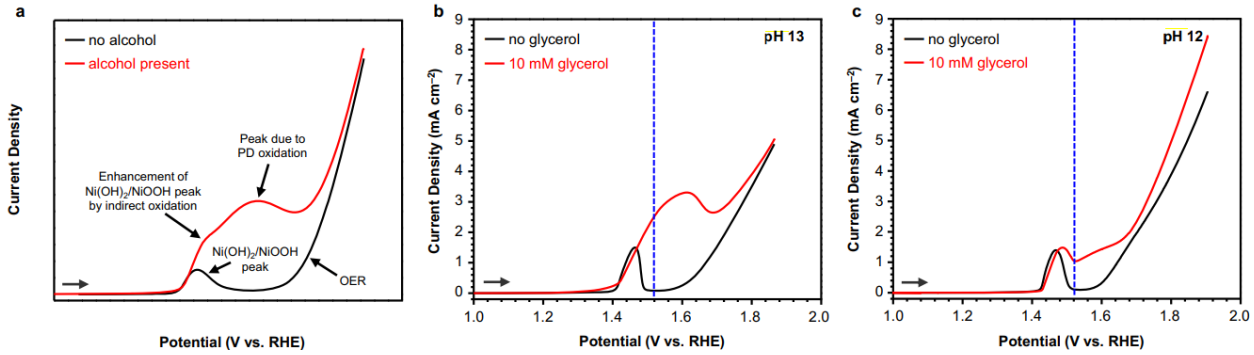

Figure 2.14) (A) Schematic LSV of the indirect and potential dependent glycerol oxidation peaks over Ni. LSV obtained with (red) or without (black) 10mM Glycerol over Ni in pH (B) 13 and (C) 12 [53].

The common practice of applying sufficiently elevated scan rates in CVs renders their reactive conditions intrinsically different from their at-scale systems and operational modes. To address this, GEOR studies perform CA measurements where a constant potential is applied for a given amount of time and the current is measured. A constant potential is applied due to the strong relationship between selectivity and potential in GEOR catalysts [50, 64]. Depending on the reaction in question and the objectives, one can extrapolate different information. In the case of GEOR, often CAs are performed to measure the catalysts selectivity for HPLC measurements and determine the deactivation of the catalysts overtime. As one can see from the CA in figure 2.15, the operating current densities are vastly reduced and evidence to a form of deactivation occurs which is not represented in the CVs of the same catalysts in Figure 2.12. Deactivation of Ni is significant enough that a loss of reactivity by as much as 79% occurred.

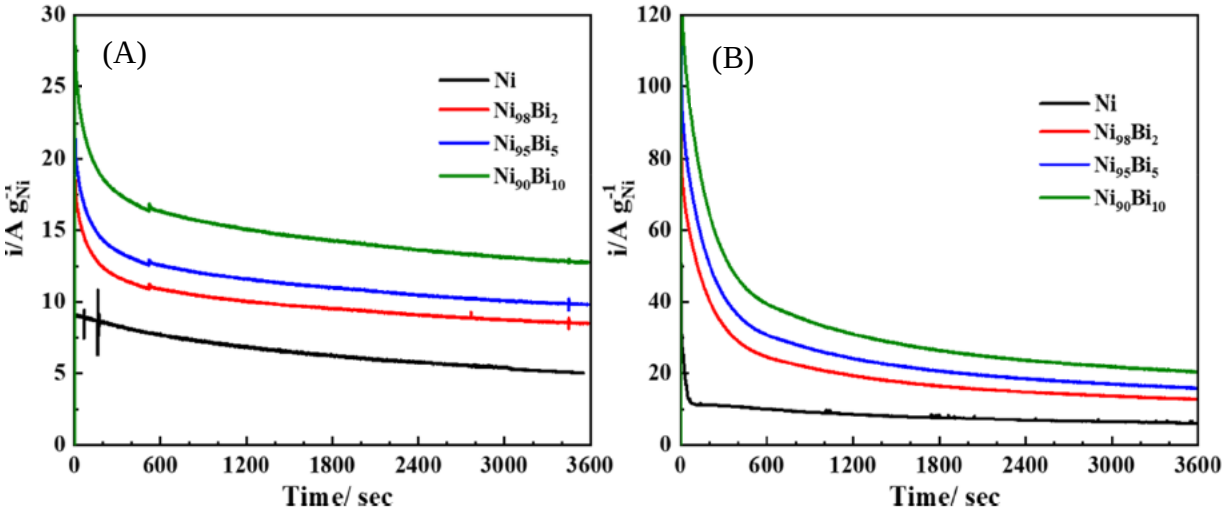

Figure 2.15) CA tests of various Ni catalysts in 1M KOH and 0.1M glycerol at potentials of (A) 0.48 and (B) 0.52 V vs Hg/HgO for 60 minutes, respectively [49].

However, several issues arise not from the use of CAs in of themselves but from the set-up by which they are used. In most studies, CAs are performed within an environment which resembles a small batch like system and report these performances as a representation of how the catalyst would perform in real system with a fresh electrolyte solution during the duration of test. However, the relevance of batch operations at-scale and comparing them to continuous water electrolysis is not trivial, poorly studied in GEOR and may lead to certain inaccurate interpretations. For example, most studies report the selectivity of the catalyst from a small batch electrolyte after operating for several hours and report high selectivity. However, is the high selectivity from the single pass conversion of glycerol to said product or competitive electrooxidation of other products? Most GEOR reported selectivity's represent the overall selectivity and not the single pass selectivity but are reported as such or omitted, where the former has a major implication for the applicability of a catalyst for continuous operation. An example would be an electrocatalyst which has a high single pass selectively of glycerol to formate, which would show its practicality for a continuous operation. However, an overall selectivity for formate does not provide the same information on this important engineering consideration. This can be counter argued for some C_3 products which are produced from a single reaction step [50], but these catalysts are too few in literature. In the case of $Ni_{90}Bi_{10}$ as shown in figure 5.16 a and b, an increase in operating time results in an increase in formate selectivity (a deeper oxidation of glycerol and its other products), which would indicate selectivity at the beginning of the test differed from the

end, suggesting glycerol's products are further oxidising which represents the overall selectivity and not the single pass selectivity. However, the work reported by Goetz et al. 2022 shows the selectivity of Ni doesn't change overtime in figure 16 c, which can be a more accurate representation of the single pass selectivity of Ni [53].

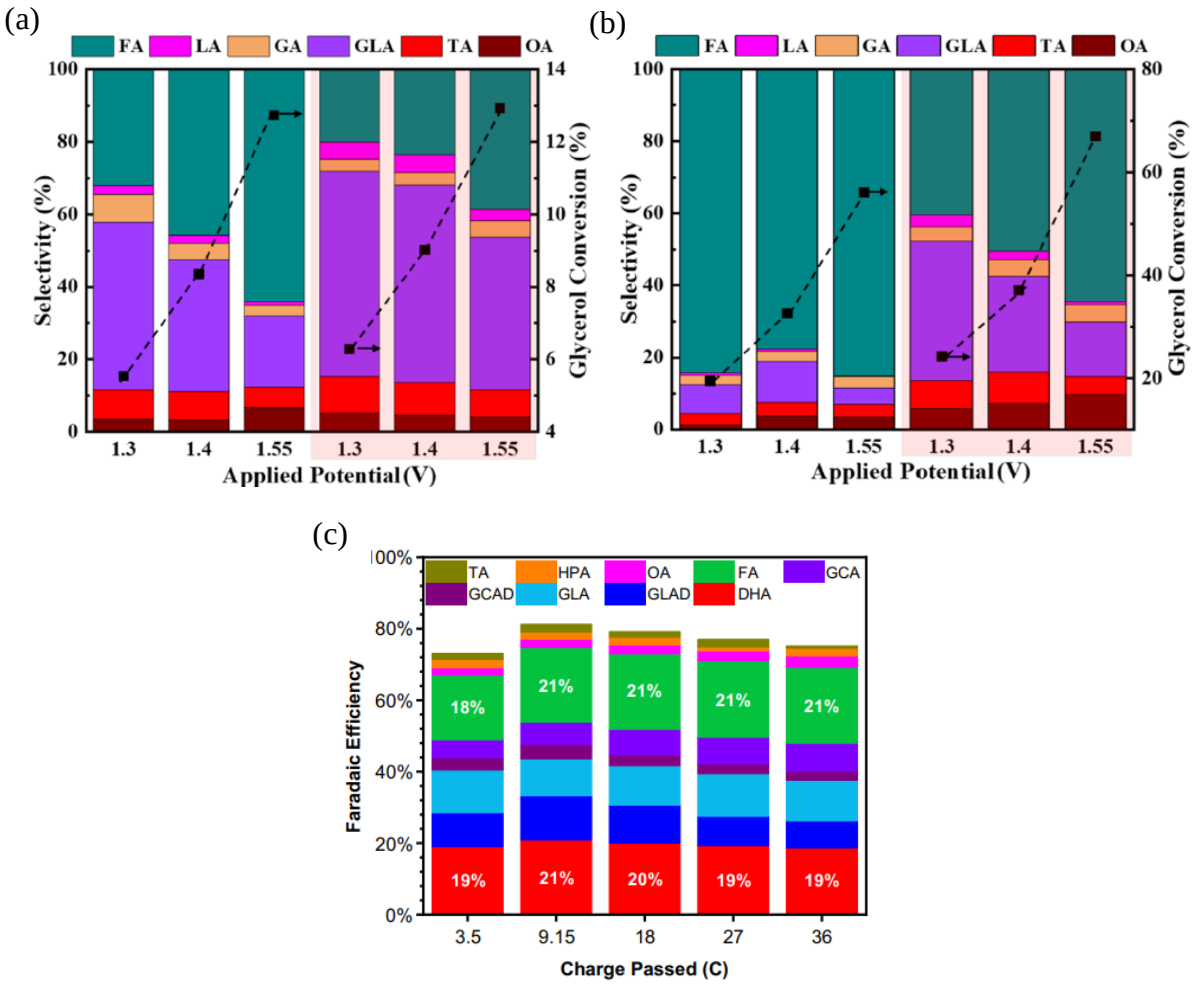

Figure 2.16) (A and B) Product distributions and glycerol conversion (dashed line) under different applied potentials and temperatures over $Ni_{90}Bi_{10}$ in 1M KOH + 0.1M glycerol. The left-hand figure (A) illustrates the product distribution after 30 minutes, while the right hand (B) illustrates the products after 6 hours. Red and not red shaded areas are performed at 25°C and 50°C. Figure from Hoauche et al. 2020 [49]. (C) $Ni(OH)_2$ electrode film faradaic efficiencies based on product distribution through electrolysis at pH 11 at 1.57 V vs RHE from Goetz et al. 2022 [53].

Another research gap is the effect of electrolyte composition for both CAs and CVs. Nearly all GEOR studies perform their experiments in fixed conditions which are considered as standard

[64, 68]. For example, Ni based GEOR is investigated in 0.1M glycerol and noble metals are investigated in 1M glycerol without investigating the impact of spent electrolyte or varying glycerol concentrations. While the reason for this decision is based on few electrolyte composition studies, the investigation of solution composition is critical for any novel catalysis study [65, 69]. In the case of GEOR for noble metals, a concern is the effect of unknown poisonous products on GEOR reactivity and glycerol competing with OH^* [50]. However, Pérez-Martinez et al. 2021 demonstrated that measuring the CA performance of the same catalyst in the same spent electrolyte consequentially reduced the catalyst durability due to the different electrolyte composition and not due to the catalyst [52]. This has major implications for large scale application since it suggests GEOR catalysts, and not OER, should consider their poison resistance along an electrolyser since the electrolyte composition evolves along the cell. Similarly, Goetz et al. [53] demonstrate that a change in pH (OH^- concentration), the selectivity of Ni changed significantly and the propensity for β-Ni(OOH) an NiO_2 to be formed (figure 2.14). If the goal is to achieve high conversion and selectivity, can the catalyst downstream of an electrolyser be selective enough to avoid further oxidising target products at low glycerol concentrations in solution and be resistant to possible poisons? However, only Pérez-Martinez et al. 2021 has investigated this question but as an observation rather than a dedicated study [52]. This is a major engineering consideration at large scale that is different from OER electrolyser designs.

Another limitation is most studies perform CAs or CVs on static 3-electrode cells with no convectional flow [62, 68]. Since GEOR selectivity and reactivity is dependent on the favourable adsorption of key reactants, the effect of convective flow is seldom investigated as well [68]. Convective flow is often measured using a rotating disk electrode in electrochemistry [62]. However, even rotating disk electrodes do not reflect the performance of the small or large electrolysers since the convective flow dynamics are sufficiently different to cause divergences for even straightforward reactions such as HER or OER [62]. In turn, studies should perform electrolyser tests (figure 2.17) [62].

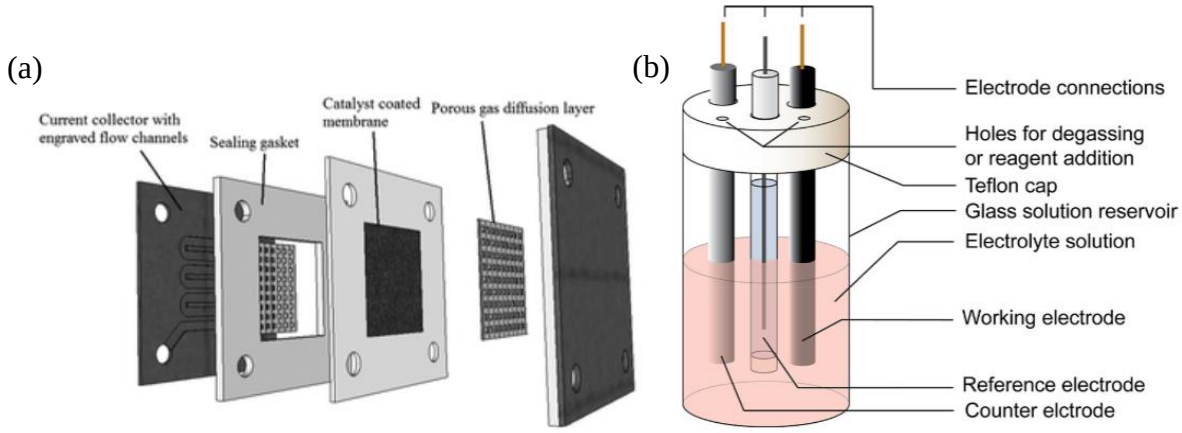

Figure 2.17: Diagrams of the physical layout of a (a) zero-gap electrolyser [1] and static three-electrode cell [59].

Finally, GEOR literature seldom reports polarization curves in an electrolyser, where electrolyser measurements are already seldom performed [54–57]. Polarization curves provide key at-scale information on the performance profile of a catalyst outputs for a potential window. The major difference between CVs or LSVs performed on small static electrodes to an electrolyser polarization curve is the environment are different as previously discussed. One can perform LSVs or CVs on an electrolyser but the issue of achieving steady state is a major concern for complex reactions where multiple reactants evolve. As seen from CAs in figure 2.15, the catalyst performance degrades significantly but also steadily overtime which represents the true performance of the catalyst (which is 4.8x smaller than the initial current). One can instead perform consecutive chronopotentiograms (CP - constant current) or CAs at increasing currents or potentials and record the measured current when steady state is achieved, respectively. However, polarization curves are rare in the field and most (if not all) are performed under LSV conditions which is appropriate for OER due to its straightforward reaction but may not be for a complex GEOR reaction as shown in Figure 2.11.

In turn, the primary objective of this thesis is to report the electrolyser performance of previously characterized Ni based catalysts from previous publications in this research group (Dr. Houache and Asma Shubair) over Ni, $Ni_{90}Bi_{10}$, Ni/C, $Ni_{95}Bi_5$/C, $Ni_{80}Au_{20}$/C and $Ni_{80}Pd_{20}$/C [48, 49, 65, 70, 71]. An emphasis will be placed on reporting CP based polarization curves, performing CP stability tests at a constant current (i.e. H_2 production rate), record the power consumption of H_2, observe and explain the effects of glycerol and KOH concentration over GEOR. Additionally, the

electrolyser is a membrane-free cell, hence an investigation on the impact of glycerol on HER will also be performed.

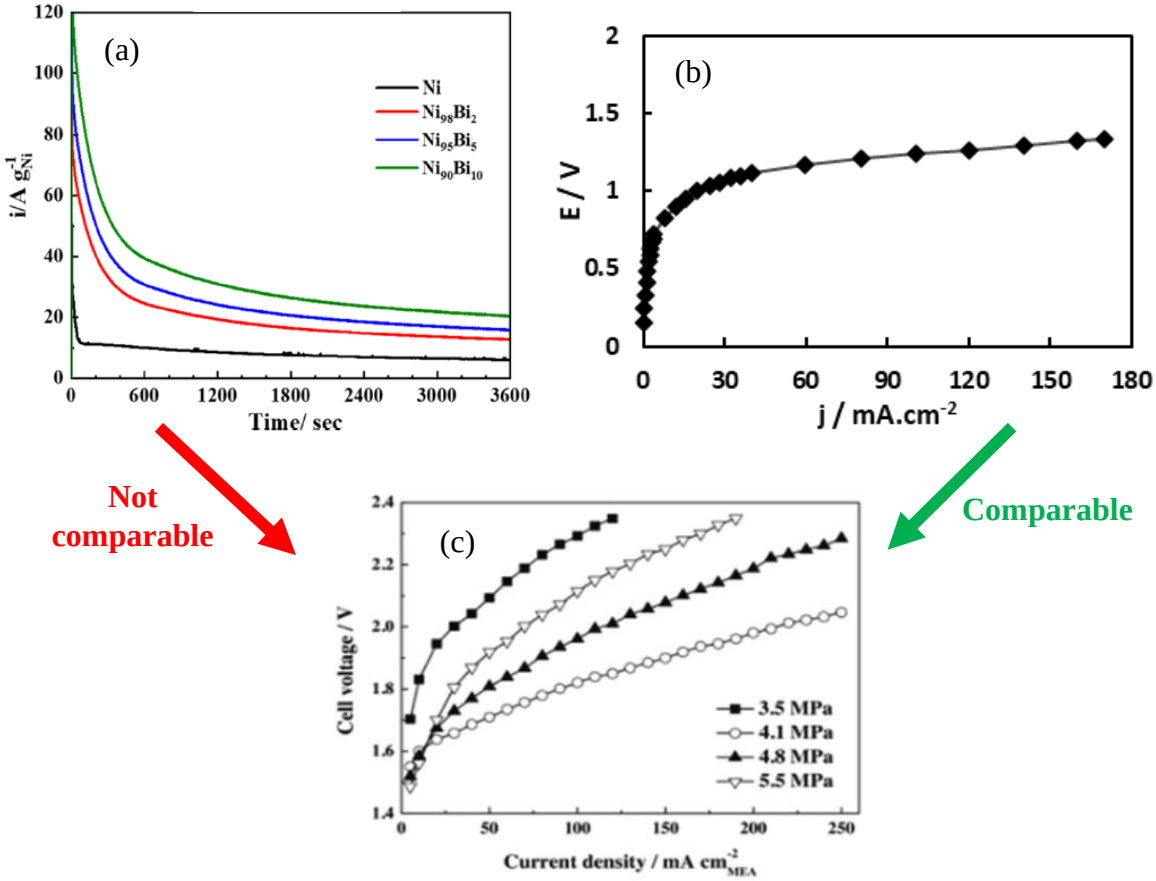

Figure 2.18) (a) CA tests in 1M KOH and 0.1M glycerol at 0.48 V of $Ni_{90}Bi_{10}$. (b) Polarization curve of $Ni_{80}Pd_{20}$/C in Chapter 5 in 1M glycerol and 1M KOH. (c) Polarization curve demonstrating the influence of operating pressure on an AEM WE. Figure (a) and (c) originates from Houache et al. 2020 [49] and Philips et al. 2016 [1].

2.5 References

[1] Phillips, R.; Dunnill, C. W. Zero Gap Alkaline Electrolysis Cell Design for Renewable Energy Storage as Hydrogen Gas. *RSC Advances*. Royal Society of Chemistry 2016, pp 100643–100651. https://doi.org/10.1039/c6ra22242k.

[2] Tremel, A. Electrolysis–Fundamental Technologies, Requirements and Current Status. In *SpringerBriefs in Applied Sciences and Technology*; Springer Verlag, 2018; pp 19–31. https://doi.org/10.1007/978-3-319-72459-1_2.

[3] Yang, B.; Zhang, R.; Shao, Z.; Zhang, C. The Economic Analysis for Hydrogen Production Cost towards Electrolyzer Technologies: Current and Future Competitiveness. *Int J Hydrogen Energy*, **2023**, *48* (37), 13767–13779. https://doi.org/10.1016/j.ijhydene.2022.12.204.

[4] Dolle, C.; Neha, N.; Coutanceau, C. Electrochemical Hydrogen Production from Biomass. *Current Opinion in Electrochemistry*. Elsevier B.V. February 1, 2022. https://doi.org/10.1016/j.coelec.2021.100841.

[5] Tlili, O.; De Rivaz, S.; Lucchese, P. *TASK 38 FINAL REPORT POWER-TO-HYDROGEN AND HYDROGEN-TO-X: SYSTEM ANALYSIS OF THE TECHNO-ECONOMIC, LEGAL AND REGULATORY CONDITIONS Report Coordinated by POWER-TO-HYDROGEN AND HYDROGEN-TO-X: SYSTEM ANALYSIS OF THE TECHNO-ECONOMIC, LEGAL AND REGULATORY CONDITIONS Task Force: Power-to-Hydrogen and Hydrogen-to-X Pathways: Clearing the Definitions from Ambiguities 31*; 2020.

[6] The Honourable Galvez, R.; The Honourable Verner, J. Hydrogen-Energy-Report_e_Final_WEB (1). *The Standing Senate committee on Energy, Natural Resources and Environment Canada*, **2023**.

[7] Shiva Kumar, S.; Himabindu, V. Hydrogen Production by PEM Water Electrolysis – A Review. *Materials Science for Energy Technologies*. KeAi Communications Co. December 1, 2019, pp 442–454. https://doi.org/10.1016/j.mset.2019.03.002.

[8] Ahmad Kamaroddin, M. F.; Sabli, N.; Tuan Abdullah, T. A.; Siajam, S. I.; Abdullah, L. C.; Abdul Jalil, A.; Ahmad, A. Membrane-Based Electrolysis for Hydrogen Production: A Review. *Membranes*. MDPI November 1, 2021. https://doi.org/10.3390/membranes11110810.

[9] Khalid, H.; Najibah, M.; Park, H. S.; Bae, C.; Henkensmeier, D. Membranes Properties of Anion Exchange Membranes with a Focus on Water Electrolysis. **2022**. https://doi.org/10.3390/membranes.

[10] Ge, Z.; Fu, B.; Zhao, J.; Li, X.; Ma, B.; Chen, Y. A Review of the Electrocatalysts on Hydrogen Evolution Reaction with an Emphasis on Fe, Co and Ni-Based Phosphides.

Journal of Materials Science. Springer October 1, 2020, pp 14081–14104. https://doi.org/10.1007/s10853-020-05010-w.

[11] Mohammed-Ibrahim, J.; Xiaoming, S. Recent Progress on Earth Abundant Electrocatalysts for Hydrogen Evolution Reaction (HER) in Alkaline Medium to Achieve Efficient Water Splitting – A Review. *Journal of Energy Chemistry*. Elsevier B.V. July 1, 2019, pp 111–160. https://doi.org/10.1016/j.jechem.2018.09.016.

[12] Ehrnst, Y.; Sherrell, P. C.; Rezk, A. R.; Yeo, L. Y. Acoustically-Induced Water Frustration for Enhanced Hydrogen Evolution Reaction in Neutral Electrolytes. *Adv Energy Mater*, **2023**, *13* (7). https://doi.org/10.1002/aenm.202203164.

[13] Dong, S.; Li, Y.; Zhao, Z.; Li, R.; He, J.; Yin, J.; Yan, B.; Zhang, X. A Review of the Application of Heterostructure Catalysts in Hydrogen Evolution Reaction. *ChemistrySelect*. John Wiley and Sons Inc April 12, 2022. https://doi.org/10.1002/slct.202104041.

[14] Anantharaj, S.; Ede, S. R.; Sakthikumar, K.; Karthick, K.; Mishra, S.; Kundu, S. Recent Trends and Perspectives in Electrochemical Water Splitting with an Emphasis on Sulfide, Selenide, and Phosphide Catalysts of Fe, Co, and Ni: A Review. *ACS Catalysis*. American Chemical Society December 2, 2016, pp 8069–8097. https://doi.org/10.1021/acscatal.6b02479.

[15] Du, N.; Roy, C.; Peach, R.; Turnbull, M.; Thiele, S.; Bock, C. Anion-Exchange Membrane Water Electrolyzers. *Chemical Reviews*. American Chemical Society July 13, 2022, pp 11830–11895. https://doi.org/10.1021/acs.chemrev.1c00854.

[16] Jia, Q.; Liu, E.; Jiao, L.; Li, J.; Mukerjee, S. Current Understandings of the Sluggish Kinetics of the Hydrogen Evolution and Oxidation Reactions in Base. *Current Opinion in Electrochemistry*. Elsevier B.V. December 1, 2018, pp 209–217. https://doi.org/10.1016/j.coelec.2018.11.017.

[17] Dong, S.; Li, Y.; Zhao, Z.; Li, R.; He, J.; Yin, J.; Yan, B.; Zhang, X. A Review of the Application of Heterostructure Catalysts in Hydrogen Evolution Reaction. *ChemistrySelect*. John Wiley and Sons Inc April 12, 2022. https://doi.org/10.1002/slct.202104041.

[18] Lao, M.; Li, P.; Jiang, Y.; Pan, H.; Dou, S. X.; Sun, W. From Fundamentals and Theories to Heterostructured Electrocatalyst Design: An in-Depth Understanding of Alkaline Hydrogen Evolution Reaction. *Nano Energy*. Elsevier Ltd July 1, 2022. https://doi.org/10.1016/j.nanoen.2022.107231.

[19] Kfle Gebremariam, G.; Jovanović, A.; Dobrota, A.; Pasti, I.; K Gebremariam, G.; Jovanović, A. Z.; Dobrota, A. S.; Skorodumova, N. V; Pašti, I. A. Hydrogen Evolution Volcano(Es)-From Acidic to Neutral and Alkaline Solutions Optimizing Fuel Cell Catalyst Stability upon Integration with Reforming-OFICeR (NATO SPS Project 2020-2023) View Project New Approaches to the Understanding of the Electrochemical

Properties of Nanocarbons under Operating Conditions View Project Hydrogen Evolution Volcano(Es)-From Acidic to Neutral and Alkaline Solutions. **2022**. https://doi.org/10.20944/preprints202211.0246.v1.

[20] Hu, Q.; Gao, K.; Wang, X.; Zheng, H.; Cao, J.; Mi, L.; Huo, Q.; Yang, H.; Liu, J.; He, C. Subnanometric Ru Clusters with Upshifted D Band Center Improve Performance for Alkaline Hydrogen Evolution Reaction. *Nat Commun*, **2022**, *13* (1). https://doi.org/10.1038/s41467-022-31660-2.

[21] Yu, X.; Qu, L.; Lee, C.; Peng, J.; Yan, Q.; Bai, H.; Yao, M. Bismuth-Nickel Bimetal Nanosheets with a Porous Structure for Efficient Hydrogen Production in Neutral and Alkaline Media. *Nanoscale*, **2022**, *5*. https://doi.org/10.1039/d2nr04407b.

[22] Yu, K.; Ning, G.; Yang, J.; Wang, Y.; Zhang, X.; Qin, Y.; Luan, C.; Yu, L.; Jiang, Y.; Luan, X.; et al. Restructured PtNi on Ultrathin Nickel Hydroxide for Enhanced Performance in Hydrogen Evolution and Methanol Oxidation. *J Catal*, **2019**, *375*, 267–278. https://doi.org/10.1016/j.jcat.2019.06.006.

[23] Dong, L.; Chang, G.-R.; Feng, Y.; Yao, X.-Z.; Yu, X.-Y. Regulating Ni Site in NiV LDH for Efficient Electrocatalytic Production of Formate and Hydrogen by Glycerol Electrolysis. https://doi.org/10.1007/s12598.

[24] Ge, Z.; Fu, B.; Zhao, J.; Li, X.; Ma, B.; Chen, Y. A Review of the Electrocatalysts on Hydrogen Evolution Reaction with an Emphasis on Fe, Co and Ni-Based Phosphides. *Journal of Materials Science*. Springer October 1, 2020, pp 14081–14104. https://doi.org/10.1007/s10853-020-05010-w.

[25] You, B.; Jiang, N.; Liu, X.; Sun, Y. Simultaneous H 2 Generation and Biomass Upgrading in Water by an Efficient Noble-Metal-Free Bifunctional Electrocatalyst . *Angewandte Chemie*, **2016**, *128* (34), 10067–10071. https://doi.org/10.1002/ange.201603798.

[26] Vo, T. G.; Tran, G. S.; Chiang, C. L.; Lin, Y. G.; Chang, H. E.; Kuo, H. H.; Chiang, C. Y.; Hsu, Y. J. Au@NiSx Yolk@Shell Nanostructures as Dual-Functional Electrocatalysts for Concomitant Production of Value-Added Tartronic Acid and Hydrogen Fuel. *Adv Funct Mater*, **2023**, *33* (4). https://doi.org/10.1002/adfm.202209386.

[27] Song, Y.; Wan, X.; Miao, Y.; Li, J.; Ren, Z.; Jin, B.; Zhou, H.; Li, Z.; Shao, M. Blocking Oxygen Evolution Reaction for Efficient Organic Electrooxidation Coupling Hydrogen Production by Using Layered Double Hydroxide Rich in Active Oxygen. *Appl Catal B*, **2023**, *333*. https://doi.org/10.1016/j.apcatb.2023.122808.

[28] Ren, Z.; Jiang, H.; Yuan, M.; Xie, Z.; Deng, L.; Han, J.; Lyu, K.; Zhu, Y.; Li, X.; Zhuang, L. Si Regulation of Hydrogen Adsorption on Nanoporous PdSi Hybrids towards Enhancing Electrochemical Hydrogen Evolution Activity. *Inorg Chem Front*, **2022**, *10* (4), 1101–1111. https://doi.org/10.1039/d2qi02182j.

[29] Husin, H.; Su, W. N.; Pan, C. J.; Liu, J. Y.; Rick, J.; Yang, S. C.; Chuang, W. T.; Sheu, H. S.; Hwang, B. J. Pd/NiO Core/Shell Nanoparticles on La0.02Na 0.98TaO3 Catalyst for Hydrogen Evolution from Water and Aqueous Methanol Solution. *Int J Hydrogen Energy*, **2013**, *38* (31), 13529–13540. https://doi.org/10.1016/j.ijhydene.2013.07.116.

[30] Li, J.; Zhou, P.; Li, F.; Ren, R.; Liu, Y.; Niu, J.; Ma, J.; Zhang, X.; Tian, M.; Jin, J.; et al. Ni@Pd/PEI-RGO Stack Structures with Controllable Pd Shell Thickness as Advanced Electrodes for Efficient Hydrogen Evolution. *J Mater Chem A Mater*, **2015**, *3* (21), 11261–11268. https://doi.org/10.1039/c5ta01805f.

[31] Sun, H. Y.; Ding, Y.; Yue, Y. Q.; Xue, Q.; Li, F. M.; Jiang, J. X.; Chen, P.; Chen, Y. Bifunctional Palladium Hydride Nanodendrite Electrocatalysts for Hydrogen Evolution Integrated with Formate Oxidation. *ACS Appl Mater Interfaces*, **2021**, *13* (11), 13149–13157. https://doi.org/10.1021/acsami.0c22106.

[32] Dong, L.; Chang, G.-R.; Feng, Y.; Yao, X.-Z.; Yu, X.-Y. Regulating Ni Site in NiV LDH for Efficient Electrocatalytic Production of Formate and Hydrogen by Glycerol Electrolysis. https://doi.org/10.1007/s12598.

[33] Han, X.; Sheng, H.; Yu, C.; Walker, T. W.; Huber, G. W.; Qiu, J.; Jin, S. Electrocatalytic Oxidation of Glycerol to Formic Acid by CuCo2O4Spinel Oxide Nanostructure Catalysts. *ACS Catal*, **2020**, *10* (12), 6741–6752. https://doi.org/10.1021/acscatal.0c01498.

[34] Yu, X.; dos Santos, E. C.; White, J.; Salazar-Alvarez, G.; Pettersson, L. G. M.; Cornell, A.; Johnsson, M. Electrocatalytic Glycerol Oxidation with Concurrent Hydrogen Evolution Utilizing an Efficient MoOx/Pt Catalyst. *Small*, **2021**, *17* (44). https://doi.org/10.1002/smll.202104288.

[35] Zhang, C.; Liu, S.; Mao, Z.; Liang, X.; Chen, B. Ag-Ni Core-Shell Nanowires with Superior Electrocatalytic Activity for Alkaline Hydrogen Evolution Reaction. *J Mater Chem A Mater*, **2017**, *5* (32), 16646–16652. https://doi.org/10.1039/c7ta04220e.

[36] Andonoglou, P. P.; Jannakoudakis, A. D. *Palladium Deposition on Activated Carbon Fibre Supports and Electrocatalytic Activity of the Modified Electrodes towards the Hydrogen Evolution Reaction*; 1997; Vol. 42.

[37] Li, Y.; Chen, S.; Long, R.; Ju, H.; Wang, Z.; Yu, X.; Gao, F.; Cai, Z.; Wang, C.; Xu, Q.; et al. Near-Surface Dilution of Trace Pd Atoms to Facilitate Pd-H Bond Cleavage for Giant Enhancement of Electrocatalytic Hydrogen Evolution. *Nano Energy*, **2017**, *34*, 306–312. https://doi.org/10.1016/j.nanoen.2017.02.048.

[38] Ledendecker, M.; Mondschein, J. S.; Kasian, O.; Geiger, S.; Göhl, D.; Schalenbach, M.; Zeradjanin, A.; Cherevko, S.; Schaak, R. E.; Mayrhofer, K. Stability and Activity of Non-Noble-Metal-Based Catalysts Toward the Hydrogen Evolution Reaction. *Angewandte Chemie*, **2017**, *129* (33), 9899–9903. https://doi.org/10.1002/ange.201704021.

[39] Yang, X.; Xi, M.; Guo, X.; Shen, J.; Liu, Z.; Jiang, H.; Zhu, Y. Ni−CeO2 Heterostructure Promotes Hydrogen Evolution Reaction via Tuning of the O−H Bond Length of Adsorbed Water at the Electrolyte/Electrode Interface. *ChemSusChem*, **2023**, *16* (17). https://doi.org/10.1002/cssc.202300348.

[40] Simões, M.; Baranton, S.; Coutanceau, C. Electrochemical Valorisation of Glycerol. *ChemSusChem*. November 2012, pp 2106–2124. https://doi.org/10.1002/cssc.201200335.

[41] Zhou, W.; Chen, S.; Meng, X.; Li, J.; Gao, J. Energy-Saving Cathodic H2 Production Enabled by Non-Oxygen Evolution Anodic Reactions: A Critical Review on Fundamental Principles and Applications. *International Journal of Hydrogen Energy*. Elsevier Ltd May 15, 2023, pp 15748–15770. https://doi.org/10.1016/j.ijhydene.2023.01.063.

[42] Pirzadi, Z.; Meshkani, F. From Glycerol Production to Its Value-Added Uses: A Critical Review. *Fuel*. Elsevier Ltd December 1, 2022. https://doi.org/10.1016/j.fuel.2022.125044.

[43] Shubair, A.; Houache, M. S. E.; Mousavi M, S. S.; Botton, G. A.; Baranova, E. A. Electrolysis of Glycerol to Value-Added Chemicals in Alkaline Media. *Journal of Chemical Technology and Biotechnology*, **2022**, *97* (8), 1950–1958. https://doi.org/10.1002/jctb.7088.

[44] Elsaid, K.; Abdelfatah, S.; Abdel Elabsir, A. M.; Hassiba, R. J.; Ghouri, Z. K.; Vechot, L. Direct Alcohol Fuel Cells: Assessment of the Fuel's Safety and Health Aspects. *Int J Hydrogen Energy*, **2021**, *46* (59), 30658–30668. https://doi.org/10.1016/j.ijhydene.2020.12.009.

[45] Kim, H. J.; Kim, Y.; Lee, D.; Kim, J. R.; Chae, H. J.; Jeong, S. Y.; Kim, B. S.; Lee, J.; Huber, G. W.; Byun, J.; et al. Coproducing Value-Added Chemicals and Hydrogen with Electrocatalytic Glycerol Oxidation Technology: Experimental and Techno-Economic Investigations. *ACS Sustain Chem Eng*, **2017**, *5* (8), 6626–6634. https://doi.org/10.1021/acssuschemeng.7b00868.

[46] Khan, M. A.; Al-Attas, T. A.; Yasri, N. G.; Zhao, H.; Larter, S.; Hu, J.; Kibria, M. G. Techno-Economic Analysis of a Solar-Powered Biomass Electrolysis Pathway for Coproduction of Hydrogen and Value-Added Chemicals. *Sustain Energy Fuels*, **2020**, *4* (11), 5568–5577. https://doi.org/10.1039/d0se01149e.

[47] Wu, J.; Yang, X.; Gong, M. Recent Advances in Glycerol Valorization via Electrooxidation: Catalyst, Mechanism and Device. *Chinese Journal of Catalysis*. Science Press December 1, 2022, pp 2966–2986. https://doi.org/10.1016/S1872-2067(22)64121-4.

[48] Houache, M. S. E.; Shubair, A.; Sandoval, M. G.; Safari, R.; Botton, G. A.; Jasen, P. V.; González, E. A.; Baranova, E. A. Influence of Pd and Au on Electrochemical

Valorization of Glycerol over Ni-Rich Surfaces. *J Catal*, **2021**, *396*, 1–13. https://doi.org/10.1016/j.jcat.2021.02.008.

[49] Houache, M. S. E.; Hughes, K.; Safari, R.; Botton, G. A.; Baranova, E. A. Modification of Nickel Surfaces by Bismuth: Effect on Electrochemical Activity and Selectivity toward Glycerol. *ACS Appl Mater Interfaces*, **2020**, *12* (13), 15095–15107. https://doi.org/10.1021/acsami.9b22378.

[50] Li, T.; Harrington, D. A. An Overview of Glycerol Electrooxidation Mechanisms on Pt, Pd and Au. *ChemSusChem*. John Wiley and Sons Inc March 22, 2021, pp 1472–1495. https://doi.org/10.1002/cssc.202002669.

[51] Swenson, H.; Stadie, N. P. Langmuir's Theory of Adsorption: A Centennial Review. *Langmuir*, **2019**. https://doi.org/10.1021/acs.langmuir.9b00154.

[52] Pérez-Martínez, L.; Balke, L.; Cuesta, A. Reactive and Inhibiting Species in the Electrocatalytic Oxidation of Glycerol on Gold. A Study Combining in-Situ Visible Reflectance and ATR-SEIRAS. *J Catal*, **2021**, *394*, 1–7. https://doi.org/10.1016/j.jcat.2020.12.010.

[53] Goetz, M. K. K.; Bender, M. T.; Choi, K. S. Predictive Control of Selective Secondary Alcohol Oxidation of Glycerol on NiOOH. *Nat Commun*, **2022**, *13* (1). https://doi.org/10.1038/s41467-022-33637-7.

[54] Ruiz-López, E.; Diaz-Perez, M. A.; de Lucas-Consuegra, A.; Dorado, F.; Serrano-Ruiz, J. C. Membrane-Less Ethanol Electrooxidation over Pd-m (M: Sn, Mo and Re) Bimetallic Catalysts. *Catalysts*, **2021**, *11* (5). https://doi.org/10.3390/catal11050541.

[55] Bambagioni, V.; Bianchini, C.; Marchionni, A.; Filippi, J.; Vizza, F.; Teddy, J.; Serp, P.; Zhiani, M. Pd and Pt-Ru Anode Electrocatalysts Supported on Multi-Walled Carbon Nanotubes and Their Use in Passive and Active Direct Alcohol Fuel Cells with an Anion-Exchange Membrane (Alcohol = Methanol, Ethanol, Glycerol). *J Power Sources*, **2009**, *190* (2), 241–251. https://doi.org/10.1016/j.jpowsour.2009.01.044.

[56] García-Cruz, L.; Sáez, A.; Ania, C. O.; Solla-Gullón, J.; Thiemann, T.; Iniesta, J.; Montiel, V. Electrocatalytic Activity of Ni-Doped Nanoporous Carbons in the Electrooxidation of Propargyl Alcohol. *Carbon N Y*, **2014**, *73*, 291–302. https://doi.org/10.1016/j.carbon.2014.02.066.

[57] Morales, E. C.; Kazakova, M. A.; Selyutin, A. G.; Golubtsov, G. V.; Morales, D. M.; Robledo, A. M. Competition between the Oxygen Evolution Reaction and the Electrooxidation of Alcohols on Heteroatom-Functionalized Multi-Walled Carbon Nanotubes-Supported Ni Oxide Catalysts. *Surfaces and Interfaces*, **2024**, *46*. https://doi.org/10.1016/j.surfin.2024.104026.

[58] Morales, D. M.; Jambrec, D.; Kazakova, M. A.; Braun, M.; Sikdar, N.; Koul, A.; Brix, A. C.; Seisel, S.; Andronescu, C.; Schuhmann, W. Electrocatalytic Conversion of Glycerol

to Oxalate on Ni Oxide Nanoparticles-Modified Oxidized Multiwalled Carbon Nanotubes. *ACS Catal*, **2022**, *12* (2), 982–992. https://doi.org/10.1021/acscatal.1c04150.

[59] Elgrishi, N.; Rountree, K. J.; McCarthy, B. D.; Rountree, E. S.; Eisenhart, T. T.; Dempsey, J. L. A Practical Beginner's Guide to Cyclic Voltammetry. *J Chem Educ*, **2018**, *95* (2), 197–206. https://doi.org/10.1021/acs.jchemed.7b00361.

[60] McKenzie, E. C. R.; Hosseini, S.; Petro, A. G. C.; Rudman, K. K.; Gerroll, B. H. R.; Mubarak, M. S.; Baker, L. A.; Little, R. D. Versatile Tools for Understanding Electrosynthetic Mechanisms. *Chemical Reviews*. American Chemical Society February 9, 2022, pp 3292–3335. https://doi.org/10.1021/acs.chemrev.1c00471.

[61] Elgrishi, N.; Rountree, K. J.; McCarthy, B. D.; Rountree, E. S.; Eisenhart, T. T.; Dempsey, J. L. A Practical Beginner's Guide to Cyclic Voltammetry. *J Chem Educ*, **2018**, *95* (2), 197–206. https://doi.org/10.1021/acs.jchemed.7b00361.

[62] Lazaridis, T.; Stühmeier, B. M.; Gasteiger, H. A.; El-Sayed, H. A. Capabilities and Limitations of Rotating Disk Electrodes versus Membrane Electrode Assemblies in the Investigation of Electrocatalysts. *Nat Catal*, **2022**, *5* (5), 363–373. https://doi.org/10.1038/s41929-022-00776-5.

[63] Khalafi, L.; Cunningham, A. M.; Hoober-Burkhardt, L. E.; Rafiee, M. Why Is Voltammetric Current Scan Rate Dependent? Representation of a Mathematically Dense Concept Using Conceptual Thinking. *J Chem Educ*, **2021**, *98* (12), 3957–3961. https://doi.org/10.1021/acs.jchemed.1c00770.

[64] Houache, M. S. E.; Hughes, K.; Ahmed, A.; Safari, R.; Liu, H.; Botton, G. A.; Baranova, E. A. Electrochemical Valorization of Glycerol on Ni-Rich Bimetallic NiPd Nanoparticles: Insight into Product Selectivity Using in Situ Polarization Modulation Infrared-Reflection Absorption Spectroscopy. *ACS Sustain Chem Eng*, **2019**, *7* (17), 14425–14434. https://doi.org/10.1021/acssuschemeng.9b01070.

[65] Houache, M. S. E.; Sandoval, M. G.; Safari, R.; Gaztañaga, F.; Escudero, F.; Hernández-Laguna, A.; Sainz-Díaz, C. I.; Botton, G. A.; Jasen, P. V.; González, E. A.; et al. Morphology Alteration of Nickel Microstructures for Glycerol Electrooxidation. *J Catal*, **2021**, *404*, 348–361. https://doi.org/10.1016/j.jcat.2021.10.010.

[66] Oliveira, V. L.; Morais, C.; Servat, K.; Napporn, T. W.; Olivi, P.; Kokoh, K. B.; Tremiliosi-Filho, G. Kinetic Investigations of Glycerol Oxidation Reaction on Ni/C. *Electrocatalysis*, **2015**, *6* (5), 447–454. https://doi.org/10.1007/s12678-015-0261-2.

[67] Puthiyapura, V. K.; Lin, W. F.; Russell, A. E.; Brett, D. J. L.; Hardacre, C. Effect of Mass Transport on the Electrochemical Oxidation of Alcohols Over Electrodeposited Film and Carbon-Supported Pt Electrodes. *Top Catal*, **2018**, *61* (3–4), 240–253. https://doi.org/10.1007/s11244-018-0893-6.

[68] White, J.; Anil, A.; Martín-Yerga, D.; Salazar-Alvarez, G.; Henriksson, G.; Cornell, A. Electrodeposited PdNi on a Ni Rotating Disk Electrode Highly Active for Glycerol

Electrooxidation in Alkaline Conditions. *Electrochim Acta*, **2022**, *403*. https://doi.org/10.1016/j.electacta.2021.139714.

[69] Oliveira, V. L.; Morais, C.; Servat, K.; Napporn, T. W.; Olivi, P.; Kokoh, K. B.; Tremiliosi-Filho, G. Kinetic Investigations of Glycerol Oxidation Reaction on Ni/C. *Electrocatalysis*, **2015**, *6* (5), 447–454. https://doi.org/10.1007/s12678-015-0261-2.

[70] Houache, M. S. E.; Safari, R.; Nwabara, U. O.; Rafaïdeen, T.; Botton, G. A.; Kenis, P. J. A.; Baranton, S.; Coutanceau, C.; Baranova, E. A. Selective Electrooxidation of Glycerol to Formic Acid over Carbon Supported Ni1- XMx(M = Bi, Pd, and Au) Nanocatalysts and Coelectrolysis of CO2. *ACS Appl Energy Mater*, **2020**, *3* (9), 8725–8738. https://doi.org/10.1021/acsaem.0c01282.

[71] Shubair, A. *Tuning the Selectivity of Bimetallic NiBi Catalysts for Glycerol Electrooxidation into Value-Added Chemicals*.

Chapter 3: The influence of reactive conditions on $Ni_{90}Bi_{10}$ and Ni catalyst on the electro-reforming of glycerol

Abstract

The influence of glycerol concentration, KOH concentration, catalyst loading and temperature on the performance of an electrolyser electro-reforming glycerol via its electrooxidation reaction over Ni catalysts (GEOR) for the production of hydrogen from the hydrogen evolution reaction was investigated. Results demonstrate the impact of glycerol onto Ni GEOR is inhibited past 0.1M glycerol. Preliminary results shows its inhibition may include the suppression of the bulk layer oxidation, reducing e^- conductivity and the necessary bulk Ni^{+3} state needed to de-intercalate inactive Ni^{+2} to its active Ni^{+3} on the catalysts surface. This is theorised to be caused by the perquisite surface Ni^{+3} oxidation state needed to oxidise the bulk Ni is unstable due to its chemical reduction by glycerol at the surface. In turn, evidence in this chapter highlights the need to understand the influence of glycerol on the catalyst's properties. Scaled up to an electrolyser, temperature and concentration tests over $Ni_{90}Bi_{10}$ revealed a novel polarization curve between 0.3-0.8V. Based on the nature of the catalysts, this new polarization curve preliminarily indicates Bi may present a novel form of GEOR reactivity. Durability tests at 4 $mA.cm^{-2}$ (100 mA) operated at 37.9 $kWh.kg_{H2}^{-1}$ with a faradaic efficiency superior to 93%.

3.1 Introduction

The theoretically low onset potential of the glycerol electrooxidation reaction (GEOR) in comparison to traditional anodic reactions like the oxygen evolution reaction (OER) can indirectly reduce the energy consumption of intensive cathodic reactions such as the hydrogen evolution reaction (HER) [1–8]. Due to the classification of glycerol as a side product, GEOR can also produce value added chemicals from the anode unlike OER [5]. In turn, recent efforts have pushed for the development of highly reactive GEOR catalysts which can take advantage of this reduced operating anodic potential [1–3]. This has been achieved for both noble metals and non-noble metals where Ni is a promising commercially viable material due to its abundance and comparable reactivity to noble metals while showing exceptional resistance to poisoning [9].

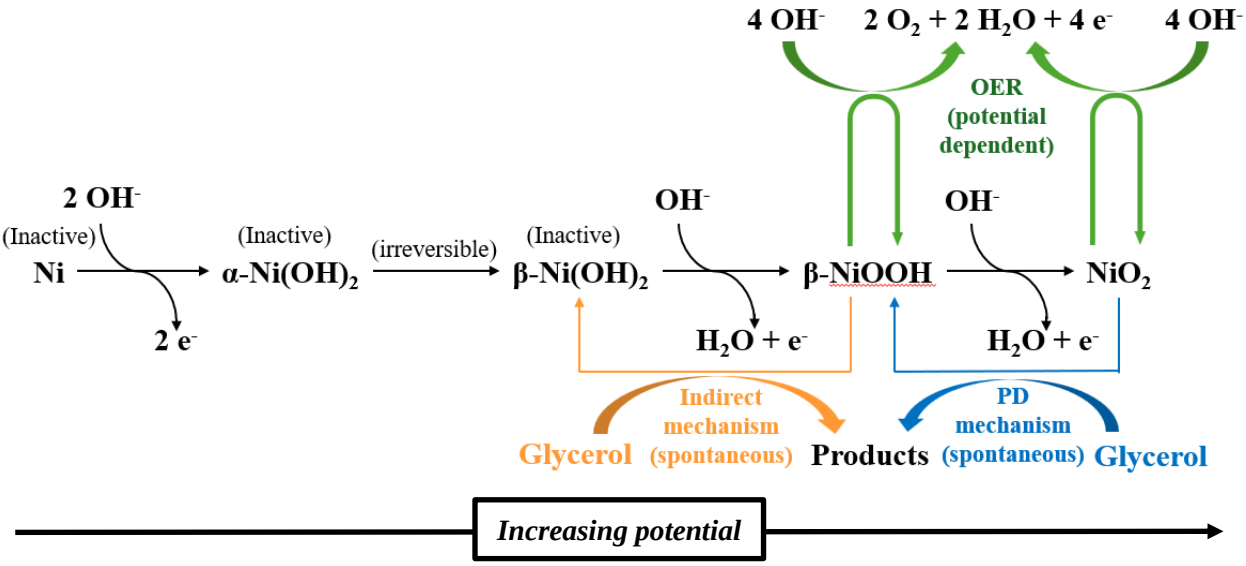

Scheme 3.1) Simplified illustration of the currently established reactive phases and respective mechanism for GEOR over Ni, and the related phases involved in OER [10–13].

That said, while the onset potential of GEOR can be as low as 0.003V, its pragmatic onset potential with a Ni catalyst is equal to the equilibrium potential for the oxidation of Ni^{+2} to generate the active Ni^{+3} site [10]. Mechanistically, Ni electrooxidation of glycerol occurs either by the indirect mechanism [14] or the potential dependent (PD) mechanism [12]. Under the indirect mechanism, glycerol chemisorbs over β-NiOOH (Ni^{+3}) at the Ni active site [14, 15]. The neighbouring O^{*} of Ni^{+3} deprotonates glycerol and Ni^{+3} itself subsequently oxidises glycerol, chemically reducing β-NiOOH back to β-$Ni(OH)_2$ [14, 15]. A similar process is observed for the PD mechanism but involves Ni^{+4}. Due to the stability of Ni in the β-$Ni(OH)_2$ (Ni^{+2}) phase in alkaline

conditions, a minimum potential is required to oxidise Ni^{+2} back to β-NiOOH [5, 6, 10, 16–20]. As a result, the expected operating potential of a GEOR-HER electrolyser is dependent on the necessary electrode oxidation state, not necessarily the Gibbs of reaction of glycerol.

However, the majority of literature has justifiably focused on improving the selectivity of Ni based GEOR catalysts due to the value-added products since it represents the majority of the revenue generated by this type of electrolyser [2, 4–6, 17, 18, 21, 22]. As an unintentional consequence of this focus, there has been an under reporting of the efficacy of the cathodic reaction like HER. Issues arise from this methodology since the practicality of any electrochemical reaction is dependent on both electrode reactions since either reaction can not occur without a closed circuit [23]. Hence, the cathodic reaction should be measured when repeatedly literature claims this should reduce the energy consumption without empirically demonstrating it. Only a few have attempted to measure the efficacy of the accompanying cathodic reaction such as HER at relevant current densities above 200 $mA.cm^{-2}$ [7].

Interestingly, few works have also varied environmental conditions to determine the optimal condition of novel catalysts. This is surprising since in any catalysis field, varying experimental parameters such as temperature or concentrations can provide useful information on the role each of these parameters have on the reaction and clarify the role of the catalyst towards the reaction [24, 25]. For example, while most Ni studies only investigate GEOR at 0.1M glycerol and 1M KOH, Goetz et al. 2022, Bender et al. 2020 and Bender et al. 2021, identified the existence of the PD mechanism through changes in concentrations and scan rates [11–13].

In turn, this chapter re-evaluated the previously characterized and selective $Ni_{90}Bi_{10}$ catalyst by Houache et al. 2020 in both three-electrode and a 25 cm^2 electrolyser cell under various reaction conditions to measure the efficacy of coupling HER with a Ni based GEOR catalyst [26]. Electrolyser testing show the effects of glycerol concentration past 0.1M is detrimental at high currents. However, changes in the oxidation state of the bulk Bi layer preliminary indicates the inhibition of GEOR by glycerol over Ni is caused by a suppression of the bulk layer oxidation. In other words, glycerol influences the properties of the Ni catalysts at the bulk. It is theorized this is caused by glycerol immediately reducing the required $Ni^{+3}_{surface}$ needed for bulk $Ni^{<+3}$ to oxidise to the necessary Ni^{+3} state for GEOR to occur. Furthermore, temperature studies highlight the existence of a low 0.3-0.8V polarization curve over $Ni_{90}Bi_{10}$ past 50°C. In comparison to literature

and the minimum potential required for Ni^{+2} to oxidise, this polarization curve may preliminarily show Bi GEOR reactivity. Due to its small current, this ohmic polarization curve is not observed in small-electrode cell tests due to the low catalyst loading and room temperature condition. Finally, durability testing with Pt/C cathode catalyst show $Ni_{90}Bi_{10}$||Pt/C achieved 37.9 $kWh.kg_{H2}^{-1}$ with a faradaic efficiency superior to 93% at 4 $mA.cm^{-2}$ (100 mA). While this does meet the D.O.E. energy target, it isn't operated at relevant industrial conditions.

3.2 Experimental Section

3.2.1 Catalyst synthesis

Prior to each synthesis, all glassware was cleaned overnight by an Aqua Regia solution. Ni and $Ni_{90}Bi_{10}$ catalysts were synthesised by sodium borohydride ($NaBH_4$) reduction in ethanol at room temperature. Firstly, Nickel (II) chloride hexahydrate ($NiCl_2 \cdot 6(H_2O)$, 99.999%, Sigma-Aldrich) and its accompanying bimetallic salt are each dissolved separately in 20 ml of ethanol for 30 minutes. To ensure complete dissolution, each precursor solution was initially treated to 1 minute of sonication in a sonicating bath (40 kHz Ultrasonic Bath 15,337,409, Fischer Scientific, Hampton, NH, USA) and was kept dissolved by magnetic stirring. The accompanying precursor Bi salt is Bismuth (III) chloride ($BiCl_3$, 99.99%, Fischer Scientific). After 30 minutes, both precursor solutions were combined, sonicated for 1 minute and stirred for 10 minutes to ensure a homogenous metal solution. Then, the precursor solution was reduced by drop wise addition of dissolved $NaBH_4$ in 10 ml of ethanol. After 30 minutes, the solution is completely reduced. Finally, the nanoparticles were washed with ethanol by centrifuging the samples three times at 6000 rpm for 15 minutes. Once washed, the samples were freeze dried overnight to remove residual ethanol.

3.2.2 XRD Characterization

X-ray diffraction (XRD) data was collected for $Ni_{90}Bi_{10}$ with a Rigaku Ultima IV multipurpose diffractometer with Cu Kα radiation (λ = 1.5418 Å) at 40 kV and 44 mA in the range of 20º-80º 2θ with 0.5º $2\theta.min^{-1}$ scanning rate. In addition to identifying different crystal phases, the crystallite size estimated by the Debye-Scherrer equation was used to determine an approximation of the particle sizes:

(equation 3.1) $$D = \frac{0.9\lambda_{Cu}}{\beta_{1/2}\cos(\theta)}$$

Where λ_{Cu} is the x-ray wavelength (0.15418 nm), $\beta_{1/2}$ is the width of the half-maximum of a given peak in radians, θ is the Bragg angle for a peak in question, and D is the size of the crystallite (nm).

3.2.3 Three-electrodes cell electrochemical tests

Electrochemical measurements were performed in a three electrode teflon cell suited for a glassy carbon (0.196 cm^2) working electrode, mercury/mercury oxide (Hg/HgO, Koslow Scientific Company, Englewood, NJ, USA) and platinum mesh reference and counter electrode, respectively. Catalyst inks were composed of 6 mg of catalyst, 1 ml of milli-Q® water Millipore deionized water (18.2 MΩ cm at 293 K), 200 µL of isopropyl alcohol (IPA, 99.9%, Fisher Scientific, Hampton, NH, USA) and 100 µL of 5 wt% Nafion^{TM} (≈5%, Sigma Aldrich, St. Louis, MO, USA). Prior to each test, the glassy carbon surface was polished on a microfabric with a slurry of 30 µm, then 5 µm of Al_2O_3 in Milli-Q® water. Once polished, 10 µL of catalyst ink was casted on the glassy carbon surface and dried in a 60^oC oven. The cell's electrolyte was purged with N_2 gas (Grade 4.8, Linde plc, Dublin, Ireland) for 15 minutes. Then, cyclic voltammetry (CV) and linear sweep voltammetry (LSV) measurements were made using a Bio-Logic Potentiostat/Galvanostat paired with EC labs software (Bio-Logic Science Instruments, Seyssinet-Pariset, France) in various KOH (85.6% purity, EMD, ACS grade) and Glycerol (>99%, Sigma-Aldrich) concentration solution. All potential measurements are presented relative to the reversible hydrogen electrode (RHE) according to the following equation with no IR compensation:

(equation 3.2) $$E_{vsRHE}=E_{vs.Hg/HgO} + 0.098V + 0.0592pH$$

Due to the pH-meter upper calibration limit is 12.9, the electrolyte solution pH was estimated empirically by the model proposed by Hausmann et al. 2021 [27]. It is assumed that glycerol has a negligeable impact on pH up to 2M glycerol as a weak acid with a pKa of 14.15, although this requires validation.

3.2.4 Membrane-free electrolyser assembly and electrochemical tests

All electrolysis measurements were performed in a custom-made zero gap single electrolyser cell with a 25 cm^2 flow field area as shown in Figure 3.S1. The cell constitutes two copper and graphite plates as the current collector and bipolar plates, respectively. The machined flow field patterns in both graphite plates are column-pin. To control the cell temperature, current collectors are fitted with heating pads and a thermocouple on the anode side. Thin Teflon gaskets

are used to electrically insulate the polar plates and ensure a sealed zero-gap cell. A paper filter is used as an inexpensive electrically insulating separator (Whatman).

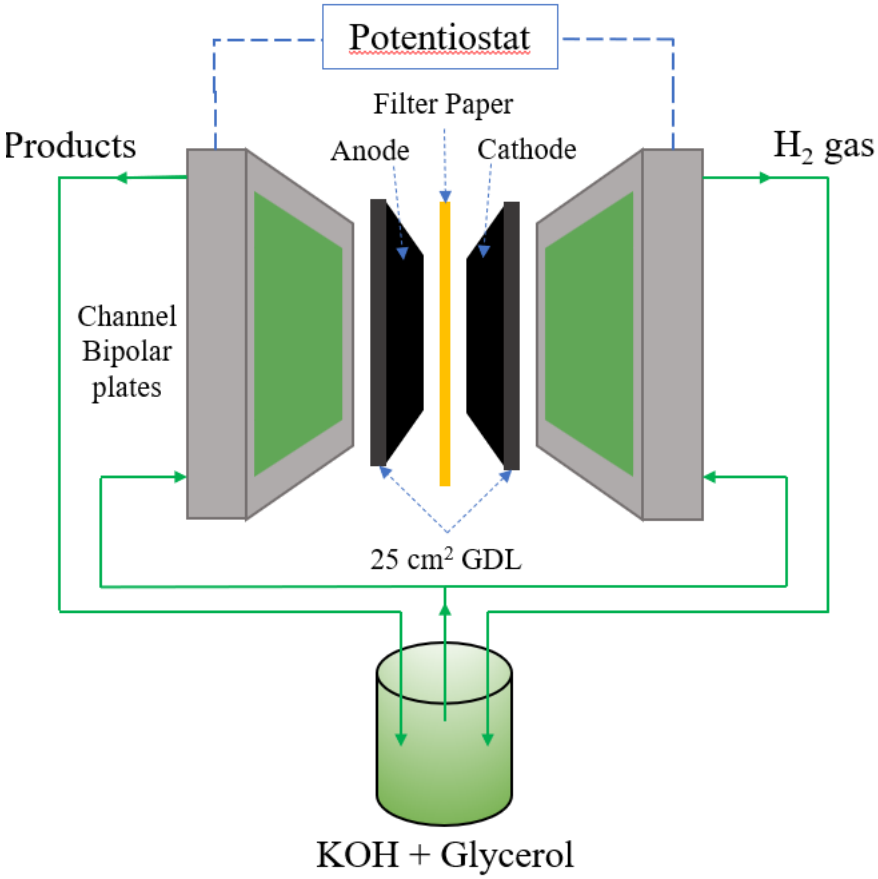

Schematic 3.2) Schematic illustration of the electrolyser setup. Gaskets are not shown but sandwiched between graphite plates.

To mitigate possible glycerol depletion, a 2L heated plastic tank was used to store the electrolyte. To collect hydrogen, the tank was connected to a water filled inverted graduated cylinder in a water bath. Hydrogen collection only began during chronopotentiometry. Prior to each experiment, the electrolyte was purged in N_2 for 2 hours. The electrolyte is pumped to the electrolysis cell at 1.6 mL.s^{-1}. To ensure the temperature of the electrolyte in the cell is close to the desired target, the electrolyte tank was also heated over a hot plate. It is strongly recommended not to do this and use a large warm bath since damage was done to the tank.

The electrodes were prepared in the CCS configuration by hand spraying catalyst ink using an airbrush (Iwata Eclipse HP-BCS, Maple Airbrush Supplies Inc., Edmonton, AB, Canada) onto carbon paper (090 value pack, wet proof, fuel cell store) heated over a hot plate set at 60°C [26, 28].

The catalyst inks were prepared by combining the respective amount of catalyst mass, with a 15 wt% Nafion® loading, diluted with 0.12 ml of H_2O per mg of catalyst and 0.024 ml of IPA per mg of catalyst. Once the ink is formed, it is then sonicated in an icebath for 15 minutes and stirred with a magnetic stir bar to ensure catalyst suspension during spraying.

To perform the electrolysis test, a polarization curve was performed under constant current density via chronopotentiometry (CP). Due to a slow evolution of the polarization curve observed near the activation potential. This is shown in Figure 3.11. Due to this, the individual CAs were performed for 10 min each. This particularly slow data collection was necessary to achieve steady state that is representative of the applied current. Due to the membrane-free operation of the cell, the selectivity of the cathode towards HER was estimated using the following equation [29]:

(equation 3.3) $$\eta_{sel} = \frac{100 * V_{H2,exp}\ (mL)}{\frac{j\ (A.cm^{-2}) * A\ (cm^2) * t\ (s)}{2F\ (C.mol_{H2}^{-1})} * 22771\ (mL.mol_{H2}^{-1})}$$

Where $V_{H2,exp}$ is the experimentally collected hydrogen gas volume; j is the current density, A is the sprayed area of the GDL (25 cm^2); t is the time of the experimental collection of H_2 gas, F is Faraday's constant (96485 C/mol_e). It is noted that $V_{H2,exp}$ represents the sum of H_2 gas collected and t is the time representing the duration of that collection. Also, A is the area of the GDL (25 cm^2) since the current density is calculated as the current divided by the GDL area in this study.

Due to the evolving cell voltage, the trapezoidal method was employed to calculate the energy consumption since the data collection was frequent enough for it to be appropriate. The energy consumption was calculated as follows:

(equation 3.4) $$P_{ele-i}(J.s^{-1}) = V_{cell-i} * I_{cell-i}$$

(equation 3.5) $$E_{tot-ele}(J) = \sum_{i=1}^{i_{max}} \left(\frac{P_{ele\,i} + P_{ele\,i-1}}{2} * (t_i - t_{i-1}) \right)$$

(equation 3.6) $$E_{tot-ele}(kWh) = E_{tot-ele} * \frac{1\ kWh}{3.5*10^6\ J}$$

(equation 3.7) $$W_e(kWh.kg_{H2}^{-1}) = \frac{E_{tot-ele-kWh}}{V_{H2,exp}\ (mL) * 8.2*10^{-8} \frac{kg}{ml}}$$

Where $V_{cell\text{-}I}$ (V) and $I_{cell\text{-}I}$ (A) are the operating votage and current of the electrolyser for a given data point i. P_{ele} is the electrical power (W) consumed for a given data point while $E_{tot\text{-}ele}$ is total

electrical energy (J) consumed during the hydrogen gas collection. W_e is the energy consumption needed to produce a kilogram of H_2 gas where $8.2*10^{-8}$ kg/ml is the density of the H_2 gas at standard temperature an pressure which are the conditions H_2 is measured.

3.3 Results and Discussion

3.3.1 X-ray diffraction of $Ni_{90}Bi_{10}$

XRD was used to validate the expected Ni and Bi lattice structures and was compared to the XRD spectra of the same $Ni_{90}Bi_{10}$ nanoparticle synthesised by Houache et al. 2020 using the same synthesis method to validate it was successfully reproduced [26].

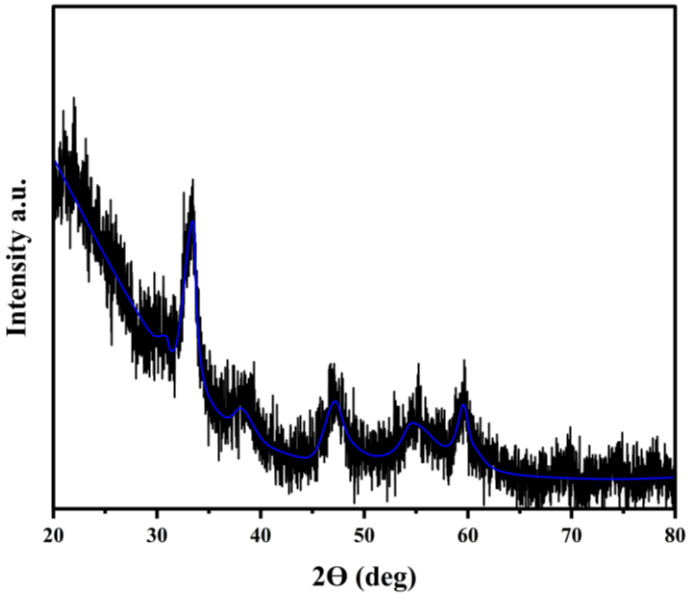

Figure 3.1. XRD pattern of $Ni_{90}Bi_{10}$ nanoparticles.

Table 3.1: Peak Position, FWHM and crystallite size of each phases over $Ni_{90}Bi_{10}$.

Phase	Position (2Θ)	FWHM (deg)	Crystallite size (nm)
β-Bi_2O_3	30.9	1.037	8.3
β-$Ni(OH)_2$ (100)	33.5	1.3171	6.5
Bi (104)	38.2	2.0951	4.2
Bi (006)	47.2	2.3184	3.8
β-Bi_2O_3	54.5	3.8185	2.4
β-$Ni(OH)_2$ (110)	59.5	1.5295	6.3

Figure 3.1 and table 3.1 presents the XRD pattern of $Ni_{90}Bi_{10}$ and its corresponding peak positions, respectively. According to the XRD scans produced by Hoauche et al. 2020 [26],

spherical Ni nanoparticles consist of three characteristic peaks which are found in figure 1 at 33.5º, 69.5º and 69.9º 2Θ which correspond to β-Ni(OH)$_2$ (100), β-Ni(OH)$_2$ (110), and β-Ni(OH)$_2$ (103), respectively. Additionally, the characteristic peaks at 38.2º, 47.2º, 54.5º and 78.0º (figure 1) correspond to Bi (104), Bi (006), β-Bi_2O_3 and Ni (220), which is similar to Houach et al. 2020 $Ni_{90}Bi_{10}$ XRD [26]. An indirect validation of the nanoparticle sizes was determined by applying the Debye-Scherrer equation (Eq 3.1) to each corresponding peak. The crystallite sizes of each peak are found to be between 9 nm and 2 nm as shown in table 3.1, validating the nanosized dimensions of the catalysts [26]. The two highest angle peaks were not included since their FWHM were wide enough that it may not be representative of the crystallite size (<1nm). Although nanosized, it is expected through strong attractive magnetic forces between colloids for the Ni nanoparticles to be agglomerated, which was observed by Houache et al. 2020 [26]. This can increase the effective particle sizes. Overall, XRD results would indicate $Ni_{90}Bi_{10}$ nanoparticles were reproduced from Houache et al. 2020 [26].

3.3.2 1M KOH three electrode electrochemical cell results

To evaluate the performance of the $Ni_{90}Bi_{10}$ electrocatalyst and further verify it was successfully duplicated from Houache et al. 2020, CVs within a 3-electrode cell was performed in 1M KOH in the absence and presence of 0.1M glycerol (Figure 3.2 & 4). A reference Ni only catalysts synthesised the same way is also tested to compare electrochemical properties.

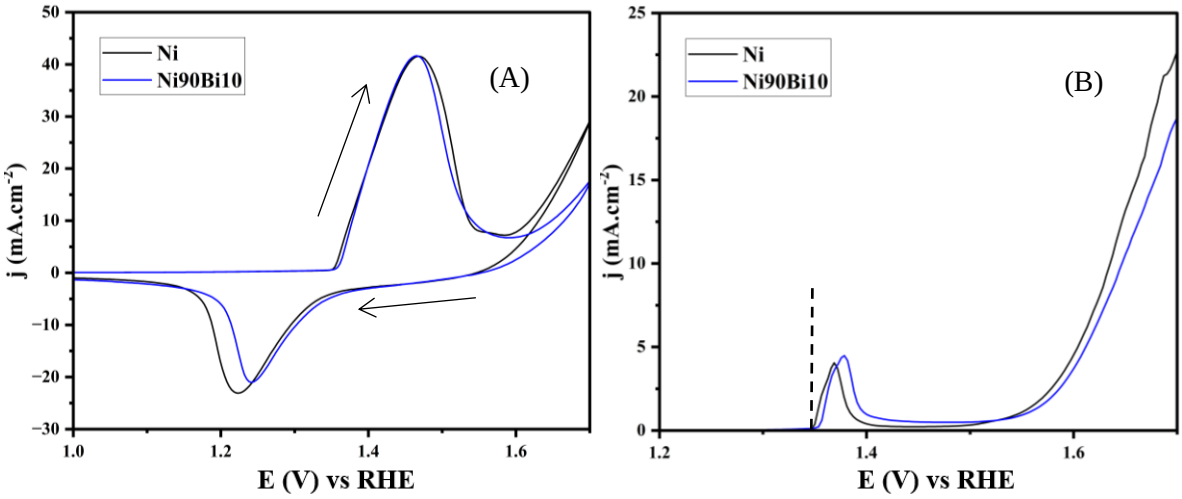

Figure 3.2) (A) 10th CV cycle at 25 mV.s^{-1} and (B) LSV at 1 mV.s^{-1} of Ni and $Ni_{90}Bi_{10}$ performed in 1M KOH and room temperature. Dashed line represents the onset potential.

Figure 3.2A presents the expected CV of Ni^{+2}/Ni^{+3} oxidation and reduction peaks for both catalysts at around 1.45V and 1.23V in 1M KOH only, respectively [10]. The increasing current density wave past 1.57V is OER [16, 30–32]. Between Ni only and $Ni_{90}Bi_{10}$, the β-$Ni(OH)_2$ oxidation peaks have a similar onset potential (≈1.355mV), oxidation peak potential (≈1.45V) and current (≈43 $mA.cm^{-2}$). The reduction peak for $Ni_{90}Bi_{10}$ is displaced positively to 1.25 V from 1.22V in reference to Ni (Figure 3.2A). Considering the Ni^{+2}/Ni^{+3} oxidation peak is similar between catalysts and the reduction current peak is smaller over $Ni_{90}Bi_{10}$, it indicates less Ni is reduced over the surface by the presence of Bi reducing the surface coverage of Ni.

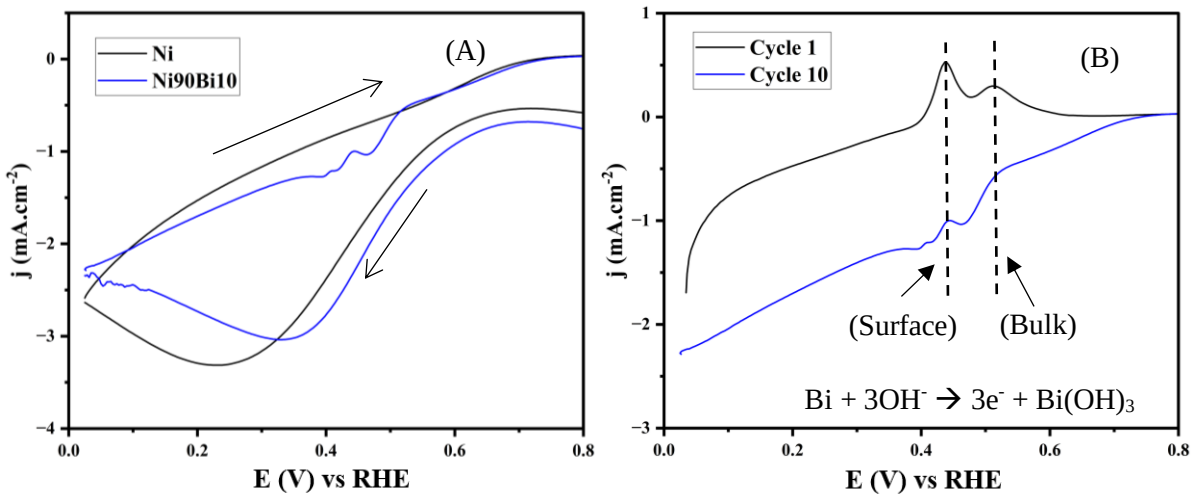

Figure 3.3) 10th cycle CV of Ni and $Ni_{90}Bi_{10}$ performed at 25 $mV.s^{-1}$. (B) The 1st and 10th cycle CVs of $Ni_{90}Bi_{10}$ in 1M KOH. The dashed line show the overlapping oxidation peaks of surface and bulk Bi in between the 1st and 10th cycle.

CV results within the potential window of 0-0.6V show the presence of a large reduction peak on both Ni based catalysts (Figure 3.3A) which is attributable to the oxygen reduction reaction [33]. Furthermore, an oxidation peak and shoulder are located at 0.44V and 0.53V in Figure 3.3 A&B for $Ni_{90}Bi_{10}$, which represent the oxidation of Bi to $Bi(OH)_3$ [26, 34]. The first peak (0.44 V) represents the oxidation of surface Bi while the shoulder (0.52 V) represents the oxidation of sublayer Bi, confirming the surface is decorated with Bi and the Ni nanoparticles have a nanosized bulk Bi layer [34]. Furthermore, the higher Bi surface oxidation peak than its bulk oxidation peak is indicative of a larger presence of Bi on the surface than in the bulk [34]. Overall, the $Ni_{90}Bi_{10}$ electrocatalysts were successfully replicated from an electrochemical standpoint.

3.3.3 Effect of glycerol concentration in three electrodes cell

The strict experimental thumb rule that Ni GEOR should be investigated at glycerol concentrations below 0.1M is seldom explained in literature and hasn't been investigated intentionally [19, 25]. The significance of this argument is important for downstream processes for GEOR since operating at low product concentrations can impact the purification steps, influencing the process profitability. In turn, CVs and LSVs were performed over Ni GEOR at various concentrations of glycerol to understand how glycerol influences its own oxidation for Ni GEOR.

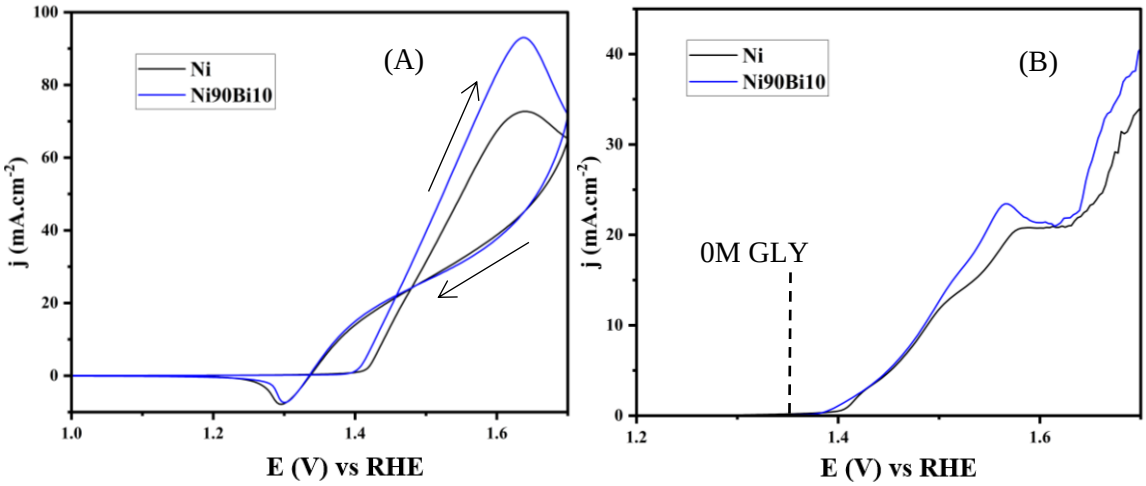

Figure 3.4) (A) 10th CV cycle at 25 mV.s^{-1} and (B) LSV at 1 mV.s^{-1} of Ni and $Ni_{90}Bi_{10}$ performed in 1M KOH and 0.1M glycerol at room temperature.

Figure 3.4 presents both the CVs and LSV of each catalyst in the presence of 0.1M glycerol. The CV shows the increase of the Ni^{+2}/Ni^{+3} oxidation peaks from 43 mA.cm^{-2} for both catalyst in 1M KOH to 72 mA.cm^{-2} for Ni and 94 mA.cm^{-2} for $Ni_{90}Bi_{10}$. This enlargement and sustained higher current is a consequence of the continuous oxidation of β-$Ni(OH)_2$ that is perpetually regenerated from the oxidation of glycerol [17–19, 21]. In the absence of glycerol, β-$Ni(OH)_2$ isn't regenerated by chemical reduction and eventually depletes, producing the oxidation peak in figure 3.2 A. In turn, the current that is measured directly represents the oxidation rate of Ni^{+2} to Ni^{+3} and eventually plateaus by the RDS of GEOR [25, 35, 36]. In comparison to Ni only, the $Ni_{90}Bi_{10}$ onset potential for GEOR is negatively displaced by 28 mV (Figure 3.4A), meaning the addition of Bi reduced the activation energy for Ni^{+2} oxidation. In addition, the GEOR oxidation peak is higher for $Ni_{90}Bi_{10}$ than Ni which confirms Bi synergistically favours GEOR over Ni based on the CV as reported by Houache et al. 2020 [26]. This synergy is further highlighted considering the surface

coverage of active Ni is decreased by the presence of surface Bi in comparison to Ni only. This synergy originates from an improved Ni^{+2} oxidation.

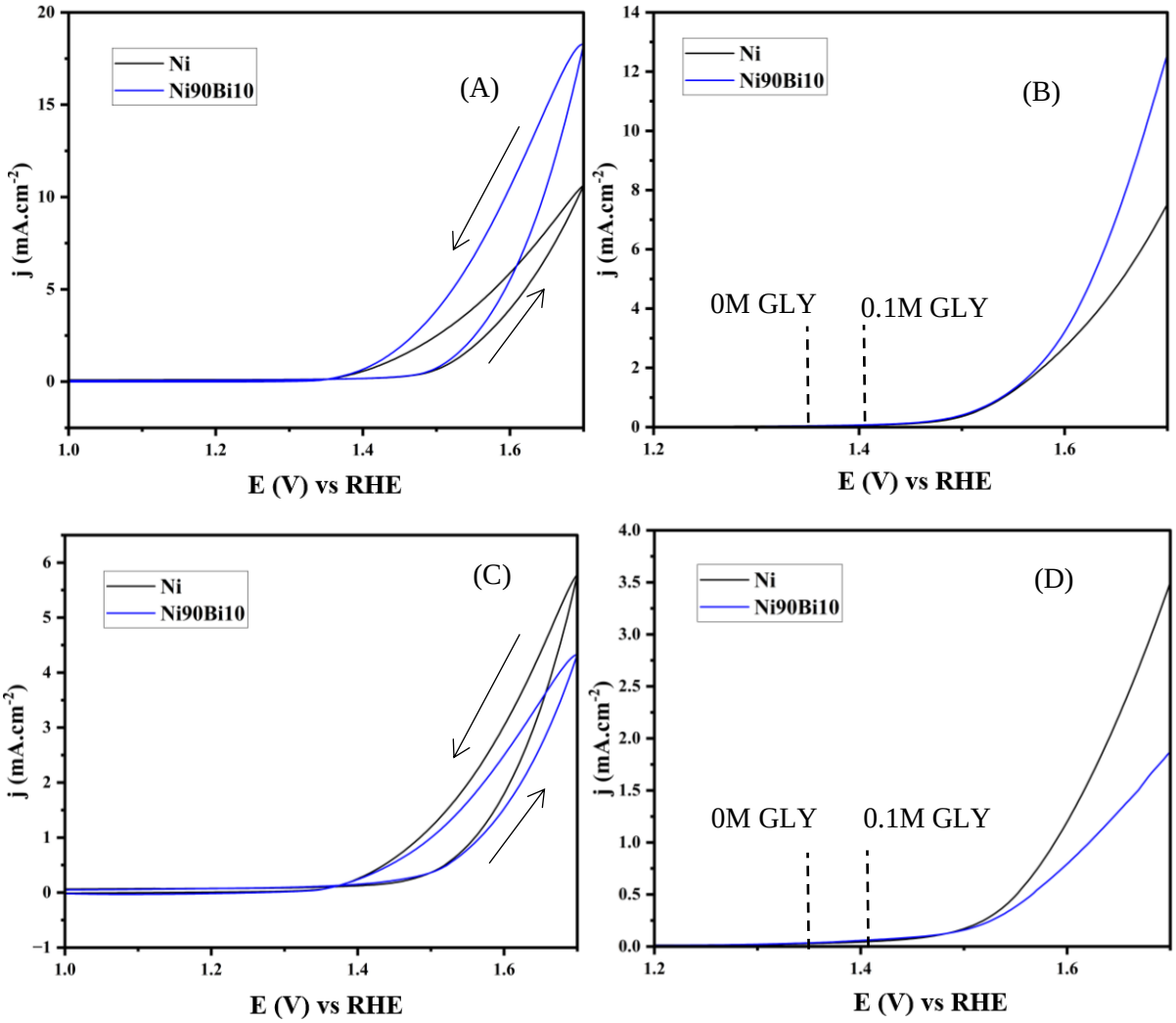

Figure 3.5) (A & C) 10th CV cycle at 25 $mV.s^{-1}$ and (B & D) LSV at 1 $mV.s^{-1}$ of Ni and $Ni_{90}Bi_{10}$ performed in 1M KOH in the presence of (A & B) 1M glycerol or (C & D) 2M glycerol at room temperature.

Based on literature, an increase in glycerol concentration to 1M and 2M progressively suppresses the reactivity of unsupported Ni for GEOR, but no clear explanation is explored other than a saturation effect [19, 25]. Regardless, this expectation would agree with CV results from figure 3.5 where from 0.1M to 2M glycerol, the reactivity of both GEOR and OER decreases significantly. Reactivity is still weakly apparent where Ni and $Ni_{90}Bi_{10}$ achieve 5.8 and 4.2 $mA.cm^{-2}$ up to 2M glycerol, respectively. In turn, there is a correlation for glycerol inhibiting Ni GEOR. Interestingly, inhibition of GEOR coincides with the positive displacement of its onset potential

by as much as 110 mV between 0.1M and 2M glycerol as shown in figure 3.5 C&D. This implies glycerol is increasing the activation energy for Ni^{+2} oxidation to occur, propounding glycerol is inhibiting the oxidation process of Ni^{+2} to Ni^{+3}. Overall, an ideal glycerol concentration is found at low concentrations for Ni catalysts, even at low scan rates.

However, a key observation is the change in the current densities of the forward and reverse scans at 1-2M glycerol (figure 3.5 A&C) to 0M glycerol (figure 3.2 A). Surprisingly, the forward scan currents operate at a current inferior to the reverse current. As discussed in section 2.4 of this thesis, the current from a heterogenous oxidation reaction during a forward scan towards higher oxidative potentials should be larger than its reverse scan [37–39]. This is due to the concentration gradients near the catalyst interface of the reactants and products are higher and lower than their steady state values (i.e. more ideal than steady state) for a given applied potential (i.e. reaction constant) [38, 39]. The opposite is true for the reverse scan where the reactant and product concentrations are lower and higher than their steady state values (i.e. less ideal than steady state), hence the measured current during a reverse scan should be lower [38, 39]. This effect is observed in figure 3.2A at OER potentials where the OER current is higher during the forward than the reverse scan due to relationship between the concentration gradient and the scan rate. However, this concentration-catalysis relationship is not observed in figure 3.5 A&C for GEOR at 1M and 2M glycerol where the reverse scan produces a higher current than the forward scan. In the case of 0.1M glycerol and 1M KOH, there is a 120 mV window (around 1.4 V) where the current of the reverse scan is 21 $mA.cm^{-2}$ higher than the forward scan current which is nearly nulled

By extension, figure 3.5 A&C shows the onset potential of GEOR during the reverse scan (1.36 V at 1M glycerol and 1.38V at 2M glycerol) is around 115 mV less than the forward scan onset potential (1.48 V at 1M glycerol and 1.49 V at 2M glycerol). The same pattern also emerges in 0.1M glycerol and 1M KOH (figure 3.4 A) between the forward and reverse sweep onset potentials with a smaller potential difference of 73 mV. This implies that the thermodynamic and reaction barriers for GEOR to occur decreased for the reverse scan [38, 39], even though the interfacial concentration gradients are less ideal than the forward scan [38, 39]. Due to this, it pinpoints that the origin of this effect to the properties of the catalyst material than the surrounding reactive environment [38, 39].

3.3.4 Effect of KOH concentration in three electrodes cell

Another external GEOR factor that was measured is the influence of KOH concentration since OH^- is both necessary to promote the Ni^{+2} oxidation reaction for GEOR and is a reactant for OER [21, 40]. However, a change in KOH also changes the pH since it is logarithmically dependent on the concentration of OH^- [21]. In turn, it was decided that the KOH concentration should double from 1M KOH to 2M KOH. This attention on mitigating changes in pH was considered since it can influence the selectivity of GEOR, hence potentially influence the mechanism [11, 13].

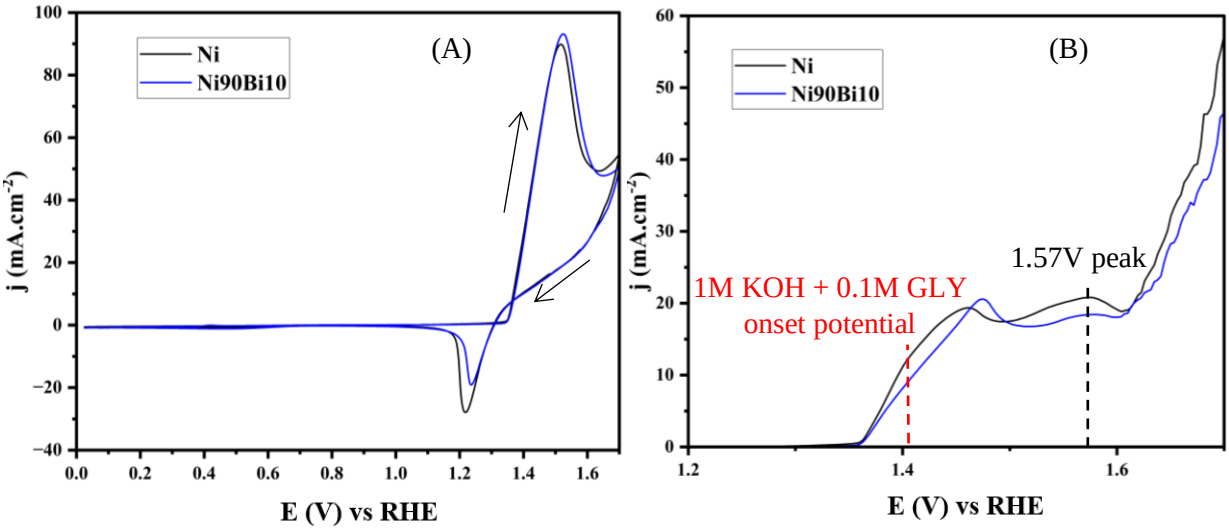

Figure 3.6) (A) 10th CV cycle at 25 $cm.s^{-1}$ and (B) LSV at 1 $mV.s^{-1}$ of Ni and $Ni_{90}Bi_{10}$ performed in 2M KOH and 0.1M glycerol at room temperature. Red and black dashed line is the onset potential and oxidation peak in 1M KOH and 0.1M glycerol, respectively.

Figure 3.6A presents the CVs of the influence of increasing OH^- concentration on both catalysts during GEOR. No change in GEOR reactivity over $Ni_{90}Bi_{10}$ was observed but the reactivity of Ni increased and is negligibly different to $Ni_{90}Bi_{10}$. In other words, CVs indicate Bi modulates Ni's GEOR sensitivity to a change in KOH concentration whereby it is nullified. Furthermore, Ni^{+3}'s reduction peak current density increased in the 2M KOH and 0.1M glycerol electrolyte solution, indicating less β-NiOOH was reduced by glycerol.

Interestingly, the onset potential of both catalysts decreased from 1.41V to 1.36V when the KOH concentration doubled (figure 3.6B), returning it to the onset potential to 1M KOH (figure 3.2). This contradicts Oliveira et al. 2015 recorded the onset potential did not increase between 0.5M to 1M KOH for GEOR over Ni/C [25, 41]. Regardless, the decrease and return of the onset potential to a similar potential found in 1M KOH indicates an increase availability of OH^-

competes against the inhibition of glycerol on Ni^{+2} oxidation. Furthermore, an increase in KOH concentration reduced GEOR's oxidation peak potential according to figure 3.6B LSV results from 1.57V to 1.505V, indicating an improvement in the oxidation rate of Ni^{+2}. Overall, the increase in KOH concentration mitigated the inhibition of glycerol on Ni^{+2} oxidation and promoted Ni^{+2} oxidation rate, reducing the GEOR overpotential. Furthermore, even though the oxidation rate of Ni^{+2} improved, the maximum plateaued current density of the LSV (figure 3.6B, around 20 $mA.cm^{-2}$) did not change from 1M KOH and 0.1M glycerol (figure 3.4B). This indicates that KOH did not improve the RDS of GEOR, highlighting how the RDS in GEOR over both catalysts isn't limited by OH^- availability at 1M KOH or the associated Ni^{+2} oxidation rate.

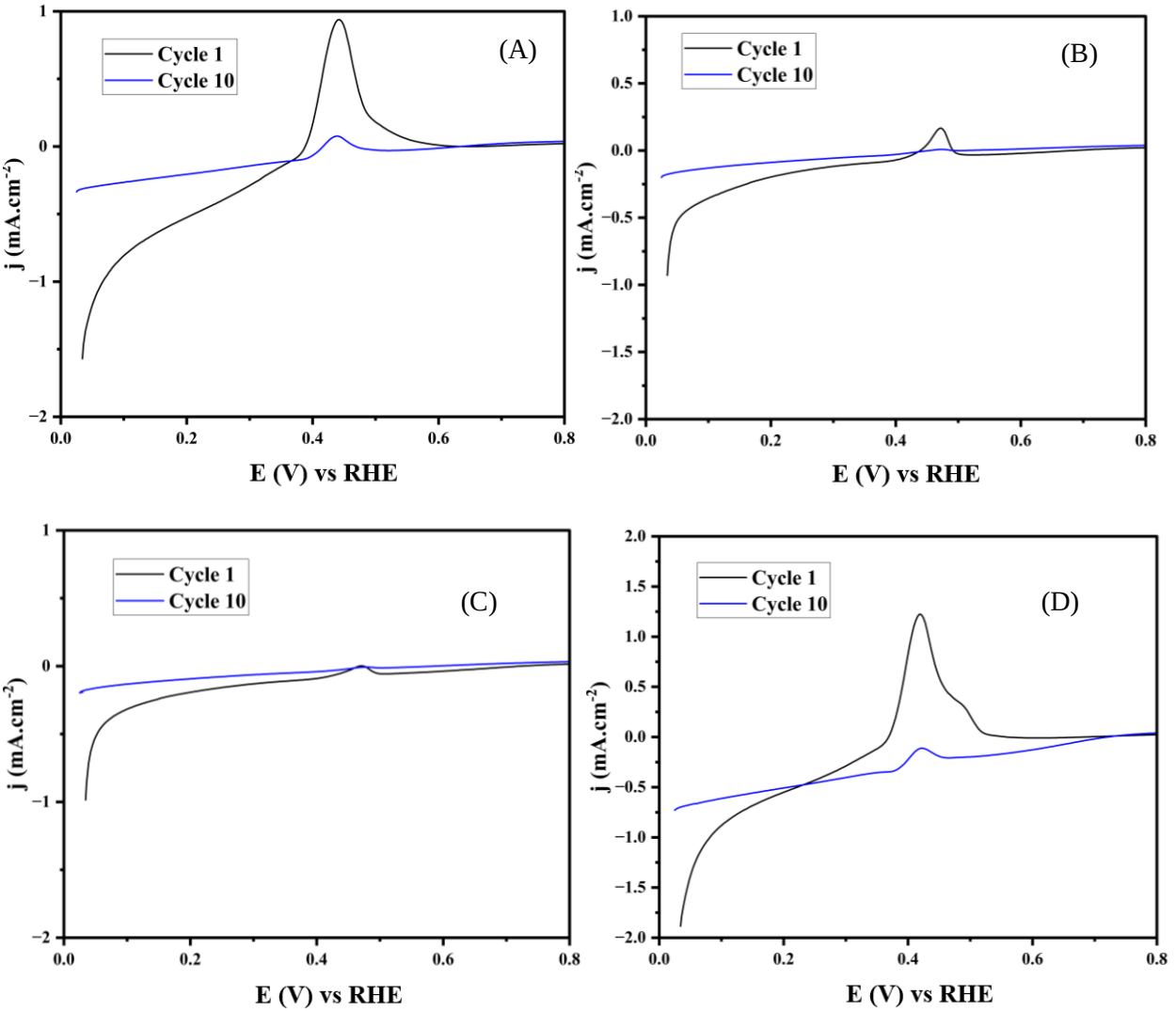

Figure 3.7) The 1st and 10th cycle CVs of $Ni_{90}Bi_{10}$ in 1M KOH and (A) 0.1M, (B) 1M or (C) 2M glycerol, or (D) 2M KOH and 0.1M glycerol measured at 25 $mV.s^{-1}$ in room temperature.

Since Bi is found on the surface of $Ni_{90}Bi_{10}$, the impact of glycerol on Bi's oxidation is shown in Figure 3.7 since its oxidation state can influence the local environment of GEOR over Ni [9, 42]. As the concentration of glycerol increases, the peak current of the first cycle surface oxidation of Bi decreases significantly. Additionally, the sublayer oxidation peak of Bi is suppressed at 1M KOH and 0.1M glycerol (Figure 3.7B). It has been previously reported that this is likely the result of alcohols competitively adsorbing over Bi which prevents the further oxidation of sub bismuth layers [34].

Increasing the KOH concentration in 0.1M glycerol (Figure 3.7D) does increase the Bi oxidation peak current density and returns the bulk layer oxidation. From this, glycerol appears to exert an influence on the $Ni_{90}Bi_{10}$ catalyst's core oxidation state. In turn, the catalytic properties of $Ni_{90}Bi_{10}$ in 1M KOH and 0.1M glycerol are different between 1M and 2M KOH. The changes in the bulk phase oxidation have significant implication for the efficacy of several heterogenous reactions in electrochemistry [41, 43–45]. This was demonstrated for alcohols by Hao et al. 2023 who recently showed the underlying bulk oxidation phase plays a critical role in their oxidation reaction rates [43].

Hao et al. 2023 demonstrated that an increase in oxidation state of the bulk also meaningfully reduced the onset potential for alcohol oxidation since a higher bulk oxidation state has a favourable electron conductivity and electronic effects to the surface layer which reduces the thermodynamic and reaction barriers for alcohol oxidation over Ni [43]. This phenomenon is a plausible explanation for the increase in current of the reverse scan as discussed in section 3.3.3. and seen in figure 3.6A since the proportion of the bulk phase that is oxidised increases as the potential increases [10, 20, 46]. Since the reverse scan starts at the highest applied potential, it begins at the highest oxidation state that bulk Ni and $Ni_{90}Bi_{10}$ can achieve which is intrinsically favourable for the surface Ni GEOR thermodynamically and kinetically. In 0.1M glycerol and 1 or 2M KOH (figure 3.4A & 3.6A), the onset potential of the reverse scan GEOR coincides with the reduction of Ni^{+3} back to Ni^{+2} that occurs both at the surface and the bulk for Ni, as if the sustained elevated reactivity of GEOR during the reverse scan is dependent on the elevated oxidation state of the bulk, as is demonstrated by Hao et al. 2023 [43]. With this in mind, it is plausible for the reverse scan current densities for GOER to be higher and operate at a lower onset potential since the bulk is in a higher oxidation state than the forward scan.

Interestingly, the established relationship between the onset potential and reaction rates for alcohol oxidation with the catalyst bulk oxidation state [43], combined with the worsened onset potential for Ni^{+2} oxidation (figure 3.4-6) and prevention of the Bi bulk layer oxidation (figure 3.7) by glycerol points to a novel perspective that glycerol exerts an influence on the bulk Ni oxidation state. This is supported by the plausible explanation that the reverse scan has a higher reactivity and reduced onset potential because of the higher intrinsic oxidation state of the bulk phase. Considering the stability of the surface oxidation state is a prerequisite for the bulk to oxidise [10] but results from Duan et al. 2024 and Luo et al 2022 showed through electron paramagnetic resonance and operando optical electrochemical spectra that Ni^{+3} is highly unstable due to the GEOR spontaneous chemical reduction of Ni^{+3}, it is mechanistically and theoretically (schematic 3.3) likely for GEOR to be suppressing the bulk oxidation layer of Ni and Bi based catalyst [6, 47]. This is further experimentally supported by the reduced reduction peak of Ni^{+3} in the presence of GEOR (figure 3.4-3.6) since it reflects the reduction of both surface and bulk Ni [10]. Overall, observations from this section highlights a novel perspective shift in GEOR catalyst design and investigation where instead of observing how a catalyst oxidises glycerol, one should record how glycerol influences the catalyst as well.

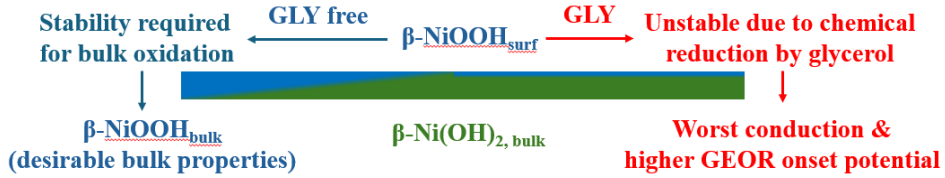

Scheme 3.3) Visual representation of the oxidation mechanism of bulk Ni (left side) [10] and the proposed pathway by which glycerol inhibits it (right side).

3.3.5 Preliminary investigation of glycerol on HER over Pt/C

To perform membrane-free electrolyser tests, the influence of glycerol on HER was measured over Pt/C (Figure 3.8) to see the influence of the different reactive conditions on the cathode to make sure what should be expected of the cathode. A thorough investigation on the influence of glycerol on HER will be performed in Chapter 4.

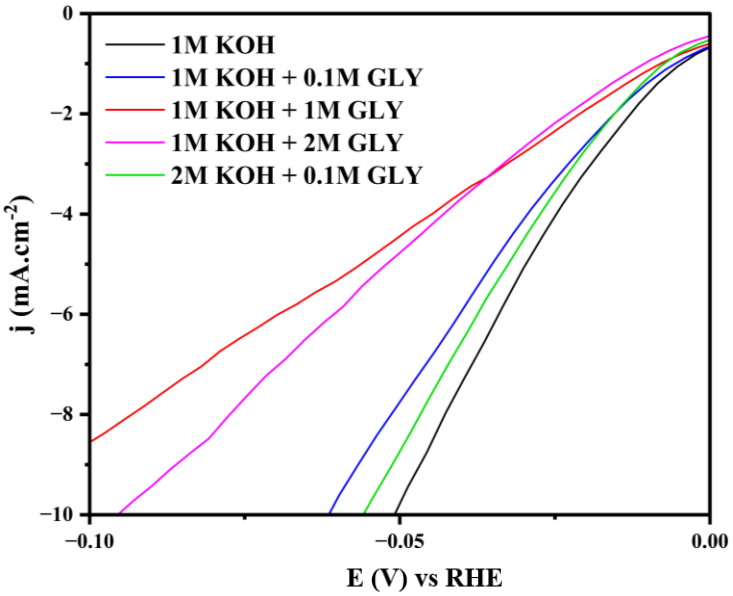

Figure 3.8) LSV of Pt/C in 1M KOH without or with 0.1M, 1M or 2M glycerol or 2M KOH and 0.1M glycerol. The scan rate is 1 $mV.s^{-1}$ at room temperature ($20^{o}C$).

Based on Figure 3.8, adding glycerol appears to inhibit HER initially over Pt/C but past 1M glycerol, the HER performance appears to be surprisingly improved. Regardless, based on literature, the likely causes for this worst performance is due to a worst OH^- conduction, increased solution viscosity and glycerol electroreduction [48, 49]. However, this fails to explain the promotional effect at 2M glycerol which will be explored in Chapter 4 where glycerol may be an indirect HER promoter and inhibitor depending on the catalyst material and specific HER mechanism. Overall, glycerol appears to worsen the HER performance over Pt/C, which will guarantee that improvements seen during the electrolyser tests should originate from the anode when changing concentrations.

3.3.6 Single-cell electrolysis tests

3.3.6.1 Effect of temperature

The effect of temperature over GEOR was investigated since very few polarization curves have been made for GEOR and changes in temperatures not only influences reaction kinetics but also the conductivity of OH^- which has a dominant role on the ohmic polarization phase of the polarization curves.

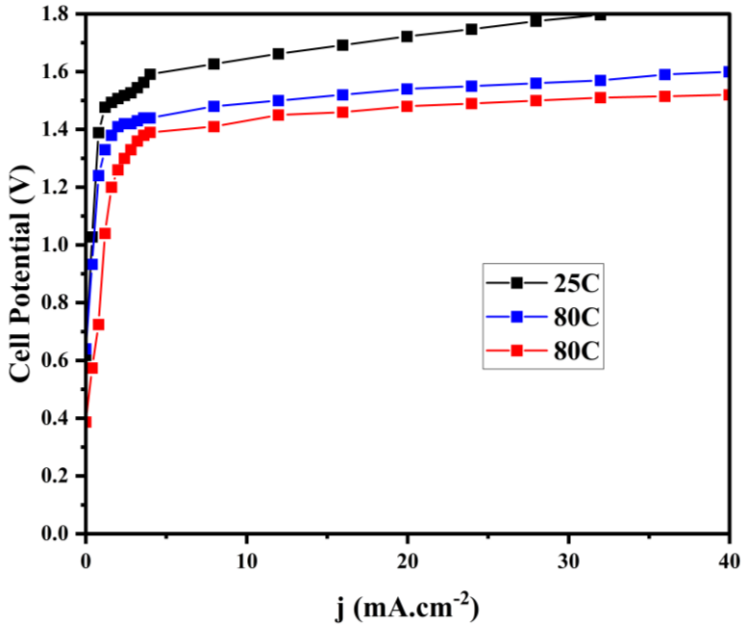

Figure 3.9) Polarizations of 1 mg.cm^{-2} $Ni_{90}Bi_{10}$ anode and 2 mg.cm^{-2} Pt/C cathode at 25ºC (Black), 50ºC (Blue) and 80ºC (Red) in 1M KOH and 0.1M glycerol electrolyte flowing at 0.5 L.min^{-1}.

Figure 3.9 presents the polarization curve of the $Ni_{90}Bi_{10}$ anode cell when the temperature of the electrolyser increases from 25ºC to 80ºC. Increasing the temperature expectedly decreased the activation polarization potential from 1.51V (= 1.2 mA.cm^{-2}) at 25ºC, to 1.41V (= 2 mA.cm^{-2}) at 50ºC and 1.38 V (= 3.2 mA.cm^{-2}) at 80ºC. This is likely a result of a decreased activation barrier for Ni^{+2} oxidation which translates to a reduced activation polarization over GEOR [10, 25]. Additionally, the ohmic polarization curve slope decreases from 950 (mV/100 mA.cm^{-2}) at 25ºC to 476 (mV/100 mA.cm^{-2}) at 50ºC and 353 (mV/100 mA.cm^{-2}) at 80ºC. The difference between the evolving ohmic slope between 25ºC and 50ºC to 50ºC and 80ºC can be explained by a decreased rate of change in viscosity which converges for glycerol aqueous solutions when the temperature increases [50]. This drop in viscosity can improve OH^- conductivity but past a 60ºC this improvement becomes negligeable [51]. Additionally, the activation barriers for GEOR and Ni^{+2} oxidation should also be reduced which further decreases the ohmic polarization slopes as well [25]. However, an interesting divergence from OER based electrolysers is worth pointing out. OER systems often have a rapidly ending activation polarization [52]. Although the ending potential of the activation polarization for OER decreases with temperature, as seen in Figure 3.9, the activation polarization should decrease in duration with an increase in temperature as well for OER [52]. However, a closer inspection of the GEOR polarization curves shows the activation

polarization stabilises for 10 minutes at 25°C, but 30 minutes at 80°C, as if the temperature is stabilising the activation polarization which differs from OER electrolysers. In turn, the nature of the activation polarization in GEOR may be different from OER. This is validated in the next section.

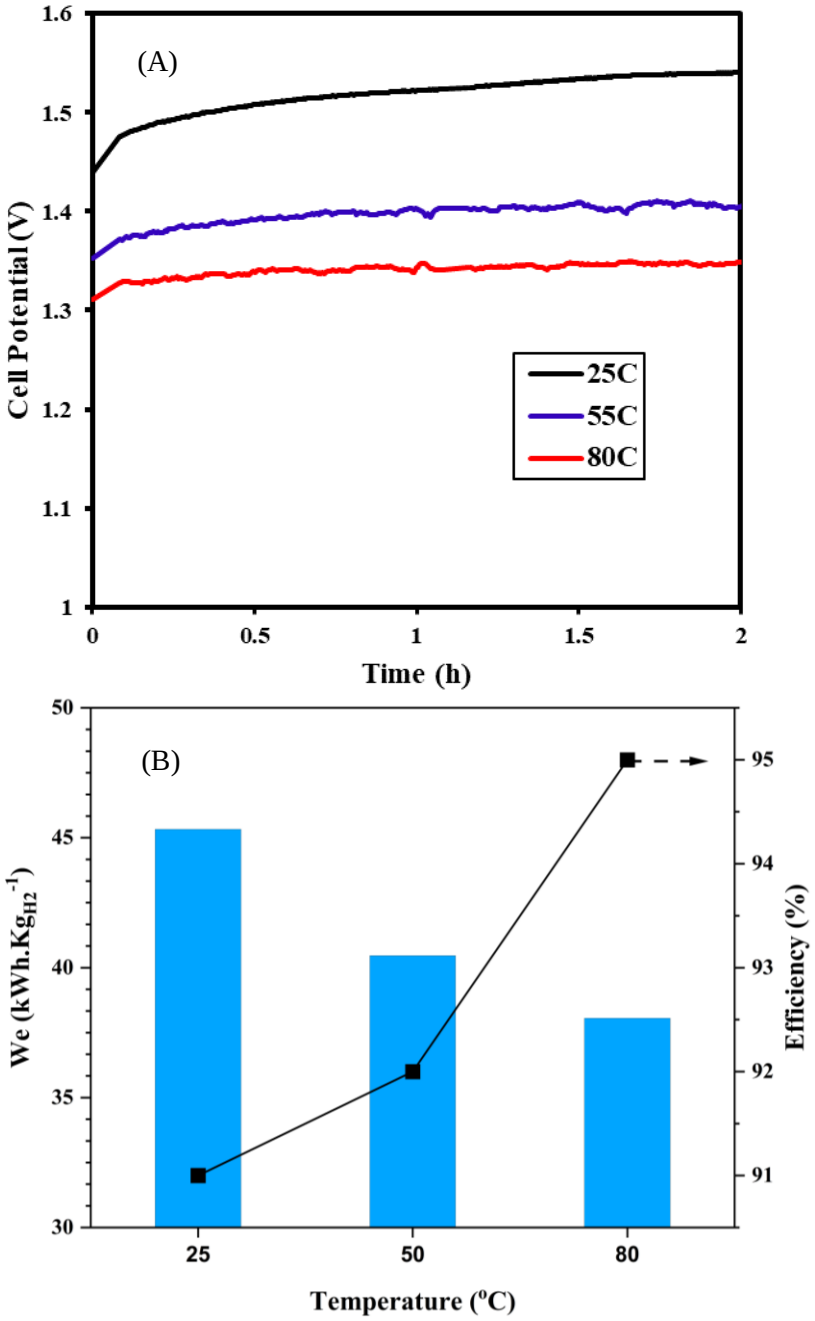

Figure 3.10) (A) CPs at 4 mA.cm^{-2} of 1 mg.cm^{-2} $Ni_{90}Bi_{10}$ anode and 2 mg.cm^{-2} Pt/C cathode at 25°C (Black), 50°C (Blue) and 80°C (Red) in 1M KOH and 0.1M glycerol electrolyte flowing at 0.5 L.min^{-1}. (B) Respective W_e and HER faradaic efficiencies for each measured temperature.

Figure 3.10 presents the CP measurements of each temperature measurement. Although it is ideal to perform CP measurements at elevated current densities such as 100 $mA.cm^{-2}$ or 200 $mA.cm^{-2}$, the available equipment at the time only permitted small current operations. Like the polarization curves, and to be expected, an increase in temperature reduced the cell operating potential significantly from 1.54V at 25°C to 1.35V at 80°C. However, what is unexpected is the drift rate at such a low current density. Often in OER systems, it is expected for cells to undergo various forms of degradation when operating at elevated potentials above 1.7V or at elevated current densities [10]. At low current densities (especially 4 $mA.cm^{-2}$) OER catalysts are often stable regardless of the temperature. Figure 3.10 reveals an insignificant degradation past 50°C, likely due to the low current density. However, the CP at 25°C reported a degradation of 31.5 $mV.h^{-1}$, which is rather quick for the low current density. This would imply that an important form of deactivation is mediated by the temperature. Based on small 3-electrode CA measurements, the degradation is likely related to a form of poisoning from intermediate products although these are unknown in literature [26]. This can explain the electrolyser results where an elevated temperature reduces the desorption energy needed for removing these unknown intermediates [24].

Surprisingly, the faradaic efficiency of the cell was relatively high (>90%) as shown in Figure 3.10B. While the anode and cathode output lines connected to the same tank, the detection of gas bubbles originating only from the cathode strongly indicates H_2 gas was the main component of the gas. Still, it is recommended for GC-MSC measurements to be made to validate this conclusion. Furthermore, no proposed electrochemical reduction of glycerol in literature produces a gas, hence the electrochemical reduction of glycerol is unlikely to have participated in the gas production from the cathode, validating the product gas is H_2 from HER [3, 53]. The W_e at 50°C and 80°C operate at or below the D.O.E. target for a Ni based anode at 40.4 and 38.1 $kWh.kg_{H2}^{-1}$, respectively (Figure 3.10B). As for 25°C, the required energy input was equal to 45.3 $kWh.kg_{H2}^{-1}$ but this cell potential is operated at 4 $mA.cm^{-2}$ (Figure 3.10B) and should not be used as a practical form of comparison to other works.

3.3.6.2 Effect of glycerol and KOH concentration

The influence of glycerol and KOH concentration was also investigated since differences in the hydrodynamic profiles of between a static 3-electrodes cell and zero-gap cell can provide further kinetic insight into the reaction in question [37].

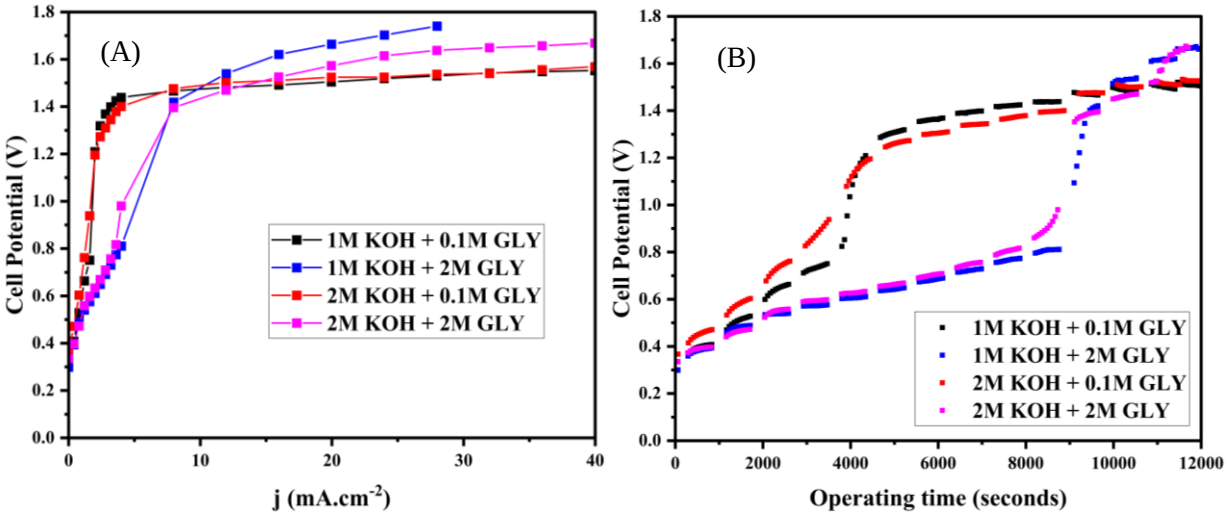

Figure 3.11) (A) Polarizations of 1 mg.cm^{-2} $Ni_{90}Bi_{10}$ anode and 2 mg.cm^{-2} Pt/C cathode at 1M KOH + 0.1M glycerol (Black), 1M KOH + 2M glycerol (Blue), 2M KOH + 0.1M glycerol (Red), 2M KOH + 2M glycerol (Magenta) electrolyte flowing at 0.5 L.min^{-1} at 50^{o}C. (B) Raw CP data plotted overtime for the same electrolytes and conditions.

Figure 3.11 presents the influence of glycerol concentration over $Ni_{90}Bi_{10}$. Increasing the glycerol concentration from 0.1M to 2M glycerol resulted in worst cell performance with a higher ohmic polarization slope from 476 (mV/mA.cm^{-2}) in 0.1M glycerol to 1630 (mV/mA.cm^{-2}) in 2M glycerol. This would agree with the 3-electrode cell results in Figure 3.4-6 where the catalyst showed signs of inhibition from glycerol. However, a significant change in behaviour of the activation polarization occurs. Figure 3.11B shows there exists a separate ohmic polarization phase between 0.3-0.8V which hasn't been reported previously for this type of catalyst or GEOR which contains Ni or Bi. Re-evaluating the temperature polarization curves also shows this ohmic polarization phase is present at 0.1M glycerol when the temperature is elevated (figure 3.9). To further understand this new ohmic polarization curve, the concentration of KOH was increased from 1M to 2M KOH for both glycerol concentrations. While an increase in KOH does improve the >1V ohmic polarization phase in 2M glycerol to 850 (mV/100 mA.cm^{-2}) and negligibly improved the 0.1M glycerol at 481 (mV/100 mA.cm^{-2}), it interestingly inhibits the low voltage ohmic polarization phase in either glycerol concentrations. It is interesting to note that an activation polarization phase does appear to exist from 0.85V to 1.2V. Furthermore, it is noticed that an increase in KOH concentration improves the >1V ohmic polarization reaction but inhibits the <1V ohmic polarization reaction while the opposite is observed by increasing the glycerol concentration. Based on the opposite effects of glycerol and KOH concentration on the high and

low potential ohmic polarizations, it does indicate the low ohmic polarization is related to GEOR, but each polarization reaction represents an entirely different mechanism.

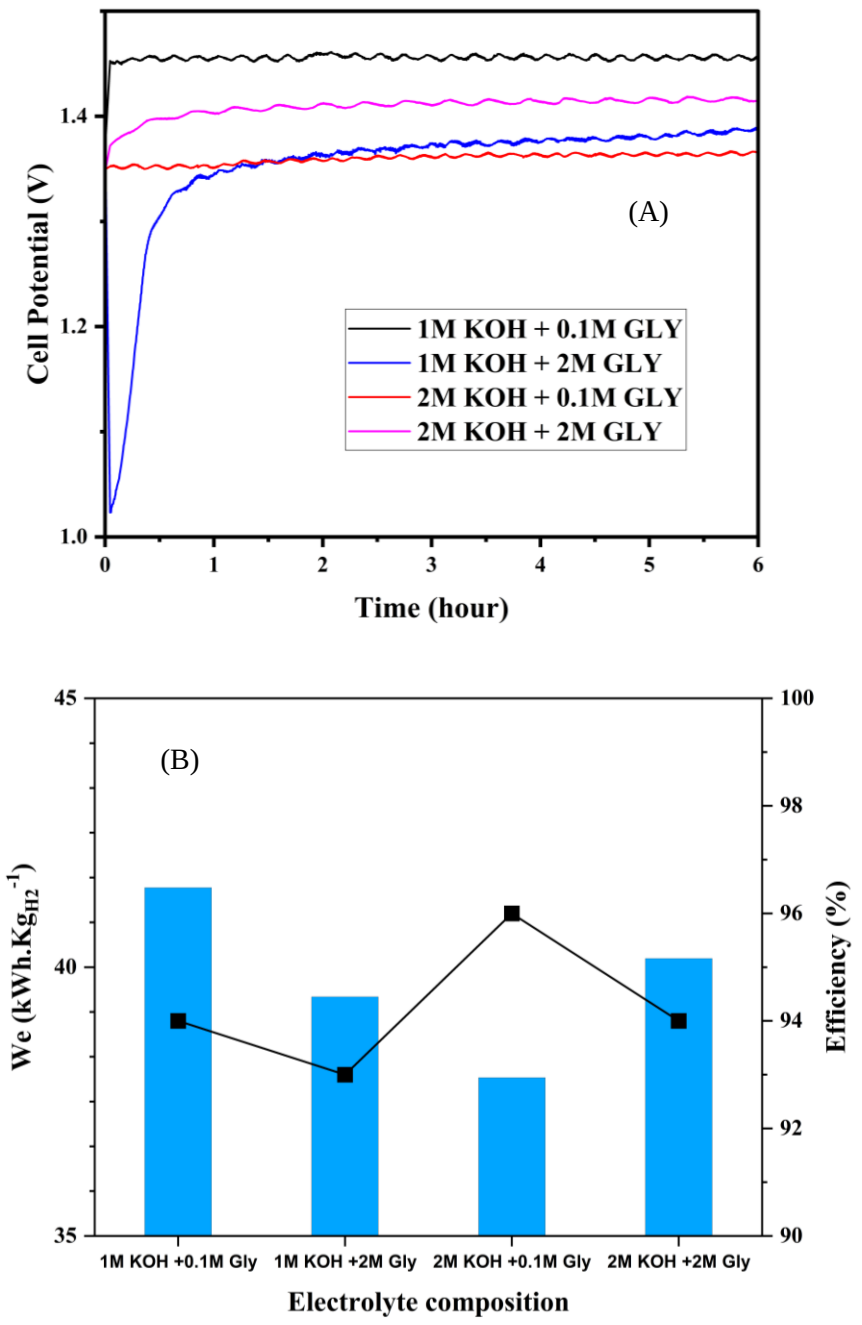

Figure 3.12) (A) CPs at 4 mA.cm^{-2} of 1 mg.cm^{-2} $Ni_{90}Bi_{10}$ anode and 2 mg.cm^{-2} Pt/C cathode at 1M KOH + 0.1M glycerol (Black), 1M KOH + 2M glycerol (Blue), 2M KOH + 0.1M glycerol (Red), 2M KOH + 2M glycerol (Magenta) electrolyte flowing at 0.5 L.min^{-1} at 50°C. (B) Respective W_e and HER faradaic efficiencies for each measured temperature.

Based on the CP results of Figure 3.12, all concentrations tested had a similar drift rate of 0.3 $mV.h^{-1}$, except for 1M KOH and 2M glycerol. The 0.3 $mV.h^{-1}$ drift rate can be explained by the temperature control responsible for the undulating behaviour of the cell potential. In turn, this low drift rate can be considered negligible. Fascinatingly, the 1M KOH and 2M glycerol CP shows an immediate drop in potential approaching the <1V ohmic polarization phase when the current density is reset to 4 $mA.cm^{-2}$. From there, the cell potential steadily and slowly increases for 34 minutes to achieve a new steady state at 1.32V with a drift rate of 10.3 $mV.h^{-1}$. This is unexpected since, the cell potential appears to transition between the polarization phases as a function of the applied current and not the oxidation states which are present or stabilised. In other words, the cell potential only transitions to the >1V polarization phase if the <1V can't satisfy the demanded current. But if it can, it returns the cell potential to the <1V oxidation phase regardless. However, this does degrade rapidly as seen in Figure 3.12. The reason for the slow increase is not clear.

Like the temperature investigation, the faradaic efficiency is above 90%. Although the faradaic efficiencies appear higher than the temperature study (Figure 3.12B), it is likely that this is a result of an improved sealing of the equipment. Regardless, an increase in hydroxide and glycerol concentration reduces the energy consumption from 41.5 $kWh.kg_{H2}^{-1}$ (1M KOH and 0.1M glycerol), to 40.2 $kWh.kg_{H2}^{-1}$ (2M KOH and 2M glycerol), 39.45 $kWh.kg_{H2}^{-1}$ (1M KOH and 2M glycerol), and 37.9 $kWh.kg_{H2}^{-1}$ (2M KOH and 0.1M glycerol) (Figure 3.12B). The reason why the 1M KOH and 2M glycerol has a lower energy consumption than 2M KOH and 2M glycerol is due to the initial low cell potential. In turn, if the low potential ohmic polarization can be theoretically stabilised, as seen in the initial moments of the 1M KOH + 2M glycerol CP, one can achieve exceptionally low cell potential over a $Ni_{90}Bi_{10}$ based catalyst.

3.3.6.3 Effect of catalyst loading

The influence of catalyst loading was investigated since little optimization of the electrode design for GEOR has been made in literature.

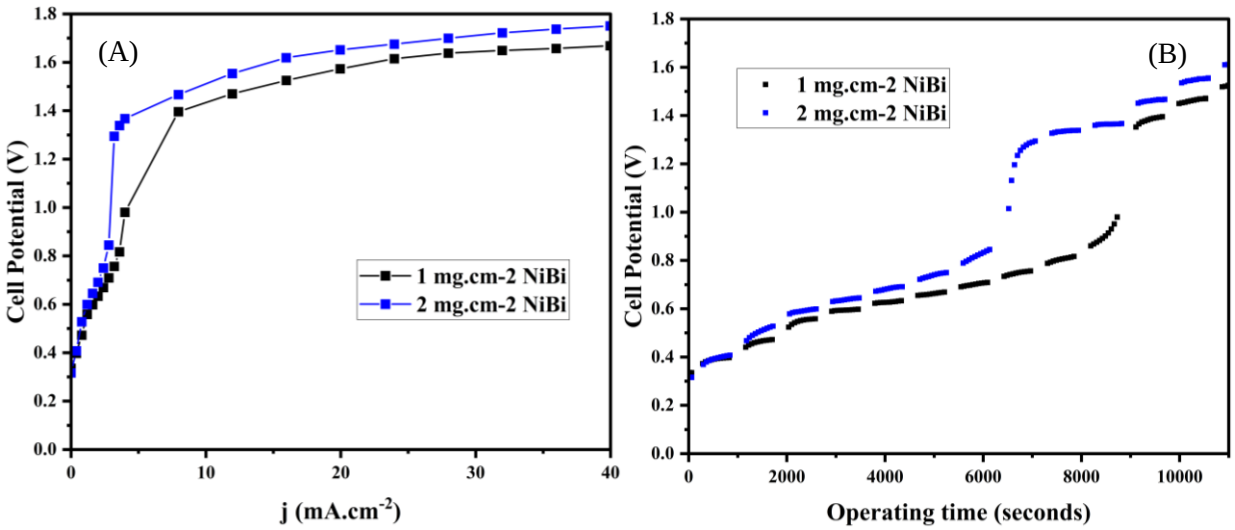

Figure 3.13) (A) Polarizations of 1 (Black) and 2 (Bleu) $Ni_{90}Bi_{10}$ anode and 2 mg.cm^{-2} Pt/ C cathode in a 2M KOH + 2M glycerol (Magenta) electrolyte flowing at 0.5 L.min^{-1} at 50^{o}C. (B) Raw CP data plotted overtime for the same anode loadings.

Figure 3.13 presents the polarization curves of the $Ni_{90}Bi_{10}$ anode and Pt/C where the anode loading was increased from 1 mg.cm^{-2} to 2 mg.cm^{-2}. Due to the presence of the <1V ohmic polarization phase from the previous tests, the anode loading was investigated in 2M KOH and 2M glycerol to extrapolate as much information of both >1V and <1V ohmic polarization reactions. Increasing the anode loading up to 2 mg.cm^{-2} universally increased the cell potential for each ohmic polarization phase, decreasing the cell performance significantly [52, 54]. Unlike the effects of KOH or glycerol, an increase in $Ni_{90}Bi_{10}$ catalyst loading reduces performance of both ohmic polarization curves. CP measurements perform similarly to their polarization curve counter part with a similarly high faradaic efficiency with 1 and 2 mg.cm^{-2} resulting in 38.1 and 39.5 kWh.kg$_H^{-1}$ (Figure 3.14B).

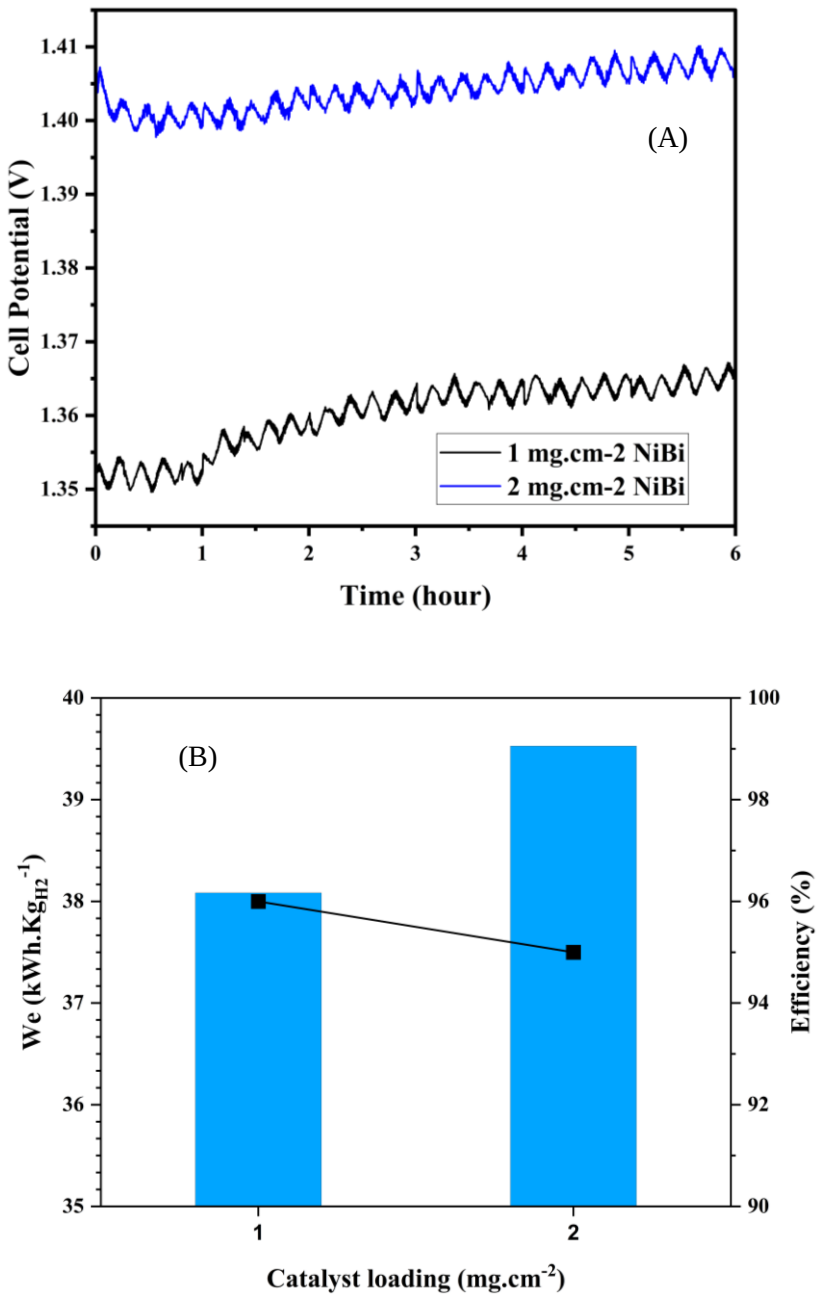

Figure 3.14) (A) CPs at 4 mA.cm^{-2} of 1 (Black and 2 (Bleu) mg.cm^{-2} in $Ni_{90}Bi_{10}$ anode and 2 mg.cm^{-2} Pt/C cathode in 2M KOH + 2M glycerol (Magenta) electrolyte flowing at 0.5 L.min^{-1} at 50^{o}C. (B) Respective W_e and HER faradaic efficiencies for each measured temperature.

3.4 Conclusion

In examining the role of environmental conditions on the performance of $Ni_{90}Bi_{10}$ in a three electrodes cell, glycerol inhibits the oxidation process of Ni^{+2}, indirectly inhibiting its own reactivity. The mechanism of this inhibition is unknown but extends also to the bulk, where the

oxidation state of Bi is reduced which can have significant effects on the oxidation process of Ni^{+2}. However, the inhibition of glycerol can be mitigated by a higher KOH concentration due to the reduced onset potential and GEOR oxidation peak. Nonetheless, an increase in OH^- availability did not improve the RDS of GEOR. In turn, an increase in OH^- availability improved Ni^{+2} oxidation rate but didn't influence the glycerol's oxidation rate. In terms of the electrolyser tests, an increase in temperature not only reduced the cell energy consumption by 16% but also revealed a novel <1V low voltage ohmic polarization phase that is stabilised with an increase in temperature. While the nature of this new ohmic polarization is unknown, it is reported its transition from one ohmic polarization phase to another is a function of current and not potential. Furthermore, both polarization phases behave oppositely to one and another from a change in glycerol concentration. In the case of the low ohmic polarization phase, it improves with an increase in glycerol and reduced OH^- availability. The reverse is observed for the high ohmic polarization curve. Also, this low ohmic polarization phase can potentially be stabilised, presenting an important pathway for a reduced cell operating voltage (i.e. energy consumption). When the anode loading was increased, both GOER mechanisms were suppressed, indicating low catalyst loadings are ideal for Ni based GEOR electrolysers. Optimization of reaction conditions in terms of energy consumption were determined to be at 2M KOH and 0.1M glycerol operating at 37.9 $kWh.kg_{H2}^{-1}$. Finally, the lowest measured faradaic efficiency was 93%, likely contributed by issues with pipe leaks. In any regards, the high faradaic efficiency highlights the cathode retains a high selectivity to HER opening the possibility for membrane-free GEOR-HER electrolyser as a means for inexpensive hydrogen production.

3.5 Reference

[1] Antolini, E. Glycerol Electro-Oxidation in Alkaline Media and Alkaline Direct Glycerol Fuel Cells. *Catalysts*, **2019**, *9* (12). https://doi.org/10.3390/catal9120980.

[2] Li, Z.; Yan, Y.; Xu, S. M.; Zhou, H.; Xu, M.; Ma, L.; Shao, M.; Kong, X.; Wang, B.; Zheng, L.; et al. Alcohols Electrooxidation Coupled with H2 Production at High Current Densities Promoted by a Cooperative Catalyst. *Nat Commun*, **2022**, *13* (1). https://doi.org/10.1038/s41467-021-27806-3.

[3] Ruiz-López, E.; Diaz-Perez, M. A.; de Lucas-Consuegra, A.; Dorado, F.; Serrano-Ruiz, J. C. Membrane-Less Ethanol Electrooxidation over Pd-m (M: Sn, Mo and Re) Bimetallic Catalysts. *Catalysts*, **2021**, *11* (5). https://doi.org/10.3390/catal11050541.

[4] Bambagioni, V.; Bianchini, C.; Marchionni, A.; Filippi, J.; Vizza, F.; Teddy, J.; Serp, P.; Zhiani, M. Pd and Pt-Ru Anode Electrocatalysts Supported on Multi-Walled Carbon Nanotubes and Their Use in Passive and Active Direct Alcohol Fuel Cells with an Anion-Exchange Membrane (Alcohol = Methanol, Ethanol, Glycerol). *J Power Sources*, **2009**, *190* (2), 241–251. https://doi.org/10.1016/j.jpowsour.2009.01.044.

[5] Wu, J.; Yang, X.; Gong, M. Recent Advances in Glycerol Valorization via Electrooxidation: Catalyst, Mechanism and Device. *Chinese Journal of Catalysis*. Science Press December 1, 2022, pp 2966–2986. https://doi.org/10.1016/S1872-2067(22)64121-4.

[6] Duan, Y.; Xue, M.; Liu, B.; Zhang, M.; Wang, Y.; Wang, B.; Zhang, R.; Yan, K. Integration of Theory Prediction and Experimental Electrooxidation of Glycerol on NiCo2O4 Nanosheets. *Chinese Journal of Catalysis*, **2024**, *57*, 68–79. https://doi.org/10.1016/S1872-2067(23)64585-1.

[7] Wu, J.; Li, J.; Li, Y.; Ma, X. Y.; Zhang, W. Y.; Hao, Y.; Cai, W. Bin; Liu, Z. P.; Gong, M. Steering the Glycerol Electro-Reforming Selectivity via Cation–Intermediate Interactions. *Angewandte Chemie - International Edition*, **2022**, *61* (11). https://doi.org/10.1002/anie.202113362.

[8] Li, T.; Harrington, D. A. An Overview of Glycerol Electrooxidation Mechanisms on Pt, Pd and Au. *ChemSusChem*. John Wiley and Sons Inc March 22, 2021, pp 1472–1495. https://doi.org/10.1002/cssc.202002669.

[9] Sarkar, S.; Peter, S. C. An Overview on Pd-Based Electrocatalysts for the Hydrogen Evolution Reaction. *Inorganic Chemistry Frontiers*. Royal Society of Chemistry September 1, 2018, pp 2060–2080. https://doi.org/10.1039/c8qi00042e.

[10] Alsabet, M.; Grdeń, M.; Jerkiewicz, G. Electrochemical Growth of Surface Oxides on Nickel. Part 3: Formation of β-NiOOH in Relation to the Polarization Potential, Polarization Time, and Temperature. *Electrocatalysis*, **2015**, *6* (1), 60–71. https://doi.org/10.1007/s12678-014-0214-1.

[11] Goetz, M. K. K.; Bender, M. T.; Choi, K. S. Predictive Control of Selective Secondary Alcohol Oxidation of Glycerol on NiOOH. *Nat Commun*, **2022**, *13* (1). https://doi.org/10.1038/s41467-022-33637-7.

[12] Bender, M. T.; Lam, Y. C.; Hammes-Schiffer, S.; Choi, K. S. Unraveling Two Pathways for Electrochemical Alcohol and Aldehyde Oxidation on NiOOH. *J Am Chem Soc*, **2020**, *142* (51), 21538–21547. https://doi.org/10.1021/jacs.0c10924.

[13] Bender, M. T.; Warburton, R. E.; Hammes-Schiffer, S.; Choi, K. S. Understanding Hydrogen Atom and Hydride Transfer Processes during Electrochemical Alcohol and Aldehyde Oxidation. *ACS Catal*, **2021**, *11* (24), 15110–15124. https://doi.org/10.1021/acscatal.1c04163.

[14] Fleischmann, M.; Korinek, K.; Pletcher, D. *THE OXIDATION OF ORGANIC COMPOUNDS AT A NICKEL ANODE IN ALKALINE SOLUTION*.

[15] Mendes, P. C. D.; Costa-Amaral, R.; Gomes, J. F.; Da Silva, J. L. F. The Influence of Hydroxy Groups on the Adsorption of Three-Carbon Alcohols on Ni(111), Pd(111) and Pt(111) Surfaces: A Density Functional Theory Study within the D3 Dispersion Correction. *Physical Chemistry Chemical Physics*, **2019**, *21* (16), 8434–8444. https://doi.org/10.1039/c9cp00752k.

[16] Asnavandi, M.; Zhao, C. Autologous Growth of Nickel Oxyhydroxides with: In Situ Electrochemical Iron Doping for Efficient Oxygen Evolution Reactions. *Mater Chem Front*, **2017**, *1* (12), 2541–2546. https://doi.org/10.1039/c7qm00367f.

[17] Oliveira, V. L.; Morais, C.; Servat, K.; Napporn, T. W.; Tremiliosi-Filho, G.; Kokoh, K. B. Glycerol Oxidation on Nickel Based Nanocatalysts in Alkaline Medium - Identification of the Reaction Products. *Journal of Electroanalytical Chemistry*, **2013**, *703*, 56–62. https://doi.org/10.1016/j.jelechem.2013.05.021.

[18] Houache, M. S. E.; Cossar, E.; Ntais, S.; Baranova, E. A. Electrochemical Modification of Nickel Surfaces for Efficient Glycerol Electrooxidation. *J Power Sources*, **2018**, *375*, 310–319. https://doi.org/10.1016/j.jpowsour.2017.08.089.

[19] Houache, M. S. E.; Sandoval, M. G.; Safari, R.; Gaztañaga, F.; Escudero, F.; Hernández-Laguna, A.; Sainz-Díaz, C. I.; Botton, G. A.; Jasen, P. V.; González, E. A.; et al. Morphology Alteration of Nickel Microstructures for Glycerol Electrooxidation. *J Catal*, **2021**, *404*, 348–361. https://doi.org/10.1016/j.jcat.2021.10.010.

[20] Huang, L. F.; Hutchison, M. J.; Santucci, R. J.; Scully, J. R.; Rondinelli, J. M. Improved Electrochemical Phase Diagrams from Theory and Experiment: The Ni-Water System and Its Complex Compounds. *Journal of Physical Chemistry C*, **2017**, *121* (18), 9782–9789. https://doi.org/10.1021/acs.jpcc.7b02771.

[21] Santana, C. S.; Gjonaj, E.; Garcia, A. C. Effect of Iron Impurities on the Electrochemical Oxidation of Glycerol on Ni(OH)2/NiOOH Electrodes. *ChemElectroChem*, **2024**, *11* (1). https://doi.org/10.1002/celc.202300570.

[22] Golikand, A. N.; Maragheh, M. G.; Irannejad, L.; Asgari, M. Electrocatalytic Oxidation of Methanol on a Nickel(II)-1-(2-Pyridylazo)-2- Naphthol Complex Modified Glassy-Carbon Electrode in Alkaline Medium. *Russian Journal of Electrochemistry*, **2006**, *42* (2), 167–172. https://doi.org/10.1134/S1023193506020108.

[23] Khan, M. A.; Al-Attas, T. A.; Yasri, N. G.; Zhao, H.; Larter, S.; Hu, J.; Kibria, M. G. Techno-Economic Analysis of a Solar-Powered Biomass Electrolysis Pathway for Coproduction of Hydrogen and Value-Added Chemicals. *Sustain Energy Fuels*, **2020**, *4* (11), 5568–5577. https://doi.org/10.1039/d0se01149e.

[24] Swenson, H.; Stadie, N. P. Langmuir's Theory of Adsorption: A Centennial Review. *Langmuir*, **2019**. https://doi.org/10.1021/acs.langmuir.9b00154.

[25] Oliveira, V. L.; Morais, C.; Servat, K.; Napporn, T. W.; Olivi, P.; Kokoh, K. B.; Tremiliosi-Filho, G. Kinetic Investigations of Glycerol Oxidation Reaction on Ni/C. *Electrocatalysis*, **2015**, *6* (5), 447–454. https://doi.org/10.1007/s12678-015-0261-2.

[26] Houache, M. S. E.; Hughes, K.; Safari, R.; Botton, G. A.; Baranova, E. A. Modification of Nickel Surfaces by Bismuth: Effect on Electrochemical Activity and Selectivity toward Glycerol. *ACS Appl Mater Interfaces*, **2020**, *12* (13), 15095–15107. https://doi.org/10.1021/acsami.9b22378.

[27] Hausmann, J. N.; Traynor, B.; Myers, R. J.; Driess, M.; Menezes, P. W. The PH of Aqueous NaOH/KOH Solutions: A Critical and Non-Trivial Parameter for Electrocatalysis. *ACS Energy Letters*. American Chemical Society October 8, 2021, pp 3567–3571. https://doi.org/10.1021/acsenergylett.1c01693.

[28] Cossar, E.; Houache, M. S. E.; Zhang, Z.; Baranova, E. A. Comparison of Electrochemical Active Surface Area Methods for Various Nickel Nanostructures. *Journal of Electroanalytical Chemistry*, **2020**, *870*. https://doi.org/10.1016/j.jelechem.2020.114246.

[29] de Paula, J.; Nascimento, D.; Linares, J. J. Influence of the Anolyte Feed Conditions on the Performance of an Alkaline Glycerol Electroreforming Reactor. *J Appl Electrochem*, **2015**, *45* (7), 689–700. https://doi.org/10.1007/s10800-015-0848-6.

[30] Hu, Q.; Xue, Y.; Kang, J.; Scivetti, I.; Teobaldi, G.; Selloni, A.; Guo, L.; Liu, L. M. Structure and Oxygen Evolution Activity of β-NiOOH: Where Are the Protons? *ACS Catal*, **2022**, *12* (1), 295–304. https://doi.org/10.1021/acscatal.1c04647.

[31] Surendranath, Y.; Kanan, M. W.; Nocera, D. G. Mechanistic Studies of the Oxygen Evolution Reaction by a Cobalt-Phosphate Catalyst at Neutral PH. *J Am Chem Soc*, **2010**, *132* (46), 16501–16509. https://doi.org/10.1021/ja106102b.

[32] del Rosario, J. A. D.; Li, G.; Labata, M. F. M.; Ocon, J. D.; Chuang, P. Y. A. Unravelling the Roles of Alkali-Metal Cations for the Enhanced Oxygen Evolution Reaction in Alkaline Media. *Appl Catal B*, **2021**, *288*. https://doi.org/10.1016/j.apcatb.2021.119981.

[33] Farjami, E.; Deiner, L. J. Kinetic Study of the Oxygen Reduction Reaction on α-Ni(OH) 2 and α-Ni(OH) 2 Supported on Graphene Oxide . *J Electrochem Soc*, **2015**, *162* (9), H571–H578. https://doi.org/10.1149/2.0041509jes.

[34] Zheng, W.; Li, Y.; Tsang, C. S.; So, P. K.; Lee, L. Y. S. Stabilizer-Free Bismuth Nanoparticles for Selective Polyol Electrooxidation. *iScience*, **2021**, *24* (4). https://doi.org/10.1016/j.isci.2021.102342.

[35] Laan, P. C. M.; de Zwart, F. J.; Wilson, E. M.; Troglia, A.; Lugier, O. C. M.; Geels, N. J.; Bliem, R.; Reek, J. N. H.; de Bruin, B.; Rothenberg, G.; et al. Understanding the Oxidative Properties of Nickel Oxyhydroxide in Alcohol Oxidation Reactions. *ACS Catal*, **2023**, *13* (13), 8467–8476. https://doi.org/10.1021/acscatal.3c01120.

[36] Oliveira, V. L.; Morais, C.; Servat, K.; Napporn, T. W.; Tremiliosi-Filho, G.; Kokoh, K. B. Studies of the Reaction Products Resulted from Glycerol Electrooxidation on Ni-Based Materials in Alkaline Medium. *Electrochim Acta*, **2014**, *117*, 255–262. https://doi.org/10.1016/j.electacta.2013.11.127.

[37] Lazaridis, T.; Stühmeier, B. M.; Gasteiger, H. A.; El-Sayed, H. A. Capabilities and Limitations of Rotating Disk Electrodes versus Membrane Electrode Assemblies in the Investigation of Electrocatalysts. *Nat Catal*, **2022**, *5* (5), 363–373. https://doi.org/10.1038/s41929-022-00776-5.

[38] Elgrishi, N.; Rountree, K. J.; McCarthy, B. D.; Rountree, E. S.; Eisenhart, T. T.; Dempsey, J. L. A Practical Beginner's Guide to Cyclic Voltammetry. *J Chem Educ*, **2018**, *95* (2), 197–206. https://doi.org/10.1021/acs.jchemed.7b00361.

[39] Khalafi, L.; Cunningham, A. M.; Hoober-Burkhardt, L. E.; Rafiee, M. Why Is Voltammetric Current Scan Rate Dependent? Representation of a Mathematically Dense Concept Using Conceptual Thinking. *J Chem Educ*, **2021**, *98* (12), 3957–3961. https://doi.org/10.1021/acs.jchemed.1c00770.

[40] Yin, X.; Wang, H.; Han, E. H. Effects of Solvation and Applied Potential on the Adsorption Behaviors of H, O, OH and H2O on Fe(110) Surface. *Surf Sci*, **2020**, *691*. https://doi.org/10.1016/j.susc.2019.121504.

[41] Diaz-Morales, O.; Ferrus-Suspedra, D.; Koper, M. T. M. The Importance of Nickel Oxyhydroxide Deprotonation on Its Activity towards Electrochemical Water Oxidation. *Chem Sci*, **2016**, *7* (4), 2639–2645. https://doi.org/10.1039/c5sc04486c.

[42] Yu, X.; Qu, L.; Lee, C.; Peng, J.; Yan, Q.; Bai, H.; Yao, M. Bismuth-Nickel Bimetal Nanosheets with a Porous Structure for Efficient Hydrogen Production in Neutral and Alkaline Media. *Nanoscale*, **2022**, *5*. https://doi.org/10.1039/d2nr04407b.

[43] Hao, Y.; Li, J.; Cao, X.; Meng, L.; Wu, J.; Yang, X.; Li, Y.; Liu, Z.; Gong, M. Origin of the Universal Potential-Dependent Organic Oxidation on Nickel Oxyhydroxide. *ACS Catal*, **2023**, *13* (5), 2916–2927. https://doi.org/10.1021/acscatal.2c04625.

[44] Xue, Q.; Xia, Z.; Gou, W.; Bu, J.; Li, J.; Xiao, H.; Qu, Y. Identification and Origination of the O*-Dominated β-NiOOH Intermediates with High Intrinsic Activity for Electrocatalytic Alcohol Oxidation. *ACS Catal*, **2023**, *13* (1), 400–406. https://doi.org/10.1021/acscatal.2c02104.

[45] Fleischmann, B. M.; Korinek, K.; Pletcher, D.; Hampson, N. A.; Lee, J. B.; Morley, J. R.; Scanlon, B.; MacDonald, K. I. *The Kinetics and Mechanism of the Oxidation of Amines and Alcohols at Oxide-Covered Nickel, Silver, Copper, and Cobalt Electrodes*; 1969; Vol. 47.

[46] Mellsop, S. R.; Gardiner, A.; Johannessen, B.; Marshall, A. T. Structure and Transformation of Oxy-Hydroxide Films on Ni Anodes below and above the Oxygen Evolution Potential in Alkaline Electrolytes. *Electrochim Acta*, **2015**, *168*, 356–364. https://doi.org/10.1016/j.electacta.2015.04.020.

[47] Luo, H.; Yukuhiro, V. Y.; Fernández, P. S.; Feng, J.; Thompson, P.; Rao, R. R.; Cai, R.; Favero, S.; Haigh, S. J.; Durrant, J. R.; et al. Role of Ni in PtNi Bimetallic Electrocatalysts for Hydrogen and Value-Added Chemicals Coproduction via Glycerol Electrooxidation. *ACS Catal*, **2022**, *12* (23), 14492–14506. https://doi.org/10.1021/acscatal.2c03907.

[48] Yu, X.; dos Santos, E. C.; White, J.; Salazar-Alvarez, G.; Pettersson, L. G. M.; Cornell, A.; Johnsson, M. Electrocatalytic Glycerol Oxidation with Concurrent Hydrogen Evolution Utilizing an Efficient MoOx/Pt Catalyst. *Small*, **2021**, *17* (44). https://doi.org/10.1002/smll.202104288.

[49] Pham, T. H.; Lee, W. H.; Byun, J. H.; Kim, J. G. Improving the Performance of Primary Aluminum-Air Batteries through Suppressing Water Activity by Hydrogen Bond-Rich Glycerol Solvent Additive. *Energy Storage Mater*, **2023**, *55*, 406–416. https://doi.org/10.1016/j.ensm.2022.12.012.

[50] Alomar, M. K.; Hayyan, M.; Alsaadi, M. A.; Akib, S.; Hayyan, A.; Hashim, M. A. Glycerol-Based Deep Eutectic Solvents: Physical Properties. *J Mol Liq*, **2016**, *215*, 98–103. https://doi.org/10.1016/j.molliq.2015.11.032.

[51] Takamura, K.; Fischer, H.; Morrow, N. R. Physical Properties of Aqueous Glycerol Solutions. *J Pet Sci Eng*, **2012**, *98–99*, 50–60. https://doi.org/10.1016/j.petrol.2012.09.003.

[52] Phillips, R.; Dunnill, C. W. Zero Gap Alkaline Electrolysis Cell Design for Renewable Energy Storage as Hydrogen Gas. *RSC Advances*. Royal Society of Chemistry 2016, pp 100643–100651. https://doi.org/10.1039/c6ra22242k.

[53] Lee, C. S.; Aroua, M. K.; Ashri, W.; Daud, W.; Cognet, P.; Pérès, Y.; Ajeel, M. A. *Electroreduction of Glycerol*; 2018; Vol. 13.

[54] Shiva Kumar, S.; Himabindu, V. Hydrogen Production by PEM Water Electrolysis – A Review. *Materials Science for Energy Technologies*. KeAi Communications Co. December 1, 2019, pp 442–454. https://doi.org/10.1016/j.mset.2019.03.002.

Chapter 4: The inhibitory and promotional role of glycerol on HER over Ni-based catalysts

Abstract

The coupling of the hydrogen evolution reaction (HER) with the low potential glycerol electrooxidation reaction (GEOR) presents an important pathway to improve the commerciality of green hydrogen due to its lower required energy demand, as opposed to traditional electrolysis. However, few works have investigated the impact of glycerol on HER for membrane-free applications. Furthermore, previous studies on the impact of glycerol on HER are either not representative of relevant HER conditions, or, since it was not the focus of their work, were lightly investigated. Collectively, literature hypothesizes that HER is inhibited by glycerol, due to either a loss of OH^- conduction from an increase in viscosity or the competitive electroreduction of glycerol.

This chapter addresses this knowledge gap, by investigating the claims of the impact of glycerol in relevant HER conditions, over 4 different Ni based catalysts: Ni/C, $Ni_{98}Bi_2$/C, $Ni_{80}Au_{20}$/C and $Ni_{80}Pd_{20}$/C. Linear sweep voltammetry (LSV), impedance spectroscopy and a critical review of the impact of glycerol, on the electrolyte, demonstrates that glycerol has a low propensity to electrochemical reduction. Additionally, a glycerol concentration of up to 2M in a 1M KOH solution is found to not significantly impact OH^- conduction in bulk liquid phase, due to the Grotthuss conduction mechanism which is independent of viscosity. That said, results and literature show that glycerol reduces OH^- conduction by destabilising Nafion®'s hydrophilic domain. It was found that glycerol acts as an inhibitor or promoter of HER depending on the tested catalyst material. For example, the presence of Bi on the surface of $Ni_{98}Bi_2$/C can modulate the inhibitory effect of glycerol over Ni HER, but contrarily, in the case of Au and Pd over $Ni_{80}Au_{20}$/C and $Ni_{80}Pd_{20}$/C, showed evidence of improvements in their HER performances. In turn, membrane-free GEOR-HER catalyst may present a realistic pathway for electrolytic hydrogen production.

4.1 Introduction

Significant political and scientific efforts have been made across the globe to reduce greenhouse gas (GHG) emissions, the leading contributor to climate change [1]. While these efforts have developed novel GHG reducing technologies for intensive GHG emitting industries, the increase in severity and frequency of the consequences related to climate change still demonstrate the need for further solutions and alternatives to GHG emitting processes [1–3]. Among these alternatives is hydrogen gas (H_2), currently a potential chemical feedstock for several intensive GHG industries, an energy carrier for automobiles [4] and energy storage systems [5]. However, barriers to its production, storage, transportation, and utilisation in major GHG emitting industries have limited its accelerated application [2]. Of the various promising production methods of H_2, steam methane reforming (SMR) with carbon capture (CC) and water electrolysis presents promising pathways for low carbon intensive hydrogen. However, both methods require high operational costs [2]. Unlike SMR coupled with CC, water electrolysis can be a non GHG emitting process if the source of electricity originates from renewable sources [2, 6, 7]. Of the various green hydrogen electrolysis processes, anion exchange membrane water electrolysis (AEMWE) presents a promising solution to scalability of the technology through its use of earth abundant materials for its catalyst and applying an efficient zero gap cell design, taking advantage of the benefits of both traditional alkaline and proton exchange membrane water electrolysers, respectively [6, 7].

However, a major limitation to AEMWE's is the catalyst layer instability and still too high overpotential that several liquid water electrolyser technologies fall short [6, 7]. This high overpotential is explained through the nature of the two half cell reactions, being the hydrogen evolution reaction (HER) and oxygen evolution reaction (OER) occurring on the cathode and anode, respectively. While HER and OER can independently be facile reactions in terms of the required potential depending on the pH (equation 4.1 & 4.2), coupling both reaction at a similar pH requires an equilibrium potential of 1.23 V, a relatively high minimum operating potential [6–9]. Furthermore, the formation of gas bubbles on both electrodes presents the formation of non ideal three phase boundary layers, which increases cell resistance and the overpotential [6, 7]. At a pH of 14:

HER (equation 4.1): $2\ H_2O + e^- \rightarrow H_{2\,(g)} + 2\ OH^-$ (0 V vs RHE or -0.826 V vs SHE)

OER (equation 4.2): $4\ OH^- \rightarrow O_{2\,(g)} + 2\ H_2O$ (1.23V vs RHE or 0.401 V vs SHE)

While these limitations can be minimized through improved fabrication, catalyst, and electrode designs [10, 11], other alternatives to traditional water electrolysis reactions have shown promise by substituting OER for the oxidation of organic substrates, particularly major waste chemicals in industries [12–14]. Glycerol (GLY) theoretically has a significantly lower onset oxidation potential than OER at 0.003V [15]. Like other potential chemical wastes, glycerol's electrooxidation reaction (GEOR) from the anode can result in selective value-added products by improving catalyst design, increasing profitability of the process, even accounting for the additional separation steps [15–17]. However, while several works have designed novel GEOR anode catalysts [16, 18–23], few works have reported membrane-free HER coupled with GEOR for H_2 production at relevant current densities [13, 16, 18, 19]. The common reasons for intuitively avoiding this topic are due to an undesirable increase in viscosity and possible competitive reduction of glycerol on the cathode against HER, increasing the cell potential and reducing the faradaic efficiency [24, 25]. In turn, most HER coupled GEOR alkaline electrolyser tested in literature are performed with a two-chamber approach with glycerol circulating on the anode with an anion/cation exchange membrane preventing the migration of glycerol at the cathode. While the anion conductivity of the membrane is vital to reduce the conduction resistance, the necessity to critically prevent the crossover of H_2 and O_2 gases at dangerous levels can be optional, due to the competitive nature of GEOR to OER which was shown in chapter 3 to be suppressed significantly or entirely [11, 26]. In turn, the requirement to utilise a membrane maybe optional, potentially reducing by the AEMWE's CAPEX 60% [11, 26].

At the time of writing, only a handful of works have measured the impact of glycerol on HER [24, 25, 27–29]. Most of these studies did a proof of concept and only one, to our knowledge, has performed an in-depth study. However, there are contradictory conclusions as to the effect of glycerol where some show no or minimal impact on HER [27, 28], while others show an impact on the conductivity, viscosity, and possible reduction on the cathode surface at HER relevant conditions [24, 25]. As for the extensive work of Pham et al 2023, they discovered that glycerol complexed with the cation's hydration shell, which improved the performance of Al-air batteries by suppressing HER [29].

However, certain conclusions from Pham et al. 2023 work are not transferable to electrolysers [29]. For example, the tested concentrations of the alkaline metal (AM^+) (1-4M) is

known to suppress HER by reducing the access of free water due to its saturation at the electrode surface [29]. Most HER electrodes in electrolysers operate at an AM^+ concentration between 0.1M-1M to minimize this effect [30, 31]. In addition, it is well established that nanosized material will behave differently than their bulk counter parts due to surface properties dictating the material properties [32]. For example, the work of Wang et al. 2019 shows nanoparticles of Pt/C produces a highly acidic interface rich with hydronium, even in alkaline media, as opposed to bulk polycrystalline Pt electrodes which remains alkaline [33]. Furthermore, Abrahami et al. 2019, at low NaOH concentration, discovered glycerol forms a protective film of self assembled glycerol molecules which protects bulk Cu when in the presence of a negative potential, a different mechanism for suppressing HER due to a difference in catalyst material [34]. Therefore, it is difficult to easily translate the results of Pham et al. 2023 to HER relevant catalysts, although certain findings are relevant for this work since theoretically the role of glycerol in the bulk electrolyte should be same. Furthermore, the cation nature has an important role in mediating HER adsorbates [35–41]. In turn, glycerol complexing with the cations can interfere with key cation properties in relation to HER.

Thus, as a continuation of the previous works on membrane-free electrolysers by Houache et al. 2020-21 [20, 22, 23] and Shubair et al. 2022 [21], a voltametric investigation of HER was performed over 4 different Ni catalysts that were developed for GEOR for membrane-free electrolysers. The 4 catalysts materials are Ni/C, $Ni_{98}Bi_2$/C, $Ni_{80}Au_{20}$/C and $Ni_{80}Pd_{20}$/C. Based on the results, evidence points to glycerol interfering with HER factors at the catalyst interface. Fascinatingly, this interaction selectively inhibits and potentially promotes HER depending on the catalyst material and HER mechanism. Results also show key evidence of the destabilising effect glycerol has on Nafion®, a key binder used in nearly all organic electrochemical studies, showing the need to change the binder in glycerol related studies. Finally, this work shows the potential of unintuitively mitigating the loss of, and, possibly promoting HER for a membrane-free HER coupled GEOR system, opening the realistic possibility for significantly reduced CAPEX for green H_2. Note that these catalysts weren't designed for HER and thus significant improvements can be made in terms of performance.

4.2 Experimental section

4.2.1 Catalyst synthesis

Prior to each synthesis, all glassware was cleaned overnight by an Aqua Regia solution. Carbon supported $Ni_{X-1}M_{biX}$ (M = Pd, Au, Bi) catalyst were synthesised by sodium borohydride ($NaBH_4$) reduction in ethanol at RT. Firstly, Nickel (II) chloride hexahydrate ($NiCl_2 \cdot 6(H_2O)$, 99.999%, Sigma-Aldrich) and its accompanying bimetallic salt are each dissolved separately in 20 ml of ethanol for 30 minutes. To ensure complete dissolution, each precursor solution was initially treated to 1 minute of sonication in a sonicating bath (40 kHz Ultrasonic Bath, Fischer Scientific, Hampton, NH, USA) and was kept dissolved by magnetic stirring. The accompanying precursor M salts are Palladium (II) chloride ($PdCl_2$, 99%, Alfa Aesar), Gold (III) chloride ($AuCl_3$, 99%, Sigma-Aldrich) and Bismuth (III) chloride ($BiCl_3$, 99.99%, Fischer Scientific). After 30 minutes, both precursor solutions were combined, sonicated for 1 minute and stirred for 15 minutes to ensure a homogenous metal solution. Afterword's, the precursor solution was reduced by drop wise addition of dissolved $NaBH_4$ in 10 ml of ethanol. After 30 minutes, the solution is completely reduced. A respective amount of carbon powder (Vulcan XC72, Cabot Corp.) is immediately added after complete reduction and kept stirring for 30 minutes, resulting in 70 wt% carbon loading. Finally, the nanoparticles were washed with ethanol by centrifuging the samples three times at 6000 rpm for 15 minutes. Once washed, the samples were freeze dried overnight to remove residual ethanol.

4.2.2 Three-electrode electrochemical cell test

Electrochemical measurements were performed in a three electrode Teflon cell with a glassy carbon (0.196 cm^2), mercury/mercury oxide (Hg/HgO, Koslow Scientific Company, Englewood, NJ, USA) and platinum mesh working, reference and counter electrodes, respectively. Catalyst inks were composed of 6 mg of catalyst suspended in 1 ml of milli-Q® Millipore deionized water (18.2 MΩ cm at 293 K), 200 µL of isopropyl alcohol (IPA, 99.9%, Fisher Scientific, Hampton, NH, USA) and 100 µL of 5 wt% Nafion™ (≈5%, Sigma Aldrich, St. Louis, MO, USA). Prior to each test, the glassy carbon (GC) surface was polished on a microfabric with a slurry of 30 µm, then 5 µm of Al_2O_3 in Milli-Q® water. Once polished, 10 µL of catalyst ink was casted on the glassy carbon surface and dried in a 60°C oven. The cell's electrolyte was purged with N_2 gas (Grade 4.8, Linde plc, Dublin, Ireland) for 15 minutes. All electrochemical measurements were

made using a Bio-Logic Potentiostat/Galvanostat paired with EC labs software (Bio-Logic Science Instruments, Seyssinet-Pariset, France) in 1M KOH and various glycerol (>99%, Sigma-Aldrich) concentration solutions. All potential measurements are in reference to the reversible hydrogen electrode (RHE) according to the following equation with no IR compensation, as will be explained in the discussion:

(equation 4.3) $$E_{vsRHE}=E_{vs.Hg/HgO} + 0.098V + 0.0592 \times pH$$

To investigate the HER performance of each nanomaterial in the presence of glycerol, linear sweep voltammograms (LSV) were performed at high current densities, above 10 $mA.cm^{-2}$, to gather a wider measure of the performance of the nanomaterial, at a scan rate of 2 $mV.s^{-1}$. A higher current density was chosen since, as long as the measurements are reproducible, qualitative information can be extrapolated even if a high H_2 bubble evolution interferes with the HER activity from the formation of three phase boundary layers. Furthermore, galvanostatic electrochemical impedance spectroscopy (GEIS) and Potentiostatic electrochemical impedance spectroscopy (PEIS) experiments were carried out to quantify the ohmic losses of the system under applied current and open circuit potential (OCP). GEIS and PEIS was run using a sinus amplitude of 0.1 mA at a DC bias of -1.96 $mA.cm^{-2}$ and 5 mV at a OCP from 0.1 Hz to 50 kHz, respectively.

4.2.3 Notes on electrochemical methodology

IR correction wasn't performed since an 85% IR correction of our 2M Glycerol resulted in an inverted voltammogram, thus IR correction isn't recommended in practice if this occurs [42]. In turn, Tafel slopes (TS) are conservative (i.e. worst performing data) and reporting Tafel slopes shouldn't be permitted since the underlying assumption to make these slopes is the uncompensated resistance is accounted for [42]. However, the reacting environment is a varied parameter, and it is of interest to see how the catalyst behaves without correcting the data since these resistances can't be corrected for at large scale.

Also, the onset potential is a key metric in evaluating the spontaneity of a reaction by representing the minimal potential needed for the initiation of a Faradaic redox reaction. Of the various methods to evaluate the onset potential, such as the tangential HER slope intercept or minimal current density, the onset potential in this work is defined as the one needed to achieve 1 $mA.cm^{-2}$. This was chosen due to the changes in HER behaviours which drastically varies between

materials and the presence of multiple TS. Also, while the electrochemical active surface area (ECSA) is key for normalizing the current density, due to the presence of bimetallics, measuring the ECSA can be inaccurate [43]. In turn, all results are normalised based on the geometric area of the G.C..

Lastly, while the work of Sengeni et al. 2022 shows that GEIS isn't recommended to use during HER [44], their work was performed within PEIS settings without current control and no mention of steady state HER was reached prior to each measurement. In this work, we performed GEIS, after achieving an HER steady state, by completing an HER LSV up to 80 $mA.cm^{-2}$. This approach is valid due the similar charge transfer resistances (R_{CT}) for HER between catalysts as shown in Figure 4.8, as would be expected for materials with similar current densities [45]. R_{CT} is highly sensitive to slight changes in current densities [45], and thus applying PEIS visually, to achieve a consistent GEIS without a current control loop by manipulating the applied potential, isn't recommended for comparison.

4.3 Results

4.3.1 Three-electrode electrochemical cell characterization

An extensive characterisation of the catalyst library has already been performed by Dr. Houache and Asma Shubar for their GEOR performances [20–23]. Based on SEM and EELS images from Houache et al. 2020, it was reported that atomic loadings passed 20% and 10 % for Pd and Au resulted in a Ni@M shell-core structure with traces and islands of Pd and Au on the Ni rich surface, respectively [23]. The formation of Pd and Au islands on the surface is a consequence of the high atomic loadings of each metal. $Ni_{95}Bi_5/C$ presented a similar Ni@M shell-core structure but with traces of Bi on the surface only [21]. This Ni@M shell-core structure is the result of an easier reduction of the decorated accompanying bimetallic metal relative to Ni during its reduction synthesis [20–23].

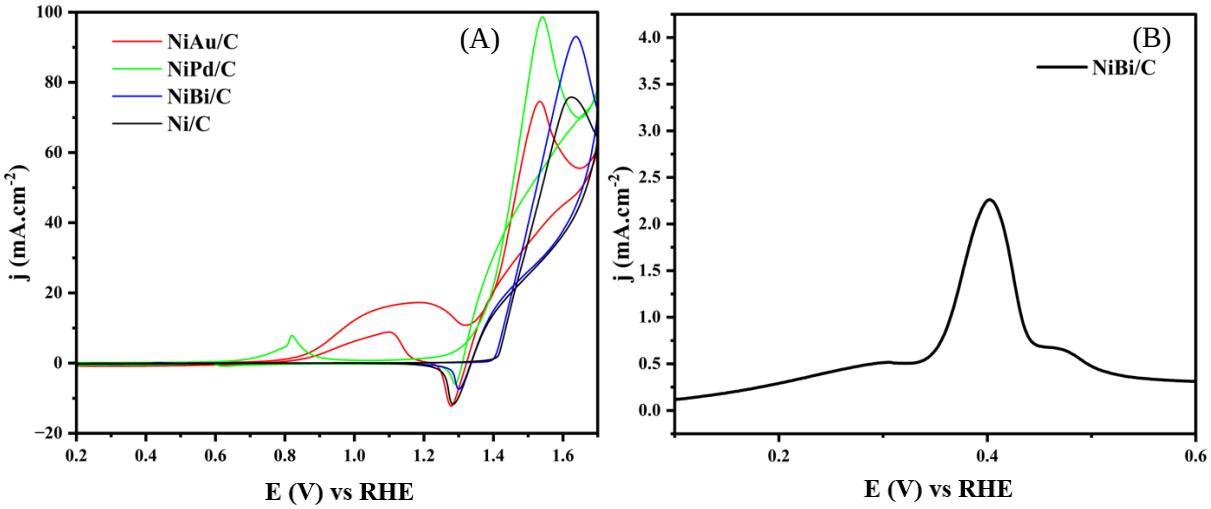

Figure 4.1) (A) 10th Cyclic Voltammogram of Ni/C (black), $Ni_{98}Bi_2$/C (bleu), $Ni_{80}Au_{20}$/C (red), $Ni_{80}Pd_{20}$/C (green) in 1 M KOH at RT scanned at a rate of 25 $mV.s^{-1}$. (B) A zoomed-in image of the bismuth oxidation peaks of $Ni_{98}Bi_2$/C from the same 10th CV cycle.

To validate the presence of Bi, Ni, Au and Pd on the surface only, CVs in alkaline glycerol solution in Figure 4.1 shows the presence of surface glycerol oxidation peaks for Ni (1.531 V vs RHE), Au (1.212 V vs RHE) and Pd (0.823 V vs RHE) at their expected potentials [22]. Bi oxidation peak (0.401 V vs RHE) is also observed at its expected potential range in 1M KOH where Bi → $Bi(OH)_3$ occurs [20, 46]. It is worth noting $Ni_{80}Pd_{20}$/C (99 $mA.cm^{-2}$) and $Ni_{98}Bi_2$/C (93 $mA.cm^{-2}$) presents a higher Ni oxidation peaks than $Ni_{80}Au_{20}$/C (75 $mA.cm^{-2}$)and Ni/C (76 $mA.cm^{-2}$). For $Ni_{98}Bi_2$/C, this can be explained by the high Ni coverage with evenly decorated Bi on the surface which synergistically boosts the reactivity of Ni [21]. For $Ni_{80}Pd_{20}$/C, the relatively low Pd GEOR peak would indicate the catalyst retains a high Ni coverage with Pd islands [22]. As for $Ni_{80}Au_{20}$/C, it represents the weakest Ni oxidation peak but presents a significant Au oxidation peak. This likely represents more Au coverage on the surface and may have resulted in a decreased Ni surface coverage.

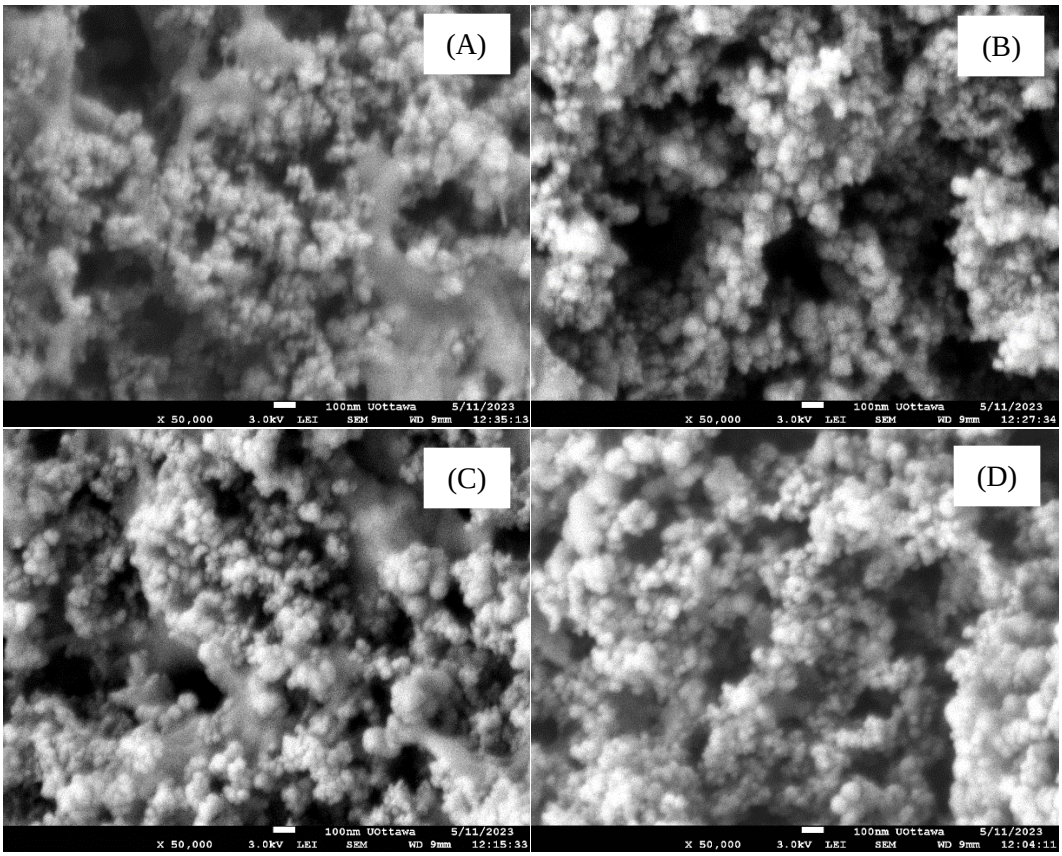

Figure 4.2) SEM images of freshly sprayed at similar magnification for (A) Ni/C; (B) $Ni_{98}Bi_2$/C; (C) $Ni_{80}Au_{20}$/C and (D) $Ni_{80}Pd_{20}$/C onto carbon gas diffusion layer paper.

Figure 4.2 presents the SEM images of each catalyst sprayed on fresh carbon paper GDL as a realistic substrate surface for electrolyser application. Based on these images, each catalyst material is spherical in nature and has a heterogenous distribution of its diameter. This heterogeneity in size is related to the synthesis process whereby dropwise addition of $NaBH_4$ can result in different catalyst sizes if deposition isn't fast enough and a lack of homogeneity within the reacting vessel [47]. The solid smooth surfaces between each nanoparticle is the Nafion® agglomeration.

4.3.2 HER performance in 1M KOH

Prior to the investigation of the effect of glycerol, an electrochemical investigation of each catalyst will be conducted first in 1M KOH.

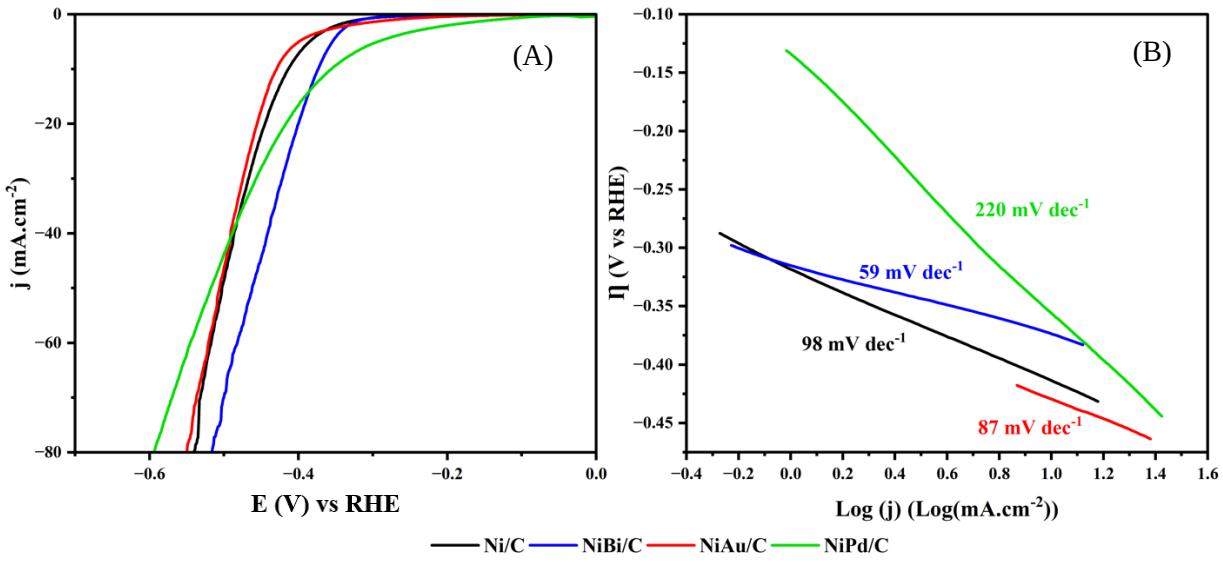

Figure 4.3) (A) LSV of Ni/C, $Ni_{98}Bi_2$/C, $Ni_{80}Au_{20}$/C and $Ni_{80}Pd_{20}$/C in 1M KOH with various concentrations of glycerol measured at RT and at a scan rate of 2 $mV.s^{-1}$. (B) Tafel slope of each respective catalyst under similar conditions.

Figure 4.3A presents the LSV of each tested nanomaterial in 1M KOH only. Based on these results, the catalysts with the lowest onset potentials are $Ni_{80}Pd_{20}$/C (-134 mV) < $Ni_{80}Au_{20}$/C (-273 mV) < Ni/C (-319 mV) < $Ni_{98}Bi_2$/C (-334 mV). In addition, the lowest η_{HER} at 10 $mA.cm^{-2}$ are $Ni_{80}Pd_{20}$/C (-333 mV) < $Ni_{98}Bi_2$/C (-392 mV) < Ni/C (-415 mV) < $Ni_{80}Au_{20}$/C (-430 mV). As for the TSs in Figure 4.3B, $Ni_{98}Bi_2$/C(-56 $mV.dec^{-1}$), $Ni_{80}Au_{20}$/C (-89 $mV.dec^{-1}$) and Ni/C (-93 $mV.dec^{-1}$) undergo a Volmer-Heyrovsky mechanism. For $Ni_{80}Pd_{20}$/C (-232 $mV.dec^{-1}$), it is rate limited by the Volmer step, hence the dissociation of water. It is important to note that a Tafel slope higher than 120 $mV.dec^{-1}$ doesn't necessarily mean an HER reaction is Volmer limited since its surface can be saturated by adsorbed H^* and be Hervosky limited instead [48]. But due to the limited surface characterizations, it will be assumed the system is Volmer limited past this point to show the extent of change the TS undergoes. It is important to highlight no $I*R_U$ correction was performed since the influence of glycerol on the uncompensated resistance would produce inverted voltammograms, even accounting for 50% of the correction [49, 50].

Based on these results, each accompanying bimetallic influences Ni HER which has been previously reported for their GEOR performances [20–23]. However, the synergistic effects of Bi, Au and Pd on Ni HER isn't consistent. For the onset potential of HER which reflects its activation energy [51], this synergy is detrimental in $Ni_{98}Bi_2$/C but promotional for $Ni_{80}Au_{20}$/C and $Ni_{80}Pd_{20}$/C. However, $Ni_{98}Bi_2$/C TS is sufficiently superior where it's overpotentials are lower than the other

catalysts (Figure 4.3). However, dedicated surface characterisations (EELS) and DFT simulations should be performed to reduce ambiguity as to the likeliest mechanism and influence Bi, Au and Pd has on Ni's HER [52].

4.3.3 The influence of glycerol on HER

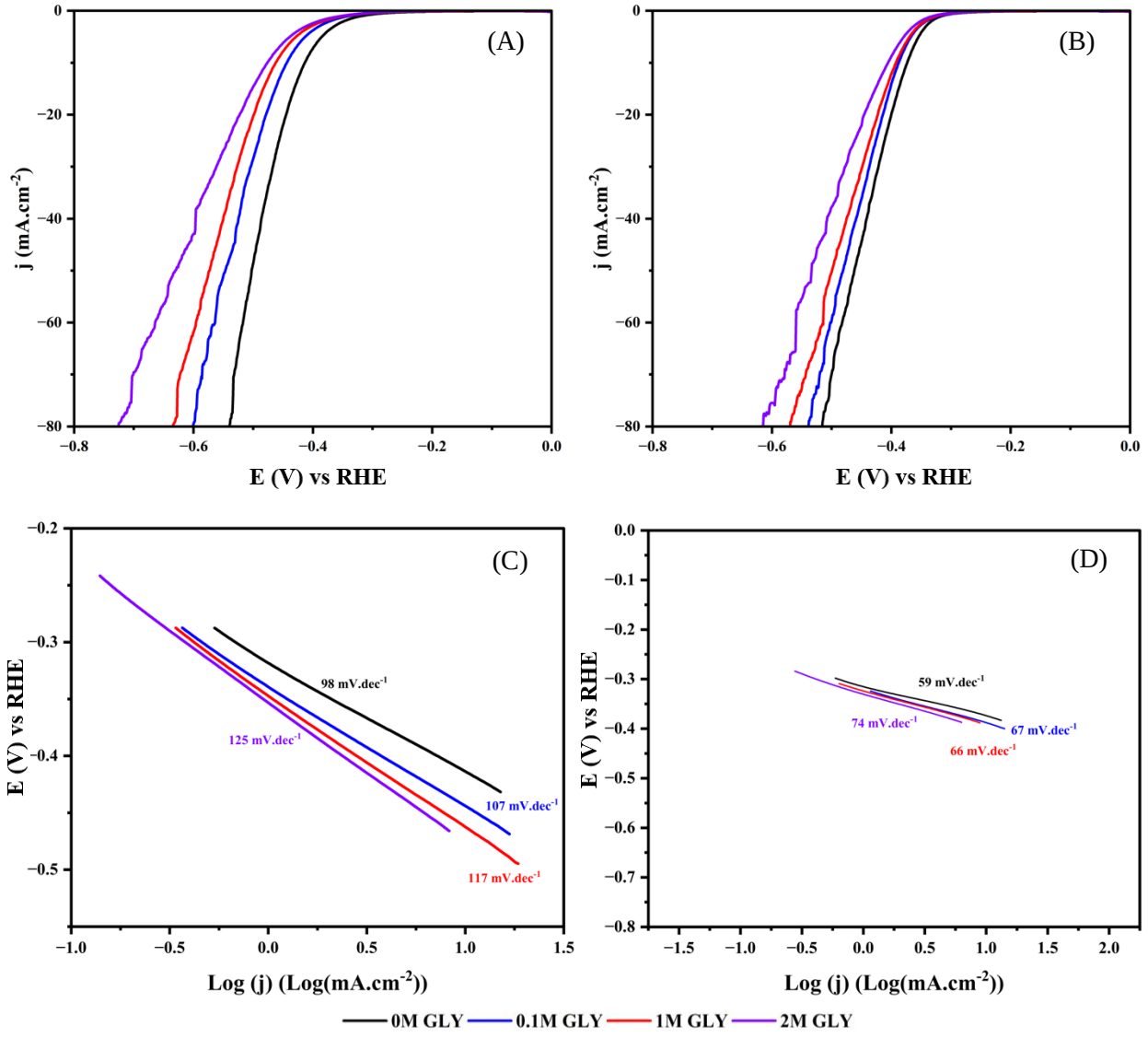

Figure 4.4) LSV of (A) Ni/C and (B) $Ni_{98}Bi_2$/C in 1M KOH and various concentrations of glycerol measured at RT and at a scan rate of 2 $mV.s^{-1}$. Tafel slope of (C) Ni/C and (D) $Ni_{98}Bi_2$/C extrapolated from their LSV results.

A summary of the influence of glycerol is shown in Figure 4.7 both in the absence and presence of glycerol. Figure 4.4 shows the impact of glycerol on HER over $Ni_{98}Bi_2$/C and Ni/C where 2 M glycerol caused the highest increase in the onset potentials for both materials,

requiring a higher driving force to initiate HER by -15 mV -34 mV in comparison to 0M glycerol, respectively. Similarly, the 10 mA.cm^{-2} η_{HER} also shifted negatively by -62 mV (15%) and -32 mV (8 %) for Ni and $Ni_{98}Bi_2$/C, respectively. Tafel slope analysis of Ni/C indicates a transition from the Volmer-Hervosky mechanism at 98 mV.dec^{-1} to a Volmer-dictated process at 120 mV.dec^{-1} (+22 mV.dec^{-1}) in the presence of 2M GLY, a change in mechanism. In the case of $Ni_{98}Bi_2$/C, the Volmer-Heyrovsky mechanism is retained, but the Tafel slope shifts from 59 mV.dec^{-1} to 74 mV.dec^{-1} (+15 mV.dec^{-1}).

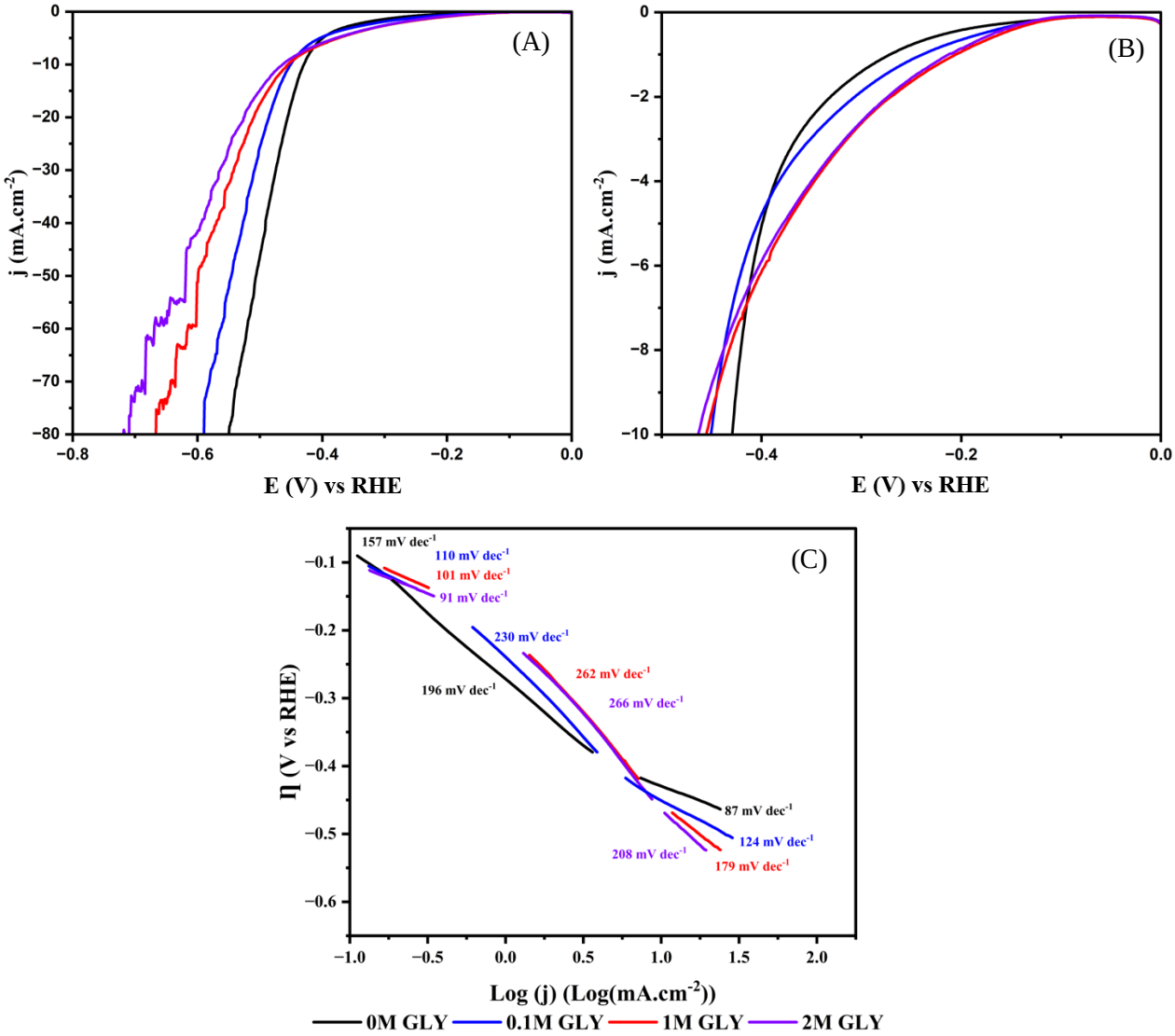

Figure 4.5) A) LSV of $Ni_{80}Au_{20}$/C and B) a magnification of its low current density measurements in 1M KOH and various concentrations of glycerol measured at RT and at a scan rate of 2 mV.s^{-1}. C) Tafel slopes of $Ni_{80}Au_{20}$/C under various glycerol concentrations.

In the case of $Ni_{80}Au_{20}$/C, an unexpected improvement in its onset potential up to 1M glycerol from -273 mV to -206 mV is observed, followed by a slight decrease to -214 mV at 2M glycerol. This would theoretically indicate an increase in [GLY] reduces the apparent activation energy of HER. As for its $\eta_{10mA.cm-2}$, it decreases and plateaus to -456 mV at 1M glycerol. To understand why a plateau behaviour occurred, it was observed three separate TSs were detected over $Ni_{80}Au_{20}$/C by varying the concentration of glycerol (Figure 4.5). The sum of the combined influence of each of these TSs caused the placement of the $\eta_{10mA.cm-2}$ to be plateaued at 1M glycerol. This observation of more than two separate TS is theoretically impossible for HER for a given catalyst material [48, 53–55]. However, the previously reported formation of Au islands on the Ni surface at atomic ratios higher than 1:9 does propose there are multiple types of HER active sites [22]. In turn, the presence of multiple TS can be explained by the presence of separate Au and Ni HER. Based on literature, Au is often ignored as a bimetallic material for HER due to its too weak hydrogen bonding energy (HBE) and hydroxide bonding energy (OHBE) [56, 57]. In turn, Au nanoparticles alone typically have a poor TS [16, 56] and little scientific work is done on Au as the main HER catalyst phase in alkaline media. Based on the three TS over $Ni_{80}Au_{20}$/C in figure 4.5, the first two low current density (<10 $mA.cm^{-2}$) TSs of 157 $mV.dec^{-1}$ and 196 $mV.dec^{-1}$ are not measurable for any other catalysts at current densities smaller than 10 $mA.cm^{-2}$. From a process of elimination and validating Au is HER active and is significantly present on the catalyst surface (figure 4.1), the first two low current TSs are likely ascribed to the HER kinetics of Au.

Intriguingly, upon inspecting why the sum of these TSs would cause a plateau of the measured $\eta_{10mA.cm-2}$ near an inflection point (Figure 4.5B & 4.7B), the lowest current density TS (<1 $mA.cm^{-2}$) improved significantly from 157 $mv.dec^{-1}$ in 0M glycerol to 91 $mV.dec^{-1}$ 2M glycerol. This represents an improved transition from a Volmer limited to Heyrovsky limited process through a change in glycerol concentration only. Furthermore, the current density window by which this TS is stabilised increases, meaning glycerol may promote this mechanism for a wider reaction rate. Additionally, the second lowest TS (1 $mA.cm^{-2}$ < j < 10 $mA.cm^{-2}$) independently worsened from 196 $mV.dec^{-1}$ at 0M glycerol to 266 $mV.dec^{-1}$ in 2M glycerol. Similarly, the highest current density TS (>10 $mA.cm^{-2}$) also worsens from 87 $mV.dec^{-1}$ at 0M glycerol to 208 $mV.dec^{-1}$ in 2M glycerol.

Based on the promotional influence on the lowest TS and the inhibitory influence on the remaining TSs, this indicates the influence of glycerol isn't dominant in the bulk electrolyte but near the catalyst interface due to the material and HER mechanistic dependence. In the case of the particular mechanisms that are improved or inhibited below 10 $mA.cm^{-2}$, it indicates the mechanism of glycerol's influence on HER isn't universal for each HER mechanism even over the same material. As for the influence of Au on Ni HER, the highest current TS significantly degraded by +121 $mV.dec^{-1}$ up to 2M glycerol, as opposed to Ni/C which only worsened by +22 $mV.dec^{-1}$ even if $Ni_{80}Au_{20}$/C has a better TS at 0M glycerol of 87 $mV.dec^{-1}$. In turn, the synergistic effect of Au on Ni's HER appears detrimental unlike Bi. In turn, there is evidence to show Bi modulates the inhibitory role of glycerol over Ni HER. This further validates the influence of glycerol on HER is weighted significantly at the catalyst surface than in just the bulk electrolyte.

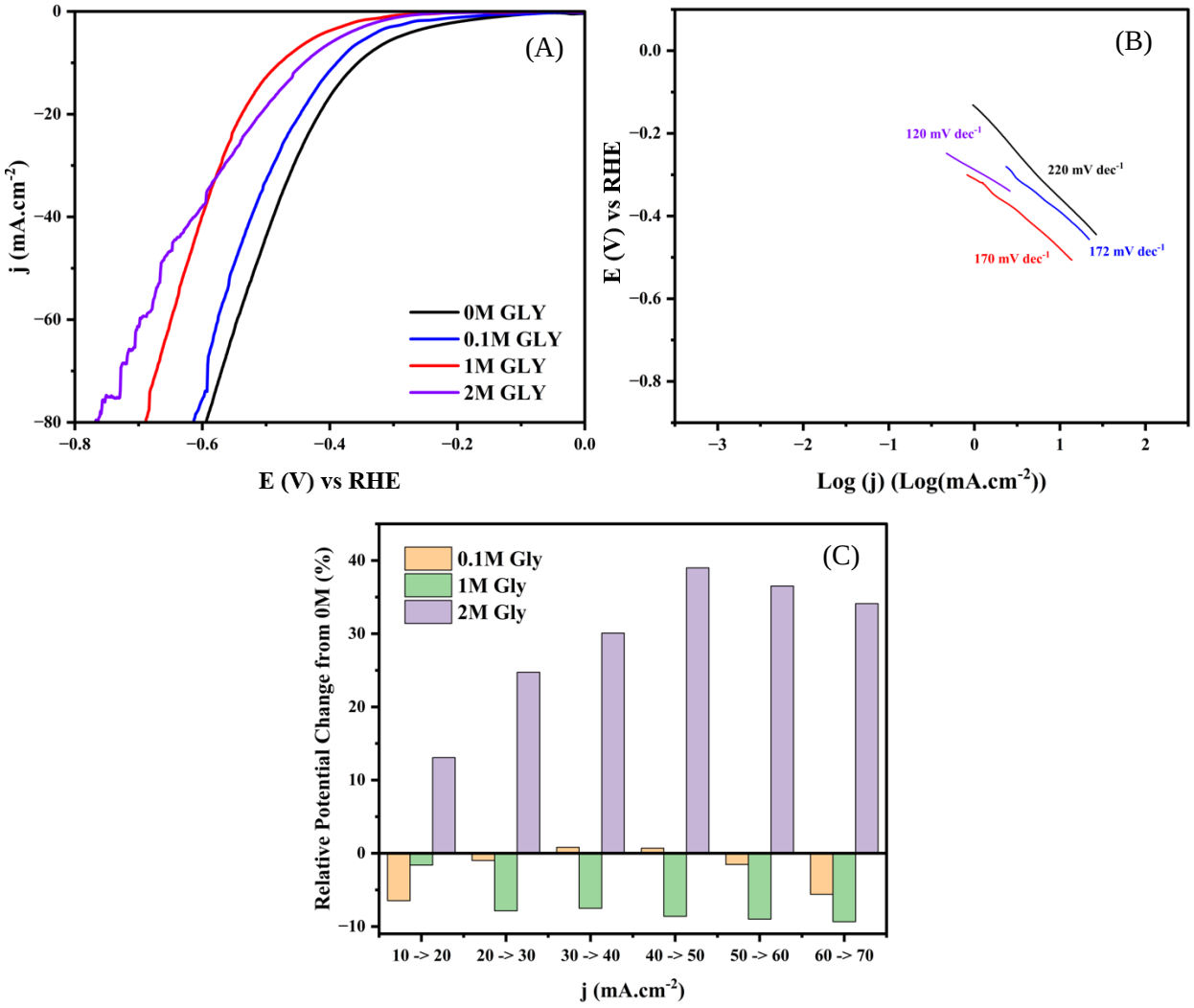

Figure 4.6) LSV of (A) $Ni_{80}Pd_{20}$/C in 1M KOH and various concentrations of glycerol measured at RT and at a scan rate of 2 mV.s^{-1}. T(C) A relative comparison of the change in potential for an increase in current density of 10 mA.cm^{-2} at a given concentration of GLY in reference to 0M GLY results.

Interestingly $Ni_{80}Pd_{20}$/C presents its own novel HER behaviour. Based on $Ni_{80}Pd_{20}$/C's significantly reduced onset potential (figure 4.7A) and elevated TS of 220 mV.dec^{-1} (figure 4.3B), these resemble the expected performance of carbon supported Pd catalysts [31, 51]. It's onset potential decreases rapidly from -134 mV to -310 mV up to 1M glycerol. But at a concentration of 2M GLY, the onset potential improves to -287 mV, the opposite in behaviour to $Ni_{80}Au_{20}$/C but very similar to the Pt/C behaviour in Chapter 3. A similar behaviour is observed for its $\eta_{10mA.cm-2}$ where it worsened from -356 mV to -479 mV at 1M glycerol but improves to -441 mV at 2M glycerol. The TS from 0M to 2M GLY improves significantly from -220 mV.dec^{-1} to -120 mV.dec^{-}

[1], while remaining Volmer limited. This is similar to what was observed for $Ni_{80}Au_{20}$/C's lowest current TS. The sum of these observations combined with the expected formation of Pd islands over Ni at an atomic ratio of 2:8 concludes $Ni_{80}Pd_{20}$/C behaves primarily as a Pd catalysts than a Ni catalyst towards HER [22, 31, 51]. In turn, $Ni_{80}Pd_{20}$/C reflect Pd HER metrics rather than Ni. While this does diverge from focusing the effect of glycerol on Ni HER, it does provide an opportunity to broaden the understanding of glycerol on HER.

To validate the TS is improving, a closer validation was done in figure 4.6C by comparing the change of the overpotential for every 10 $mA.cm^{-2}$ increment of each tested glycerol concentration in reference to the 0M glycerol test. For the concentrations 0.1M and 1M glycerol, we observe an improved HER mechanism across the current density range compared to 0M GLY. Thus, if the current density range was increased, it would be possible to see 0.1M and 1M glycerol surpass 1M KOH only. As for 2M glycerol, we observe a rapidly worsening HER performance unlike its TS which improved. This discrepancy at 2M glycerol is explained by TS being measured below 10 $mA.cm^{-2}$ due to a sooner mass diffusion limitation, which is outside the range used to perform the sanity check.

Based on LSV results, Bi, Au and Pd have synergistic effects and dictates how Ni's HER behaves in the presence of glycerol. The novel behaviours of each catalyst, in the presence of glycerol, show evidence of a surface interaction between glycerol and key surface HER factors which are dependent on the catalyst material. This indicates glycerol has a major influence on HER in alkaline conditions near the catalyst interface, disagreeing with the previous preliminary works stating that glycerol must negatively influence OH^- conduction and should worsen HER.

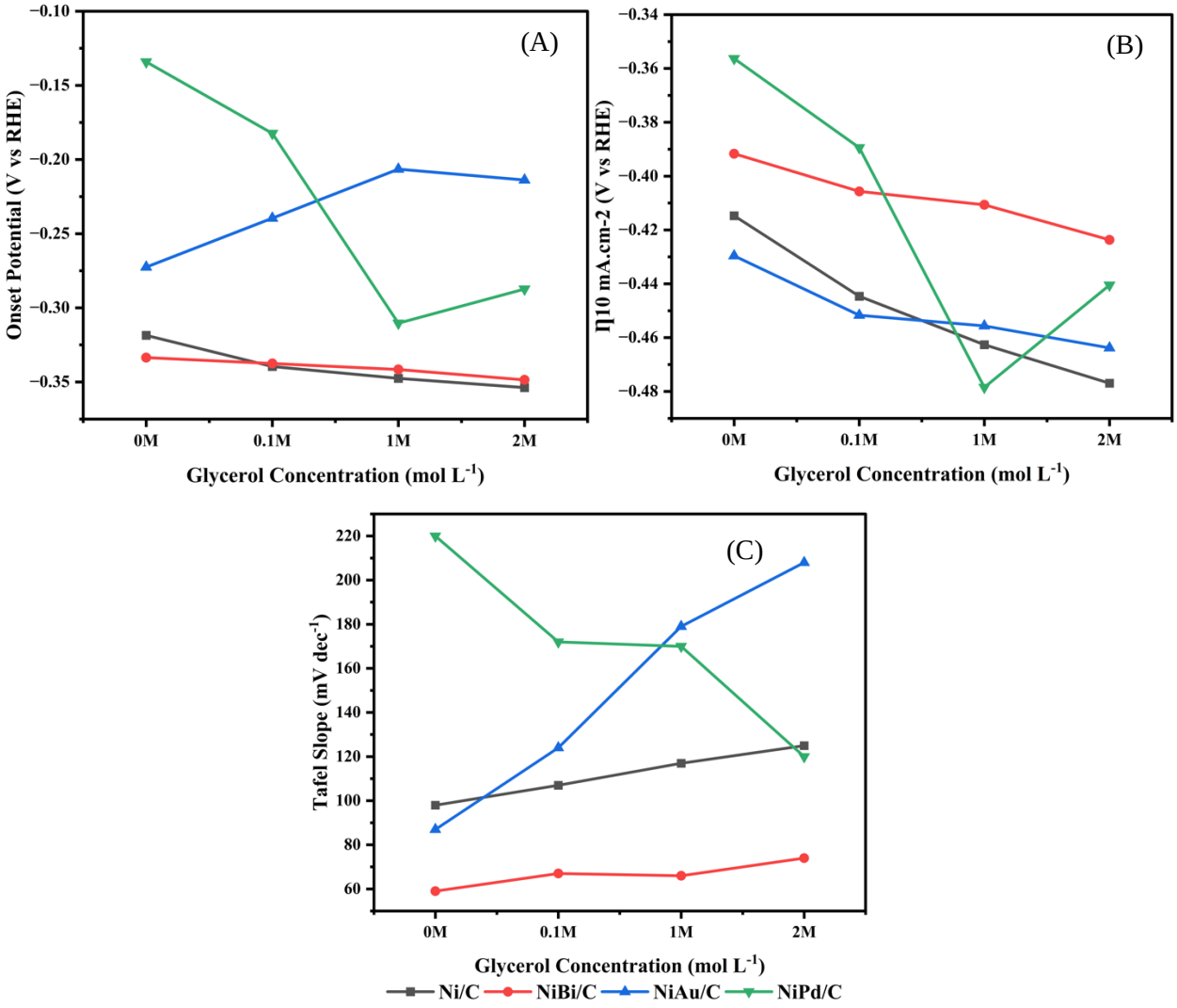

Figure 4.7) Summary of the influence of glycerol concentration on the (A) onset potential, (B) $Ƞ_{10mA.cm-2}$, (C) Tafel slope of Ni/C, $Ni_{98}Bi_2$/C, $Ni_{80}Au_{20}$/C and $Ni_{80}Pd_{20}$/C in 1M KOH in various glycerol concentrations measured at a scan rate of 2 $mV.s^{-1}$ and RT.

4.3.4 Glycerol's competitive electroreduction to HER

Based on these results, unexpected differences to other works are apparent. The question of glycerol's electroreduction will be addressed first. For Ni/C, as a base line of comparison, a transition from a Heyrovsky to Volmer limited process occurs as the [GLY] is increased from 0M to 2M. A commonly referenced explanation is the electroreduction of glycerol or its occupation of adsorption sites, which increases the TS since fewer sites are available to perform HER [24, 25]. The electroreduction of glycerol was shown by Yu et al. 2021 and Kongjao et al. 2011 from the detection of possible reduction products through HPLC measurements [24, 25]. However, each of these studies performed their tests in a single chamber 3-electrodes cell where the counter Pt mesh

electrode (anode) underwent GEOR, cross contaminating the electrolyte with GEOR products [24, 25]. This can be an experimental issue since certain products of GEOR on the anode do show the propensity to electrochemically reduce to the products Yu et al. 2021 and Kongjao et al. 2011 recorded [58]. Thus, the conclusion from these works can be put into question and may require revision. Interestingly, different alcohols have a different propensity for electrochemical reduction [59]. In the case of glycerol, glycerol's reduction (not electrochemical reduction!) often requires an electrochemical mediator such as Amberlyst-15 [58] and extreme reactive conditions [58, 60], demonstrating its novel inertness to electroreduction at standard conditions. To our knowledge, Steen et al. 2023 has shown glycerol can electrochemically reduce over Cu at standard conditions but still requires a high overpotential with glycerol as the primary electrolyte constituent, as a eutectic solvent, for measuring the reduction of other organic substrates [32], demonstrating its electro-reductive inertness. In the case of Yu et al. 2021, they reported that glycerol increased their Pt catalyst overpotential for HER on the cathode due to a reduction in conductivity (which will be discussed later) and referenced the work of Dam et al. 2012 in their work, which shows evidence for the electroreduction of glycerol over Pt based catalysts [24]. However, the results of Dam et al. 2012 were performed at 200^{o}C and a highly reductive atmosphere of 40 bar of H_2 [61], which is very different from the standard temperatures and pressures in an inert atmosphere reported by Yu et al. 2021 and this work. This shouldn't be used lightly as a point of comparison to our conditions or Yu et al. 2021. Works dedicated to the issue of glycerol electroreduction have extensively shown that glycerol has a wide cathodic window of electrochemical stability, unlike other alcohols to the author's knowledge, and shows no clear evidence of reactive adsorption even at high cathodic potentials [29, 32, 58]. This is supported in Chapter 3 which showed a high faradaic efficiency to hydrogen production in a membrane-free cell and the absence of electro-reductive products during HPLC measurements from previous colleagues [20–23]. In conclusion, it is assumed in this work the reduction of glycerol is insignificant in the measurements. This is not to say that it doesn't occur but is a negligeable parameter. However, the question of electrochemical reduction of glycerol in standard conditions should be addressed conclusively for membrane-free applications.

4.3.5 Glycerol's influence on conductivity

Based on the work of Pham et al. 2023 and theorised by Yu et al. 2021, a dominant influence of glycerol to HER is a combination of an increase in viscosity, a reduction in H_2O_{free} concentration and a reduction in H_2O_{free} permittivity should increase the bulk electrolyte

conduction resistance [24, 29]. This expectation is supported by the capacity of glycerol to form hydrogen bonds (HB) with the surrounding water which can affect waters' dielectric properties and complex with the conductive cation [29, 50, 62, 63]. However, using the conclusion on resistivity of the electrolyte reported by Pham et al. 2023 to our experiments isn't translatable due to the nature of the systems. In the case of Pham's work, Na^+ is the conductive ion, while OH^- is the conductive ion in this work. Although no previous work has shown glycerol substitutes coordinated water within an anion's hydration shell, alcohols can reduce an anion's conduction (such as Cl^-) but the way organic substrates interact between anions and cations can differ significantly [64, 65]. To validate if there is a change in electrolyte conductivity, GEIS and PEIS measurements were made for each material at 10 $mA.cm^{-2}$ and open circuit potential (OCP) to extrapolate the uncompensated resistance (R_U), respectively.

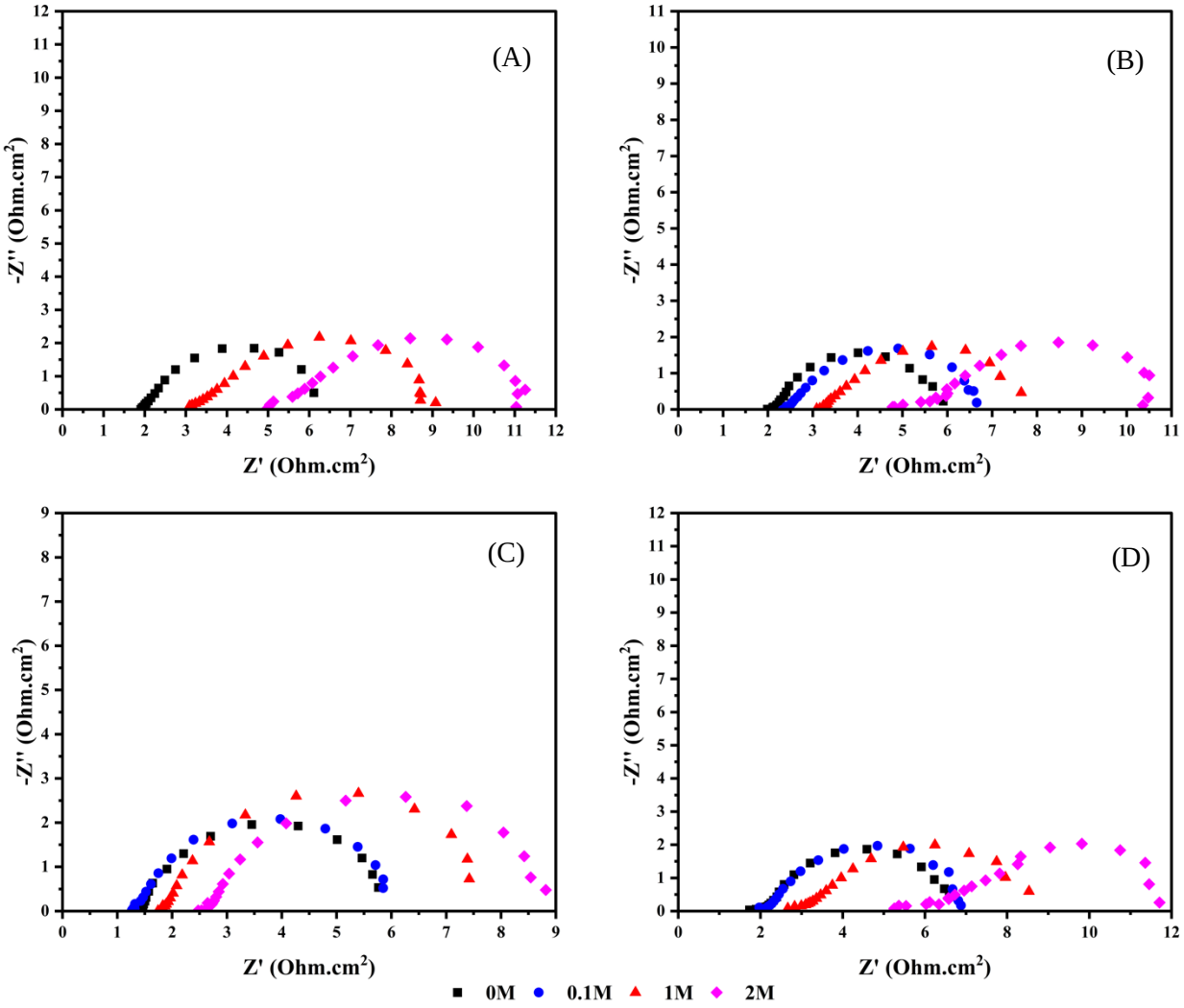

Figure 4.8) Galvanostatic electrochemical impedance spectra at 10 mA.cm^{-2} of (A) Ni/C, (B) $Ni_{98}Bi_2$/C, (C) $Ni_{80}Pd_{20}$/C and (D) $Ni_{80}Au_{20}$/C catalysts during HER within different glycerol concentrations (0M, 0.1M, 1M and 2M) in 1M KOH.

Based on the results of Figure 4.8, each catalyst material presents a GEIS response which was modelled by a Voight circuit in series, composed of parallel resistances and constant phase elements (CPE) (Schematic 3.S1). This model was chosen since each GEIS profile presented a Warburg like response as is indicated by the low inclined angle between 55-35º of each low frequency (LF) charge transfer process. This response is expected for heterogenous reactions [66–69]. Theoretically, a Randles circuit is used to model a Warburg response. However, due to the high error in fitting a Randles model, which isn't uncommon, an approximation of the Warburg was used with a large series of Voight circuits [66–71].

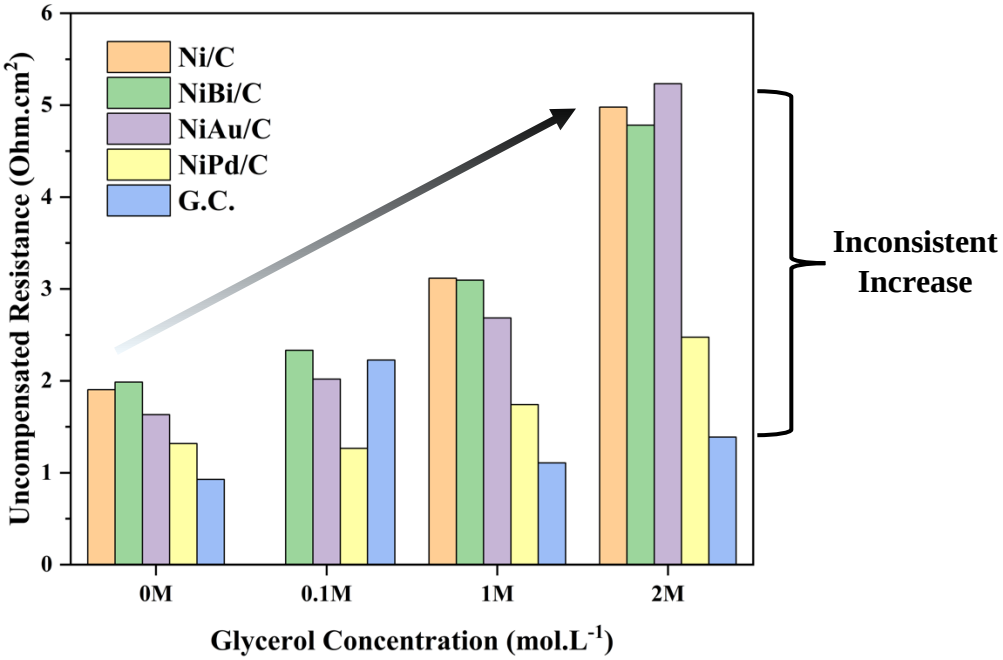

Figure 4.9) Summary of the change in R_U as a function of the glycerol concentration over Ni/C, $Ni_{98}Bi_2$/C, $Ni_{80}Pd_{20}$/C, $Ni_{80}Au_{20}$/C and G.C..

Based on figure 4.8 and figure 4.S1-4, Ni/C, $Ni_{98}Bi_2$/C and $Ni_{80}Au_{20}$/C present a similar increase of their R_U while $Ni_{80}Pd_{20}$/C shows a smaller increase as glycerol's concentration increases in both GEIS and PEIS. A summary of the R_U is found in figure 4.9. This indicates the impact of glycerol on OH^- conductivity isn't consistent between each material. This difference challenges a reduction in bulk electrolyte conductivity is the main contributor to the increase in R_U, since it is independent of the catalyst material. From the similar R_U values between PEIS at OCP and GEIS, this demonstrates the increase in R_U by glycerol isn't caused by HER but from the electrolyte. This pinpoints the effects of glycerol on EIS data in the electrolyte solution and not necessarily the HER mechanism directly. However, due to the difference in R_U between $Ni_{80}Pd_{20}$/C and the remaining catalysts, the effect can also originate from the catalyst interface but this effect isn't consistent between materials.

Based on the Warburg response in Figure 4.8, an increase in glycerol concentration (2M) rendered more significant an already present charge transfer process at high frequencies (HF) on all catalysts but less obvious on $Ni_{80}Pd_{20}$/C under GEIS conditions only. However, the absence of an HF process at OCP during PEIS shows the HF process is related to HER, but not necessarily itself HER. This indicates R_U and the HF process ($R_{CT\text{-}HF}$) aren't related to the same phenomena. Since this HF process is a charge transfer resistance in equivalent circuitry (EC), glycerol increases

resistances related to the HER process itself, on top of the changes related to R_U. Based on HER related EIS precedence, an R_{CT-HF} is often associated with porous materials and is expected for carbon supported catalysts, like the ones in this work [72–75]. While glycerol increases R_{CT-HF}, it is difficult to state if glycerol is influencing an already present HF process or adding new resistances in series that creates the illusion of a single HF charge transfer that is growing due to the quality of the data. This is often a limitation of EIS [67, 76, 77]. Regardless, changes in HF processes related to porous electrocatalysts often occurs when there are changes in the electrolyte properties in the pores (surface tension, viscosity, resistance, bubble formation) and the catalyst interface (such as surface poisoning which blocks active sites and reduces the ECSA) [66]. Based on this, it would indicate an increase in glycerol concentration undesirably changes the electrolyte properties and/or the catalyst interface in relation to the pore properties of the catalyst layer, the same conclusion from R_U.

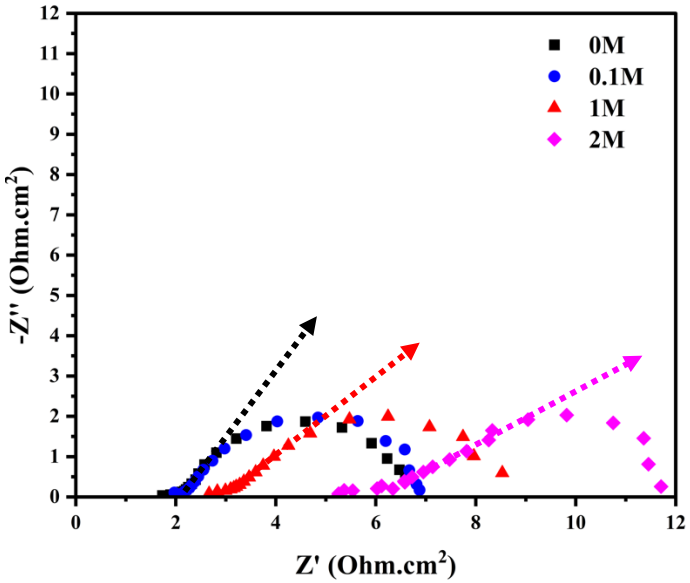

Figure 4.10) Galvanostatic electrochemical impedance spectra at 10 mA.cm^{-2} of $Ni_{80}Au_{20}$/C catalysts during HER within different glycerol concentrations (0M, 0.1M, 1M and 2M) in 1M KOH. The arrows visually indicate the angle of the transmissive line of their respective EIS.

Fitting a Voigt circuit model also led to observe the α exponent value in the constant phase element (CPE) of the low frequency (R_{CT-LF}) charge transfer process decreases by the decreasing inclined angle from 54° at 0M glycerol to 37° at 2M glycerol (figure 4.10). Based on HER literature precedence, a reduced α value is indicative of a reduction in conductivity within the catalyst pores [69, 71]. Considering R_{CT-HF} are strongly related to porous materials [72–74], these changes in these EC

parameters repeatedly point to the impact of glycerol on HER to the porosity of the catalyst layer. However, these are literature-based precedence and validation is needed to know if changes in EIS results are correlated to the catalyst porosity, since the implication that changes in electrolyte properties originate from the pores (and not from the bulk electrolyte phase) disagrees with previous works [24, 29]. It is important to clarify the catalyst layer is not to be confused to the metal catalyst since the latter has no porous structure in of itself based on SEM images shown in figure 4.2 and the work of Dr. Houache and Asma Shubar [20–23]. The catalyst layer does retain a porous structure according to figure 4.2 due to the carbon support and the even decoration of the electrocatalyst.

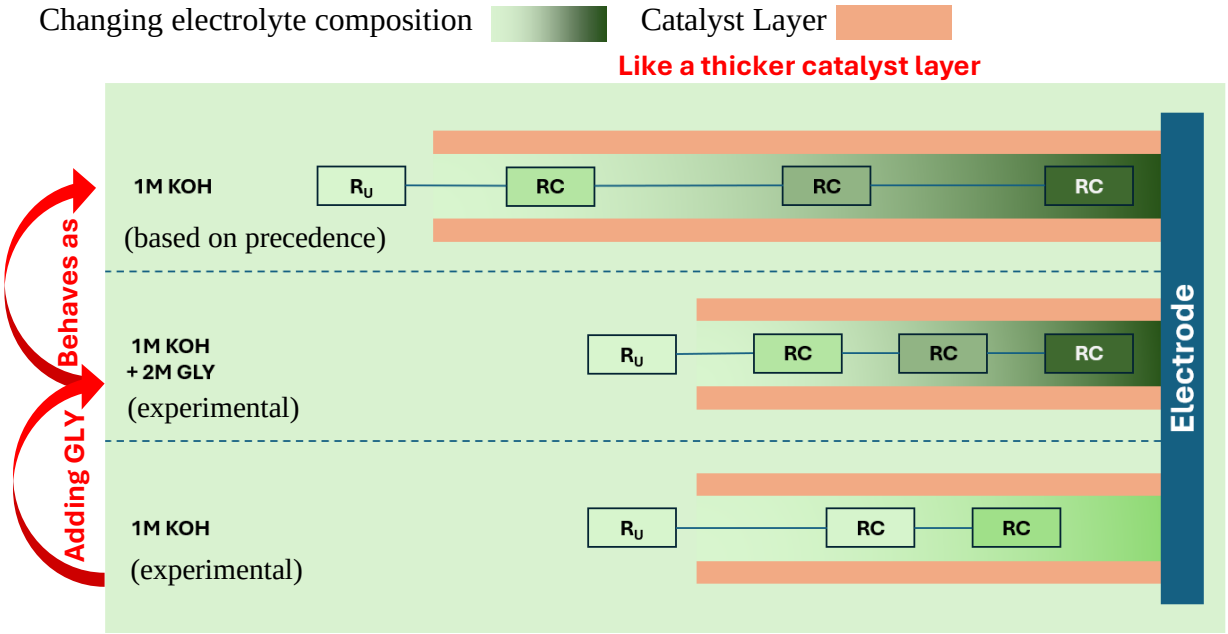

Schematic 4.1) A visual representation of what an increase in glycerol concentration causes to the EIS of Ni/C, $Ni_{98}Bi_2$/C, $Ni_{80}Pd_{20}$/C, $Ni_{80}Au_{20}$/C. An increase in glycerol concentration causes the EIS to change as if a porous electrode is becoming thicker in depth due to the requirement to fit more RC circuits to fit the Voight model to the EIS spectrum. The changing colour of the RC circuits is a representation of the changing electrolyte resistance and capacitance at said thickness of electrode due to the electrolyte properties evolving.

Furthermore in relation to the reduced α value, there is also an increased transmissive behaviour (increased linear section between the HF and LF process) in figure 4.8 and 4.10 which is synonymous with a thicker diffusion layer that is often associated with a change in electrode pore depth, where the reactant in question is steadily depleted the deeper it travels within the electrode [66, 68, 69, 78, 79]. This is schematically shown in schematic 4.1 with an increase in the required number of RC series to model the EIS response. This indicates that the addition of

glycerol further evolves the diffusion properties of key HER components, such as H_2O or OH^-, along the electrode thickness, pointing again to the catalyst layer and its porous properties being influenced by glycerol.

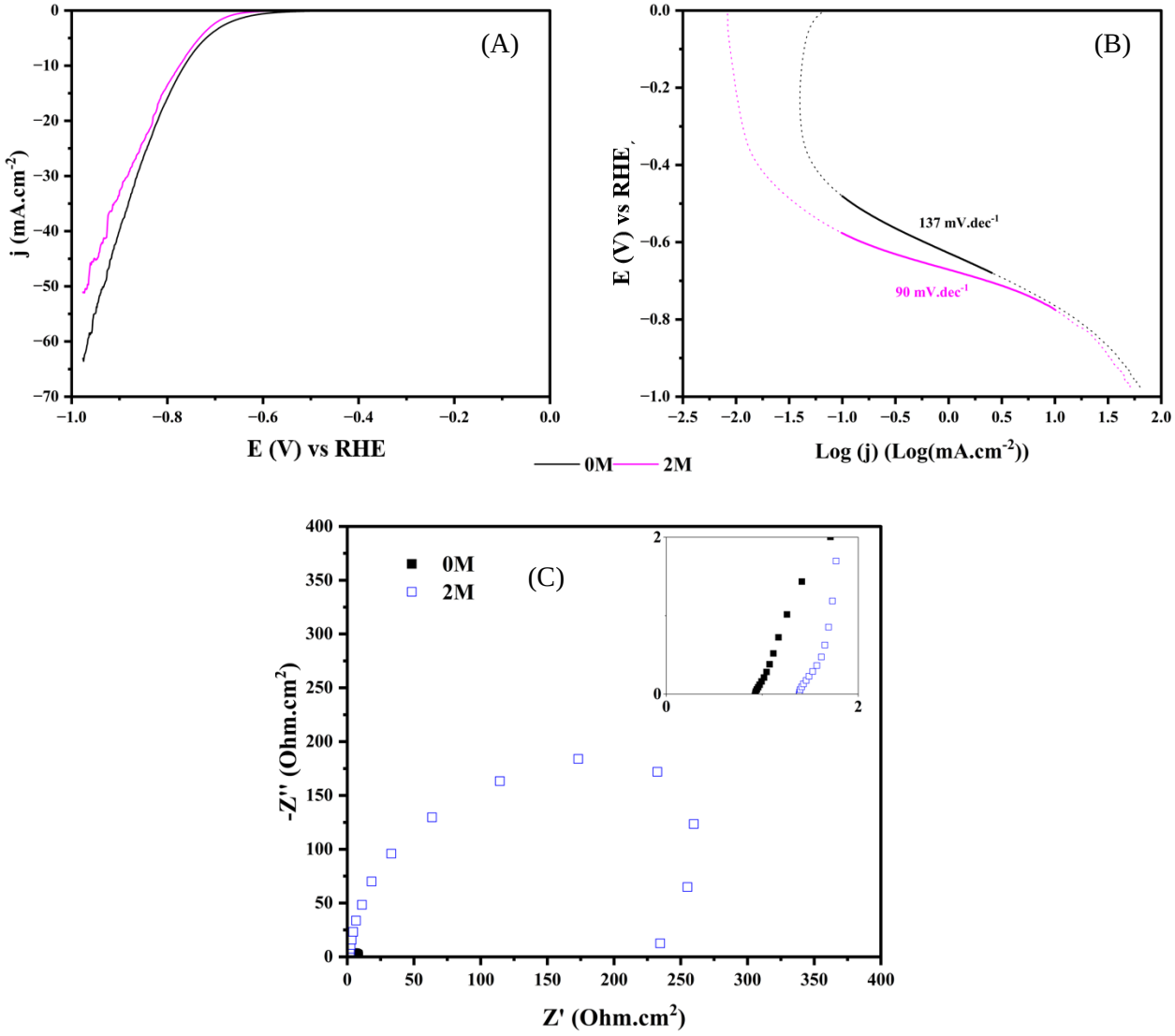

Figure 4.11) (A) LSV and (B) Tafel slope of G.C. in the absence or presence of 2M glycerol and 1M KOH at RT and at a scan rate of 2 $mV.s^{-1}$. (C) Potentiostatic impedance spectrum at -600 mV vs RHE in 1M KOH and 0M or 2M glycerol.

To validate if glycerol induces changes to the catalyst pore properties specifically, figure 4.11 presents the HER LSV, TS and PEIS of polished G.C. electrode at -600 mV in 0M and 2M glycerol. G.C. was selected since it can perform HER at elevate potentials and it is a nonporous surface behaving as a bulk material which doesn't degrade during HER [80–83]. Fascinatingly in

figure 4.11C, a significantly smaller and potentially negligeable R_U increase was observed unlike the porous Ni based catalysts, no HF charge transfer resistance and no Warburg like response was identified even at 2M glycerol. Considering G.C. is not porous, this reinforces the $R_{CT\text{-}HF}$ is related to the catalyst's porosity, as stated in literature. Interestingly, a nearly constant R_U is significant since it shows the R_U in the bulk is unchanged up to 2M glycerol in 1M KOH. Combining this observation with the R_U results of the porous Ni catalysts shows glycerol influences the properties of the electrolyte and HER in the pores only. This is supported by the changes in $R_{CT\text{-}HF}$ in figure 4.8 which is a pore related charge transfer process for HER and the extended transmission behaviour which indicates mass diffusion limitations are amplified (i.e. H_2O_{free} and OH^-).

However, how can OH^- conduction not be affected in the bulk electrolyte when cations and anions (for other alcohols) are known to be affected [29]? Upon review, the conduction mechanism of many ions is based on a vehicular transport mechanism from one electrode to another which is dependent on the diffusion properties of said ion in the electrolyte in question. This is sometimes confused for OH^- conduction (an exception similar to H^+) since it is based on a rapid proton transfer (PT) reaction where the negative charge of OH^- is carried from the cathode to the anode from a neighboring $H_2O_{coordinated}$ donating its hydrogen, that is hydrogen bonded to the oxygen of OH^- [84, 85]. This mechanism is termed the Grotthuss mechanism which is demonstrated in Schematic 4.2 [84, 85]. In turn, the PT based OH^- conduction mechanism is primarily dependent on the integrity of the long-distance HB network of H_2O_{free} and less sensitive to changes in viscosity as opposed to metal ions [84, 85]. This explains why glycerol did not impact the electrolyte conductivity for G.C..

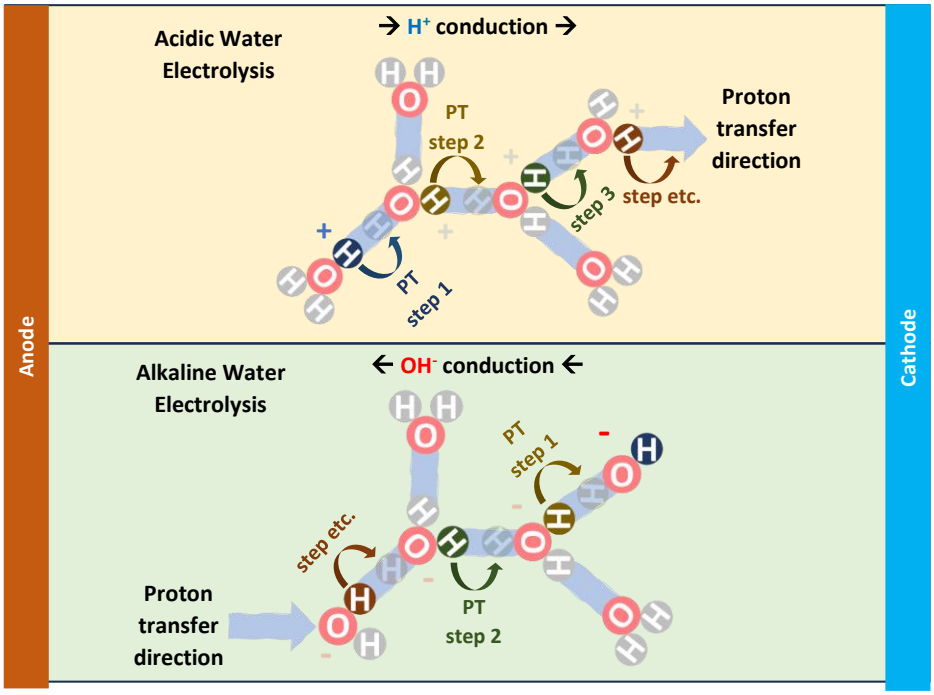

Schematic 4.2) A representation of the proton transfer mechanism of OH^- (bottom) and H^+ (top). The mechanism for either depends on a transfer of a proton to transport the charge of the conductive ions which is dependent on long distance hydrogen bonds.

In addition, figure 4.11 R_U results from G.C. shows this hydrogen bond network conduction mechanism, that OH^- is dependent on, is primarily unaffected up to 2M glycerol. Since this mechanism is dependent on long distance hydrogen bonds from H_2O_{free}, the unchanged R_U of G.C. also reaffirms that 2M glycerol has a minimal impact on H_2O_{free} availability and dielectric properties in the bulk liquid phase from the previous section. This is significant for membrane-free applications, since a popular trivial reason to ignore this electrolysis route is the hypothesized impact of glycerol on vehicular conduction of ions. But this ignores that OH^- conduction is an entirely different charge transport mechanism in the bulk liquid electrolyte, as opposed to other ions, which is shown here to not be affected.

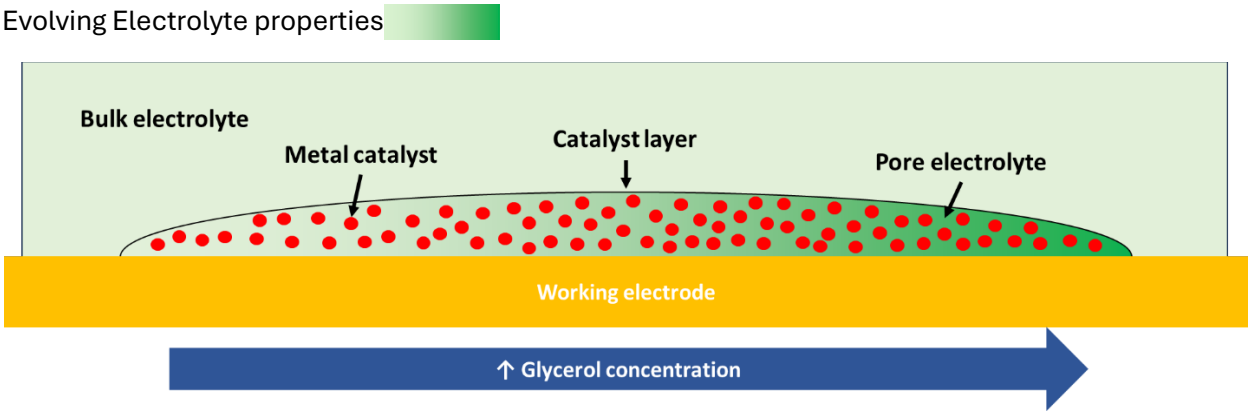

Schematic 4.3) A representation of the evolving electrolyte properties as GLY's concentration increases. As the concentration increases, the influence of GLY is focused near the interface and the catalyst layer pore structure but the effects are nearly muted in the bulk electrolyte. This evolving electrolyte property is shown through a change in the electrolyte medium colour (i.e. light green to dark green). Note, to this point, it isn't certain what is occurring but the effects are focused in the catalyst layer pores.

Having found that the influence of glycerol on OH^- conduction (R_U) is localised at the catalyst layer, and considering the elongation of the transmissive lines which represents an increasingly diffusion limited process (figure 4.10), pinpoints to changes in the electrolyte properties as a function of the depth of the pores during HER [67–69, 71]. This is reflected in the Voight circuit model, where an additional number of RC (table 4.S1-4) circuits is needed to fit the model as if the resistance and capacitance further evolves along the depth of the electrode, as if the electrode was thicker. A visual representation is shown in Schematic 4.1, where fitting the Voight model at 2M glycerol required additional RC circuits, indicating that the electrolyte properties are changing more intensely along the pores as if they were thicker. However, how can glycerol produce mass diffusion effects and changes in conduction of the liquid electrolyte in the pores but not in the bulk liquid phase?

4.3.6 The underestimated impact of glycerol on Nafion®

Based on SEM images (figure 4.2), an ignored factor in the electrolysis literature is the Nafion® ionomer which is the main component of the catalyst layer pores other than the liquid electrolyte. Nafion® is a widely used catalyst binder in alkaline organic electrolytic systems due to its mechanical stability [86–88]. Due to its high loading within the catalyst layer pores, and coverage over the catalyst surface, ionomers also present a barrier to the mass diffusion of relevant molecules within heterogeneous electrolytic reactions [86]. To resolve or reduce this mechanical

barrier, polymeric binders are engineered with functional side chains to conduct the relevant ions within the pores [86–88]. In the case of Nafion®, it possesses a hydrophobic polytetrafluoroethylene (PTFE) backbone with a hydrophilic sulfonic acid functional group on the end of a perfluorovinyl ether side chains [86–89]. The SO_3H functional groups form HBs with neighboring $H_2O_{coordinated}$ of cations and the hydrophobic backbones agglomerating to one and other via Van der Wals interactions forms separate hydrophilic and hydrophobic microphase like channels [90–92].

The hydrophilic channels, rich in water, act as an ion conductive pathway [90–92]. In the case of H^+ conduction, these hydrophilic channels not only provide a physical pathway for the Grotthuss mechanism to conduct to and from electrodes, but the SO_3H forming HBs with surrounding H_2O molecules also participates in the Grotthuss mechanism directly, promoting H^+ conduction [90–92]. In turn, the dimensions and stability of the microphase channels are paramount for both the vehicular and PT conduction mechanisms to function [90–92].

It is known the sulfonic acid group will be deprotonated to SO_3^- in the presence of OH^- [90]. This change in charge and proton can influence the PT mechanism that OH^- is dependent on. While this may be affected, and is a subject of future works, the microphase channel shouldn't be significantly affected since SO_3^- can still form HBs with $H_2O_{coordinated}$ with K^+ in an aqueous KOH solution, hence holding the integrity of the hydrophilic microphase channels [90–92].

While organic electrolytic literature hasn't considered the influence of glycerol on Nafion®, a large collection of scientific works in fuel cells shows alcohols (methanol, ethanol and propanol) negatively impacts the conduction of protons in Nafion® membranes [87, 92–94]. Fascinatingly, this is related to the capacity of the alcohols to interfere with the strict hydrophobic and hydrophilic domains by interacting with both the hydrophobic perfluorovinyl ether side chains and hydrophilic sulfonated groups, reducing the size of the hydrophilic domains [87, 92–94]. This consequentially inhibits the Grotthuss mechanism and vehicle transport of ions due to the reduction of the channel/pore sizes [87, 92–94]. While the influence of glycerol over Nafion® hasn't been investigated explicitly in this work, this collection of literature references points to an important need to investigate the impact of glycerol over different ionomers in organic electrolysis. This is a plausible explanation for the distinct inhibition of glycerol on OH^- conduction in the catalyst pores, altering the HER measurements. This is significant for guiding future works since several studies have performed GEOR measurements with Nafion®.

4.3.7 Relationship between R_U and HER

After elaborating the destabilising effect of glycerol on Nafion® as a cause for the increase in R_U, an important discussion is if the increase in R_U dictated the HER performance in the LSV results. In other words, is a change in R_U responsible for the changes seen in HER or are there other key factors that glycerol influences? Interestingly, this R_U (figure 4.9) behaviour is inconsistent with the TS and $\eta_{10\ mA.cm\text{-}2}$ (figure 4.3-4.7). For example, the observed worsening TS of Ni/C, $Ni_{98}Bi_2$/C and the high current TSs of $Ni_{80}Au_{20}$/C (Figure 4.4C/D & 4.5C) can arguably be explained by an increase in electrolyte resistance within the pores, since TSs were not $I*R_U$ corrected. However, certain results put into question this being a major contributor to its reduced performance at these conditions. Theoretically, since the conductive resistance originates from the electrolyte, it should result in similar transitions of the overpotential $\Delta V_{IR\ corrected}$ (with 85%-100% correction) for any given current density. Hence, the changes in $\eta_{10\ mA.cm\text{-}2}$ should be similar. However, Figure 4.7B shows the $\eta_{10\ mA.cm\text{-}2}$ evolves uniquely for Ni/C and $Ni_{80}Pd_{20}$/C. In addition, the reason why $Ni_{98}Bi_2$/C and $Ni_{80}Au_{20}$/C have a similarly changing $\eta_{10\ mA.cm\text{-}2}$ is due to $Ni_{80}Au_{20}$/C lowest current TS which improves and evolves $Ni_{80}Au_{20}$/C $\eta_{10\ mA.cm\text{-}2}$ similar to $Ni_{95}Bi_5$/C.

Furthermore, the TS of $Ni_{80}Pd_{20}$/C (figure 4.6B), the lowest current TS of $Ni_{80}Au_{20}$/C (figure 4.5C) and the TSs of G.C. (figure 4.11) improves as the concentration of glycerol is increased. This means an improvement of HER kinetics when the measurements are not R_U corrected and would change the conclusion from glycerol being an HER inhibitor to a noticeable promoter of HER. Just from a basis of theory between conduction and reactivity, a loss of conductivity (i.e. worst OH^- removal) can't be the cause of the improvement in TS results. In turn, these improved kinetics would allude to glycerol influencing HER not only through a change in the properties related to the catalyst pore (Nafion®) but also the catalyst interface, due to the clear dependence on the nature of the material of the cathode.

4.4 Conclusion

This work has collected evidence to show the influence of glycerol on HER over Ni based catalysts is not trivial as was previously reported. A compilation of evidence disproves glycerol up to 2M in a 1M KOH solution has an influence on the Grotthuss conduction mechanism of OH^- in the liquid phase. It is theorised that this is due to its incapacity to alter the long-distance HB

network of the electrolyte at 2M glycerol. Furthermore, no results in this work in conjunction with a critical analysis of previous publications show conclusive evidence that glycerol undergoes electrochemical reduction at standard temperatures and pressures up to 2M glycerol, nor is there clear evidence of blocking active sites. That said, conduction measurements of GEIS and PEIS reveal the loss in conduction is localised at the catalyst layer, resulting in worst diffusion properties within the pores. Based on a literature review, it is very likely this localised effect at the catalyst layer is caused by the destabilising role glycerol has onto the structure of the Nafion® binder.

Lastly, preliminary results revealed that glycerol is both an inhibitor and promotor of HER at the catalyst interface, depending on the catalyst materials and HER mechanism in question. In the case of Ni/C, glycerol inhibited Ni HER performance. That said, the addition of Au ($Ni_{80}Au_{20}$/C) and Bi ($Ni_{98}Bi_2$/C) both worsened and modulated this inhibition over Ni HER. For $Ni_{80}Pd_{20}$/C, its Ni HER performance could not conclusively be measured due to the likelihood that the catalyst behaves more like a Pd catalyst than a Ni catalyst. That said, $Ni_{80}Pd_{20}$/C demonstrated an improvement in its TS as the concentration of glycerol increased. Overall, glycerol's inhibition and possible promotion of HER can be modulated and improved, respectively. This opens the realistic pathway for efficient HER catalyst in the presence of alcohols for membrane-free electrolyser.

4.5. References

[1] Ritchie, H.; Roser, M. CO2 and Greenhous Gas Emissions.

[2] Hydrogen-Energy-Report_e_Final_WEB (1).

[3] Tu, Q.; Parvatker, A.; Garedew, M.; Harris, C.; Eckelman, M.; Zimmerman, J. B.; Anastas, P. T.; Lam, C. H. Electrocatalysis for Chemical and Fuel Production: Investigating Climate Change Mitigation Potential and Economic Feasibility. *Environ Sci Technol*, **2021**, *55* (5), 3240–3249. https://doi.org/10.1021/acs.est.0c07309.

[4] Verhelst, S.; Maesschalck, P.; Rombaut, N.; Sierens, R. Efficiency Comparison between Hydrogen and Gasoline, on a Bi-Fuel Hydrogen/Gasoline Engine. *Int J Hydrogen Energy*, **2009**, *34* (5), 2504–2510. https://doi.org/10.1016/j.ijhydene.2009.01.009.

[5] Saeedmanesh, A.; Mac Kinnon, M. A.; Brouwer, J. Hydrogen Is Essential for Sustainability. *Current Opinion in Electrochemistry*. Elsevier B.V. December 1, 2018, pp 166–181. https://doi.org/10.1016/j.coelec.2018.11.009.

[6] Ahmad Kamaroddin, M. F.; Sabli, N.; Tuan Abdullah, T. A.; Siajam, S. I.; Abdullah, L. C.; Abdul Jalil, A.; Ahmad, A. Membrane-Based Electrolysis for Hydrogen Production: A Review. *Membranes*. MDPI November 1, 2021. https://doi.org/10.3390/membranes11110810.

[7] Du, N.; Roy, C.; Peach, R.; Turnbull, M.; Thiele, S.; Bock, C. Anion-Exchange Membrane Water Electrolyzers. *Chemical Reviews*. American Chemical Society July 13, 2022, pp 11830–11895. https://doi.org/10.1021/acs.chemrev.1c00854.

[8] Jia, Q.; Liu, E.; Jiao, L.; Li, J.; Mukerjee, S. Current Understandings of the Sluggish Kinetics of the Hydrogen Evolution and Oxidation Reactions in Base. *Current Opinion in Electrochemistry*. Elsevier B.V. December 1, 2018, pp 209–217. https://doi.org/10.1016/j.coelec.2018.11.017.

[9] Liang, Q.; Brocks, G.; Bieberle-Hütter, A. Oxygen Evolution Reaction (OER) Mechanism under Alkaline and Acidic Conditions. *JPhys Energy*, **2021**, *3* (2). https://doi.org/10.1088/2515-7655/abdc85.

[10] Dong, S.; Li, Y.; Zhao, Z.; Li, R.; He, J.; Yin, J.; Yan, B.; Zhang, X. A Review of the Application of Heterostructure Catalysts in Hydrogen Evolution Reaction. *ChemistrySelect*. John Wiley and Sons Inc April 12, 2022. https://doi.org/10.1002/slct.202104041.

[11] Lagadec, M. F.; Grimaud, A. Water Electrolysers with Closed and Open Electrochemical Systems. *Nature Materials*. Nature Research November 1, 2020, pp 1140–1150. https://doi.org/10.1038/s41563-020-0788-3.

[12] Carneiro, J.; Nikolla, E. Electrochemical Conversion of Biomass-Based Oxygenated Compounds. **2019**. https://doi.org/10.1146/annurev-chembioeng.

[13] You, B.; Jiang, N.; Liu, X.; Sun, Y. Simultaneous H 2 Generation and Biomass Upgrading in Water by an Efficient Noble-Metal-Free Bifunctional Electrocatalyst . *Angewandte Chemie*, **2016**, *128* (34), 10067–10071. https://doi.org/10.1002/ange.201603798.

[14] Araujo, R. B.; Martín-Yerga, D.; Santos, E. C. dos; Cornell, A.; Pettersson, L. G. M. Elucidating the Role of Ni to Enhance the Methanol Oxidation Reaction on Pd Electrocatalysts. *Electrochim Acta*, **2020**, *360*. https://doi.org/10.1016/j.electacta.2020.136954.

[15] Simões, M.; Baranton, S.; Coutanceau, C. Electrochemical Valorisation of Glycerol. *ChemSusChem*. November 2012, pp 2106–2124. https://doi.org/10.1002/cssc.201200335.

[16] Vo, T. G.; Tran, G. S.; Chiang, C. L.; Lin, Y. G.; Chang, H. E.; Kuo, H. H.; Chiang, C. Y.; Hsu, Y. J. Au@NiSx Yolk@Shell Nanostructures as Dual-Functional Electrocatalysts for Concomitant Production of Value-Added Tartronic Acid and Hydrogen Fuel. *Adv Funct Mater*, **2023**, *33* (4). https://doi.org/10.1002/adfm.202209386.

[17] Kim, H. J.; Kim, Y.; Lee, D.; Kim, J. R.; Chae, H. J.; Jeong, S. Y.; Kim, B. S.; Lee, J.; Huber, G. W.; Byun, J.; et al. Coproducing Value-Added Chemicals and Hydrogen with Electrocatalytic Glycerol Oxidation Technology: Experimental and Techno-Economic Investigations. *ACS Sustain Chem Eng*, **2017**, *5* (8), 6626–6634. https://doi.org/10.1021/acssuschemeng.7b00868.

[18] Sun, H. Y.; Ding, Y.; Yue, Y. Q.; Xue, Q.; Li, F. M.; Jiang, J. X.; Chen, P.; Chen, Y. Bifunctional Palladium Hydride Nanodendrite Electrocatalysts for Hydrogen Evolution Integrated with Formate Oxidation. *ACS Appl Mater Interfaces*, **2021**, *13* (11), 13149–13157. https://doi.org/10.1021/acsami.0c22106.

[19] Dong, L.; Chang, G.-R.; Feng, Y.; Yao, X.-Z.; Yu, X.-Y. Regulating Ni Site in NiV LDH for Efficient Electrocatalytic Production of Formate and Hydrogen by Glycerol Electrolysis. *Rare Metals*, *41*. https://doi.org/10.1007/s12598.

[20] Houache, M. S. E.; Hughes, K.; Safari, R.; Botton, G. A.; Baranova, E. A. Modification of Nickel Surfaces by Bismuth: Effect on Electrochemical Activity and Selectivity toward Glycerol. *ACS Appl Mater Interfaces*, **2020**, *12* (13), 15095–15107. https://doi.org/10.1021/acsami.9b22378.

[21] Shubair, A.; Houache, M. S. E.; Mousavi M, S. S.; Botton, G. A.; Baranova, E. A. Electrolysis of Glycerol to Value-Added Chemicals in Alkaline Media. *Journal of Chemical Technology and Biotechnology*, **2022**, *97* (8), 1950–1958. https://doi.org/10.1002/jctb.7088.

[22] Houache, M. S. E.; Shubair, A.; Sandoval, M. G.; Safari, R.; Botton, G. A.; Jasen, P. V.; González, E. A.; Baranova, E. A. Influence of Pd and Au on Electrochemical Valorization of Glycerol over Ni-Rich Surfaces. *J Catal*, **2021**, *396*, 1–13. https://doi.org/10.1016/j.jcat.2021.02.008.

[23] Houache, M. S. E.; Safari, R.; Nwabara, U. O.; Rafaïdeen, T.; Botton, G. A.; Kenis, P. J. A.; Baranton, S.; Coutanceau, C.; Baranova, E. A. Selective Electrooxidation of Glycerol to Formic Acid over Carbon Supported Ni1- XMx(M = Bi, Pd, and Au) Nanocatalysts and Coelectrolysis of CO2. *ACS Appl Energy Mater*, **2020**, *3* (9), 8725–8738. https://doi.org/10.1021/acsaem.0c01282.

[24] Yu, X.; dos Santos, E. C.; White, J.; Salazar-Alvarez, G.; Pettersson, L. G. M.; Cornell, A.; Johnsson, M. Electrocatalytic Glycerol Oxidation with Concurrent Hydrogen Evolution Utilizing an Efficient MoOx/Pt Catalyst. *Small*, **2021**, *17* (44). https://doi.org/10.1002/smll.202104288.

[25] Kongjao, S.; Damronglerd, S.; Hunsom, M. Electrochemical Reforming of an Acidic Aqueous Glycerol Solution on Pt Electrodes. *J Appl Electrochem*, **2011**, *41* (2), 215–222. https://doi.org/10.1007/s10800-010-0226-3.

[26] Yang, B.; Zhang, R.; Shao, Z.; Zhang, C. The Economic Analysis for Hydrogen Production Cost towards Electrolyzer Technologies: Current and Future Competitiveness. *Int J Hydrogen Energy*, **2023**, *48* (37), 13767–13779. https://doi.org/10.1016/j.ijhydene.2022.12.204.

[27] Dong, L.; Chang, G.-R.; Feng, Y.; Yao, X.-Z.; Yu, X.-Y. Regulating Ni Site in NiV LDH for Efficient Electrocatalytic Production of Formate and Hydrogen by Glycerol Electrolysis. https://doi.org/10.1007/s12598.

[28] Han, X.; Sheng, H.; Yu, C.; Walker, T. W.; Huber, G. W.; Qiu, J.; Jin, S. Electrocatalytic Oxidation of Glycerol to Formic Acid by CuCo2O4Spinel Oxide Nanostructure Catalysts. *ACS Catal*, **2020**, *10* (12), 6741–6752. https://doi.org/10.1021/acscatal.0c01498.

[29] Pham, T. H.; Lee, W. H.; Byun, J. H.; Kim, J. G. Improving the Performance of Primary Aluminum-Air Batteries through Suppressing Water Activity by Hydrogen Bond-Rich Glycerol Solvent Additive. *Energy Storage Mater*, **2023**, *55*, 406–416. https://doi.org/10.1016/j.ensm.2022.12.012.

[30] Ge, Z.; Fu, B.; Zhao, J.; Li, X.; Ma, B.; Chen, Y. A Review of the Electrocatalysts on Hydrogen Evolution Reaction with an Emphasis on Fe, Co and Ni-Based Phosphides. *Journal of Materials Science*. Springer October 1, 2020, pp 14081–14104. https://doi.org/10.1007/s10853-020-05010-w.

[31] Mohammed-Ibrahim, J.; Xiaoming, S. Recent Progress on Earth Abundant Electrocatalysts for Hydrogen Evolution Reaction (HER) in Alkaline Medium to Achieve Efficient Water Splitting – A Review. *Journal of Energy Chemistry*. Elsevier B.V. July 1, 2019, pp 111–160. https://doi.org/10.1016/j.jechem.2018.09.016.

[32] Vander Steen, J.; Boissou, F.; Luhmer, M.; Buess-Herman, C.; Baranton, S.; Coutanceau, C.; Doneux, T. Furfural Electroreduction in Choline-Glycerol Deep Eutectic Solvent.

Journal of Electroanalytical Chemistry, **2023**, *933*. https://doi.org/10.1016/j.jelechem.2023.117269.

[33] Wang, X.; Xu, C.; Jaroniec, M.; Zheng, Y.; Qiao, S. Z. Anomalous Hydrogen Evolution Behavior in High-PH Environment Induced by Locally Generated Hydronium Ions. *Nat Commun*, **2019**, *10* (1). https://doi.org/10.1038/s41467-019-12773-7.

[34] Abrahami, S. T.; Chiter, F.; Klein, L. H.; Maurice, V.; Terryn, H.; Costa, D.; Marcus, P. In Situ EC-STM Study and DFT Modeling of the Adsorption of Glycerol on Cu(111) in NaOH Solution. *Journal of Physical Chemistry C*, **2019**, *123* (36), 22228–22238. https://doi.org/10.1021/acs.jpcc.9b04856.

[35] Dubouis, N.; Serva, A.; Salager, E.; Deschamps, M.; Salanne, M.; Grimaud, A. *The Fate of Water at the Electrochemical Interfaces: Electrochemical Behavior of Free Water vs. Coordinating Water*.

[36] Holovko, M.; Druchok, M.; Bryk, T. Computer Modelling of Hydration Structure of Highly Charged Ions and Cationic Hydrolysis Effects. In *Current Opinion in Colloid and Interface Science*; 2004; Vol. 9, pp 64–66. https://doi.org/10.1016/j.cocis.2004.05.006.

[37] Liu, E.; Li, J.; Jiao, L.; Doan, H. T. T.; Liu, Z.; Zhao, Z.; Huang, Y.; Abraham, K. M.; Mukerjee, S.; Jia, Q. Unifying the Hydrogen Evolution and Oxidation Reactions Kinetics in Base by Identifying the Catalytic Roles of Hydroxyl-Water-Cation Adducts. *J Am Chem Soc*, **2019**, *141* (7), 3232–3239. https://doi.org/10.1021/jacs.8b13228.

[38] Huang, B.; Rao, R. R.; You, S.; Hpone Myint, K.; Song, Y.; Wang, Y.; Ding, W.; Giordano, L.; Zhang, Y.; Wang, T.; et al. Cation- and PH-Dependent Hydrogen Evolution and Oxidation Reaction Kinetics. *JACS Au*, **2021**, *1* (10), 1674–1687. https://doi.org/10.1021/jacsau.1c00281.

[39] Gao, L.; Bao, F.; Tan, X.; Li, M.; Shen, Z.; Chen, X.; Tang, Z.; Lai, W.; Lu, Y.; Huang, P.; et al. Engineering a Local Potassium Cation Concentrated Microenvironment toward the Ampere-Level Current Density Hydrogen Evolution Reaction. *Energy Environ Sci*, **2022**, *16* (1), 285–294. https://doi.org/10.1039/d2ee02836k.

[40] Goyal, A.; Koper, M. T. M. The Interrelated Effect of Cations and Electrolyte PH on the Hydrogen Evolution Reaction on Gold Electrodes in Alkaline Media. *Angewandte Chemie - International Edition*, **2021**, *60* (24), 13452–13462. https://doi.org/10.1002/anie.202102803.

[41] Monteiro, M. C. O.; Goyal, A.; Moerland, P.; Koper, M. T. M. Understanding Cation Trends for Hydrogen Evolution on Platinum and Gold Electrodes in Alkaline Media. *ACS Catal*, **2021**, *11* (23), 14328–14335. https://doi.org/10.1021/acscatal.1c04268.

[42] Anantharaj, S.; Noda, S. How Properly Are We Interpreting the Tafel Lines in Energy Conversion Electrocatalysis? *Mater Today Energy*, **2022**, *29*. https://doi.org/10.1016/j.mtener.2022.101123.

[43] Cossar, E.; Houache, M. S. E.; Zhang, Z.; Baranova, E. A. Comparison of Electrochemical Active Surface Area Methods for Various Nickel Nanostructures. *Journal of Electroanalytical Chemistry*, **2020**, *870*. https://doi.org/10.1016/j.jelechem.2020.114246.

[44] Anantharaj, S.; Noda, S. Appropriate Use of Electrochemical Impedance Spectroscopy in Water Splitting Electrocatalysis. *ChemElectroChem*, **2020**, *7* (10), 2297–2308. https://doi.org/10.1002/celc.202000515.

[45] Magdić, K.; Kvastek, K.; Horvat-Radošević, V. Impedance Approach to Activity of Hydrogen Evolution Reaction on Spatially Heterogeneous GC Electrode Surfaces: Metal Free vs. Ru Catalysed Case. *Electrochim Acta*, **2015**, *167*, 455–469. https://doi.org/10.1016/j.electacta.2015.03.155.

[46] Zheng, W.; Li, Y.; Tsang, C. S.; So, P. K.; Lee, L. Y. S. Stabilizer-Free Bismuth Nanoparticles for Selective Polyol Electrooxidation. *iScience*, **2021**, *24* (4). https://doi.org/10.1016/j.isci.2021.102342.

[47] Samal, A. K.; Sreeprasad, T. S.; Pradeep, T. Investigation of the Role of NaBH4 in the Chemical Synthesis of Gold Nanorods. *Journal of Nanoparticle Research*, **2010**, *12* (5), 1777–1786. https://doi.org/10.1007/s11051-009-9733-8.

[48] Bao, F.; Kemppainen, E.; Dorbandt, I.; Bors, R.; Xi, F.; Schlatmann, R.; van de Krol, R.; Calnan, S. Understanding the Hydrogen Evolution Reaction Kinetics of Electrodeposited Nickel-Molybdenum in Acidic, Near-Neutral, and Alkaline Conditions. *ChemElectroChem*, **2021**, *8* (1), 195–208. https://doi.org/10.1002/celc.202001436.

[49] Charkhesht, A.; Lou, D.; Sindle, B.; Wen, C.; Cheng, S.; Vinh, N. Q. Insights into Hydration Dynamics and Cooperative Interactions in Glycerol-Water Mixtures by Terahertz Dielectric Spectroscopy. *Journal of Physical Chemistry B*, **2019**, *123* (41), 8791–8799. https://doi.org/10.1021/acs.jpcb.9b07021.

[50] Gong, Y.; Xu, Y.; Zhou, Y.; Li, C.; Liu, X.; Niu, L.; Huang, Y.; Zhang, X.; Sun, C. Q. Hydrogen Bond Network Relaxation Resolved by Alcohol Hydration (Methanol, Ethanol, and Glycerol). *Journal of Raman Spectroscopy*, **2017**, *48* (3), 393–398. https://doi.org/10.1002/jrs.5060.

[51] Lao, M.; Li, P.; Jiang, Y.; Pan, H.; Dou, S. X.; Sun, W. From Fundamentals and Theories to Heterostructured Electrocatalyst Design: An in-Depth Understanding of Alkaline Hydrogen Evolution Reaction. *Nano Energy*. Elsevier Ltd July 1, 2022. https://doi.org/10.1016/j.nanoen.2022.107231.

[52] Yu, X.; Qu, L.; Lee, C.; Peng, J.; Yan, Q.; Bai, H.; Yao, M. Bismuth-Nickel Bimetal Nanosheets with a Porous Structure for Efficient Hydrogen Production in Neutral and Alkaline Media. *Nanoscale*, **2022**, *5*. https://doi.org/10.1039/d2nr04407b.

[53] Khanova, L. A.; Krishtalik, L. I. Kinetics of the Hydrogen Evolution Reaction on Gold Electrode. A New Case of the Barrierless Discharge. *Journal of Electroanalytical Chemistry*, **2011**, *660* (2), 224–229. https://doi.org/10.1016/j.jelechem.2011.01.016.

[54] Kibler, L. A.; Hermann, J. M.; Abdelrahman, A.; El-Aziz, A. A.; Jacob, T. New Insights on Hydrogen Evolution at Au Single Crystal Electrodes. *Current Opinion in Electrochemistry*. Elsevier B.V. June 1, 2018, pp 265–270. https://doi.org/10.1016/j.coelec.2018.05.013.

[55] Krishtalik, L. I.; Frumkin, A. N. *Kinetic Isotope Effect in the Hydrogen Evolution Reaction*; 2001; Vol. 46.

[56] Chen, X.; Wang, X. T.; Le, J. B.; Li, S. M.; Wang, X.; Zhang, Y. J.; Radjenovic, P.; Zhao, Y.; Wang, Y. H.; Lin, X. M.; et al. Revealing the Role of Interfacial Water and Key Intermediates at Ruthenium Surfaces in the Alkaline Hydrogen Evolution Reaction. *Nat Commun*, **2023**, *14* (1). https://doi.org/10.1038/s41467-023-41030-1.

[57] Sarkar, S.; Peter, S. C. An Overview on Pd-Based Electrocatalysts for the Hydrogen Evolution Reaction. *Inorganic Chemistry Frontiers*. Royal Society of Chemistry September 1, 2018, pp 2060–2080. https://doi.org/10.1039/c8qi00042e.

[58] Lee, C. S.; Aroua, M. K.; Wan Daud, W. A.; Cognet, P.; Pérès, Y.; Ajeel, M. A. Selective Electrochemical Conversion of Glycerol to Glycolic Acid and Lactic Acid on a Mixed Carbon-Black Activated Carbon Electrode in a Single Compartment Electrochemical Cell. *Front Chem*, **2019**, *7* (MAR). https://doi.org/10.3389/fchem.2019.00110.

[59] Lopez-Ruiz, J. A.; Andrews, E.; Akhade, S. A.; Lee, M. S.; Koh, K.; Sanyal, U.; Yuk, S. F.; Karkamkar, A. J.; Derewinski, M. A.; Holladay, J.; et al. Understanding the Role of Metal and Molecular Structure on the Electrocatalytic Hydrogenation of Oxygenated Organic Compounds. *ACS Catal*, **2019**, *9* (11), 9964–9972. https://doi.org/10.1021/acscatal.9b02921.

[60] TenDam, J.; Djanashvili, K.; Kapteijn, F.; Hanefeld, U. Pt/Al2O3 Catalyzed 1,3-Propanediol Formation from Glycerol Using Tungsten Additives. *ChemCatChem*, **2013**, *5* (2), 497–505. https://doi.org/10.1002/cctc.201200469.

[61] TenDam, J.; Djanashvili, K.; Kapteijn, F.; Hanefeld, U. Pt/Al2O3 Catalyzed 1,3-Propanediol Formation from Glycerol Using Tungsten Additives. *ChemCatChem*, **2013**, *5* (2), 497–505. https://doi.org/10.1002/cctc.201200469.

[62] Alomar, M. K.; Hayyan, M.; Alsaadi, M. A.; Akib, S.; Hayyan, A.; Hashim, M. A. Glycerol-Based Deep Eutectic Solvents: Physical Properties. *J Mol Liq*, **2016**, *215*, 98–103. https://doi.org/10.1016/j.molliq.2015.11.032.

[63] Charkhesht, A.; Lou, D.; Sindle, B.; Wen, C.; Cheng, S.; Vinh, N. Q. Insights into Hydration Dynamics and Cooperative Interactions in Glycerol-Water Mixtures by Terahertz Dielectric Spectroscopy. *Journal of Physical Chemistry B*, **2019**, *123* (41), 8791–8799. https://doi.org/10.1021/acs.jpcb.9b07021.

[64] Saw, E. N.; Kanokkanchana, K.; Amin, H. M. A.; Tschulik, K. Unravelling Anion Solvation in Water-Alcohol Mixtures by Single Entity Electrochemistry. *ChemElectroChem*, **2022**, *9* (7). https://doi.org/10.1002/celc.202101435.

[65] Hosseini, S.; Han, S. J.; Arponwichanop, A.; Yonezawa, T.; Kheawhom, S. Ethanol as an Electrolyte Additive for Alkaline Zinc-Air Flow Batteries. *Sci Rep*, **2018**, *8* (1). https://doi.org/10.1038/s41598-018-29630-0.

[66] Laschuk, N. O.; Easton, E. B.; Zenkina, O. V. Reducing the Resistance for the Use of Electrochemical Impedance Spectroscopy Analysis in Materials Chemistry. *RSC Advances*. Royal Society of Chemistry August 8, 2021, pp 27925–27936. https://doi.org/10.1039/d1ra03785d.

[67] Huang, J. Diffusion Impedance of Electroactive Materials, Electrolytic Solutions and Porous Electrodes: Warburg Impedance and Beyond. *Electrochim Acta*, **2018**, *281*, 170–188. https://doi.org/10.1016/j.electacta.2018.05.136.

[68] *Electrochemical Impedance Spectroscopy*.

[69] Bai, L.; Gao, L.; Conway, B. E. *Problem of in Situ Real-Area Determination in Evaluation of Performance of Rough or Porous, Gas-Evolving Electrocatalysts Part 2.- Unfolding of the Electrochemically Accessible Surface of Rough or Porous Electrodes : A Case-Study with an Electrodeposited Porous Pt Electrode*; 1993; Vol. 89.

[70] Nguyen, T. Q.; Breitkopf, C. Determination of Diffusion Coefficients Using Impedance Spectroscopy Data. *J Electrochem Soc*, **2018**, *165* (14), E826–E831. https://doi.org/10.1149/2.1151814jes.

[71] Sharma, T.; Holm, T.; Diaz-Real, J. A.; Mérida, W. Experimental Verification of Pore Impedance Theory: Drilled Graphite Electrodes with Gradually More Complex Pore Size Distribution. *Electrochim Acta*, **2019**, *317*, 528–541. https://doi.org/10.1016/j.electacta.2019.05.119.

[72] Yin, X.; Sun, G.; Song, A.; Wang, L.; Wang, Y.; Dong, H.; Shao, G. A Novel Structure of Ni-(MoS2/GO) Composite Coatings Deposited on Ni Foam under Supergravity Field as Efficient Hydrogen Evolution Reaction Catalysts in Alkaline Solution. *Electrochim Acta*, **2017**, *249*, 52–63. https://doi.org/10.1016/j.electacta.2017.08.010.

[73] Alobaid, A.; Wang, C.; Adomaitis, R. A. Mechanism and Kinetics of HER and OER on NiFe LDH Films in an Alkaline Electrolyte. *J Electrochem Soc*, **2018**, *165* (15), J3395–J3404. https://doi.org/10.1149/2.0481815jes.

[74] Hitz, C.; Lasia, A. *Experimental Study and Modeling of Impedance of the Her on Porous Ni Electrodes*; 2001; Vol. 500.

[75] Pérez-Rodríguez, S.; Pastor, E.; Lázaro, M. J. *Electrochemical Behavior of the Carbon Black Vulcan XC-72R: Influence of the Surface Chemistry*.

[76] Montella, C. Voigt Circuit Representation Model for Electrochemical Impedances under Finite-Length Diffusion Conditions. *Journal of Electroanalytical Chemistry*, **2020**, *879*. https://doi.org/10.1016/j.jelechem.2020.114785.

[77] Barbero, G.; Lelidis, I. Analysis of Warburg's Impedance and Its Equivalent Electric Circuits. *Physical Chemistry Chemical Physics*, **2017**, *19* (36), 24934–24944. https://doi.org/10.1039/c7cp04032f.

[78] Sharma, T.; Holm, T.; Diaz-Real, J. A.; Mérida, W. Experimental Verification of Pore Impedance Theory: Drilled Graphite Electrodes with Gradually More Complex Pore Size Distribution. *Electrochim Acta*, **2019**, *317*, 528–541. https://doi.org/10.1016/j.electacta.2019.05.119.

[79] Saghafi, M.; Chinnathambi, S.; Lemay, S. G. High-Frequency Phenomena and Electrochemical Impedance Spectroscopy at Nanoelectrodes. *Current Opinion in Colloid and Interface Science*. Elsevier Ltd February 1, 2023. https://doi.org/10.1016/j.cocis.2022.101654.

[80] Jeon, I. Y.; Choi, H. J.; Choi, M.; Seo, J. M.; Jung, S. M.; Kim, M. J.; Zhang, S.; Zhang, L.; Xia, Z.; Dai, L.; et al. Facile, Scalable Synthesis of Edge-Halogenated Graphene Nanoplatelets as Efficient Metal-Free Eletrocatalysts for Oxygen Reduction Reaction. *Sci Rep*, **2013**, *3*. https://doi.org/10.1038/srep01810.

[81] Abdel-Aziz, A. M.; Hassan, H. H.; Badr, I. H. A. Activated Glassy Carbon Electrode as an Electrochemical Sensing Platform for the Determination of 4-Nitrophenol and Dopamine in Real Samples. *ACS Omega*, **2022**, *7* (38), 34127–34135. https://doi.org/10.1021/acsomega.2c03427.

[82] Coustan, L.; Shul, G.; Bélanger, D. Electrochemical Behavior of Platinum, Gold and Glassy Carbon Electrodes in Water-in-Salt Electrolyte. *Electrochem commun*, **2017**, *77*, 89–92. https://doi.org/10.1016/j.elecom.2017.03.001.

[83] Noel, M.; Anantharaman, P. N. *VOLTAMMETRIC STUDIES ON GLASSY CARBON ELECTRODES I: ELECTROCHEMICAL BEHAVIOUR OF GLASSY CARBON ELECTRODES IN H 2SO4, Na2SO4 AND NaOH MEDIA*; 1986; Vol. 28.

[84] Tuckerman, M. E.; Marx, D.; Parrinello. Michele. The Nature and Transport Mechanism of Hydrated Hydroxide Ions in Aqueous Solution. *Natur5*, **2002**, *417* (6892), 925–929. https://doi.org/10.1038/nature00797.

[85] Long, Z.; Tuckerman, M. E. Hydroxide Diffusion in Functionalized Cylindrical Nanopores as Idealized Models of Anion Exchange Membrane Environments: An Ab Initio Molecular Dynamics Study. *Journal of Physical Chemistry C*, **2023**, *127* (6), 2792–2804. https://doi.org/10.1021/acs.jpcc.2c05747.

[86] Plazanet, M.; Torre, R.; Sacchetti, F. Confinement, Entropic Effects and Hydrogen Bond Network Fluctuations of Water in Nafion Membrane Confinement, Entropic Effects and Hydrogen Bond Network Fluctuations of Water in Nafion Membrane Confinement,

Entropic Effects and Hydrogen Bond Network Fluctuations of Water in Nafion Membrane. *J Mol Liq*, **2016**, 219. https://doi.org/10.1016/j.molliq.2016.01.079ï.

[87] Affoune, A. M.; Yamada, A.; Umeda, M. Conductivity and Surface Morphology of Nafion Membrane in Water and Alcohol Environments. *J Power Sources*, **2005**, *148* (1–2), 9–17. https://doi.org/10.1016/j.jpowsour.2005.01.039.

[88] Kumar, K. S. S.; Vijayalakshmi, K. P.; Sivanath, S.; Jayalatha, T.; Mohanty, S.; Shaneeth, M. Interaction of Nafion Ionomers toward Various Solvents. *J Appl Polym Sci*, **2013**, *128* (6), 3710–3719. https://doi.org/10.1002/app.38421.

[89] Vuilleumier, R.; Brogis, D. Hopping along Hydrogen Bonds. *Nat Chem*, **2012**, *4*, 432–433. https://doi.org/doi.org/10.1038/nchem.1365.

[90] Hu, J.; Zhang, H.; Xu, W.; Yuan, Z.; Li, X. Mechanism and Transfer Behavior of Ions in Nafion Membranes under Alkaline Media. *J Memb Sci*, **2018**, *566*, 8–14. https://doi.org/10.1016/j.memsci.2018.08.057.

[91] Kusoglu, A.; Weber, A. Z. New Insights into Perfluorinated Sulfonic-Acid Ionomers. *Chem Rev*, **2017**, *117* (3), 987–1104. https://doi.org/10.1021/acs.chemrev.6b00159.

[92] Katzenberg, A.; Angulo, A.; Kusoglu, A.; Modestino, M. A. Impacts of Organic Sorbates on the Ionic Conductivity and Nanostructure of Perfluorinated Sulfonic-Acid Ionomers. *Macromolecules*, **2021**, *54* (11), 5187–5195. https://doi.org/10.1021/acs.macromol.1c00494.

[93] Saito, M.; Tsuzuki, S.; Hayamizu, K.; Okada, T. Alcohol and Proton Transport in Perfluorinated Ionomer Membranes for Fuel Cells. *Journal of Physical Chemistry B*, **2006**, *110* (48), 24410–24417. https://doi.org/10.1021/jp0643496.

[94] Rivin, D.; Kendrick, C. E.; Gibson, P. W.; Schneider, N. S. *Solubility and Transport Behavior of Water and Alcohols in Nafion*.

4.6. Supplementary

Table 4.S1) EIS model parameters of $Ni_{80}Au_{20}$/C with the number of RC series. Resistances (R_U, R_1, R_2, R_3) are expressed in Ohm. The capacitance (C_{eq}) values in each constant phase elements are expressed in microfarad.

[GLY]	Overall Error (%)	Ru	#series	R1 (ohm)	Ceq (microF)	alpha	R2	Ceq (microF)	alpha	R3	Ceq (microF)	alpha
0M	8.79	8.33	2	10.1	46.7	0.2	19.3	358	0.93	-	-	-
0.1M	3.72	10.3	2	5.08	592	0.541	20	643	0.943	-	-	-
1M	6.09	13.7	2	8.8	5550	0.421	20.3	612	0.931	-	-	-
2M	8.66	26.7	3	7.86	571	0.822	11.5	275	1.15	16	7290	0.29

Table 4.S2) EIS model parameters of $Ni_{98}Bi_2$/C with the number of RC series. Resistances (R_U, R_1, R_2, R_3) are expressed in Ohm. The capacitance (C_{eq}) values in each constant phase elements are expressed in microfarad.

[GLY]	Overall Error (%)	Ru	#series	R1 (ohm)	Ceq (microF)	alpha	R2	Ceq (microF)	alpha	R3	Ceq (microF)	alpha
0M	8.79	8.33	2	10.1	46.7	0.2	19.3	358	0.93	-	-	-
0.1M	3.72	10.3	2	5.08	592	0.541	20	643	0.943	-	-	-
1M	6.09	13.7	2	8.8	5550	0.421	20.3	612	0.931	-	-	-
2M	8.66	26.7	3	7.86	571	0.822	11.5	275	1.15	16	7290	0.29

Table 4.S3) EIS model parameters of $Ni_{80}Pd_{20}$/C with the number of RC series. Resistances (R_U, R_1, R_2, R_3) are expressed in Ohm. The capacitance (C_{eq}) values in each constant phase elements are expressed in microfarad.

[GLY]	Overall Error (%)	Ru	#series	R1 (ohm)	Ceq (microF)	alpha	R2	Ceq (microF)	alpha
0M	3.62	6.73	2	2.37	91900	0.271	21.6	745	0.931
0.1M	2.5	6.46	2	2.04	6940	0.628	22.4	836	0.947
1M	4.87	8.89	2	4.09	21300	0.437	27.3	575	0.963
2M	4.54	12.63	2	28.7	417	0.932	3.7	11500	0.41

Table 4.S4) EIS model parameters of Ni/C with the number of RC series. Resistances (R_U, R_1, R_2, R_3) are expressed in Ohm. The capacitance (C_{eq}) values in each constant phase elements are expressed in microfarad.

[GLY]	Overall Error (%)	Ru	#series	R1 (ohm)	Ceq (microF)	alpha	R2	Ceq (microF)	alpha
0M	3.36	9.71	2	3	6380	0.58	20	603	0.93
0.1M	-	-	-	-	-	-	-	-	-
1M	3.73	15.9	2	7.96	1.69	0.608	21.6	481	0.937
2M	5.63	25.4	2	10.4	1580	0.533	21.1	289	0.955

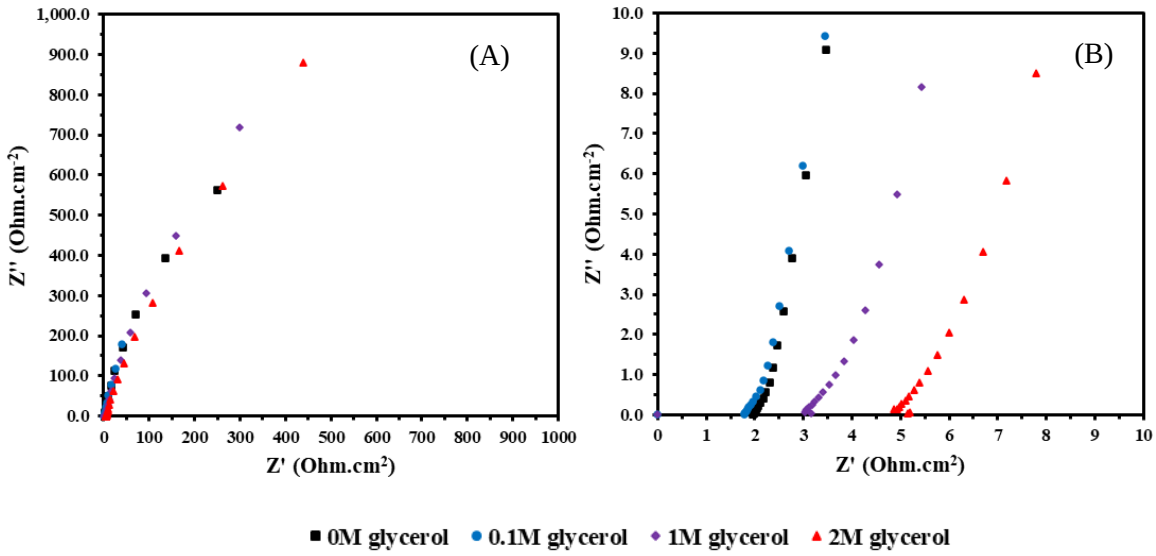

Figure 4.S1) PEIS of Ni/C at OCP in 1M KOH and various concentrations of glycerol measured at RT. Frequency range is between 100-0.1 kHz with a decade step of 5 with an AC amplitude of 10 mV.

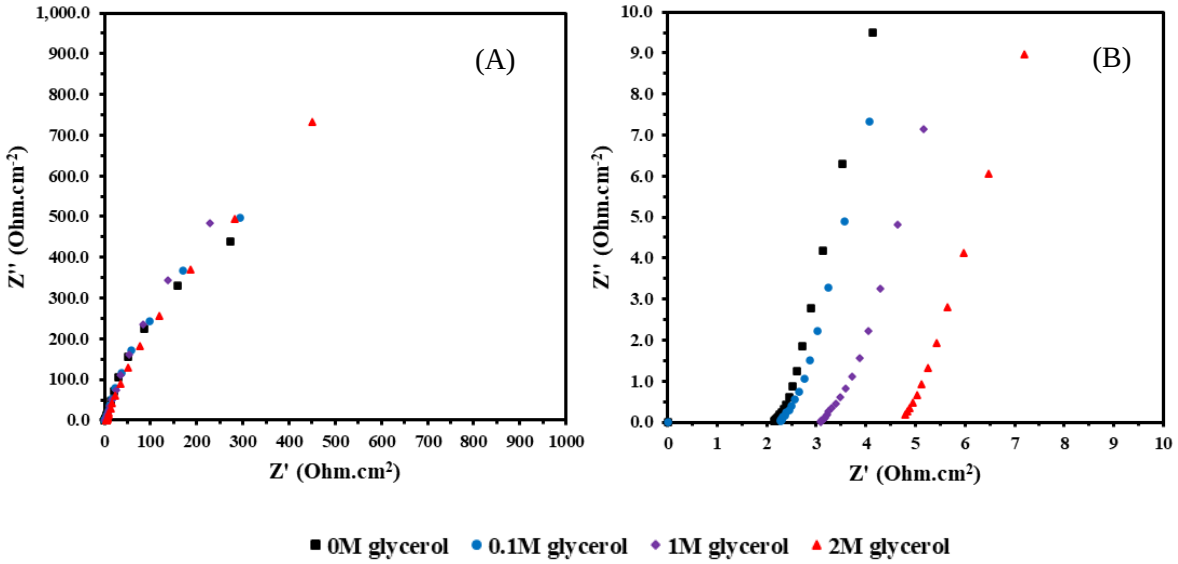

Figure 4.S2) PEIS of $Ni_{98}Bi_2$/C at OCP in 1M KOH and various concentrations of glycerol measured at RT. Frequency range is between 100-0.1 kHz with a decade step of 5 with an AC amplitude of 10 mV.

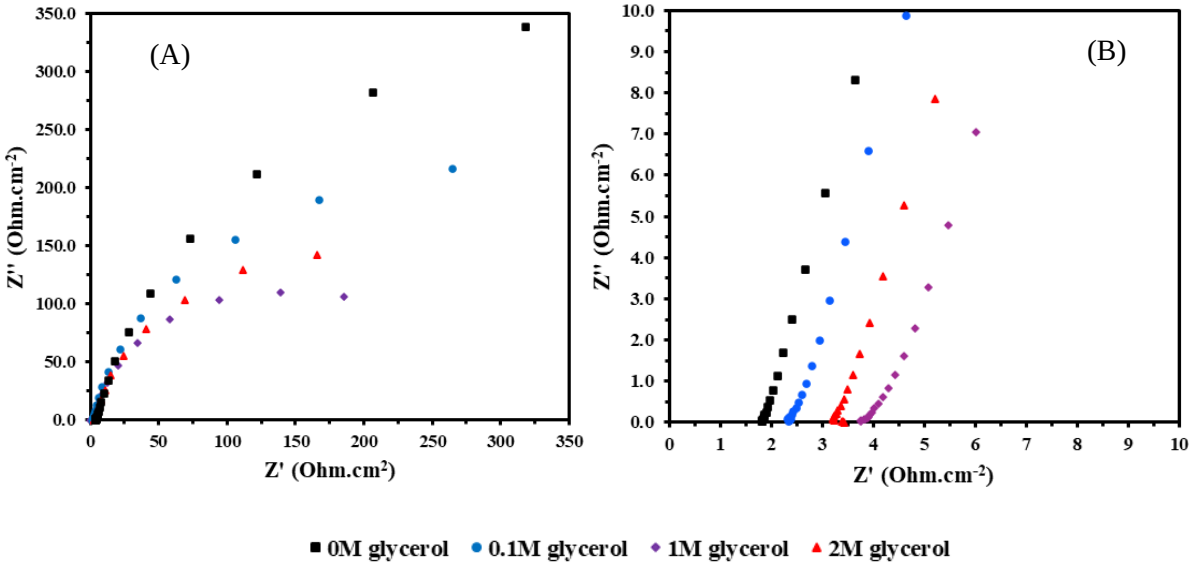

Figure 4.S3) PEIS of $Ni_{80}Pd_{20}$/C at OCP in 1M KOH and various concentrations of glycerol measured at RT. Frequency range is between 100-0.1 kHz with a decade step of 5 with an AC amplitude of 10 mV.

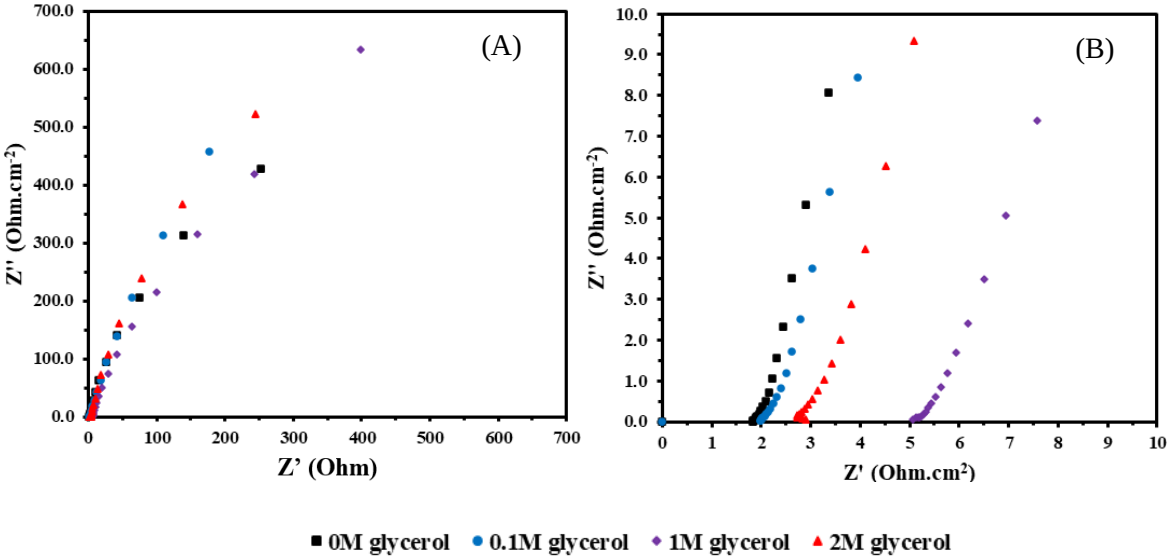

Figure 4.S4) PEIS of $Ni_{80}Au_{20}$/C at OCP in 1M KOH and various concentrations of glycerol measured at RT. Frequency range is between 100-0.1 kHz with a decade step of 5 with an AC amplitude of 10 mV.

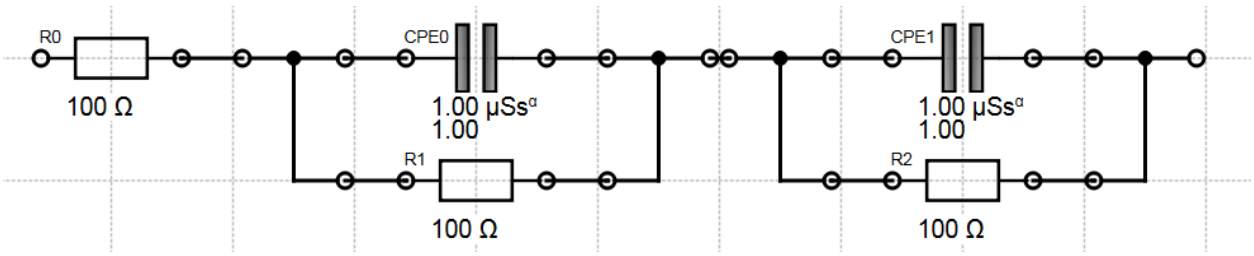

Schematic 4.S1) Voight EC diagram used to fit GEIS data. R and CPE represent resistances and constant phase elements.

Chapter 5: Coupling of glycerol oxidation and hydrogen production in membrane-free zero-gap electrolyser using carbon supported Ni-based catalyst

Abstract

The glycerol electrooxidation reaction (GEOR) is considered a promising glycerol pathway for the reduction in energy demand for the production of H_2 via the hydrogen evolution reaction. This is due to its lower onset potential relative to other electrooxidation of water. In addition, the selective conversion of glycerol to value added products has led to a significant scientific effort to design selective catalysts. However, this emphasis on selectivity has led to an underreporting of how coupling HER with GEOR could practically reduce the energy consumption of HER. This is relevant since this is an often cited advantage of GEOR but seldom demonstrated.

To address this gap, this chapter investigated the electrolyser performance of coupling HER with GEOR in a symmetrical/asymmetrical Ni cell. The investigated Ni catalysts are: Ni/C, $Ni_{98}Bi_2$/C, $Ni_{80}Au_{20}$/C and $Ni_{80}Pd_{20}$/C. Results showed the Ni phase GEOR reactivity of the Ni catalysts weren't capable of achieving the D.O.E. energy target of 40 $kWh.Kg_{H2}^{-1}$. That said, several engineering improvements can significantly reduce the energy consumption such as optimizing the operating concentrations of glycerol and KOH, and designing more effective HER catalysts. However, novel polarization curves were recorded and are caused by the Au and Pd phase GEOR which produced potential jumps if under suboptimal conditions. Upon further investigations, these jumps weren't caused by oxide formation but by a competitive equilibrium adsorption between glycerol and its intermediates where intermediates require a potential to oxidise. Furthermore, KOH concentration tests revealed a depletion of OH^- in solution, resulting in the electrolyte acidification which has important implications for catalysts design, downstream processing and a new metric which must be measured during GEOR stability testing. Overall, results of this chapter revealed novel behaviours and perspectives as to the limitations and new opportunities to improve HER coupled GEOR.

5.1 Introduction

Glycerol electrooxidation reaction (GEOR) is considered a promising anodic reaction to reduce the energy demands of intensive cathodic reactions such as CO_2 electrochemical reduction or the alkaline hydrogen evolution reaction (HER) due to its low theoretical onset potential [1–3]. Based on chapter 3, HER faradaic efficiencies (η_{FE}) in a GEOR-HER coupled cell surpassed 95% with an operating cell voltage comparable to alkaline water electrolysers (AWE) but at low currents [1–3]. In addition to the reduced energy consumption, process simulations studying the efficacy of coupling GEOR with HER determined the valorization of glycerol significantly increased the profitability and commerciality of this process unlike AWE which is entirely dependent on the profitability of H_2 [1, 4, 5]. In addition, the safety benefits of operating a GEOR over OER and the electro reductive inertness of glycerol can further simplify the electrolyser design [6]. For example, Chapter 3 safely operated a membrane-free HER coupled GEOR electrolyser due to the absence of O_2 from the anode up to 2.5V, proposing the realistic application of membrane-free electrolysers.

Since the commercial viability of GEOR-coupled HER comes from the value-added products, GEOR studies remain dedicated to the catalyst design to improve selectivity, reactivity and reduce the tendency for the catalyst to deactivate [3, 7]. However, most GEOR studies evaluate catalyst performances primarily from cyclic voltammetry (CV) and chronoamperometry (CA) at two different potentials coupled with HPLC [8–12]. While information on reactivity and selectivity can be gained from these types of tests, testing an electrocatalyst requires considering the electrical energy consumed since a potential and current is supplied to drive GEOR which is an important operational cost [1, 4, 5]. However, few papers perform GEOR studies in an electrolyser, which are mostly H-cells and not zero-gap cells, fewer perform comparable polarization curves and fewer measure the energy consumption per Kg_{H2} when coupling GEOR with HER [13–28]. While GEOR CVs and CAs can be argued as a close resemblance to how an electrolyser could behave, it is known in electrochemistry that even rotating disk electrodes (RDE) do not reflect the environment an electrocatalyst undergoes in an electrolyser [29].

Furthermore, unlike the interchangeability in information between CA and chronopotentiometry (CP) tests for AWE, Zhang et al. 2012 and other works have shown GEOR CA and CP results aren’t interchangeable in the information they provide due to the additional

factors glycerol influences at the anode [29–32]. Unlike the relatively straightforward potential dependent OER, GEOR requires multiple potential dependent/independent steps in a viscous electrolyte with competing adsorbates from byproducts and the risk of deactivation [3, 27, 32]. In turn, certain CP results may indicate a rapid degradation and deactivation of the catalyst during GEOR that wouldn't be observable under CA [29–32]. As a result, omitting key electrolyser results for GEOR catalysts limits the wider understanding of its GEOR performance. For example, chapter 4 revealed the influence of glycerol poisons the ionomer/membrane, significantly penalising OH^- conduction. Chapter 3 revealed glycerol can inhibit the oxidation of the catalyst bulk layer and Bi has a form of glycerol reactivity at elevated temperatures. These conclusions were only observable when varying reactive conditions and conducting a complete electrolysis polarization curve study instead of relying only on CVs and CAs. In turn, CV and CA procedures may not sufficiently reflect the important properties of a GEOR catalysts when scaled up.

In turn, this chapter investigated the polarization curves and stability of GEOR-HER coupled asymmetrical zero-gap membrane-free electrolysers with previously characterized carbon supported Ni catalysts from this research group [10–12, 33]. These anode catalysts are $Ni_{80}Pd_{20}$/C, $Ni_{80}Au_{20}$/C, $Ni_{98}Bi_2$/C and Ni/C. The selected cathode catalyst is $Ni_{80}Pd_{20}$/C. By performing complete polarization curves and 12-hour CP measurements, multiple new catalyst behaviours were observable with significant cell/catalyst design considerations for GEOR which wasn't previously observable from conducting polarization curves. Firstly, the Pd and Au phase GEOR of $Ni_{80}Pd_{20}$/C and $Ni_{80}Au_{20}$/C show several distinct GEOR related ohmic polarization phases at low overpotentials which are not observable at small loadings within a three-electrodes cell. These different ohmic polarization phases indicate different GEOR mechanisms over Pd and Au, requiring multiple potential jumps. Based on the reverse ohmic polarization behaviours, these jumps are not caused by the deactivation of Pd or Au but by a change in a complex adsorption equilibrium favouring different adsorbates along the electrolyser as the current increases due to changes in concentrations of glycerol and its products. Due to the galvanostatic operation of the polarization curves, a critical coverage of these unknown intermediate adsorbates induces the cell to jump in potential to sustain the demanded current. Also, CP results point to the neutralization of the electrolyte pH overtime which has been mentioned seldom in literature in theory but never observed empirically and has significant implications in terms of the process profitability. Due to this acidification, it is theorised that combining HPLC with pH monitoring can be a useful

approach to estimate the production of CO_3^- in solution. pH monitoring is required regardless since it's change overtime can be drastic depending on the catalyst products and provide a better validation of which parameter evolves overtime. This change in pH is unique to organic electrolysis as opposed to AWE. Additionally, the influence of concentration on the electrolyser and three electrode cells places into question the mechanism by which noble metal deactivation occurs within this field. A critical review of multiple works suggests intermediates and not oxide layer formation is responsible for GEOR deactivation but was never explicitly reported. Oxide formation is a subsequent event near the deactivation. In turn, it is recommended for GEOR catalysts studies utilising small 3-electroded measurements to observe the selective conversion of glycerol in the presence of other intermediates and different pH to measure the resilience of the catalyst to changes in solution composition and environmental conditions.

5.2 Experimental Section

5.2.1 Catalyst synthesis

Prior to each synthesis, all glassware was cleaned overnight by an Aqua Regia solution. Carbon supported $Ni_{X-1}M_{biX}$ (M = Pd, Au, Bi) catalyst were synthesised by sodium borohydride ($NaBH_4$) reduction in ethanol at room temperature. Firstly, Nickel (II) chloride hexahydrate ($NiCl_2 \cdot 6(H_2O)$, 99.999%, Sigma-Aldrich) and its accompanying bimetallic salt are each dissolved separately in 20 ml of ethanol for 30 minutes. To ensure complete dissolution, each precursor solution was initially treated to 1 minute of sonication in a sonicating bath (40 kHz Ultrasonic Bath, Fischer Scientific, Hampton, NH, USA) and was kept dissolved by magnetic stirring. The accompanying precursor M salts are Palladium (II) chloride ($PdCl_2$, 99%, Alfa Aesar), Gold (III) chloride ($AuCl_3$, 99%, Sigma-Aldrich) and Bismuth (III) chloride ($BiCl_3$, 99.99%, Fischer Scientific). After 30 minutes, both precursor solutions were combined, sonicated for 1 minute and stirred for 15 minutes to ensure a homogenous metal solution. Afterword's, the precursor solution was reduced by drop wise addition of dissolved $NaBH_4$ (>98%, ACROS) in 10 ml of ethanol. After 30 minutes, the solution is completely reduced. A respective amount of carbon powder (Vulcan XC72, Cabot Corp.) is immediately added after complete reduction and kept stirring for 30 minutes, resulting in 70 wt% carbon loading. Finally, the nanoparticles were washed with ethanol by centrifuging the samples three times at 6000 rpm for 15 minutes. Once washed, the samples were freeze dried overnight to remove residual ethanol.

5.2.2 Three-electrode electrochemical cell test

Electrochemical measurements were performed in a three electrode Teflon cell with a glassy carbon (0.196 cm^2), mercury/mercury oxide (Hg/HgO, Koslow Scientific Company, Englewood, NJ, USA) and platinum mesh working, reference and counter electrodes, respectively. Catalyst inks were composed of 6 mg of catalyst suspended in 1 ml of milli-Q® Millipore deionized water (18.2 MΩ cm at 293 K), 200 µL of isopropyl alcohol (IPA, 99.9%, Fisher Scientific, Hampton, NH, USA) and 100 µL of 5 wt% Nafion^{TM} (≈5%, Sigma Aldrich, St. Louis, MO, USA). Prior to each test, the glassy carbon surface was polished on a microfabric with a slurry of 30 µm, then 5 µm of Al_2O_3 in Milli-Q® water. Once polished, 10 µL of catalyst ink was casted on the glassy carbon surface and dried in a 60^{o}C oven. The cell's electrolyte was purged with N_2 gas (Grade 4.8, Linde plc, Dublin, Ireland) for 15 minutes. Then, cyclic voltammetry (CV) measurements were made using a Bio-Logic Potentiostat/Galvanostat paired with EC labs software (Bio-Logic Science Instruments, Seyssinet-Pariset, France) in various concentrations of KOH and various glycerol (>99%, Sigma-Aldrich) concentration solutions. CV scan rates were at 25 $mV.s^{-1}$ within a potential range of -0.926V to 0.773V. All reported potential measurements are in reference to the reversible hydrogen electrode (RHE) according to the following equation with no IR compensation:

(equation 5.1) $$E_{vsRHE}=E_{vs.Hg/HgO} + 0.098V + 0.0592 \times pH$$

Due to the upper limit of the pH meter calibration is 12.8, the pH for each solution was estimated by using Husmann et al. 2021's extrapolation model at 25^{o}C [34].

5.2.3 Single-cell membrane free electrolyser test

All electrolyser measurements were performed in a custom-made zero gap single cell with a 5 cm^2 and 25 cm^2 flow field area as shown in figure 5.S1. The cell constitutes two copper and graphite plates as the current collector and bipolar plates, respectively. The machined flow field patterns for the 5 cm^2 cell are parallel while the 25 cm^2 is composed of pin-type patterns. To control the cell temperature, current collectors are fitted with heating pads and a thermocouple on the cathode side. Thin Teflon gaskets are used to electrically insulate the polar plates and ensure a sealed zero-gap cell. A paper filter is used as an inexpensive electrically insulating separator material between both electrodes. To ensure a sufficient seal and intimate electrode contact with the filter paper, pressure tests were performed with Fujifilm pressure test paper. To mitigate

possible glycerol depletion during testing and to mitigate the influence of intermediates during polarization curve measurements, a 2L heated plastic tank was used to store the electrolyte. To collect hydrogen, the tank was connected to a water filled inverted graduated cylinder in a water bath. Hydrogen collection only began during chronopotentiometry. Prior to each experiment, the electrolyte was purged in N_2 for 2 hours while circulating the electrolyte. The electrolyte is pumped to the electrolysis cell at 1.4 ml/s. Electrodes were prepared in the CCS configuration by hand spraying catalyst ink using an airbrush (Iwata Eclipse HP-BCS, Maple Airbrush Supplies Inc., Edmonton, AB, Canada) onto carbon paper (090 value pack, wet proof, fuel cell store) heated over a hot plate set at 60°C with inert N_2 gas. The potentiostat used for the electrolyser tests was a Hokuto Denko HA-303 equipped with LabView software.

5.2.4 Notes on electrochemical methodology

To investigate the GEOR performance, the onset potential is defined as either the lowest current density between two faradaic peaks or when the current achieves 1 $mA.cm^{-2}$. Polarization curves were performed by applying CP measurements where steady state was observably achieved every 10-15 minutes for the first dozen of data points at low current. After, the potential was recorded after 1 minute of CP operation since steady state appears to be achieved sooner at higher current densities after the slow start-up.

Due to the membrane-free operation of the cell, the selectivity of the cathode towards HER is estimated using the following equation [35]:

(equation 5.2)
$$\eta_{far} = \frac{100 * V_{H2,exp}\ (mL)}{\frac{j\ (A.cm^{-2}) * A\ (cm^2) * t\ (s)}{2F\ (C.mol_{H2}^{-1})}} * 22771\ (mL.mol_{H2}^{-1})$$

Where $V_{H2,exp}$ is the experimentally collected hydrogen gas volume (ml); j is the current density ($A.cm^{-2}$), A is the sprayed area of the GDL (25 cm^2); t is the time of the experimental collection of H_2 gas (s), F is Faraday's constant (96485 C/mol_e). It should be noted that the $V_{H2,exp}$ represents the sum of H_2 gas collected and t is the time representing the duration of that collection. Also, A is the area of the GDL (25 cm^2) since the current density is calculated as the current divided by the GDL area in this study.

Due to the evolving cell voltage, the trapezoidal method was employed to calculate the energy consumption since the data collection was frequent enough for it to be appropriate. The energy consumption was calculated as follows [36]:

(equation 5.3) $$P_{ele-i}(J.s^{-1}) = V_{cell-i} * I_{cell-i}$$

(equation 5.4) $$E_{tot-ele}(J) = \sum_{i=1}^{i_{max}} \left(\frac{P_{ele\,i} + P_{ele\,i-1}}{2} * (t_i - t_{i-1}) \right)$$

(equation 5.5) $$E_{tot-ele}(kWh) = E_{tot-ele} * \frac{1\ kWh}{3.6*10^6\ J}$$

(equation 5.6) $$W_e(kWh.kg_{H2}^{-1}) = \frac{E_{tot-ele-kWh}}{V_{H2,exp}\ (mL) * 8.2*10^{-8} \frac{kg}{ml}}$$

Where $V_{cell\text{-}I}$ (V) and $I_{cell\text{-}I}$ (A) are the operating votage and current of the electrolyser for a given data point i. P_{ele} is the electrical power (W) consumed for a given data point while $E_{tot\text{-}ele}$ is total electrical energy (J) consumed during the hydrogen gas collection. W_e is the energy consumption needed to produce a kilogram of H_2 gas where $8.2*10^{-8}$ kg/mL is the density of the H_2 gas at standard temperature an pressure which are the conditions H_2 is measured.

5.3 Results

5.3.1 Cathode selection

Due to the nature of the membrane free electrolyser, this cathode selection section will quickly discuss key findings of chapter 4 of this thesis on the impact of glycerol on HER over the same catalysts. Catalyst physical characterisations were performed by previous colleagues within their respective works [11, 12, 33]. While the impact of glycerol on HER has been suggested to be inhibitory [37, 38], chapter 4 demonstrated glycerol has both an inhibitory and promotional role on HER. In fact, glycerol didn't impact the conduction of OH^- in solution as is popularly hypothesised due to a misunderstanding that OH^- conduction is vehicular in nature in aqueous solution [37]. OH^- conduction is primarily dependent on the Grotthuss mechanism in liquid phase [39, 40], nulling most of the influence glycerol should have on conduction [38, 41]. Instead, glycerol impacts the stability of the microphase structure of the Nafion® polymer binder that is solely used in the field [42, 43]. In turn, high frequency charge transfer resistances confused as a conduction loss in solution were a result of a binder instability issue impacting OH^- conduction and H_2O displacement (Chapter 4)

[42, 43]. Furthermore, preliminary evidence showed glycerol promoted HER depending on the catalyst material and the specific HER mechanism by interfering with the catalyst surface. Due to the previous HER characterisation of the same Ni catalysts with an understanding of glycerol's impact on HER, all anode tests were run with a Ni based cathode to demonstrate the feasibility of asymmetric/symmetric Ni based GEOR-coupled HER cells.

Due to unanswered questions on the role of glycerol on HER at the catalyst interface, the cathode catalyst selection between Ni/C, $Ni_{98}Bi_2$/C, $Ni_{80}Au_{20}$/C and $Ni_{80}Pd_{20}$/C was done in 1M KOH and 0.1M glycerol. The anode material of choice is Ni/C due to its abundance during synthesis. Electrolyser testing is required since chapter 4's 3-electrode results may not be representative of an electrolyser performance since: i) the use of the G.C. surface area to normalize the HER current isn't useful to translate the results from a 3-electrodes cell to an electrolyser [44]; ii) there is an inherit difference in structure and environmental conditions between a polished G.C. in a static fluid and a porous electrolyser GDL with a displaced fluid [29].

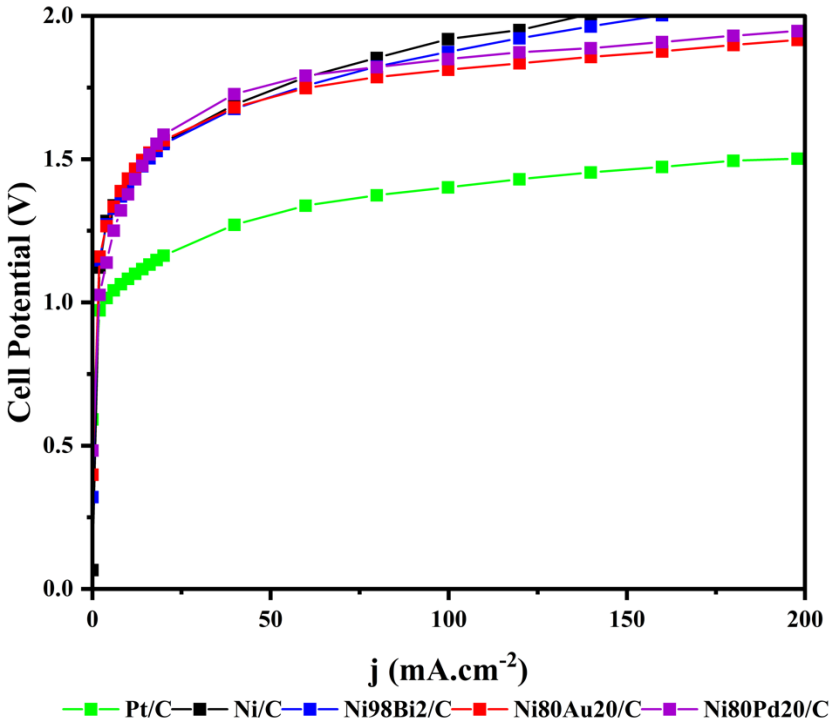

Figure 5.1) GOER-HER coupled electrolyser polarization curves with 1 mg.cm^{-2} loading of Ni/C at the anode and 2 mg.cm^{-2} loading of Pt/C; Ni/C; $Ni_{98}Bi_2$/C; $Ni_{80}Au_{20}$/C and $Ni_{80}Pd_{20}$/C at the cathode with a 1M KOH and 0.1M glycerol circulating electrolyte solution at 80°C.

Figure 5.1 presents the polarization curve of the catalyst library at the cathode. In concordance with chapter 4, figure 5.1 demonstrates all four catalysts aren't ideal for HER as opposed to Pt/C. To remain within the scope of this work on the anode, 0.1M glycerol was the only tested glycerol concentration for the cathode selection since the influence of glycerol on HER is saturated at 0.1M for all catalyst based on chapter 4. It should be said several other works have achieved high performing Ni based HER catalyst that outcompete Pt/C [45–47].

The polarization curves in figure 5.1 shows $Ni_{80}Au_{20}$/C (1.92V) and $Ni_{80}Pd_{20}$/C (1.93V) outperforming $Ni_{98}Bi_2$/C (2.0V) and Ni/C (2.1V) up to 200 $mA.cm^{-2}$. This is unexpected for $Ni_{80}Au_{20}$/C to be comparable to $Ni_{80}Pd_{20}$/C, and outperform $Ni_{98}Bi_2$/C and Ni/C due to its overall higher overpotential in chapter 4's 3-electrodes results and detrimental sensitivity to glycerol unlike all other catalysts. Amazingly, this can be explained by the three separate HER mechanisms observed over $Ni_{80}Au_{20}$/C due to the distinct Au and Ni phases where the lowest current HER mechanism operated at an overpotential of ≈-100 mV vs RHE in chapter 4, similar to $Ni_{80}Pd_{20}$/C's onset potential at -134 mV vs RHE. These electrolyser results confirm the low current HER mechanism in chapter 4 isn't an artifact but a real phenomenon which is accentuated by operating a larger electrolyser. This discrepancy between 3-electrode measurements and electrolysers for GEOR systems can be due to the catalyst loading differences as seen in chapter 3. To provide perspective, the cathode contains 1087 times more catalyst (50 mg) than the G.C. at 46 µg at the cathode. From this larger loading, the similar performance between $Ni_{80}Au_{20}$/C and $Ni_{80}Pd_{20}$/C, and chapter 4's HER results, the current densities near the onset-potential (around 1 $mA.cm^{-2}$) recorded under CV and LSV will be of relevance for this study when scaled up.

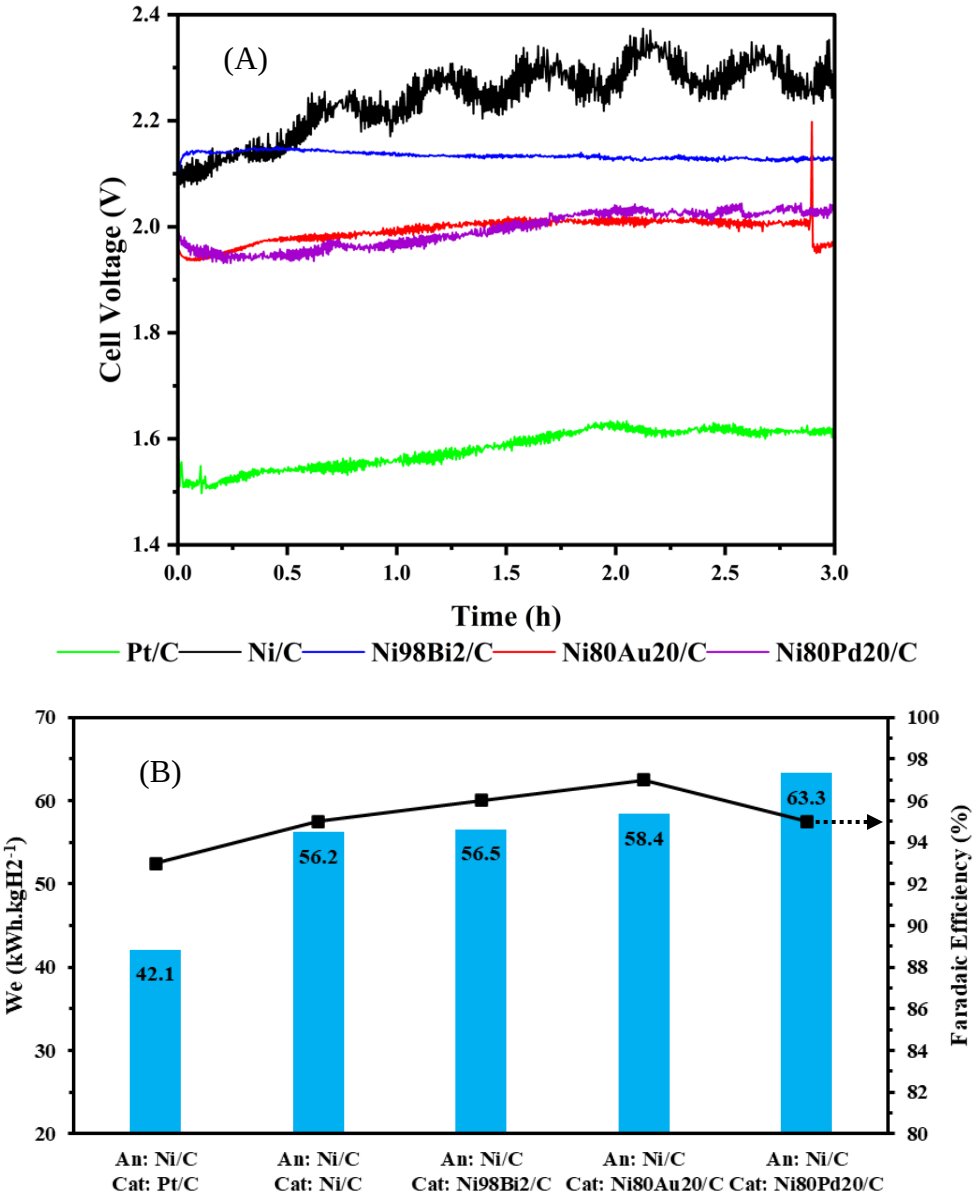

Figure 5.2) the 3 hour CP measurements (V) at 200 mA.cm^{-2}, and B) the respective energy consumption (kWh.kg$_{H2}^{-1}$) and faradaic efficiencies (%) of an electrolyser with 1 mg.cm^{-2} of Ni/C at the anode and 2 mg.cm^{-2} of Pt/C; Ni/C; $Ni_{98}Bi_2$/C; $Ni_{80}Au_{20}$/C or $Ni_{80}Pd_{20}$/C at the cathode with 1M KOH and 0.1M glycerol electrolyte solution circulating at 80°C.

To evaluate the catalyst stability considering the Nafion® binder is altered [42, 43], a 200 mA.cm^{-2} CP test was performed for 3 hours. A faradaic efficiency above 93% was recorded for each test with 42.1 kWh.kg$_{H2}^{-1}$ recorded for Pt/C. While a faradaic efficiency of 100% wasn't recorded for each test, the lower efficiency is explained in part by the delay between the hydrogen produced from the electrolyser to the inverted cylinder. To ensure consistency, collection of

hydrogen stopped strictly after the collection cylinder was inverted for 5 minutes. A loss of hydrogen can also be explained by H_2 crossing over to the anode side and oxidising, but this appears to be a minor loss, though this conclusion can be different for a larger cell. Additionally, while a gas leak test was performed prior to each test with the N_2 purged gas and during the tests, hydrogen gas may have leaked due to the challenge in properly spotting bubbling at such low leak rates during operation. However, considering η_{FE} > 90% for each catalyst, leaking is not a major issue. Additionally, the competitive electro-reduction of the oxidation products of glycerol [48] (but not glycerol itself) is a possible factor for the reduced η_{FE}, as discussed in chapter 4. However, due to the elevated faradaic efficiency of HER, HER is more favourable to occur than the reduction of the oxidation products in these testing conditions, although a separate study should be performed to evaluate if electroreduction of GEOR products occurs.

The order of the CP performances of each cathode in figure 5.2 is similar to the polarization curves in figure 5.1 where $Ni_{80}Au_{20}$/C (2.00V) and $Ni_{80}Pd_{20}$/C (2.04V) are operating at a lower cell voltage than $Ni_{98}Bi_2$/C (2.13V) and Ni/C (2.26V). These results reaffirm none of the catalysts are ideal for HER as opposed to Pt/C which required a cell potential of 1.61V to sustain 200 $mA.cm^{-2}$. In turn, figure 5.1-2 shows around 400 mV of the electrolyser operating potential can be attributed to the cathode overpotential for the rest of the measurements in this chapter. In terms of stability, both $Ni_{80}Au_{20}$/C and $Ni_{80}Pd_{20}$/C show promise as a catalyst of choice for this chapter (figure 5.2). Since the electrolyser performance appears to follow the trends of the onset potential of each catalyst measured in the small three-electrodes tests in chapter 4, $Ni_{80}Au_{20}$/C should be chosen since it's onset potential improves as glycerol's concentration increases. However, $Ni_{80}Pd_{20}$/C was chosen due to $Ni_{80}Au_{20}$/C's unclear promotional relationship with glycerol during HER while there is a greater certainty of what is occurring on $Ni_{80}Pd_{20}$/C's surface, and it is known its onset potential should worsen with an increase in glycerol concentration. In turn, improvements in cell potentials by changing concentrations will be known to originate from the anode and not the cathode and avoid confusion as to the influence of glycerol.

5.3.2 Influence of glycerol concentration over supported Ni catalyst

While chapter 3 of this thesis investigated the influence of hydroxide and glycerol concentration over Ni GEOR and discovered glycerol has an influence on the bulk oxidation state

of the catalysts, it is of similar interest to investigate the same question when the catalyst is supported over a conductive support.

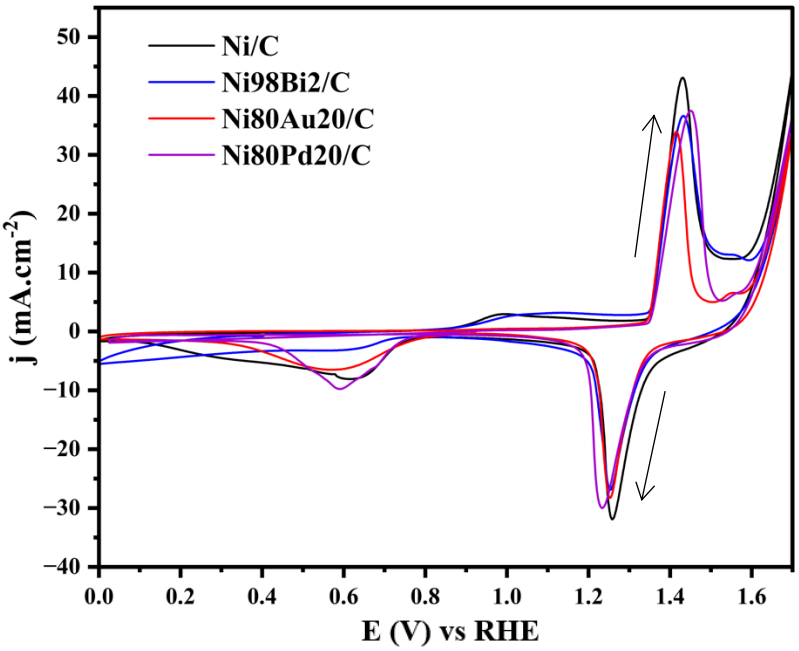

Figure 5.3) 10th cycle CVs of Ni/C, $Ni_{98}Bi_2$/C, $Ni_{80}Au_{20}$/C and $Ni_{80}Pd_{20}$/C measured at 25 $mV.s^{-1}$ in N_2 purged 1M KOH at RT.

Figure 5.3-5 present's the 10th CV cycle results of each catalyst when the concentration of glycerol is varied from 0 to 2M in 1M KOH solution at a scan rate of 25 $mV.s^{-1}$. In 1M KOH (figure 5.3), the Ni oxidation and reduction peaks for the β-$Ni(OH)_2$/β-NiOOH redox surface reactions are observable on each catalyst at ~1.38 and ~1.25V [10, 11, 31, 33, 49–52]. The Ni^{+2} oxidation peak current density of each catalyst's β-$Ni(OH)_2$ oxidation reaction is 42 $mA.cm^{-2}$ for Ni/C, 36 $mA.cm^{-2}$ for $Ni_{98}Bi_2$/C, 30 $mA.cm^{-2}$ for $Ni_{80}Au_{20}$/C and 37 $mA.cm^{-2}$ for $Ni_{80}Pd_{20}$/C. The reduced Ni oxidation peak over the Ni bimetallic catalysts is related to the reduced Ni surface coverage from the even surface decoration of Bi and by the surface agglomeration of Au and Pd atoms forming Au/Pd islands on the surface at their respective atomic loadings based on EELS imagery from a previous work investigating the same catalysts [12, 33]. The onset potential for β-$Ni(OH)_2$ oxidation for each catalyst is around 1.33 V. As for the β-$Ni(OH)_2$/β-NiOOH redox process reversibility, the potential window between the redox peaks are smaller for $Ni_{98}Bi_2$/C (213 mV), $Ni_{80}Pd_{20}$/C (213 mV) and $Ni_{80}Au_{20}$/C (180 mV) than Ni/C (247 mV), which is attributed to the synergistic role Pd, Au and Bi have at these atomic loadings on the oxidation of Ni as was

previously investigated for the same catalysts [10, 11, 33]. Overall, these results reaffirm previous reports of the synergistic effects Pd, Au and Bi have on Ni's β oxidation reaction [10, 11, 33].

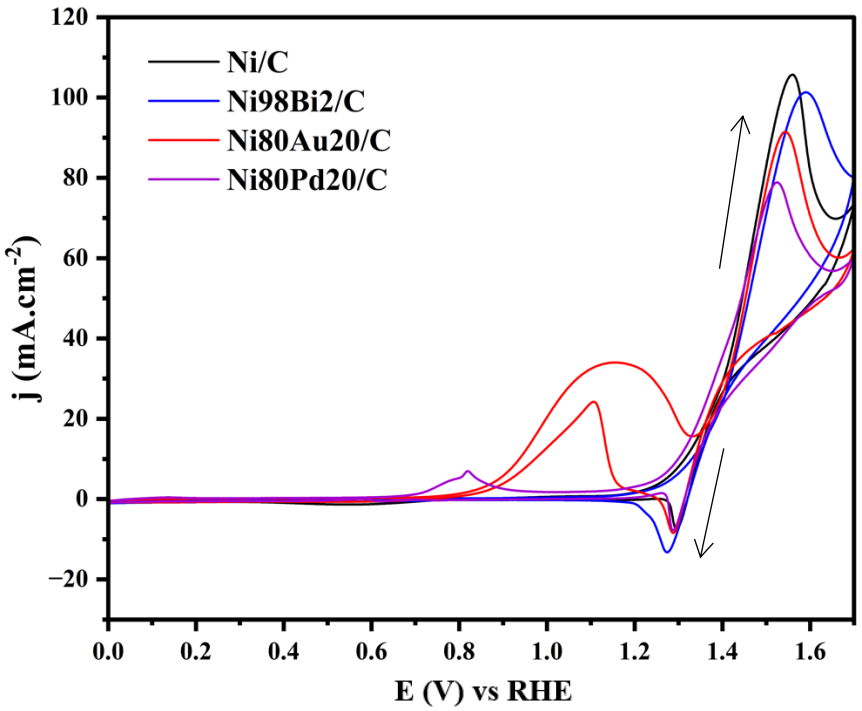

Figure 5.4) 10th cycle CVs of Ni/C, $Ni_{98}Bi_2$/C, $Ni_{80}Au_{20}$/C and $Ni_{80}Pd_{20}$/C measured at 25 $mV.s^{-1}$ in N_2 purged 1M KOH and 0.1M glycerol at RT.

Figure 5.4 presents the electro-oxidation of glycerol at 0.1M for each catalyst. In 0.1M glycerol, all catalysts present an increased Ni oxidation peak relative to 0M glycerol by a factor of 3 approximately. This increased peak current density is caused by the production of β-NiOOH oxidising glycerol molecules at the surface to value added products, consequentially reducing itself (β-NiOOH) back to regenerate β-$Ni(OH)_2$ [10, 12]. The continued regeneration of β-$Ni(OH)_2$ by glycerol requires the system to operate at higher potentials to induce higher currents where the production rate of surface β-NiOOH outcompetes it's reduction by glycerol, pushing the β-$Ni(OH)_2$/β-NiOOH oxidation peak to higher potentials [10, 11]. The reduction of β-NiOOH is made evident by the decrease of its electrochemical reduction peak at ~1.24V, indicating less surface β-NiOOH is present prior to its electrochemical reduction when compared to 1M KOH [9–11, 31, 49–53].

Compared to 0M glycerol, the β-$Ni(OH)_2$ oxidation reaction in 0.1M glycerol in figure 5.4 has a reduced onset potential on each catalyst, with the exception of $Ni_{98}Bi_2$/C. For Ni/C and $Ni_{80}Pd_{20}$/C, their onset potentials reduced to 1.182 (-152 mV) and 1.095 (-234 mV), respectively.

As for $Ni_{98}Bi_2$/C, an increase in onset potential is observed up to 1.384 V (+65 mV). However, it is difficult to identify the onset potential for the β-Ni oxidation reaction for $Ni_{80}Au_{20}$/C due to the overlap with the surface Au phase GEOR. A linear tangential x-intercept of at current above 40 $mA.cm^{-2}$ of the β-Ni oxidation peak approximates the onset potential to 1.324 V (-6mV). It should be noted this intercept can represent a high estimate of the onset potential.

The presence of Au and Pd GEOR peaks at 1.164 V and 813 mV demonstrates Ni is not the only reactive phase, respectively [10, 11]. This complicates the catalyst analysis since multiple phases are reactive for GEOR other than Ni. While it may be dismissed at elevated potentials in an electrolyser that Ni will only be active since Pd or Au can deactivate from the formation of Pd and Au oxides [3, 54, 55], the cathode section figure 5.1-2 showed that small currents may have a dictating role on the electrolyser operating potential. In turn, these catalysts may resemble more Pd and Au catalysts than Ni catalysts.

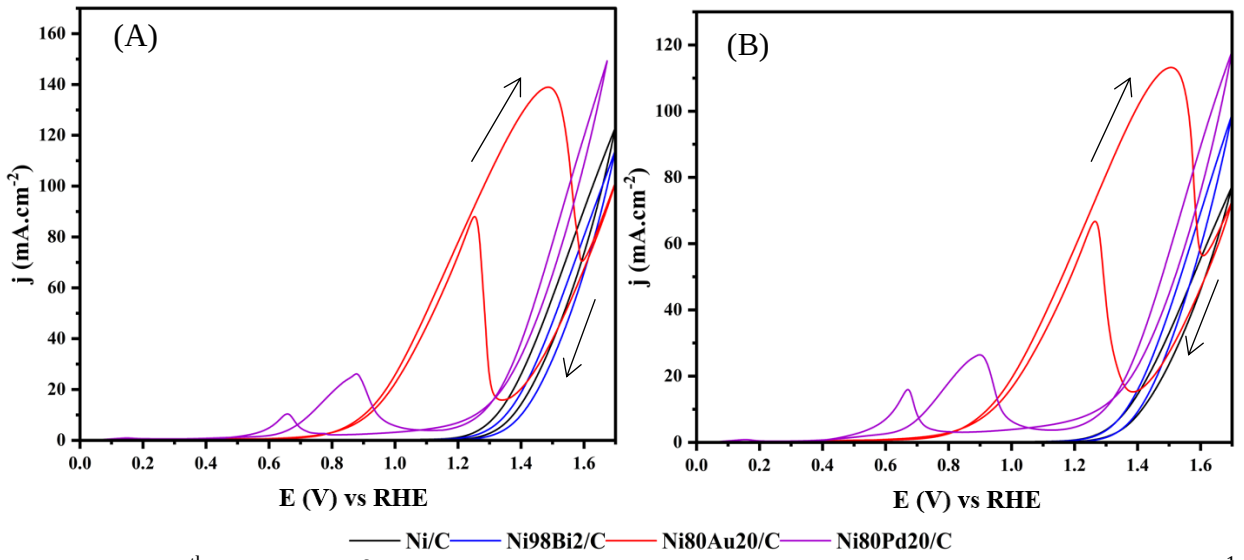

Figure 5.5) 10th CV cycle of Ni/C, $Ni_{98}Bi_2$/C, $Ni_{80}Au_{20}$/C and $Ni_{80}Pd_{20}$/C measured at 25 $mV.s^{-1}$ in N_2 purged 1M KOH and (A) 1M or (B) 2M glycerol electrolyte solution at RT.

As the concentration of glycerol increases to 1M glycerol, the oxidation peak of Ni over each catalyst is no longer detectable as seen in figure 5.5A. The absence of an oxidation peak doesn't mean the GEOR reaction is suppressed but the availability of glycerol to the catalyst surface is sufficiently elevated to regenerate β-$Ni(OH)_2$ even at the maximum applied potential [10]. This is confirmed by the onset potential of the faradaic slopes of each catalyst is approximately near those measured at 0.1M glycerol where β-$Ni(OH)_2$ oxidation occurs and the absence of the β-NiOOH reduction peak [10]. However, a striking divergence is observed when compared to

results of chapter 3. For Ni/C, an increase in glycerol concentration reduces the onset potential up to 1.23 V (-104 mV from 0M) in 1M glycerol. The same is also observed for $Ni_{80}Pd_{20}$/C to 1.132 V (-197 mV from 0M). Interestingly, the onset potential of $Ni_{98}Bi_2$/C reduces to 1.282 V (- 37 mV from 0M). As is reported in chapter 3, the onset potential of Ni^{2+}/Ni^{3+} oxidation reaction is known to be influenced by the concentration of glycerol but is always reported to be significantly inhibitory at and past 0.1M glycerol [12]. Houache et al. 2021 observed glycerol inhibited Ni oxidation past 0.15M over different unsupported Ni catalysts [10]. However, 1M glycerol in figure 5.5 presents a superior Ni GEOR current density at 123 $mA.cm^{-2}$, 114 $mA.cm^{-2}$, 102 $mA.cm^{-2}$ and 151 $mA.cm^{-2}$ on Ni/C, $Ni_{98}Bi_2$/C, $Ni_{80}Au_{20}$/C and $Ni_{80}Pd_{20}$/C, respectively. This entails that the carbon support has changed significantly the influence glycerol has on its oxidation over Ni, changing from an inhibitor to a promoter. This observation places into question the universal inhibition glycerol has on its own Ni GEOR mechanism [56, 57]. This change in how glycerol impacts Ni GEOR is plausibly related to the superior electron conductivity of carbon supports and the inability of carbon to be reduced/oxidised within the operating potentials, hence the inhibitory role of glycerol to suppress oxidation of the bulk between tests is avoided as is discussed in chapter 3. This is further supported by the current from the reverse scant no longer surpassing the forward scan current, which entails that the hysteresis from the application of an elevated potential in chapter 3 is no longer apparent, which can also be explained by the inability of the carbon support to change oxidation state regardless of the applied potential at a given moment [58]. The implication of this observation provides a new design strategy to practically reduce downstream separation costs due to the opportunity to increase the product selectivity from a higher reactant concentration.

As for the Pd and Au GEOR phases, both experienced an increased peak current density by a factor of 4 (39 $mA.cm^{-2}$ and 140 $mA.cm^{-2}$) from 0.1M glycerol, respectively. Furthermore, Pd and Au's onset potential both reduce significantly down to 479 mV and 620 mV, respectively. The difference in peak oxidation current is caused by a higher Au surface coverage than Pd [12], a higher intrinsic GEOR reactivity of Au with glycerate (deprotonated form of glycerol [30]) and reduced poisoning sensitivity of Au as opposed to Pd [27, 32, 59].

Increasing the concentration further up to 2M glycerol reduces Ni GEOR reactivity from 1M glycerol to 78 $mA.cm^{-2}$, 99 $mA.cm^{-2}$, 73 $mA.cm^{-2}$ and 118 $mA.cm^{-2}$ over Ni/C, $Ni_{98}Bi_2$/C, $Ni_{80}Au_{20}$/C and $Ni_{80}Pd_{20}$/C, respectively (figure 5.5B). As for Ni's oxidation onset potential, all

catalyst shows an unchanged onset potential, except for $Ni_{98}Bi_2$/C where a continued reduction is observed to 1.239 V (-80 mV). In the case of Au phase GEOR, there is a decrease in peak current density from 140 mA.cm^{-2} in 1M glycerol to 115 mA.cm^{-2} and an increase in oxidation peak potential from 1.489 V to 1.501 mV with an unchanged onset potential (figure 5.5B). This indicates an increase in glycerol concentration may suppress the deactivation of Au. The oxidation peak of Pd also marginally decreased from 39 mA.cm^{-2} to 38 mA.cm^{-2} with a similar increase in peak potential to 895 mV in 2M glycerol from 882 mV in 1M glycerol (figure 5.5B). In turn, an elevated concentration of glycerol prevents Pd or Au deactivation but also reduces its reactivity. Literature theorises that this is caused by a saturated glycerol coverage over the Pd/Au surface which competes with OH^- adsorption, a key adsorbed reactant for GEOR and the deactivation process [60]. Due to the pH sensitivity of Au based GEOR [30], it is assumed glycerol doesn't change the solution pH since this would present an external factor to account for. However, this assumption may not be valid at 2M glycerol since it is a weak acid [3]. pH measurements showed a marginal change from 13.79 in 1M KOH to 13.58. However, due to the upper calibration limit of the in-hand pH meter is set to 12.9, the pH measurements may not accurately reflect the true pH [34].

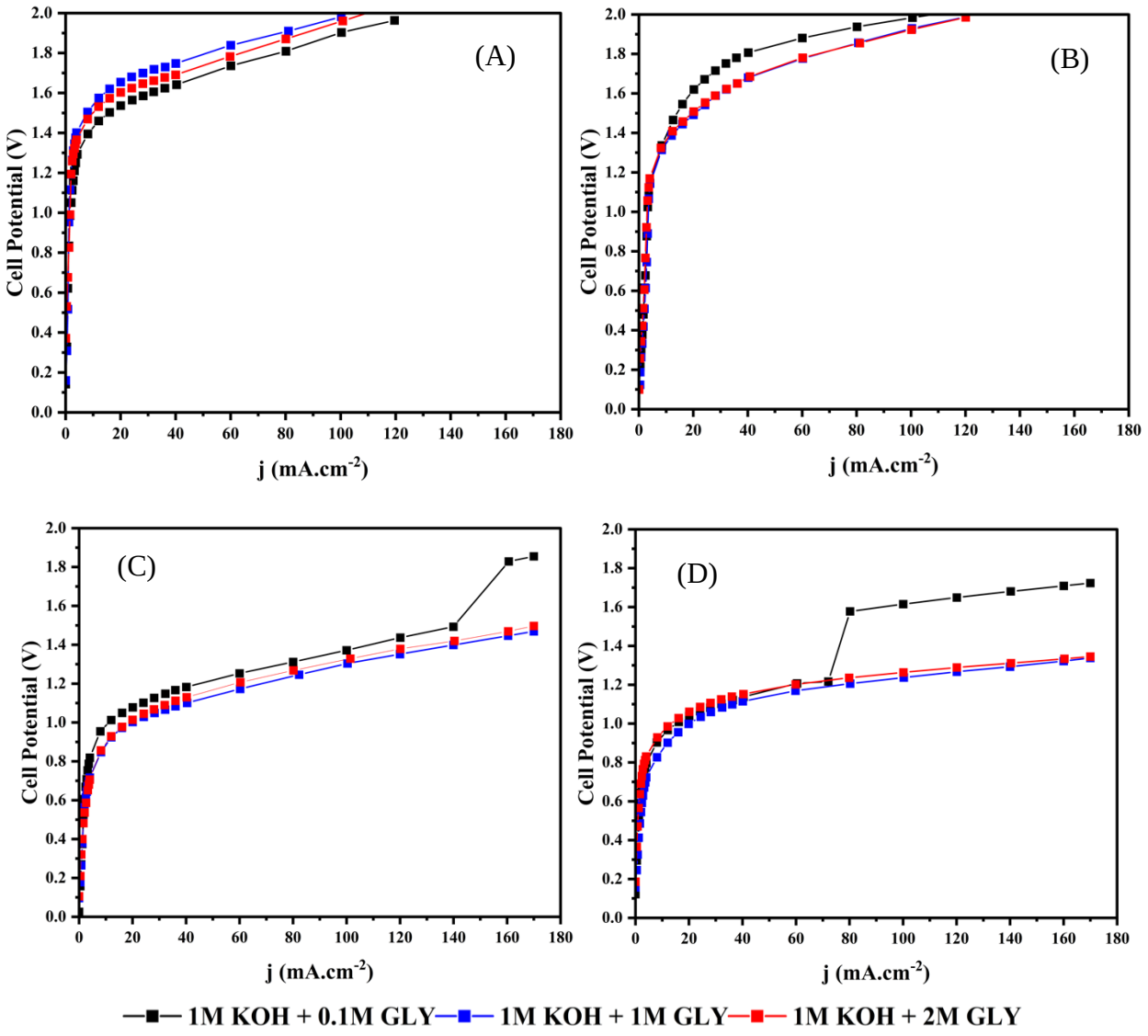

Figure 5.6) Electrolyser polarization curves of a 2 mg.cm^{-2} loading of $Ni_{80}Pd_{20}$/C at the cathode with 1 mg.cm^{-2} loading (A) Ni/C; (B) $Ni_{98}Bi_2$/C; (C) $Ni_{80}Au_{20}$/C and (D) $Ni_{80}Pd_{20}$/C at the anode in 0.1M; 1M and 2M glycerol and 1M KOH circulating electrolyte solution at 80^{o}C.

Figure 5.6 presents the polarization curves of each tested catalyst as the anode material at 80^{o}C with $Ni_{80}Pd_{20}$/C as the cathode material. For Ni/C (figure 5.6A), the lowest cell potential occurred at 0.1M glycerol. However, the lowest operating cell potential over $Ni_{98}Bi_2$/C occurred at 1-2M glycerol, a difference to Ni/C. It should be clarified that while $Ni_{98}Bi_2$/C performs better at 1M and 2M glycerol than 0.1M glycerol, it is observed the ohmic polarization phase at 0.1M glycerol converges to towards the ohmic polarization phases in 1M and 2M glycerol. Due to stopping the polarization curve measurements at 2V for safety reasons, it is difficult to productively state that 1M and 2M glycerol are ideal for the $Ni_{98}Bi_2$/C anode electrolyser at higher

current densities. It is also worth pointing out that $Ni_{98}Bi_2$/C appears to show a small and low potential ohmic polarization phase prior to 1.2V. A similar behaviour was also observed in chapter 3's $Ni_{90}Bi_{10}$ polarization curve, pointing to a recuring novel reactivity correlated with Bi and glycerol.

Interestingly, $Ni_{80}Au_{20}$/C's ending activation polarization potential is significantly lower than Ni/C and $Ni_{98}Bi_2$/C and decreases when increasing the glycerol concentration from 722 mV in 0.1M glycerol, to 652 mV in 1M glycerol and 650 mV 2M glycerol. From there, the ohmic polarization phase of each concentration tested retains a consistent overpotential difference between each other and remains under 1.5V up to 200 $mA.cm^{-2}$. However, the cell potential jumps positively at 0.1M glycerol at a critical current density of approximately 160 $mA.cm^{-2}$. From there a new steady state is achieved towards a second ohmic polarization phase up until 200 $mA.cm^{-2}$. This type of jump behaviour is a significant departure from OER electrolyser behaviour and absent in CV results [61]. As for $Ni_{80}Pd_{20}$/C, its ending activation polarization potential is similarly low and steadily decreases to lower potentials when glycerol's concentration increases from 832 mV in 0.1M glycerol, to 793 mV in 1M glycerol and 724 mV in 2M glycerol. For all glycerol concentrations, $Ni_{80}Pd_{20}$/C retains a cell potential below 1.4V during its first ohmic polarization phase up until 200 $mA.cm^{-2}$. Like $Ni_{80}Au_{20}$/C, $Ni_{80}Pd_{20}$/C potential also jumps at 0.1M glycerol but at a different critical current density of 72 $mA.cm^{-2}$ in 0.1M glycerol. Interestingly, although $Ni_{80}Au_{20}$/C and $Ni_{80}Pd_{20}$/C both have different noble metals with different GEOR reactivity and deactivation potentials as seen in the figure 5.4-5, the cell potential positively jumps by a similar 330mV and 360 mV, respectively. Based on the overall performance of the polarization curves in figure 5.6 C and D, it appears 1M glycerol is most ideal for $Ni_{80}Au_{20}$/C and 2M glycerol at higher current densities for $Ni_{80}Pd_{20}$/C.

Based on the different GEOR active phases over the CVs of each catalyst (figure 5.4-5) and the significantly reduced steady state potentials achieved immediately after the initial activation polarization for $Ni_{80}Au_{20}$/C and $Ni_{80}Pd_{20}$/C at all glycerol concentrations (< 1V) to those achieved by Ni/C and $Ni_{98}Bi_2$/C (~1.2V), the first ohmic polarization phase observed at low potentials is a product of surface Au and Pd phase GEOR. Due to this, $Ni_{80}Au_{20}$/C and $Ni_{80}Pd_{20}$/C primarily act as Au and Pd based catalyst within the first ohmic polarization phase. However, this doesn't exclude the participating role of Ni in aiding Au or Pd sustain the demanded current [10–12,

[53, 61–63] or the co-reactivity of Ni phase GEOR once the anode potential reaches relevant Ni phase GEOR potentials (figure 5.6 A-B). Based on the reported observation of no gas evolution in the anode output line, it is certain the second polarization phase does not represent a change from GEOR to OER. In turn, the second polarization phase represents another organic oxidation reaction mechanism, likely another GEOR mechanism.

Unexpectedly, a critical current density is observed at a concentration of 0.1M glycerol which increases the cell potentials of $Ni_{80}Au_{20}$/C and $Ni_{80}Pd_{20}$/C anodes by +330 mV and +360 mV, respectively. Considering this effect is observable on certain anode catalysts, it can be concluded that this behaviour originates from the anode. The occurrence of an accelerated increase in potential isn't new in electrochemistry and is observed in some RDE GEOR [32, 61, 64] and OER electrolyser studies [29, 65], although it is seldom discussed or reported since studies are designed to avoid these behaviours and is reported as a failure state [32]. While GEOR studies concluded a potential jump is attributed to the deactivation of noble catalysts [32, 61, 64], it will be shown later how this interpretation is not an accurate explanation of what is observed in figure 5.6.

Overall, results of this section show accompanying Au, Pd and Bi does not appear to influence significantly the impact of glycerol over Ni phase GEOR performances when changing the concentration of glycerol, in concordance with chapter 3. However, the addition of the carbon support completely changes the response of Ni to glycerol. In chapter 3, it was observed how unsupported Ni and $Ni_{90}Bi_{10}$ is significantly de-activated at concentrations past 0.1M glycerol. However, when Ni is supported on a conductive carbon support as seen in figure 5.4-5, the Ni phase of each catalyst continuously improves in reactivity up to 1M glycerol, regardless of the accompanying metal (Bi, Au or Pd) and even decreases the β-NiOOH onset potential, suggesting glycerol no longer suppresses the oxidation of Ni when supported on a conductive support but promotes it. The application of this observation is significant in literature since it suggests higher concentrations of glycerol can be applied for Ni based catalysts.

Also, considering the Nafion® loadings are similar between chapter 3 and 5, this also eliminates the detrimental effect of glycerol on Nafion® (chapter 4) for being the primary cause for the loss in reactivity observed in chapter 3 since its effects should have been observed in both chapter 3-5. The effects of glycerol on Nafion® can explain in part the decrease in catalyst reactivity at 2M glycerol where chapter 4 demonstrates a significant increase in $R_{uncompensated}$ from

1 to 2M glycerol. In turn, the influence of Nafion® shouldn't be ignored regardless for future works as an external factor which may artificially impact the measurements of the catalyst performance. Additionally, Au and Pd over $Ni_{80}Au_{20}$/C and $Ni_{80}Pd_{20}$/C are reactive for glycerol and can be the dominant reactive phases up to 200 $mA.cm^{-2}$ even if they are present in trace amounts on the catalyst surface as shown in figure 5.6 C-D. This does raise the concern that previous publications utilising the same catalyst may not have had solely Ni as the reactive phase but also Au and Pd, even if they intentionally operated at Ni active potentials where Au and Pd should be deactivated. This confusion can be avoided by performing polarization curves and a concentration study to identify the reactive phase responsible at a given potential. Finally, results repeatedly demonstrate that small currents measured over a CV (figure 5.1 & 5.3) can have a substantial influence on an upscaled systems (figure 5.2 & 5.6 C/D), presenting opportunities to reduce the energy consumption for electrolysers.

5.3.3 influence of KOH concentration over supported Ni catalyst

The concentration of hydroxide was changed to extrapolate the catalyst sensitivity to its concentration since OH^- is a critical adsorbate for GEOR which can reduce the cell potential [3, 7, 61, 66]. Based on the previous section, Ni, Pd and Au are reactive phases and an understanding how OH^- influences each material in relation to GEOR is important to understand what could be responsible for the performance on the electrolyser anode. In the case of Ni, OH^- is required to regenerate the active Ni^{+3} site but doesn't compete against glycerol adsorption when Ni^{+3} is formed below OER potentials as discussed in chapter 3. However, there is evidence in chapter 3 that glycerol interferes with the oxidation of Ni. As for Pd and Au, a neighboring OH^* is required to oxidise glycerol and directly competes with glycerol as an adsorbate [32]. In turn, an increase in OH^- can inhibit GEOR over Au and Pd by favouring OH^- adsorption which can promote oxide formation and theoretically deactivate the catalyst [3, 32, 61].

However, an increased OH^- adsorption over Pd may advantageously desorb poisonous intermediates such as CO_{ads} from GEOR to produce CO_2 or CO_3^- via the Langmuir-Hinshelwood mechanism, reactivating Pd for GEOR [7, 12, 55, 61, 64, 67, 68]. White at al. 2022 found an increase in hydroxide concentration results in high current densities and delays Pd deactivation [61]. This disagreed with Habibi et al. 2012 who found an increase in hydroxide concentration negatively shifted the deactivation potential [32]. However, Melle et al. 2021 reported under CP conditions

only, an oscillating behaviour between deactivation and reactivation occurs from CO_{ads}/intermediate saturation and removal [64, 67, 69]. Thus, the relationship of OH^- towards GEOR is complex and needs to be understood as it relates to Pd and Au due to its relevant reactivity in this chapter. Based on the previous section, the chosen glycerol concentration to investigate the role of OH^- was 1M glycerol since it is the least amount of glycerol to universally avoid potential jumps while also being the most optimal concentration for each anode in terms of cell potential.

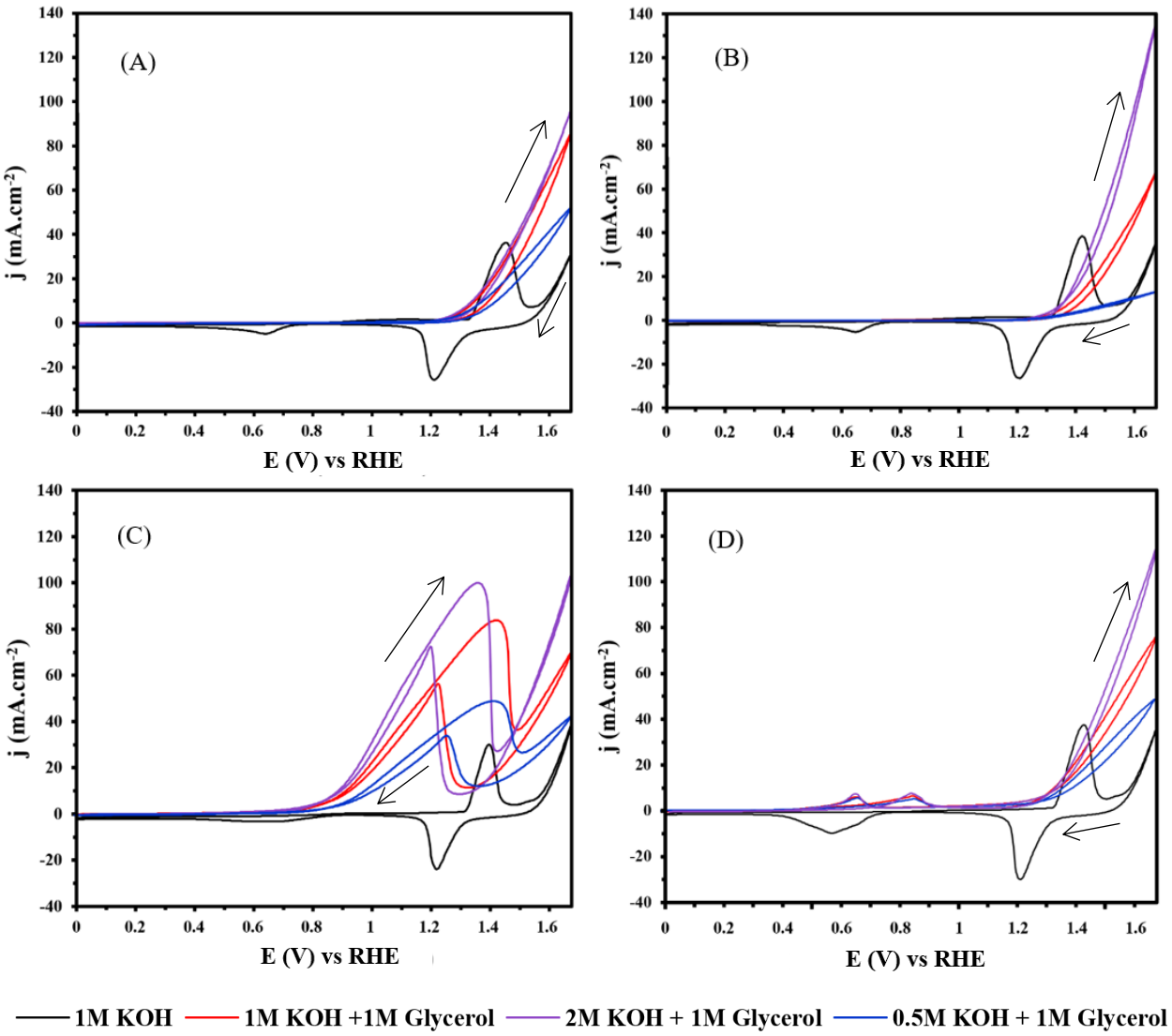

Figure 5.7) 10th CV cycle of A) Ni/C, B) $Ni_{98}Bi_2$/C, C) $Ni_{80}Au_{20}$/C and D) $Ni_{80}Pd_{20}$/C measured at 25 $mV.s^{-1}$ in 1M glycerol and various concentrations of KOH at RT.

Figure 5.7 presents the 10th CV cycle of each catalyst with different OH^- concentrations from 0.5M, 1M and 2M KOH. For each catalyst, an increase in KOH concentration improves significantly Ni phase GEOR, unlike glycerol which has a maxima at 1M in 1M KOH, suggesting

OH^- oxidation of β-$Ni(OH)_2$ is a rate limiting step. However, the Ni phase GEOR sensitivities to changes in OH^- concentration varies depending on the accompanying metal. As a baseline for comparison, Ni/C (figure 5.7 A) presents an increase in peak GEOR current density from 86 $mA.cm^{-2}$ in 1M KOH to 97 $mA.cm^{-2}$ (+12.7%) in 2M KOH. Its onset potential remains constant 1.229 V for all KOH concentrations, unlike the influence of glycerol's concentration. Reducing the KOH concentration to 0.5M, the current density reduces to 52 $mA.cm^{-2}$ (-39.6%).

For $Ni_{98}Bi_2$/C (figure 5.7 B), increasing the KOH concentration to 2M KOH from 1M KOH doubled the Ni peak current density to 136 $mA.cm^{-2}$ from 68 $mA.cm^{-2}$ (+100%) and surpasses the maximum GEOR current density of Ni/C at 2M KOH. Furthermore, a reduction in KOH concentration to 0.5M detrimentally reduced the peak current density down to 13 $mA.cm^{-2}$ (-81%), a significant reduction compared to Ni/C and could even be said to be nearly deactivated. The explanation for this larger deactivation is similarly unclear but can be explained by the interference of glycerol on the oxidation of Ni as discussed in chapter 3. As for the onset potential, it reduced from 1.294V in 1M KOH to 1.258V in 2M KOH. In 0.5M KOH, the onset potential remained unchanged.

In terms of $Ni_{80}Au_{20}$/C (figure 5.7 C), an increase in OH^- concentration increased the peak current density of Ni from 70 $mA.cm^{-2}$ in 1M KOH to 107 $mA.cm^{-2}$ in 2M KOH (+52%). Reducing the concentration of OH^- to 0.5M KOH reduced the peak current density down to 42 $mA.cm^{-2}$ (-40 %). As for the Au phase GEOR, an increase in peak current and reduction in peak potential was observed at 2M KOH up to 100 $mA.cm^{-2}$ (+19%) at 1.365 V (-67 mV) in 2M KOH, compared to 84 $mA.cm^{-2}$ from 1.431 V at 1M KOH. Decreasing the concentration down to 0.5M KOH worsened the peak current density to 49 $mA.cm^{-2}$ (-42%), but the peak potential remained unchanged. As for the reactivation peaks, there is an increase in current density and reduction in potential as the concentration of OH^- increases from 34 $mA.cm^{-2}$ (-32%) at 1.258 V (+21 mV) at 0.5M KOH, to 56 $mA.cm^{-2}$ at 1.236 V in 1M KOH and 72 $mA.cm^{-2}$ (+29%) at 1.212 (-25 mV) in 2M KOH. These results demonstrate an increase in KOH improves Ni phase GEOR reactivity over $Ni_{80}Au_{20}$/C. However, an increase in OH^- availability inhibits the Au reactivation and promotes its deactivation.

As for $Ni_{80}Pd_{20}$/C, a similar behaviour is observed. It's Ni oxidation reaction achieved a peak current of 117 $mA.cm^{-2}$ (+40%) in 2M KOH and 48 $mA.cm^{-2}$ (-38%) in 0.5M KOH compared

to 77 mA.cm^{-2} in 1M KOH. The onset potential for Ni phase GEOR marginally increases as the KOH concentration increases from 1.112 V (0.5 M KOH and 1M KOH) to 1.137 mV (2M KOH). A similar trend is observed for Pd phase GEOR from 5 mA.cm^{-2} (-23%) in 0.5M KOH, to 6.5 mA.cm^{-2} 1M KOH and 7.9 mA.cm^{-2} (+22%) 2M KOH. Interestingly, the onset potential for Pd GEOR fluctuated and appeared to have a maximum at 477 mV in 1M KOH as opposed to 0.5M KOH and 2M KOH at 578 mV and 654 mV, respectively. As for the oxidation and reactivation peak potentials of Pd, they remain unchanged at around 850 mV and 668 mV, respectively.

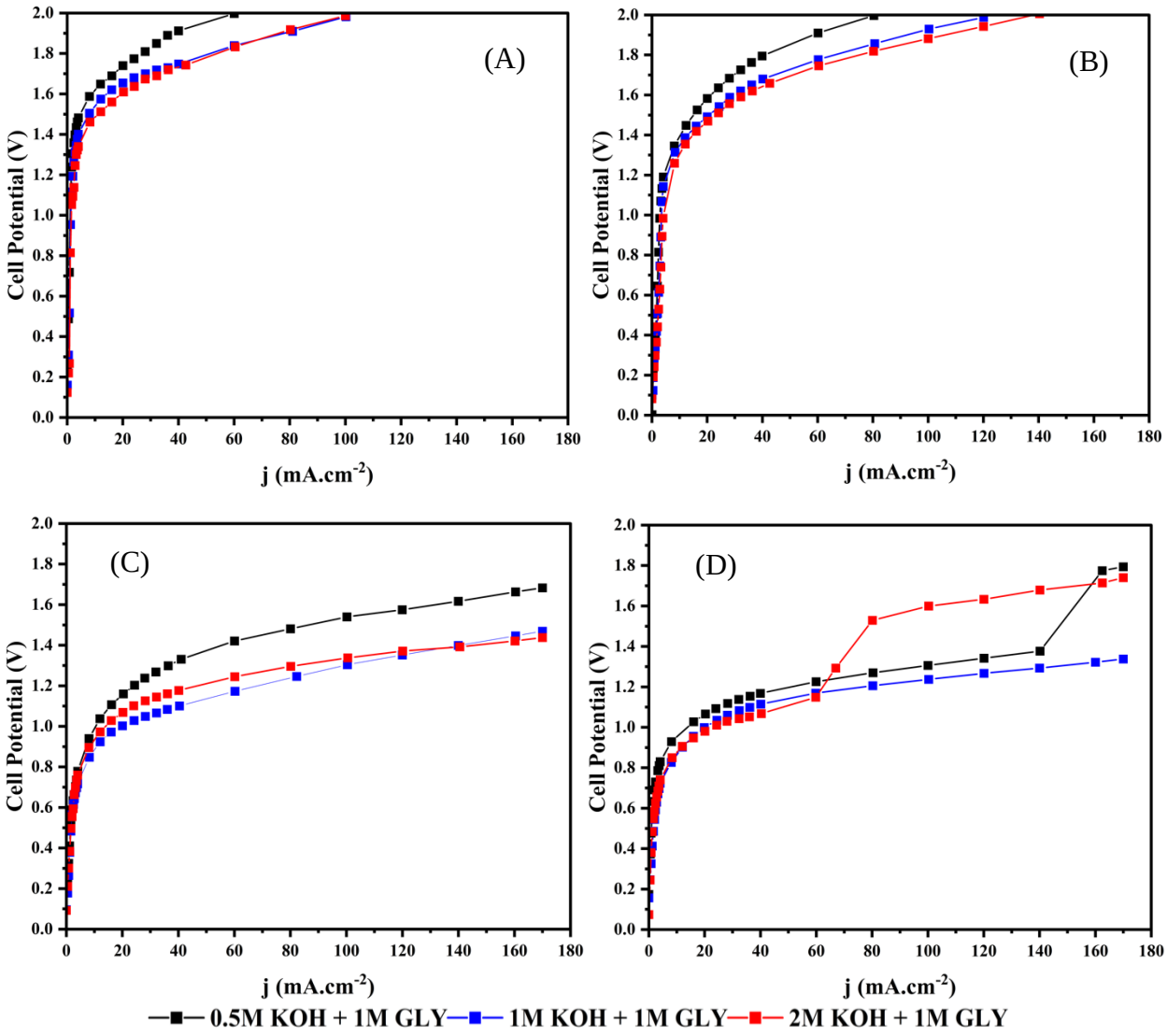

Figure 5.8) Polarization curves of a 2 mg.cm^{-2} $Ni_{80}Pd_{20}$/C cathode electrolyser with 1 mg.cm^{-2} (A) Ni/C; (B) $Ni_{98}Bi_2$/C; (C) $Ni_{80}Au_{20}$/C and (D) $Ni_{80}Pd_{20}$/C anode catalyst in (Black) 0.5M; (Bleu) 1M and (Red) 2M KOH and 1M glycerol circulating solution at 80^{o}C.

Figure 5.8 presents the polarization curves each catalyst in 0.5M, 1M and 2M KOH in a 1M glycerol solution. The activation polarizations curves of Ni/C (figure 5.8 A) and $Ni_{98}Bi_2$/C (figure 5.8 B) remains unchanged while their polarization curves improve noticeably with increasing hydroxide concentration, which agrees with CV results (figure 5.7 A & B). As for the $Ni_{80}Au_{20}$/C (figure 5.8 C), no potential jumps are recorded. It's polarization curve shows an inflexion point at 120 $mA.cm^{-2}$ in terms of the cell potential where 2M KOH operates at a lower potential than 1M KOH. Furthermore, $Ni_{80}Au_{20}$/C's activation polarization ending potential decreases from 0.779V in 0.5M KOH to 0.717V in 1M KOH but increases up to 0.76V in 2M KOH. Interestingly, a widening gap in operating potential is observed between 1-2M KOH to 0.5 KOH, unlike the steady potential difference observed when changing the glycerol concentration (figure 5.6 C). This implies the role of KOH maybe more complex over Au than previously thought.

In the case of $Ni_{80}Pd_{20}$/C, the ending potential of the activation polarization decreases from 0.83 V to 0.724V from 0.5M to 1M KOH but increases up to 0.741 V in 2M KOH, similar in behaviour to $Ni_{80}Au_{20}$/C. Soon after, the first ohmic polarization curve of 2M KOH operates at a lower cell potential. Interestingly, although the potential jump recorded for 0.1M glycerol in 1M KOH occurred passed 72 $mA.cm^{-2}$, a potential jump is recorded at 140 $mA.cm^{-2}$ in 0.5M KOH. This critical current density is approximately double the current density recorded for 0.1M glycerol. The smallest critical current density measured in this study at 60 $mA.cm^{-2}$ was recorded at 2M KOH, smaller than the critical current density of 0.1M glycerol. The resulting potential jumps increase by 380 mV for 2M KOH and 400 mV for 0.5M KOH. These jumps are also like those recorded at 0.1M glycerol (figure 5.6). Unlike $Ni_{80}Au_{20}$/C, the difference in cell potential between concentrations remains unchanged within the same ohmic polarization phases.

Overall, results from this section show Ni phase GEOR has significant differences in sensitivities towards changes in pH/OH^-, depending on the accompanying bimetallic (figure 5.7) [32]. This differs from the effects of glycerol concentration from the previous section which showed Au, Pd and Bi had weaker effect on Ni phase GEOR. However, up until this point the nature of the polarization curves potential jumps is unclear but the investigation of the role of OH^- on both a 3-electrode and electrolyser result does shed some light on its nature. As discussed in the previous section, the first low potential ohmic polarization phases over $Ni_{80}Au_{20}$/C and $Ni_{80}Pd_{20}$/C are the

result of Au and Pd phase GEOR. Although CV result in figure 5.7D show $Ni_{80}Pd_{20}/C$ has the highest Pd GEOR oxidation peak at 2M KOH and 1M glycerol with an unchanged deactivation potential, it paradoxically has the earliest polarization curve potential jump between all measurements. In turn, CV results which state that an increase in KOH concentration should decrease the risk of deactivation in 1M glycerol accelerates the deactivation of the first ohmic polarization phase. In turn, there is a possibility these potential jumps aren't the result of the deactivation process observed over the CVs but another transition.

5.3.4 Durability test

CP analysis of $Ni_{80}Au_{20}/C$ and $Ni_{80}Pd_{20}/C$ was performed to extrapolate the stability of the catalysts under a current density of 100 $mA.cm^{-2}$. While 200 $mA.cm^{-2}$ would be a more relevant current density for industrial applications, due to the nature of the current density jumps recorded, it was of interest to see what would occur operating at current densities near these critical current densities while still operating at an elevated current. Ni/C and $Ni_{98}Bi_2/C$ weren't investigated due to the high cell potential (>2V) which induce side reactions to occur other than GEOR which can interfere with the measurements. For example, such high voltages did lead to the formation of bubbles from leak prone regions between the graphite plates outside the gaskets on the cell which is clearly not a part of the catalyst layer, indicating the graphite is likely a reactive phase at potentials higher than 2V and worsened the risk of leaking. The side reactivity of the graphite plates would interfere with the with the current measurements.

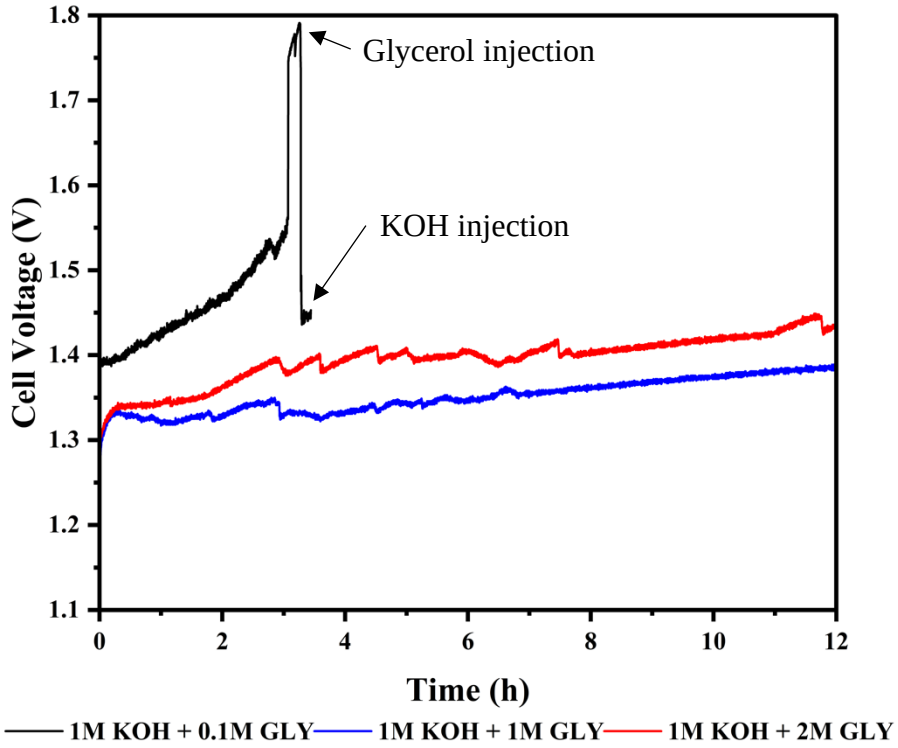

Figure 5.9) 12hour CP measurement at 100 mA.cm^{-2} of a 1 mg.cm^{-2} $Ni_{80}Au_{20}$/C anode and mg.cm^{-2} $Ni_{80}Pd_{20}$/C electrolyser in 1M KOH and 0.1M glycerol; 1M glycerol; 2M glycerol circulating solution at 80^{o}C

Figure 5.9 presents the CP performance of $Ni_{80}Au_{20}$/C under varying glycerol concentrations. At 0.1M glycerol and 1M KOH, $Ni_{80}Au_{20}$/C initially attains at 1.398V where it then rapidly increases in potential to 1.528V after 3 hours. Past 3 hours, the cell potential jumps instantly by 227 mV to 1.755 V and stabilises at potentials higher than 1.8V. To understand the nature of this increase, an injection of 10 ml of pure glycerol solution was added and immediately reduced the cell potential nearly back to the cell potential at the beginning of the CP to 1.453V. This presents significant evidence that the observed potential jump at 0.1M glycerol during CP isn't related to changes occurring to the anode but by a reduction in glycerol availability. Interestingly, it is important to highlight no bubble formation is observed in the anodic output line of the cell after the cell potential jump, implying the post jump reaction is not OER but related to another oxidation reaction where glycerol's availability is significantly diminished.

In 1M glycerol, the cell potential is initially reduced to 1.293V and converges up to 1.332 V after 12 minutes. This convergence behaviour to a steady state response demonstrates an important difference to reporting electrolyser data between an organic electrolyser cell to a

traditional water electrolysis cell, which will be explored later in the discussion. After 12 hours, the cell potential increased up to 1.387 V. This represents a cell drift rate of 4.6 $mV.h^{-1}$. An injection of glycerol after 12 hours reduced the cell potential marginally. To confirm if this rate loss is related to the catalyst, the same anode was retested after 2 weeks of continuous circulation after all tests were performed, but the polarization curve of $Ni_{80}Au_{20}/C$ did not change (figure 5.S3), suggesting a change in the electrolyte environment is responsible. This also demonstrates the catalyst stability which is often reported for GEOR catalysts which is unique compared to traditional electrolysis [3, 7, 54, 64, 70, 71]. At 2M glycerol, the cell operated at a higher cell potential with an initial potential of 1.339 V at steady state. After 12 hours, the cell potential increased up to 1.429 V, representing a drift rate of 7.5 $mV.h^{-1}$. This does align with polarization curves where 1M glycerol does outperform 2M glycerol in terms of potential.

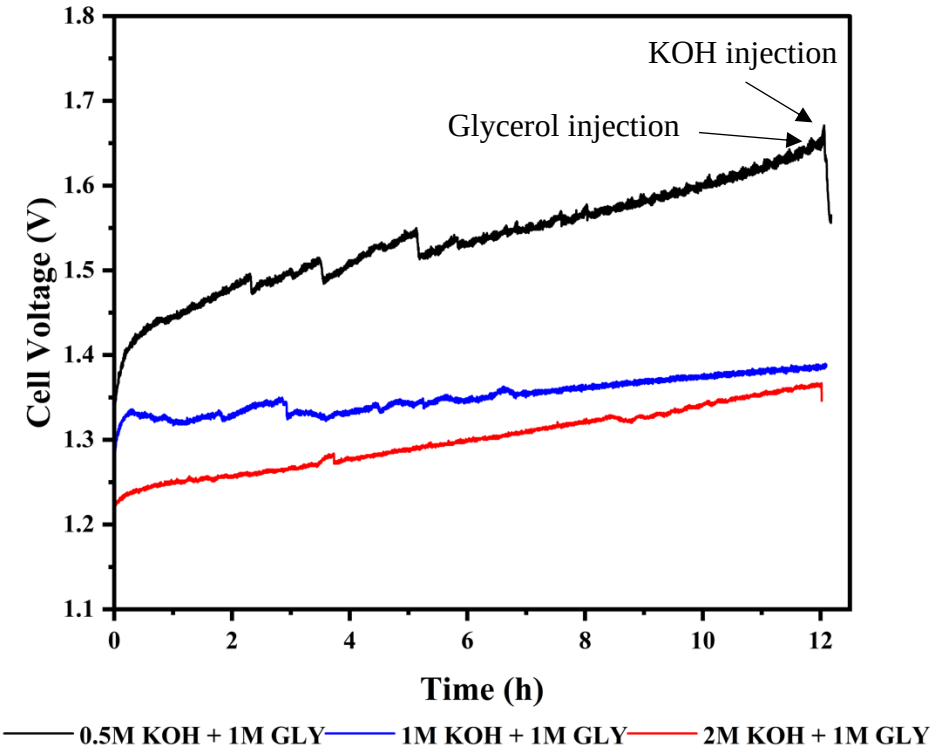

Figure 5.10) 12hour CP measurement at 100 $mA.cm^{-2}$ of a 1 $mg.cm^{-2}$ $Ni_{80}Au_{20}/C$ anode and $mg.cm^{-2}$ $Ni_{80}Pd_{20}/C$ electrolyser in 1M glycerol and 0.5M KOH; 1M KOH; 2M KOH circulating solution at 80°C

When increasing the KOH concentration to 2M KOH in 1M glycerol (figure 5.10), the drift rate of the electrolyser remains approximately similar to 1M KOH at 4.9 $mV.h^{-1}$ but at a noticeable drop in operating potential by roughly 100 mV was observed for the 12-hour test starting from

1.238 V up to 1.299V. However, 0.5M KOH presented a noticeable increase in cell potential and a larger drift rate of 17 $mV.h^{-1}$ that renders it unrecommendable at first glance. Fascinatingly, an injection of glycerol did not ameliorate the cell potential, and the rate increase appears unchanged. It should be noted that it took 1 minute for the injection of glycerol in in figure 5.9 to take effect. Injecting 10 ml of a 4 mol/L of KOH solution to the electrolytic tank drastically reduced the operating cell potential from 1.66 V to 1.56 V after a few seconds. Amazingly, this would implicate that hydroxide was steadily being depleted overtime. This will be discussed later but is a major engineering event of organic electrolysis which is seldom discussed in terms of upscaling for alkaline systems or catalyst design and testing.

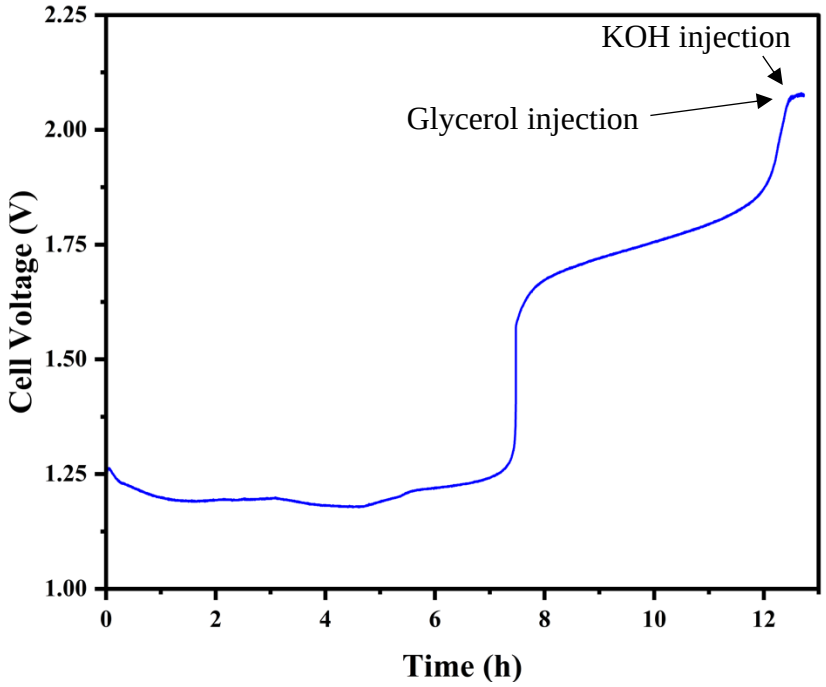

Figure 5.11) A 12hour CP measurement at 100 $mA.cm^{-2}$ of a 1 $mg.cm^{-2}$ $Ni_{80}Pd_{20}$/C anode and $mg.cm^{-2}$ $Ni_{80}Pd_{20}$/C cathode electrolyser in 1M KOH and 1M glycerol circulating solution at 80°C.

As for $Ni_{80}Pd_{20}$/C (figure 5.11), a novel behaviour is observed. Only a single anode was sprayed since this catalyst was used in each test as the cathode, issues related to time, material delivery of GDLs, equipment replacement and capital availability eventually required the writing of this thesis. Due to a novel instability related to the first test, only a single CP test was run at 1M glycerol and 1M KOH. At 100 $mA.cm^{-2}$, the cell potential initially decreased for 4.5 hours from an initial potential of 1.261 V down to 1.178 V (-83 mV). Interestingly, the cell potential increased

up to 1.255V at 7.2h. Immediately after, the cell potential jumps up to ~1.62V (similar in magnitude to the polarization curve potential jumps). From there, the cell potential rapidly increased up to ~1.85V at 11.5 hours. Past 11.5 hours another but slower jump is observed. Furthermore, an injection of glycerol did not reduce the cell potential, neither did an injection of 10 ml of 4.24 ml of KOH. After 30 minutes at OCP [72], the cell operated only at 2V and remained there (data not shown). This second CP run was cut short to avoid potential cell damage but shows a change on the anode occurred since all electrolyser experiments have shown complete reversibility after 30 minutes of OCP operation. It's only when a low reductive current (i.e. the anode becomes the cathode, and the cathode becomes the anode) is applied for 5 minutes that $Ni_{80}Pd_{20}$/C appeared to be regenerated but its performance had significantly been degraded (data not shown). Considering the first potential jump is like those recorded by Au and the polarization curves, it is likely it is not the result of a deactivation. However, the second potential jump does appear to be the result of a change in Pd oxidation state due to the requirement of a reductive environment to reactivate the Pd phase GEOR [72].

5.4. Discussion

A summary of efficacy of coupling HER and GEOR over carbon supported electrocatalysts for a membrane free electrolyser will be discussed first in order to address the original intent of this chapter. However, due to the abnormal behaviour of the potential jumps over the Au and Pd anodes, an in-depth review of the underlying mechanism will be performed later in this discussion since electrolyser testing hasn't previously been performed for Au, Pd and Ni catalysts, based on a literature review of the author.

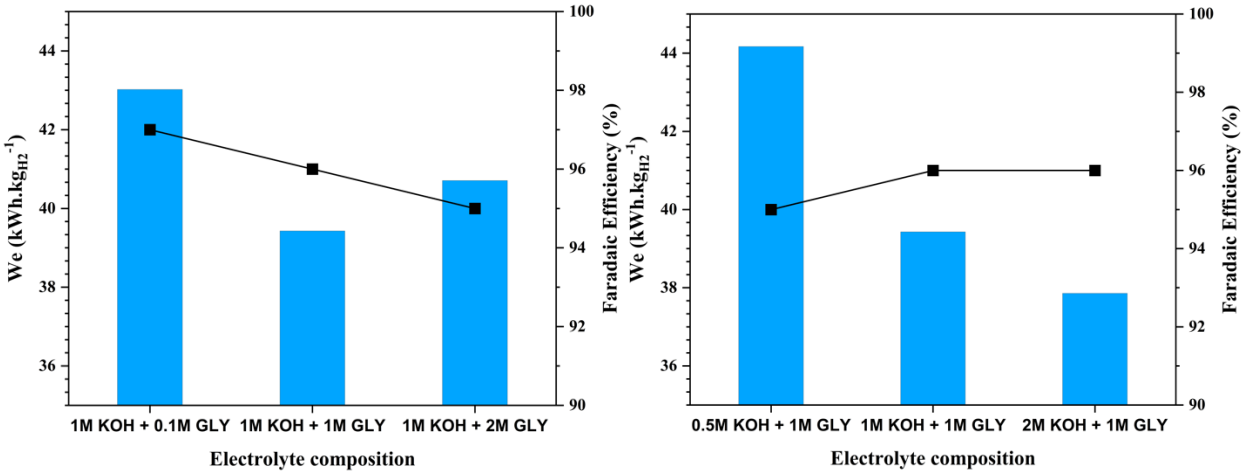

Figure 5.12) The W_e and HER faradaic efficiency of CPs at 100 mA.cm^{-2} of 1 mg.cm^{-2} $Ni_{80}Au_{20}$/C anode and 2 mg.cm^{-2} $Ni_{80}Pd_{20}$/C cathode at various glycerol and KOH concentrations flowing at 1.4 L.min^{-1} at 80°C.

Based on Figure 5.12, nearly all tests that were run had a faradaic efficiency superior to 93%, which was further improved between runs by maintaining the pipping connections in the entire system, highlighting some of the loss in faradaic efficiency can be correlated with the equipment, similar to chapter 3. While chapter 4 has discussed the competitive electro-reduction of GEOR products [48], the elevated HER faradaic efficiency in figure 5.12 shows a preferred selectivity towards HER for the duration of these tests. However, a dedicated study should be performed to investigate the impact of GEOR products on HER. Overall, the best performing cell according to figure 5.12 in term of total consumed energy was the $Ni_{80}Au_{20}$/C anode in a 1M glycerol and 2M KOH electrolyte solution at 37.9 kWh.kg$_{H2}^{-1}$ with a drifted rate of 10.6 mV.h^{-1}. The catalyst which achieved the lowest cell potential was $Ni_{80}Pd_{20}$/C at 1.178 V with a faradaic efficiency of 97%, representing 35.1 kWh.kg$_{H2}^{-1}$ during its first polarization phase while under CP (figure 5.S1).

While these results show coupling HER with GEOR over carbon supported catalyst can meet the D.O.E. target of 40 kWh. kg$_{H2}^{-1}$ [73], this was due to Au and Pd being the main or sole reactive phases during GEOR which oxidises glycerol at significantly lower potentials than Ni alone (Figure 5.6 & 5.8). In turn, empirical results from this work places into question the utility of symmetrical/asymmetrical carbon supported Ni anodes for coupling GEOR with HER. However, figures 5.1 & 5.2 did show the Ni catalysts (which were originally designed for GEOR) are not high performing for HER as opposed to Pt/C [45–47]. If these electrolysers were coupled with

Ni based HER catalysts that performs similarly to Pt/C, an opportunity to reduce the cell voltages by as much as 400 mV (figure 5.1) is feasible [45–47]. From an energetic standpoint for the lowest measured potential over $Ni_{80}Pd_{20}$/C at 1.178V, a feasible reduction in the cathode overpotential by as much as 400 mV through a dedicated HER catalyst can result in a decrease in energy consumption from 35.1 $kWh.kg_{H2}^{-1}$ to 23.2 $kWh.kg_{H2}^{-1}$. Furthermore, an operating potential no higher than 1.45 V is needed to meet the D.O.E. target as shown in the introduction of this thesis assuming a 100% faradaic efficiency towards HER. Based on figure 5.1, a Ni/C anode coupled with a Pt/C cathode achieved an ending activation polarization potential at around 1V, representing a 450 mV potential window to meet the D.O.E. target by improving the anode assuming 100% faradaic efficiency. Considering these factors, the practicality of operating a competitive Ni cathode and anode cell is feasible considering the already existing literature of high performing Ni HER catalyst [45–47].

Additionally, the utility of the membrane can be considered optional due to the elevated HER faradaic efficiency, reducing the cell's CAPEX significantly and simplifies the plant process by requiring a single electrolyte stream instead of two dedicated for HER and OER. Furthermore, the installation of a filter paper is significantly more facile and rapid with no occurrence of a failed zero gap cell assembly across multiple studies from this group, which can further reduce CAPEX in terms of assembly time and complexity [10, 12, 33]. In turn, the conclusion to the original objective of this chapter and thesis is operating a membrane free Ni electrolyser cell coupling HER and GEOR not only is feasible based on the D.O.E. target but also shows multiple opportunities for improvements and clarifications from both a scientific and engineering standpoint.

However, due to the scarcity of polarization curves in literature and investigating the failure states of GEOR electrolysers, the $Ni_{80}Pd_{20}$/C and $Ni_{80}Au_{20}$/C catalysts presented novel polarization curves for a GEOR electrolyser. That is to say, jumps in potential similar to what is reported in figures 5.8 and 5.6 were observed for GEOR and other alcohols over Pd, Au and Pt but in small 3-electrode cells [30, 32, 61]. In these works, they attribute the potential jumps to the formation of inactive noble metal oxides once a threshold potential is reached.

Lastly, while there is certainty to show the first ohmic polarization phases over $Ni_{80}Pd_{20}$/C and $Ni_{80}Au_{20}$/C (figure 5.6 & figure 5.8) are a result of Au and Pd GEOR, there is no direct explanation to what the second polarization phase is, which may be Ni phase GEOR if Pd and Au

are inactive as there is no OER evolution in the anode output line. In turn, an examination of what this second polarization phase will be done. Furthermore, the lack of Pd and Au phase electrolyser polarization curves in literature also provide an opportunity in this work to contribute to their understanding in the field of GEOR.

5.4.1 Is the second polarization phase Ni GEOR?

To evaluate the applicability of literature theory, it will first be assumed that Au and Pd are inactive as is concluded in literature [30, 32, 61]. In such a case, there are two possibilities, either OER is occurring over AuO, PdO and β-NiOOH, or Ni based GEOR is occurring. Due to the absence of gas evolution from the anode output line and the strong oxidative current applied at the anode after the jumps, this leaves Ni GEOR as the sole reactive process sustaining the second ohmic polarization phases. However, this conclusion does present important contradictions and doubts.

Firstly, the inactivation of AuO and PdO means only Ni is the active phase for GEOR. Due to the galvanostatic operation of the cell, the active Ni phase must sustain 72 and 160 $mA.cm^{-2}$ once Pd and Au are inactive, respectively. Based on Figure 5.6 & 5.8, Ni in $Ni_{80}Pd_{20}/C$ and $Ni_{80}Au_{20}/C$ must be capable of sustaining these currents at around 300 mV less at the very least than the Ni phases GEOR over Ni/C and $Ni_{98}Bi_2/C$. While synergistic effects are reported from Pd and Au to Ni which may improve the GEOR reactivity of Ni and reduce its overpotential (figures 5.7, 5.3-5.5) [11, 33], the magnitude difference in overpotential and reactivity between the Ni phase GEOR CVs (figure 5.5-5.6) over all the catalyst libraries isn't to the same order of magnitude. For example, the largest difference in onset potential seen over the CVs is 100 mV between $Ni_{80}Pd_{20}/C$ and Ni/C in 1M glycerol and 1M KOH (figure 5.6A). While an increase in temperature can reduce the GEOR overpotential as seen in chapter 3, in addition to the improved diffusion/replenishment of glycerol and removal of products, it does so similarly for each phase [56]. The differences in onset potential between Ni/C and $Ni_{98}Bi_2/C$ are similar on the CVs (figure 5.4-5.5) as $Ni_{80}Pd_{20}/C$ and $Ni_{80}Au_{20}/C$ to Ni/C, but this difference isn't materialised significantly on the polarization curves (figure 5.7 & 5.8). In turn, there is a degree of ambiguity and doubt to state the second GEOR polarization phase is solely sustained by Ni GEOR.

Secondly, a major quandary is the voltage where the potential jumps occur. As reported in literature over 3-electrode RDE cells, these jumps are a result of the oxidation of Au and Pd to AuO and PdO that is inactive for glycerol oxidation [32, 61, 64]. This conclusion was rationalised in

these works due to the voltage where the jumps occurred were the same for any condition [32, 61, 64]. In other words, due to the consistency in the potential where the jump occurred, there must be a potential dependent reaction which must be the oxidation of Au and Pd. In turn, the potential where the jump occurs in figure 5.6 & 5.8 should be a transition from Pd and Au GEOR active potentials to Ni GEOR active potentials. While the previous paragraph presented ambiguity to Ni being the main active phase due to how low potential is for Ni to be sustaining such reactivity, the inactivation potentials of Pd and Au in figure 5.6 & 8 are also inconsistent with this narrative. Based on White et al. 2022 temperature and concentration study of PdNi, regardless of changes occurring in CVs deactivation potential, the potential whereby the jump occurs in an RDE polarization curve remains the same [61]. However, this effect is not observed for $Ni_{80}Pd_{20}$/C in figure 5.6D where the 1-2M glycerol polarization curves are able to operate at potentials past the potential jump observed at 0.1M glycerol in 1M KOH. By extension, the same can be said between each tested KOH concentration in figure 5.8D. In addition, the same is also said of $Ni_{80}Au_{20}$/C where no potential jumps are observed in 0.5M KOH (figure 5.8C) even though its polarization phase operates at potentials higher than the potential jump observed at 0.1M glycerol and 1M KOH (figure 5.6C) . In turn, there is empirical ambiguity in stating these jumps are a consequence of the deactivation of Au and Pd through the formation of oxide since jumps are not observed at or past voltages where it should occur based on the rational of previous publications [32, 61, 64].

Thirdly, the potential jump from AuO or PdO to Ni active potentials are also inconsistent since the potential for Au and Pd to oxidise differ and should produce different values in potential jumps as reported by Habibi et al. 2012 [32, 61, 64]. While increasing the temperature can drastically shift the deactivation potential, the 330-360 mV similar jump between both catalysts in figure 5.6 raises the question if Au or Pd deactivation is also the cause [32, 61, 64].

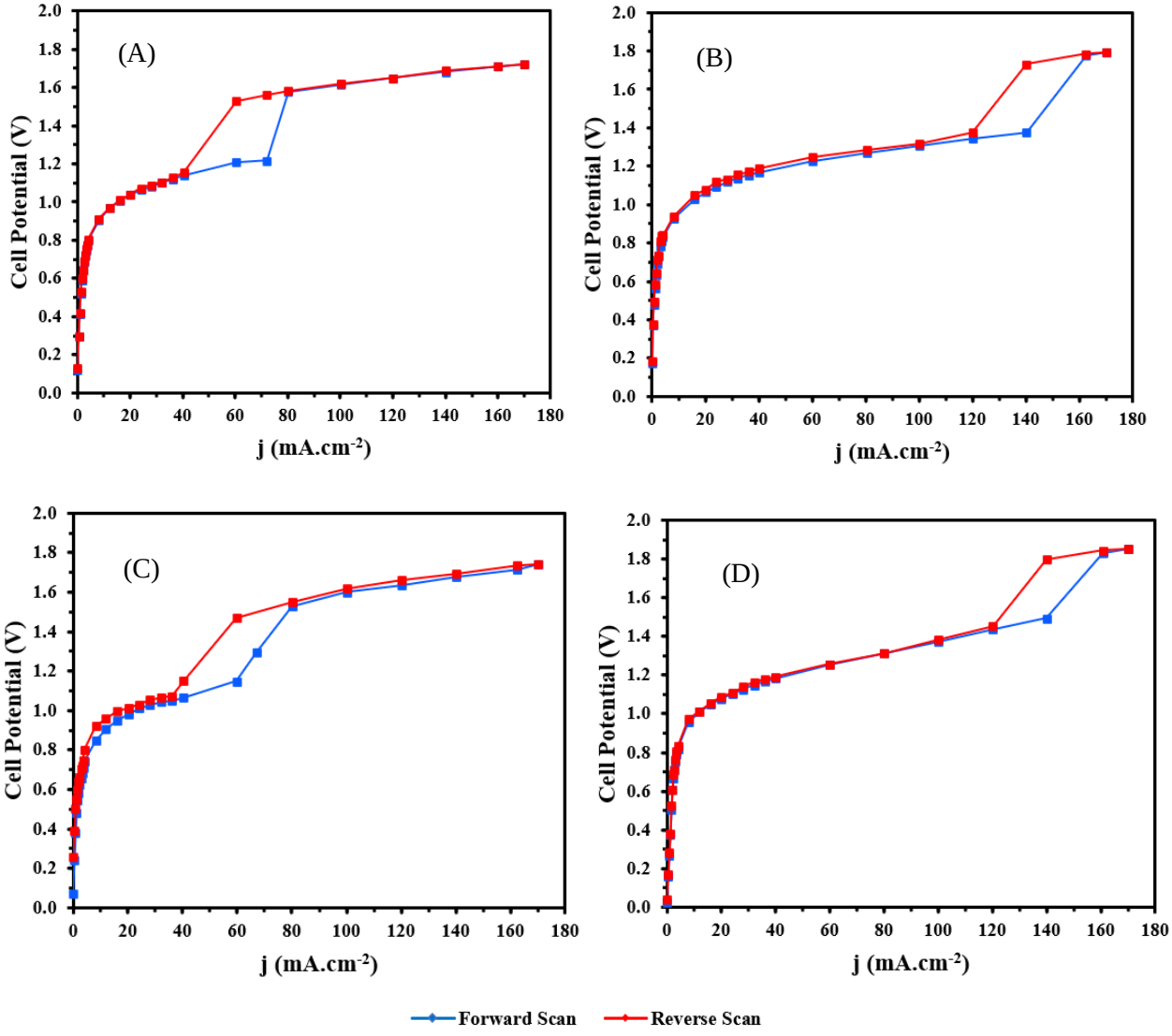

Figure 5.13) Forward and reverse CP scans of $Ni_{80}Pd_{20}$/C in (A) 1M KOH + 0.1M glycerol,(B) 0.5M KOH + 1M glycerol,(C) 2M KOH + 0.1M glycerol and $Ni_{80}Au_{20}$/C in (D) 1M KOH + 0.1M glycerol. All tests were conducted at 80°C and reverse scans were conducted immediately after the completion of the forward scan.

Lastly, if the potential jump was the result of a potential dependent electrochemical oxidation reaction of Pd/Au to their oxides, it should be noted the behaviour of the polarization curves when reducing the current (figure 5.14). Although the potential jumps weren't expected, it was of interest at the time of observing them to record what occurs when decreasing the current once the polarization curve was complete (figure 5.14). As can be seen in figure 5.14 A over Ni, the cell potential remains initially within the second ohmic polarization phase until past 120 $mA.cm^{-2}$ where the cell voltage returns to the first ohmic polarization phase by a similar 330 mV

potential drop. Increasing the current again immediately after reaching the OCP at 0A produced the same polarization curve as the previous positive going scan, meaning the bulk electrolyte composition was negligibly altered and these potential jumps do not produce irreversible changes on the anode. The latter is significant since it further challenges that the first jump was caused by the formation of oxides since its reactivation can only be achieved by inducing reduction based on literature [32, 61, 64]. This contradiction originates from CVs which show the reactivation occurs at a potential lower than its deactivation (figure 5.5 & 5.7), which differs from the polarization curves reverse scans (figure 5.14). If oxide formation is the cause, a lower reduction potential relative to the oxidation potential in the CVs (figure 5.5 & 5.7) should be expected since Au/PdO formation is only reversible via a potential dependent electrochemical reduction process as seen in figure 5.15 and equations 5.7-5.12 [3]. In turn, one should expect a polarization curve (galvanostatic control) similar to scheme figure 5.15, where the potential drop occurs at a potential lower than where the potential jump occurred. However, figures 5.14 shows the opposite behaviour where the potential drop occurs at a potential higher than the jump. The implication of this would be the reactivation occurs at a potential higher than its own deactivation which isn't possible thermodynamically if oxide formation is the cause of the jump [74]. In turn, it is difficult and arguably contrary to state that this return to the first ohmic polarization phase was the result of an electrochemical reduction of oxides due to the improbable higher reduction potential from its own oxidation and the presence of a still highly oxidative current in the electrolyser. As a consequence, there is a compilation of evidence that challenges the argument that these potential GEOR jumps under polarization curves in an electrolyser are related to the deactivation of Au and Pd. Because of this, there is ambiguity and doubt to claim the second ohmic polarization phase is solely sustained by Ni GEOR since Au and Pd may not be deactivated via inert oxide formation.

$E_{applied} >= E_{Au/Pd\ ox\ +1}$

(equation 5.7) $Au + OH^- \rightarrow Au^{+1}\text{-}OH^* + e^-$

(equation 5.8) $Pd + OH^- \rightarrow Pd^{+1}\text{-}OH^* + e^-$

(Potential dependence due to electron transfer and non-spontaneity)

$E_{applied} >= E_{Au/Pd\ ox\ +2}$

(equation 5.9) $Au^{+1}\text{-}OH^* + OH^- \rightarrow Au^{+2}{=}O^* + H_2O + e^-$

(equation 5.10) $Pd^{+1}\text{-}OH^* + OH^- \rightarrow Pd^{+2}{=}O^* + H_2O + e^-$

(AuO and PdO are inactive for GEOR, no oxidation proceeds)

$$E_{applied} =< E_{Au/Pd\ red\ +2} < E_{Au/Pd\ ox\ +2}$$

(equation 5.11) $Au^{+2}=O^{*}+ H_2O + e^- \rightarrow Au^{+1}\text{-}OH^{*}+ OH^-$

(equation 5.12) $Pd^{+2}=O^{*} + H_2O + e^- \rightarrow Pd^{+1}\text{-}OH^{*} + OH^-$

(Au and Pd regeneration only possible via potential dependent electrochemical reduction)

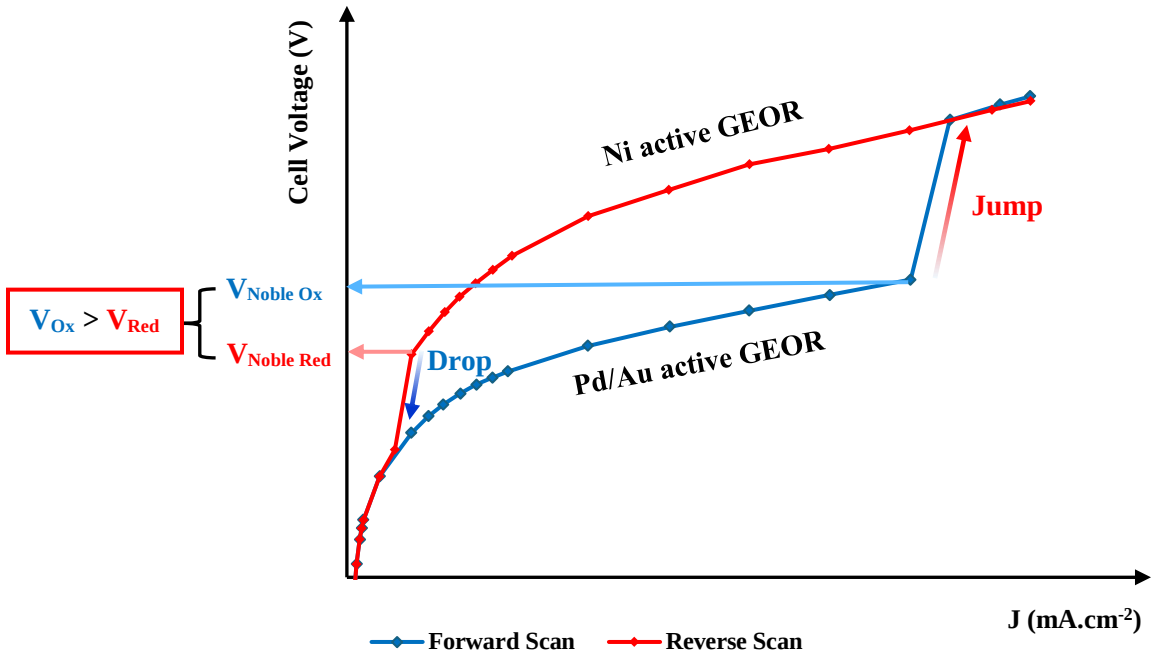

Figure 5.14) A theoretical expectation of a $Ni_{80}Au_{20}$/C and $Ni_{80}Pd_{20}$/C GEOR CP polarization curve if Pd/Au deactivation is caused from its potential dependent oxidation and its reduction is only possible by potential reduction.

While there is ambiguity in the nature of the jump in potential, what is certain is the occurrence of these jumps are a function of the concentration of glycerol, OH^- and on the material. It should also be said the composition may also be a factor, but this is beyond the scope of this work since it is not a parameter which is investigated here. To elucidate the nature of these jumps, an investigative review of literature as to the proposed Au and Pd deactivation mechanisms and if they corroborate with what is observed here will be performed. This description will also provide further evidence to if Ni is responsible for the second polarization phase.

5.4.2 $Ni_{80}Au_{20}$/C's potential jumps

To elucidate the nature of these jumps, Au over $Ni_{80}Au_{20}$/C will first be investigated. Based on literature, GEOR's potential jumps on noble metals are associated with the deactivation of the

active phase in question [61, 71, 75, 76]. Direct evidence was performed by Martinez et al. 2021 whereby ATR-SEIRAS measurements in a three-electrode cell recorded AuO formation coincided with the deactivation of the catalyst [77]. AuO and PdO formations are similar, whereby an adsorbed OH^* is oxidised to O^* by a nearby OH^- to the surface [3, 32, 66, 78–80]. Due to the non-spontaneity of the required transfer of an electron from OH^* to the electrode, a potential is needed for the oxidation to proceed [3, 32, 66, 77–80]. In addition, the oxidation of Au to AuO requires a critical OH^* coverage and a sufficiently elevated potential since it is a potential dependent oxidation reaction [77]. In turn, Au GEOR requires a higher potential to oxidise Au to AuO since adsorbed glycerate and its oxidation intermediates perpetually reduces nearby OH^*, affecting the coverage of OH^*. This theoretical higher required potential is reflected between figure 5.4C to 5.5C where the deactivation potential displaces to higher potential due to the higher glycerate adsorption from an increase in glycerol concentration. In addition, Figure 5.7C demonstrates how an increase in KOH concentration decreases the deactivation potential due to a higher OH^* coverage at lower potentials [3, 32, 66, 77, 78].

However, Martinez et al. 2021 showed evidence to unknown carboxylate products from GEOR on the surface which blocks or has a rate determining step in GEOR, effectively favouring OH_{ads} oxidation to oxide in a relative sense [30, 53, 77]. In turn, the deactivation of Au oxide requires both a favourable coverage of OH_{ads} and relatively rate limited GEOR process. However, this proposes a competitive adsorption equilibrium between these carboxylate products and glycerol exists which is an indirect factor to the deactivation potential. These blocking intermediates have not been identified in literature but frequently reported to be present when deactivation occurs [22, 30, 55, 60, 61, 64, 67, 69, 81]. This proposition of an existing competitive adsorption equilibrium over Au and Pd (i.e. dependent on concentration and temperature) [3, 7, 22, 27, 59, 82] aligns with a key observation during the CP of $Ni_{80}Au_{20}$/C in figure 5.9 in 0.1M glycerol and 1M KOH. The jump in potential did not perform OER due to the absence of gas evolution and the injection of glycerol returned the potential to a pre-jump potential window. This implies: i) the cell was capable of performing an electrochemical oxidation reaction which utilised an organic substrate after the jump; ii) the injection of glycerol immediately returning the cell potential back to its previous ohmic polarization phase (i.e. reaction mechanism) without a reductive current. The latter statement is significant since the reversibility of the potential jump in figure 5.9 in 0.1M glycerol and 1M KOH over $Ni_{80}Au_{20}$/C is a function of glycerol availability, not potential. In turn, this

concludes that Au did not oxidise to AuO at or after the jump during its CP. This is a critical disagreement to literature since if it is supposed AuO is formed after the CP jump because intermediates are blocking any further oxidation, how does the injection of glycerol reduce AuO back to Au (figure 5.9)? Based on literature, it is hypothesised the reactivation of Au is similar to Pd where AuO is electrochemically reduces back to AuOH as a function of potential, and it oxidises neighboring adsorbed glycerate, hence producing the expected anodic current during the reverse scan [3, 77, 80]. However, Martinez et al. 2021 showed AuO is inactive for GEOR within their potential window [3, 7, 74]. As a consequence, it isn't clear how glycerol could electrochemical reduce inert AuO in the CP of figure 5.9 in 0.1M glycerol [3, 7, 77]. Thus, results from figure 5.9 CP at 0.1M glycerol indicates AuO can't be the cause or consequence of the jump. It should be noted that no other work to our knowledge injected glycerol in a spent electrolyte enriched with GEOR products. Therefore, the observations seen here are novel. Furthermore, the CP results of $Ni_{80}Au_{20}$/C in 0.5M KOH and 1M glycerol (figure 5.10) shows a steep increase potential overtime and operating at the second ohmic polarization phase potentials without a potential jump. This further implies that a critical potential isn't necessarily a dictating factor on weather jumps occur and that there exists a correlation between reactant availability, further questioning the potential dependent AuO formation is responsible for the jumps [66, 83].

Instead, the higher critical current drop potential to the jump potential in the polarization curves, CP jumps seen in 0.1M glycerol and 1M KOH for $Ni_{80}Au_{20}$/C in oxidative conditions, with the lack of jumps in high voltage operations in 0.5M KOH and 1M glycerol aligns with the argument that a competing adsorption between glycerate and an unknown intermediate are responsible. This proposes the second polarization curve is instead a shift to a second organic oxidation reaction where Au isn't inactivated to AuO. However, this proposition is a new one in literature. In turn, is there evidence to this statement? A key literature result of Martinez et al. 2021 is spent glycerol electrolytes can trigger a sooner potential jump [77]. Upon using a fresh electrolyte, the potential jump is delayed significantly [77]. This, combined with the CP results of figure 5.9, polarization curve hysteresis in figure 5.6C at 0.1M glycerol, point to there being a glycerate-intermediate equilibrium which is responsible for the jumps to occur. Then how do potential jumps occur during the polarization curves if it is a function of glycerate and intermediate concentration?

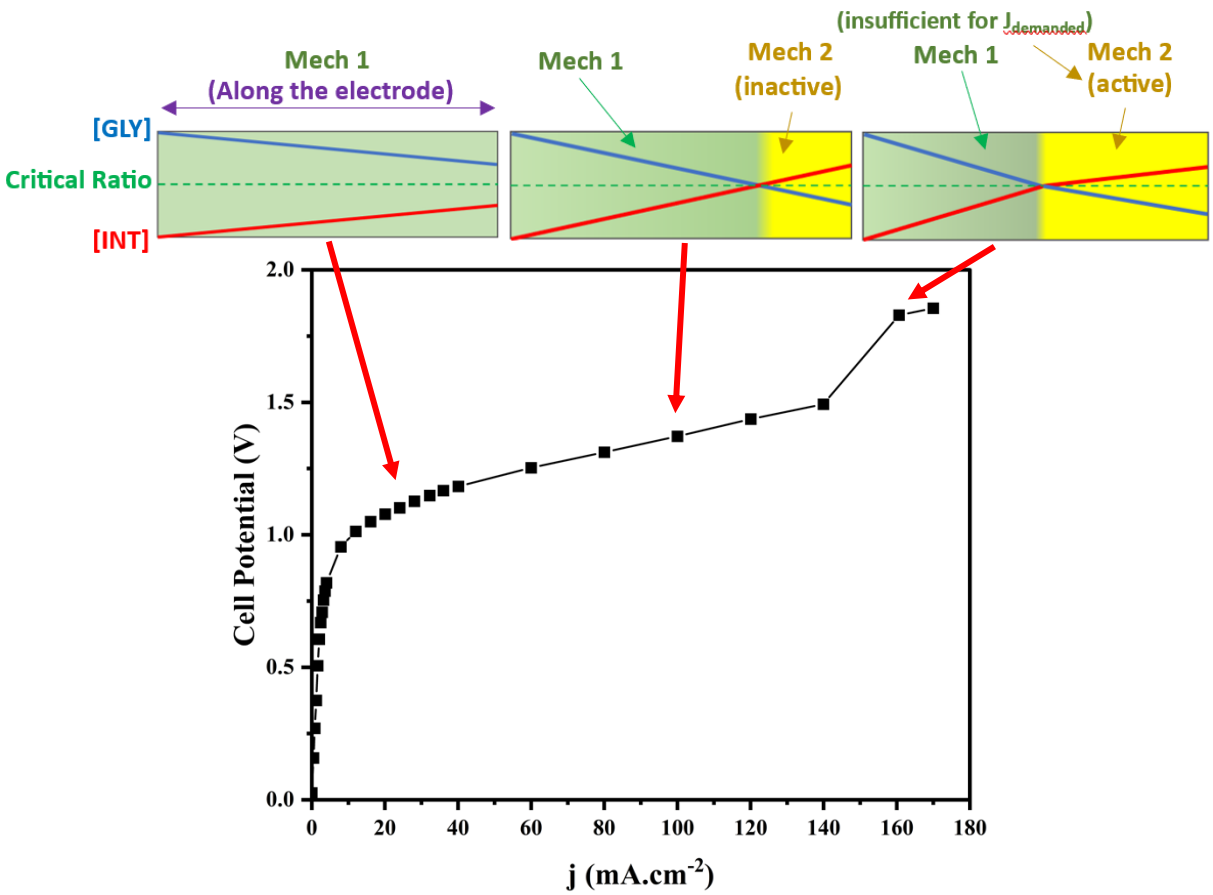

Scheme 5.1) Illustration of the change in glycerol and intermediate/products along the electrolyser cell for a given current. The green shaded area represents a glycerol covered surface area responsible for the low ohmic polarization phase reaction and the yellow represents the area where a different surface coverage is present and requires a higher potential to initiate. Mech 1 & 2 represent Mechanism 1 and 2.

Based on the notion of an adsorption equilibrium between competing organic adsorbates, a possibility is the reversible potential jumps recorded are a consequence of a change in electrolyte composition between competing adsorbates along the anode surface as a function of current [77]. This is illustrated in Scheme 5.1 with the following. If a competitive adsorption equilibrium between different organic adsorbates is present which is supported by the CP results at 0.1M glycerol in this work and Martinez et al. 2021 [77, 84–89], then as the electrolyte passes through the cell for a given low current within the first ohmic polarization phase, the concentration of glycerate is sufficiently elevated across the electrode surface compared to its products/intermediates. In turn, glycerate based reactions are dominant since glycerate is favourably adsorbed and can sustain the demanded current (Scheme 1, phase1). As the current nears the critical current density, glycerate's concentration further decreases along the cell while its competitive products concentration

increases where certain sites near the output have favourable intermediate covered surfaces, being in a state of inactivity since they require a higher potential for a deeper oxidation rate (Scheme 1, phase 2). This notion of deeper oxidation requiring a higher potential for noble metals is a repeated observation in literature [3, 28, 68, 80, 90, 91]. As the current slightly passes the critical current density, the concentration of glycerate is sufficiently decreased relative to the competitive intermediates/products concentration that there is an insufficient number of active sites where glycerate oxidation can take place to sustain the demanded current past the critical current density. In turn, the cell jumps to a sufficient potential where intermediate covered sites can induce a deeper oxidation and cover the remaining demanded current (Scheme 1, phase 3). Hence, this produces a new ohmic polarization which is a consequence of inactive intermediates, since their adsorption is independent of potential and is primarily dependent on temperature and concentration [3, 7, 22, 27, 59, 82].

To the author's knowledge, only Martinez et al. 2021 has investigated the impact of intermediates on GEOR unintentionally by not replacing the electrolyte [77, 84–89, 92–94]. In addition, to the authors knowledge, no papers have performed a competitive GEOR study between glycerol and its products. In turn, it is theorized the difference between the second and first ohmic polarization phases are a change in reaction selectivity towards a deeper oxidation of glycerate products. The lower critical current density for the drop potential vs the potential jump is likely a result of a hysteresis originating from adsorption intermediates. This has been shown to be the case with adsorbed CO_{ads} by Carvalho et al. 2023 where CO_{ads} reduced the favourability of glycerol and OH^- adsorption [95]. To our knowledge only Zalineeva et al. 2014 performed FTIR measurements at both forwards and reverse scans and identified carboxylates and intermediates which remain on the catalyst surface in between the deactivation and reactivation peaks during the reverse scan [96]. This reduced favourability can present a hysteresis, and require a higher glycerate:intermediate molar ratio for the return to the first ohmic polarization phase as opposed the glycerate:intermediate molar ratio that caused the positive jump in potential. Furthermore, chapter 4, Pham et al. 2023 [38], Melle et al. 2021 [64], Hiltrop et al. 2018 [97] and Wu et al. 2022 [98] demonstrated the cation can displace the selectivity and has a major role on the adsorption/desorption mechanism of glycerol and it's adsorbates, which is not modelled in simulations in this field to the authors knowledge [99]. However, if organic adsorption isn't potential dependent [7], then why did the unknown adsorbates from Zalineeva et al. 2014 remained

on the surface during the reverse scan where reactivity is decreased significantly [96]? This raises the question if certain intermediates have a potential dependent adsorption and is beyond the scope of this work.

From an engineering perspective, this provides a pathway to avoid (or delay) potential jumps over Au by increasing the concentration of glycerate. It is mentioned the word delayed since eventually the anode will be found in a situation where glycerate will be outcompeted by its intermediates either along the large cell if it is a continuous operation as the current increases or overtime if it is a batch system (figure 5.9).

However, this does pose the question as to why this is not observable over a small electrode cell CVs or polarization curves from previous works [3, 32, 66, 78–80]? As mentioned above, this effect becomes more pronounced as the electrolyte travels along the electrode and glycerate is consumed. In turn, the electrolyte has a larger area to travel from the input to output on a 25 cm^2 anode as opposed from the center to perimeter of a circular 0.196 cm^2 rotating or static W.E.. Thus, the effect of changing electrolyte composition maybe more relevant within a single pass of the electrolyte in a larger cell than it is in a small cell in a batch electrolyte solution. However, several experimental ideas can originate from this by combining small and large cell tests. For example, collecting the output line electrolyte solution of the electrolyser and running a CVs or CAs of that sample in a three-electrode cell and observing any differences if this theory holds true. Furthermore, there is evidence in this work that points to the risk of catalyst underutilization along the cell if this theory holds true, which was shown by Lind et al. 2023 [100] by changing the catalyst layer thickness and chapter 3 on $Ni_{90}Bi_{10}$.

Furthermore, important differences between performing a swept potential scan and a stepped potential/current scan (i.e. the polarization curves from this thesis) are also important to note if intermediates and glycerol/glycerate play a critical role since stepped scans can permit steady state to be achieved for an applied condition as discussed in chapter 3.

It should be noted that stating AuO being inactive isn't accurate of a statement either since a critical analysis of previous FTIR results from other works of Au based catalysts past their deactivation peak shows CO_2 being produced regardless [12, 59]. This appears counterintuitive in concluding AuO is responsible for GEOR deactivation. This will be discussed later in this chapter.

5.4.3 $Ni_{80}Pd_{20}$/C's potential jumps

Due to the similar reversible hysteresis of all $Ni_{80}Pd_{20}$/C polarization curves (figure 5.6D & 5.8D), the same conclusion for the jumps in $Ni_{80}Au_{20}$/C is applicable for all $Ni_{80}Pd_{20}$/C potential jumps where a competitive adsorption between glycerol and key blocking intermediates, instead of PdO deactivation, is responsible. However, there are important differences between the two catalysts. The biggest difference is the potential jumps recorded when reducing and increasing the KOH concentration from 1M KOH and 1M glycerol solution (figure 5.8D). This difference demonstrates noble metals do not necessarily share similar sensitivities towards key operating factors even though their oxide deactivation/reactivation mechanisms in literature are similar [3, 77, 80].

However, certain key theoretical inconsistencies between CVs and polarization curves are important to highlight. Unlike the CV results which show that an increase in KOH increases Pd GEOR reactivity and the deactivation/reactivation potentials remain unchanged (figure 5.7D), Pd under the polarization curve transitions to the second ohmic polarization phase sooner with increasing KOH concentration (figure 5.8D). Firstly, this demonstrates the role of KOH and the sensitivity of Pd to it differs significant to Au even though their deactivation mechanism is similar. Secondly, it also highlights KOH has a distinctive important role in the glycerol/intermediate factor leading to the second ohmic polarization phase. However, there is an insufficient collection of evidence to elucidate this relationship.

Understanding this relationship is limited in part by the absence of a complete CP investigation (figure 5.12). However, the sole CP of $Ni_{80}Pd_{20}$/C in 1M glycerol and 1M KOH does present significant additional information. Unlike any $Ni_{80}Au_{20}$/C CP result, a second potential jump occurring at ~1.8V increased the cell potential up to 2V and sharply flattened from there, indicating another reaction had taken over to respect the demanded current at 2V. Due to the lack of any gas evolution in the output line, the 2V reaction isn't OER but an organic oxidation reaction.

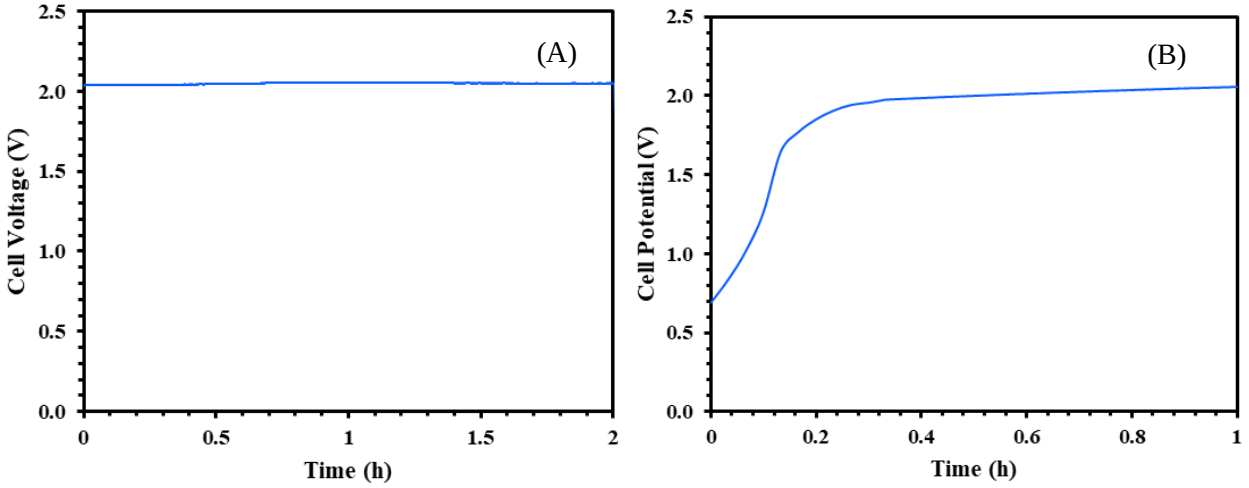

Figure 5.15) A) 100 mA.cm^{-2} CP of $Ni_{80}Pd_{20}$/C at 80°C after 24hs OCP with continuous circulating new 0.1M glycerol and 1M KOH electrolyte solution from the first CP measurement (figure 5.12). B) 100 mA.cm^{-2} CP of $Ni_{80}Pd_{20}$/C at 80°C after 5 min of a small reductive current applied to anode and 24hs OCP in a 0.1M glycerol and 1M KOH solution.

After leaving the $Ni_{80}Pd_{20}$/C cell at OCP for 24 hours with a fresh electrolyte after the CP test, the potential remained at 2V at 100 mA.cm^{-2} (figure 5.16 A). Usually, the cell regenerates in less than 5 minutes at OCP. By applying a small reductive current on the anode for 5 minutes (i.e. the anode became temporarily the cathode), the catalyst returned some of its previous behaviour (figure 5.12) when redoing a CP with a fresh electrolyte (figure 5.16 B) but was noticeably altered and a sooner degradation up to 2V [70, 72]. This indicates the sum in potential jumps up to 2V induced changes to the anode material itself. Based on the requirement for a reductive current to reactivate the catalyst, this is important evidence to Pd being deactivated to PdO since the reduction of PdO can only occur under reductive conditions [80]. Furthermore, the +2V operation under 100 mA.cm^{-2} is similar to the Ni based GEOR potential window (figure 5.6 A/B & 5.8 A/B), further supporting Pd is deactivated. In addition, the reversibility of $Ni_{80}Pd_{20}$/C second ohmic polarization phase and the irreversibility of the 2V CP operation validates Pd is not oxidised to PdO in the second ohmic polarization phase (figure 5.6D & 5.8D). Lastly, the 2V potential window (figure 5.12) is far higher than the potential window of the second ohmic polarization phase under the polarization curve (figure 5.6D & 8D). In turn, the cell operating at 2V during the CP and the second ohmic polarization phase potential window are exercising distinct oxidation reactions where Pd is and isn't deactivated, respectively. Due to the too low voltage for Ni to solely sustain the demanded current in the second ohmic polarization phase of the polarization curves (figure 5.6D & 5.8D), this leaves Pd as the primary remaining reactive phase possible. Similar to

$Ni_{80}Au_{20}$/C, Ni can operate GEOR within the second ohmic polarization phase potential window but can't sustain it entirely.

That said, the second potential jump under CP condition at ~1.8V (figure 5.12) is less of a jump and more of a lethargic transition to a quicker drift rate since it lasts for 46 minutes upon closer inspection and operates under a sharp and stable drift rate of ≈162 $mV.s^{-1}$. This is noticeably different from the instantaneous first jump in the same CP and $Ni_{80}Au_{20}$/C CP under 0.1M glycerol. In turn, it is possible to state that there exist 4 separate distinct polarization phases in this CP. The first from 0-7.5h (E_{cell} < 1.3V), the second from 7.5-11.7h (~1.8 > E_{cell} > ~1.6), third from 11.7-12.5 (2 > E_{cell} > ~1.8) and finally fourth from 12.5-12.7 (Ni phase GEOR at E_{cell} > 2V). That said, the lethargic transition is similar to a transition from GEOR to OER [101]. Due to the absence of OER in the output line at 2V, it is unlikely for glycerol and its reactive intermediates to be depleted.

Combining PdO is formed once this second jump or third drift rate occurs (figure 5.12), and organic oxidation still occurs, this third jump or drift rate is likely caused by or induces the oxidation of Pd to PdO. While this process is usually rapid, its dependence on potential, the competitive adsorption of glycerol/intermediates reducing OH^* (an oxide prerequisite) and the reactivity of Ni GEOR increasingly filling in the demanded current and is reactive of a phase past 1.2V can produce the lethargic behaviour.

The next question is why $Ni_{80}Pd_{20}$/C presents multiple jumps while $Ni_{80}Au_{20}$/C doesn't in 1M glycerol and 1M KOH. If it is assumed glycerol oxidation selectivity is 100% to the first intermediate (glyceraldehyde requires $2e^-.mol_{GLY}^{-1}$) or to formate (requiring $12e^-.mol_{GLY}^{-1}$) for the 12 hour CP test, only 0.560 mol and 0.093 mol of glycerol is converted, respectively. In the 2L tank, this translates to a decrease in glycerol concentration from 1M to 0.720 M and 0.953 M, respectively. In turn, the depletion of glycerol shouldn't be complete and at worst glycerol should have a final concentration of 0.72M. In turn, the depletion of glycerol can't be the cause. Instead, it is known for Pd's surface to be more susceptible to be poisoned by a wider library of organic molecule as opposed to Au [27, 32, 59, 102]. In the case of GEOR for example, CO is known to have a higher affinity to the Pd surface than Au or Ni [27, 32, 59, 102]. Because of this, Au has a higher GEOR mass activity as opposed to Pd since it is susceptible to be blocked by a narrower spectrum of possible products [59]. This only encompasses a single intermediate and can explain the presence and absence of a potential jump at 7.5h for $Ni_{80}Pd_{20}$/C and $Ni_{80}Au_{20}$/C at 1M glycerol and 1M

KOH, respectively [64, 69]. In turn, the first potential jump during $Ni_{80}Pd_{20}$/C CP test can be explained by surface Pd's higher blocking susceptibility to intermediates than Au. Furthermore, PdO is inactive for GEOR at these potentials and can't be a product of the first potential jump unless the cell potential reaches expected Ni GEOR potentials for the applied current. In turn, a summary of evidence indicates PdO is not formed after the first potential jump and an evolving electrolyte solution is the most likely explanation where a different organic oxidation mechanism has taken over in figure 5.12 between 1.6-1.8V.

5.4.4 Investigative review of Pd and Au deactivation

However, the results for either $Ni_{80}Au_{20}$/C and $Ni_{80}Pd_{20}$/C in this work proposes the mechanism of deactivation differs from the commonly proposed formation of a surface oxide layer in literature as the cause. The significant discrepancy is the presence of a second ohmic polarization phase that is reversible based on current and glycerol replenishment than on irreversible oxide formation. But how could these secondary polarization curves not be recorded in previously literature? In an attempt to identify the nature of these secondary ohmic polarization curve when first interpreting them, it was first considered the literature theory on oxide formation was the cause at first but too many practical inconsistencies were present that this often-cited conclusion could not be argued here. However, a closer inspection of the data from previous works highlights key similarities between this work which haven't been further explored but, in hindsight of the use of a larger cell, may be non-negligeable factors. In turn, the following is a critical investigative review of the proposed deactivation mechanism in literature of Pd and Au, an enumeration of similar undiscussed observations and to illustrate key inconsistencies with a focus on Pd primarily since this material is often utilized in this field unlike Au [3]. Ni will not be included here since its deactivation appears to not be of concern in terms of intermediates both in this thesis or literature but will be shown in the next section. The reason why this review is performed is because few electrolyser tests are performed in this field and the value of its interpretation for Pd and Au may have important implications for future works for these materials.

While there is a consensus that PdO formation occurs during deactivation, this is primarily backed by CV results which show that the deactivation and reactivation superimposes where PdO oxidation and reduction occurs, respectively [22, 28, 53, 55, 96, 103, 104]. Because of these superimposed potentials, it is rationalised PdO must be responsible or a consequence of the material deactivation.

However, coincidences are not synonymous with cause or consequence without an explicit investigation on this question which hasn't been done in literature to the author's knowledge. Only the work of Wang et al. 2015 and Berretti et al. 2019 on the subject of ethanol oxidation have performed XAS to confirm PdO is present at and after the moment of deactivation [105–107]. But Wang et al. 2015 is unclear as to when the XANES were measured over Pd/C (is it at the end of the CP measurement? beginning? Middle?) [107]. In turn, there is a degree irresolution towards PdO is the cause or consequence of the deactivation of alcohol oxidation.

This brings the question as to what the proposed deactivation/reactivation mechanism is and what evidence and rational indicates to PdO is responsible. Surprisingly, there is a literature debate on Pd and Au oxide is the cause or consequence to the deactivation [3, 10, 27, 32, 55, 59, 60, 70, 77, 82, 91, 107–109]. In some works, they state oxide is the cause of the deactivation since the deactivation peak and drop coincides with the formation of oxides in the absence of alcohols with CVs . In other works, they show through FTIR measurements of the catalyst surface, temperature and concentration tests that certain intermediates coincide with the deactivation peak [10, 22, 27, 55, 64, 67, 75, 109, 110]. Although these intermediates have not been identified other than CO^*, it is theories the increasing potential will favour OH^* oxidation to O^* (oxide) since the oxidation or removal of these intermediates or CO^* eventually will be rate determining [10, 22, 27, 55, 64, 67, 75, 109, 110]. In turn, oxide causes the deactivation, but it is preferred eventually compared to the slow oxidation of unknown intermediates which could be delayed if faster oxidative intermediates were adsorbed instead [55, 64, 67, 69, 104, 109, 111]. In other words, it is a consequence from the adsorption of unknow GEOR intermediates that are slower to oxidise, favouring oxide formation in a relative sense. But in both arguments, the drop in reactivity is caused by the formation of oxide since it is inactive towards GEOR or other alcohol oxidation.

In addition, there is no debate as to how the reactivation occurs, likely since the goals of Pd and Au GEOR studies is to ultimately delay the deactivation, diverting most of the interest away from understanding the reactivation mechanism. Since Pd or Au oxide is the cause for no reactivity, the reactivation must be the electrochemical reduction of PdO/AuO to active Pd/PdOH or Au/AuOH [3]. This is experimentally supported by the reactivation peak coinciding with the reduction peak of Pd or Au in the absence of alcohols on CVs. But how could the electrochemical reduction of PdO to PdOH/Pd produce an oxidative current as seen in figure 5.4, 5.5 & 5.7D? This

is rationalised that the produced PdOH/Pd at GEOR active potentials is immediately reactive for GEOR, and thus is resuming GEOR perpetually until the potential is below the onset potential [3]. In other words, the oxidative current is the net difference between the negative electrochemical reduction current of PdO to PdOH/Pd with the positive oxidative current of GEOR when Pd/PdOH is immediately formed. This rational explanation (since there is no empirical evidence supporting this), is possible.

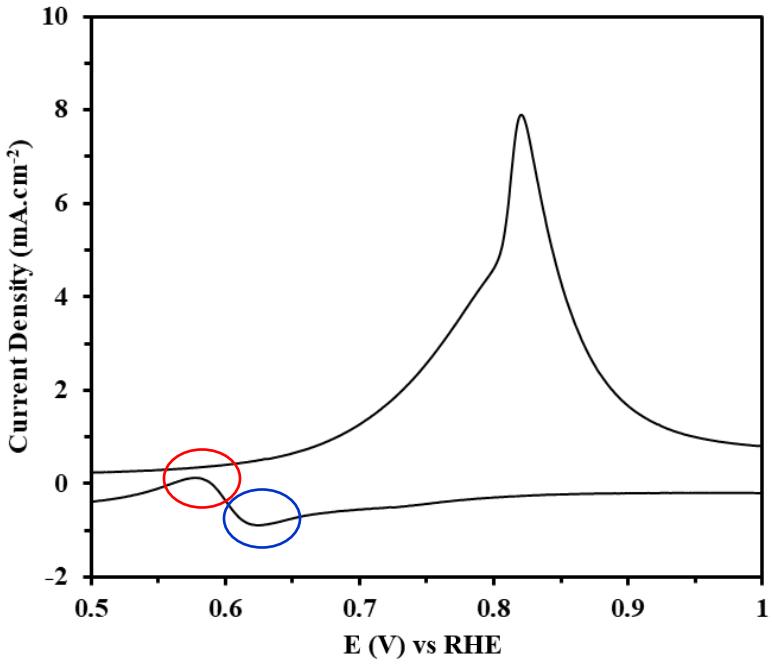

Figure 5.16) 10th cycle CV of $Ni_{80}Pd_{20}$/C in 0.1M glycerol and 1M KOH measured at a scan rate of 25 $mV.s^{-1}$ and room temperature. Bleu circle indicates a reduction peak. Red circle is the reactivation peak.

However, figure 5.16 presents a major inconsistency from this deactivation theory due to the presence of a separate reduction peak which precedes the reactivation peak over $Ni_{80}Pd_{20}$/C in 0.1M glycerol and 1M KOH [107]. Based on the available materials in the catalysts layer and the potential window of this reduction peak, there is a reduction of PdO. Based on the reactivation mechanism proposed in literature, this reduction peak should not be possible or even exist [22, 28, 53, 55, 96, 103, 104]. The question was raised, is this the only work where this phenomenon was observed or is this an experimental error?

A critical independent analysis of previous CVs in other works do show a reduction peak is observable which are enumerated here. It is important to highlight that while the discussions of

these works say one thing, their data clearly show this similar inconsistency. To demonstrate this is not human error or bias, Houache et al. 2021 who tested a similar NiPd catalyst (and from whom this catalyst originates from) without carbon support show's the exact same reduction peak in its CV in the presence of glycerol (figure 5.S4) at similar potentials but did not report or discuss it [10]. This reduction peak is also observable over other Pd based GEOR studies when independently verifying their CVs such as Yildiz et al.1994 (figure 5.S5) [108], Holade et al. 2013 (figure 5.S6) [111], Holade et al. 2014 (figure 5.S7) [91], Habibi et al. 2012 (figure 5.S8) [32] and Ivanov et al. 2022 (figure 5.S9) [112] to the author's knowledge. This also doesn't just apply to glycerol but other alcohols such as methanol by Beden et al. 1982 [113], ethanol by Vyas et al. 2023 [114] and Ipadeola et al. 2023 [115]. In turn, there is literature precedence for the reduction peak of PdO even though an alcohol is present. In each of these cases, the reduction of PdO as an independent reduction peak from the reactivation and should not be possible.

The question was then raised why this reduction peak was only observable on these works. When comparing experimental conditions between studies which showed and didn't show this reduction peak, it was found that the alcohol in question was at low concentration in each of them and this work at 0.1M (except for Vyas et al. 2023). From the same rational interpretation of the reactivation mechanism, this can be explained that a higher KOH concentration relative to the competitive alcohol adsorbate increases the relative OH^* coverage for oxide formation with fewer O^* neighboring adsorbed alcohols during their reduction, leading to a reduction peak since no alcohol is nearby to react with OH_{ads} when it is reduced. However, some of these studies also had a concentration of KOH as low as 0.1M [91]. Furthermore, the literature theory and this rational explanation is paradoxical since why is the PdO reduction peak a separate electrochemical peak from the reactivation peak in the same CV? This also importantly contradicts the reactivation mechanism in literature since it suggests PdO is reduced to Pd/PdOH and remains inactive until it becomes oxidative at the reactivation peak while the forward scan clearly shows this potential gap is GEOR active over Pd. In other words, why is Pd/PdOH formed after the electrochemical reduction of PdO not GEOR active when it should be?

Furthermore, Vyas et al. 2023 performed a EQCM of Pd during ethanol electrooxidation (EOR) and found PdO reduced prior to the reactivation, an important physical characterisation that validates this process is PdO reduction, and that reactivation is distinct from PdO reduction [114].

Fascinatingly, although Vyas et al. 2023 states in their discussion that PdO formation inhibits EOR, it's CV-EQCM measurements shows that PdO formation begins roughly 100 mV prior to the deactivation of Pd based on changes in mass, it is encouraged for the reader to observe this themselves since the author doesn't report it) [114]. In other works which compare electrolytes in the absence and presence of alcohols to show the PdO is responsible for Pd deactivation due to the oxidation peak overlap, also clearly shows the catalyst is active far after PdO is formed, contradicting their own statements when investigating their data independently [96]. Surprisingly, some works show a very clear detection of Pd and Pt oxide reduction peaks that is significant and clearly shown to be a separate process to the reactivation, further questioning the theory that oxides are responsible for the deactivation [108, 113]. In the case of the work of Yildiz et al. 1994 [108], they showed several key observations for Pd GEOR which are: 1) an increase in the upper potential window increases the PdO reduction peak but reduces the reactivation peak, as though PdO formation strips the surface of the factor which causes the reactivation peak (this entirely disproves the modern deactivation theory); 2) PdO or PdO_x is active for glycerol electrooxidation prior to OER (questioning oxides are inactive); 3) Pd reactivation oxidation peak is needed to reactivate the catalyst; 4) PdO or PdO_x increases Pd GEOR reactivity when it is reduced and the reactivation peak occurred [108]. Surprisingly, this information appears to not be mentioned in recent works or reviews [32]. Also, a critical analysis of Berretti et al. 2019 XAS results show PdO only covers 38% of the catalyst surface after deactivation (questioning the weighted contribution of PdO deactivating the entire Pd surface) and PdO appears to reduce after the reactivation peaks, although the data is noisy [106]. Combining these works, it would appear PdO is an independent process who's influence on GEOR deactivation and reactivation may not be as dominant as previously thought due to a number of experimental and literature inconsistencies.

In reviewing works of today, there is a clear disinclination to increase the potential window past the deactivation peak or change the electrolyte compositions and concentrations between works which may have restricted the view of how these mechanisms function, although this is not understood why these stringent experimental conditions were chosen [82, 90, 97, 100, 105, 116–120]. Overall, these contradictions demonstrate ambiguity for PdO is the cause of the deactivation, is an oxidation state which forms near the deactivation but isn't as a decisive factor on the deactivation. This doesn't contradict the XAS measurements of Wang et al. 2015 on Pd EOR or Berretti et al. 2019 [106, 107]. However, it will be shown later that due to the wider intermediate library of glycerol

compared to ethanol due to the differences in functionality, there exists different sensitivities to different alcohols [117, 121].

This also led to seeing a conflicting explanation to how PdO reduction occurs in alkaline conditions. Certain works state that PdO reduces directly to Pd [79] (sometimes with no references) and others point to PdOH is formed [3, 11, 27, 28, 80, 82, 105, 106, 116–120, 122]. This confusion appears to stem from the popular citation (both directly and second hand) of Grdeń et al. 2008 review of Pd electrochemical oxidation which showed the different opinions on the matter since it wasn't resolve at that point [79]. But the following year, Grdeń et al. 2009 (same author) appeared to resolve this confusion through EQCM measurement and showing PdO reduces to PdOH but was cited only 12 times [80]. In turn, there appears to be some confusion in how Pd oxidises and reduces and there clearly needs to be a refresher review about its electrochemical reactions in common electrolytes.

In turn, if there is historical and present data in this work which challenges oxide formation as the cause or consequence of the GEOR deactivation over Pd or Au, further removing oxides as the cause for the potential jumps, then what could be? An important observation from the potential jumps (figure 5.6D & 5.8D) and CP results (figure 5.10 & 5.12) is their reversibility from replenishing the electrolytic solution with glycerol and KOH without OER still occurring. This strongly correlates glycerol availability with the occurrence of these jumps even when it is not depleted and a substituting organic reaction is occurring, implying an alternate intermediate adsorbate is competing and oxidising but requiring a higher potential to initiate. This conclusion does not detract significantly from literature's theory that unknown intermediates are responsible for oxide formation due to their slower oxidation reaction (assuming oxide are responsible for the deactivation [3, 77]. However, if oxides are not responsible for the deactivation but are a coincidental oxidation process, the repeated detection of unknown intermediates on the surface near or preceding the deactivation and the reversibility of the polarization curves from this work would hypothesise the role of these intermediates on the deactivation are more important than previously thought.

The question then is how do different intermediates cause these jumps? Since the identity of the intermediates are unknown in literature and this work doesn't perform IR measurements, attempting to hypothesize which intermediate causes these jumps isn't constructive or wouldn't

contribute to the field. However, information can be pulled from the polarization curve and the CV results. Firstly, the deactivation process observed on GEOR CVs differ from the polarization curve jumps since the reversibility of the polarization curves can be achieved by reducing the current. However, even when the current is nearly nulled after the deactivation on a GEOR Pd/Au CV (figure 5.4, 5.5 & 5.7C/D), the reactivation doesn't occur until a minimum potential during the cathodic scan is achieved. In turn, the deactivation process occurring over a CV for Pd or Au are not the same process causing the polarization curve jumps or CP jump. In turn, a literature study of understanding how intermediates cause a catalyst deactivation over a CV will not be performed in depth, although certain findings are applicable for the following discussion.

A key element of catalyst deactivation during alcohol electrooxidation involving intermediates as a cause is their competitive adsorption against each other and glycerol, and their slower oxidation rate relative to oxide formation [3, 61, 77, 111]. Since it was already discussed how there is empirical CV studies which show oxide formation may not be the cause and consequence of the deactivation, what evidence points to intermediates being responsible if there exists a competitive adsorption process with glycerol? Several studies performing IR measurements during the deactivation process have identified carboxylate products near or after the deactivation [10, 22, 55, 59, 68, 82, 109]. However, Falase et al. 2012 observed both carboxylate intermediates appear and the CO_3^- production switching to CO_2 past 0.84V over Pt during IRRAS measurements [109]. This switching of CO_3^- to CO_2 is emblematic of a change in pH in the thin film over the catalyst [68]. The latter is important since it highlights a design consideration for GEOR catalysts which is the conversion of glycerol to any product (especially C-C scission products) requires a higher concentration of KOH than glycerol. For example, formate production requires 12 OH^- for every glycerol molecule [3]. In turn, the catalyst surface during GEOR presents a concentration gradient of OH^-. Therefore, knowing the product distribution shifts towards C2 and C1 products requiring more OH^- at higher potentials and the current increases (i.e. reaction rate) [3, 21, 61, 78, 111], the surface of the catalyst will be less alkaline than the bulk [68]. However, Falase et al. 2012 results also show the surface reaction condition evolves in changes in time/current/potential which can be significant enough to even acidify the catalyst surface [109]. This acidification alone, as highlighted by Li et al. 2021 review, can have drastic implications in terms changing the reaction mechanism where GEOR is known to have either a distinct acidic or OH^* present pathway alone on Pd and Au [3]. Other works have also highlighted intermediates may be responsible for the deactivation such as

Ivanov et al. 2022 observed the effects of poisonous species through an electroanalytical study of Pd over different porous supports [112]. Bambagioni et al. 2009 and other studies have demonstrated certain alcohols have a higher tendency for deactivation under CP than others [22, 30, 32, 64, 122]. In fact, glycerol produces a wider range of products which was theorized by Ivanov et al. 2022 to explain why certain noble metals a higher tendency for deactivation with glycerol have than ethanol since both should produce CO_{ads} but deactivate at different rates [30, 112]. The same author also theorized the removal rate of these intermediates is key to the catalyst reactivity which is alleviated via improved catalyst support and RDE rotation, which agrees with previous works on the impact of support [76, 97, 123], RDE rotation [64, 69, 77], temperature [27, 32] and catalyst loading [100]. This intermediate poisoning relationship is also observed over Au, which is widely seen to be resistant to it [27, 30, 32, 82]. Habibi et al 2012 also found evidence that an increase in temperature does not continuously reduce the activation energy for GEOR at specific potentials, which could only be explained by blocking intermediates that are more favourable for adsorption than glycerol [32].

Carvalho et al. 2023 observed that CO_{ads}, an important intermediate, reduced the favourability of glycerol and OH^- adsorption [95]. This hysteresis highlights a key unaddressed investigation in the field of GEOR which is the impact of adsorbates on other adsorbates. For either Au or Pd, the adsorption of alcohols and certain organic molecules produces large islands of similar compounds which hysterically inhibit the adsorption of others. This type of hysteresis may explain the potential jump hysteresis observed in the polarization curves and the CP measurements.

5.4.5 The dynamic change in large systems' pH

While a hypothesis was proposed as to the behaviour of potential jumps when changing the concentration of glycerol, this hasn't yet explained the rapid drift rate of $Ni_{80}Au_{20}/C$ in 0.5M KOH and 1M glycerol in figure 5.11 under CP conditions is influenced not by glycerol, but by KOH injection. This states that glycerate depletion isn't as weighted as a kinetic factor in these conditions as opposed to OH^- since an injection of glycerol should have increased the concentration of glycerate, as is seen with the concentration section of this work. Instead, we see an injection of KOH reduce the cell potential, as if OH^- was being depleted. This implies the solution in the electrolyte is undergoing acidification overtime.

Based on literature only few works mention net hydroxide consumption as a theoretical factor for consideration [36, 107]. Based on Li et al. 2021 and Simone et al 2012 in alkaline conditions, net OH^- consumption when coupled with HER theoretically occurs during C-C cleaving [3, 36]. As a simplified mass balance visualization, Scheme 2 presents a mass balance of the GEOR reaction coupled with HER when accounting for the charge balance on each electrode which is based on the OH_{ads} pathway proposed by Li et al. 2021 [3, 36, 124]. Through a deeper form of oxidation of glycerol towards C_2 and C_1 products, the electrolyte must undergo neutralisation of its pH.

This effect of pH neutralization is more weighted at 0.5M KOH than 1-2M KOH due to the logarithmic scale of pH, where a 0.1M change from 0.5M than from 1M or higher incurs a larger change in pH. This larger rate of change in pH can significantly reduce OH_{ads} coverage over Au [66, 103, 125]. Furthermore, the reduced pH also accelerates the reduction in glycerate. In addition, pH studies for noble metal based GEOR studies demonstrates the alkaline oxidation peak is composed of two separate oxidation peaks that are pH dependent which diverge with a decrease in pH [59, 64, 102]. The shift in pH can cause important changes in selectivity by shifting the reaction pathway as proposed by Li et al. 2021 as well [3]. In addition, a reduction in OH^- reduces the electrolyte conductivity, further increasing the electrolyte resistance.

Although it wasn't understood what was observed at the time of measuring the electrolyser performance, pH strip at room temperature produced a pH of approximately 14. While this may conclude the solution is still alkaline, the work of Hausmann et al. 2021 demonstrated how an increase in temperature from 25°C to 80°C reduced the solution pH of a 1M KOH solution from 13.8 to 12.45, a magnitude decreases in pH by 1.35 [34]. In turn, the pH measurements made at room temperature are not representative of the solution pH during electrolysis under CP.

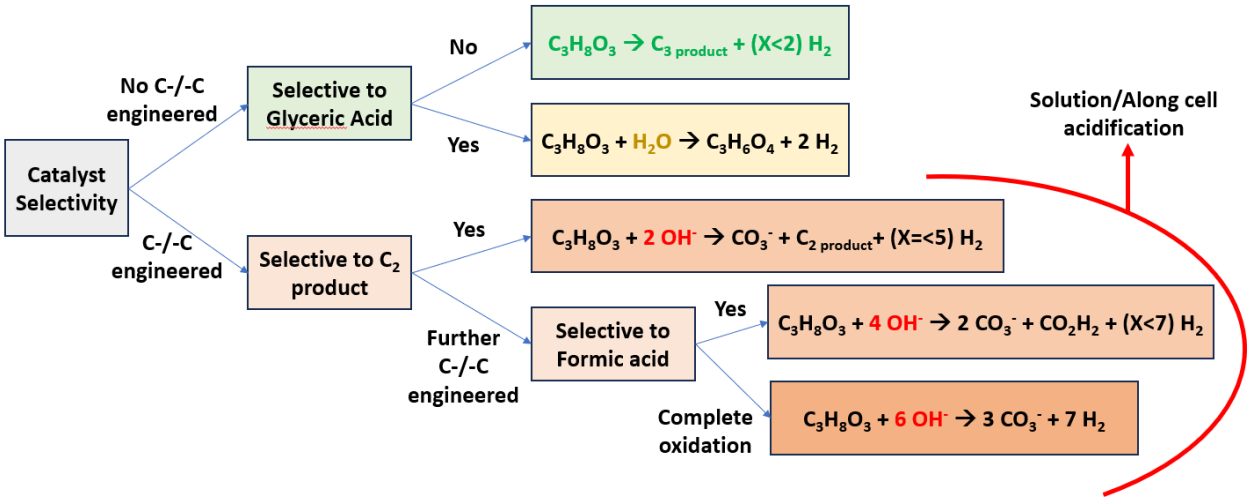

Scheme 5.2) (A) reaction pathway's general mass balance of an alkaline HER coupled GEOR electrolyser based on catalyst selectivity with a focus on how a chosen selectivity will impact the solution pH. This scheme assumes the catalyst will utilise an OH_{ads}-present pathway as outlined by Li et al. 2021 [3], Simoes et al. 2012 [36] and Antolini et al. 2019 [124].

5.5 Conclusion

In this work, polarizations curves and CP results have demonstrated the existence of a complex equilibrium adsorption competition between multiple adsorbates. Depending on the active material, particularly noble material, these intermediates may be potential dependent rate limiting adsorbates whose coverage is favoured not only overtime within the same electrolyte tank but along the cell as the current is increased. A critical review of GEOR in literature to explain the obtained results also pointed to key inconsistencies in the field as to what causes the catalyst to deactivate and what is the reactivation process over Pd and Au. It is theorized in this work that oxide formation is independent from the deactivation process and key unknown intermediates are the cause, although oxide formation does occur and isn't reactive. Furthermore, key CP results point to the observable effect of in-solution acidification which can be detrimental to GEOR over certain key materials such as Au. This acidification is proposed as a useful phenomenon where pH measurements can be used to estimate CO_3^- production and if a catalyst surface is sufficiently alkaline. Regardless, pH measurements should be made in any setting, particularly for GEOR, where an increase in temperature can drastically reduce the pH by over 1 unit and miss-associate room temperature results at small scale cells to high temperature performances on a large scale. This also applies to surface characterization tools such as FTIR.

This requires the cell to jump in potential to oxidise these intermediates. However, the presence of different potential dependent GEOR mechanisms is not observable over CPs on small cells due to their small electrode size where this effect theorizes to not be as noticeable. The same is applied to CVs on small cells. However, due to the prolonged time needed to achieve steady state on for the first dozen of data points on the CP measurements in a large cell (10-15 minutes), it is advisable to not perform LSV as a substitute for consecutive CP measurements for making a polarization curve since the complex adsorption equilibrium is believed to be the cause of this prolonged required steady state and won't be reflected in LSVs unless the scan rates are exceptionally slow. To this end, the changes in

This work illustrates the importance of an in-depth zero-gap electrochemical cell investigations for completing the electrochemical GEOR properties of the catalyst of interest. From CV alone, no prediction or obvious indicators would have lead to the presence of critical current densities which lead to potential jumps which are likely the result of a change in surface adsorbate coverage equilibrium which possibly leads to different GEOR mechanisms. This was only made possible in an electrolyser who's catalyst loading is larger noticeably larger than 3 electrode set-up, even at low catalyst loading on the anode. Furthermore, this work critically reviewed the previous understanding of how catalyst deactivation and reactivation occurs. It was found through previous and new electrochemical evidence from this work which sheds light to the possibility that Pd deactivation is not the result of PdO formation but through the poisoning of an unknown intermediate which previously was mentioned but not demonstrated until now to be critical at large scale. In fact, inducing PdO formation leads to a stripping action on these poisonous intermediates although irreversible damage to Pd may occur. This critical review also points out the need to in the GEOR field to properly understand the deactivation mechanism of Pd and its reactivation to better engineer future catalyst which may reduce these events. Furthermore, a further critical review of GEOR mechanisms and CP results from this work point to evidence of GEOR being a OH^- net consumption process and a water neutral H_2 production process, which may shed light to the possibility of alcohol electro-oxidation as an alternative to water consuming H_2 production pathways. Finally, this work highlights the need to understand how newly designed catalysts need to be tested in different electrolytic environments in order to understand their adaptation to changes along an electrolytic cell whose ratio of glycerol (or glycerate) to intermediates favour the adsorption of said intermediates the higher the current density.

5.6 References

[1] Braun, M.; Santana, C. S.; Garcia, A. C.; Andronescu, C. From Waste to Value – Glycerol Electrooxidation for Energy Conversion and Chemical Production. *Current Opinion in Green and Sustainable Chemistry*. Elsevier B.V. June 1, 2023. https://doi.org/10.1016/j.cogsc.2023.100829.

[2] khalafallah, D.; Zhang, Y.; Wang, H.; Lee, J. M.; Zhang, Q. Energy-Saving Electrochemical Hydrogen Production via Co-Generative Strategies in Hybrid Water Electrolysis: Recent Advances and Perspectives. *Chinese Journal of Catalysis*. Science Press December 1, 2023, pp 44–115. https://doi.org/10.1016/S1872-2067(23)64544-9.

[3] Li, T.; Harrington, D. A. An Overview of Glycerol Electrooxidation Mechanisms on Pt, Pd and Au. *ChemSusChem*. John Wiley and Sons Inc March 22, 2021, pp 1472–1495. https://doi.org/10.1002/cssc.202002669.

[4] Khan, M. A.; Al-Attas, T. A.; Yasri, N. G.; Zhao, H.; Larter, S.; Hu, J.; Kibria, M. G. Techno-Economic Analysis of a Solar-Powered Biomass Electrolysis Pathway for Coproduction of Hydrogen and Value-Added Chemicals. *Sustain Energy Fuels*, **2020**, *4* (11), 5568–5577. https://doi.org/10.1039/d0se01149e.

[5] Kim, H. J.; Kim, Y.; Lee, D.; Kim, J. R.; Chae, H. J.; Jeong, S. Y.; Kim, B. S.; Lee, J.; Huber, G. W.; Byun, J.; et al. Coproducing Value-Added Chemicals and Hydrogen with Electrocatalytic Glycerol Oxidation Technology: Experimental and Techno-Economic Investigations. *ACS Sustain Chem Eng*, **2017**, *5* (8), 6626–6634. https://doi.org/10.1021/acssuschemeng.7b00868.

[6] Elsaid, K.; Abdelfatah, S.; Abdel Elabsir, A. M.; Hassiba, R. J.; Ghouri, Z. K.; Vechot, L. Direct Alcohol Fuel Cells: Assessment of the Fuel's Safety and Health Aspects. *Int J Hydrogen Energy*, **2021**, *46* (59), 30658–30668. https://doi.org/10.1016/j.ijhydene.2020.12.009.

[7] Fu, X.; Wan, C.; Huang, Y.; Duan, X. Noble Metal Based Electrocatalysts for Alcohol Oxidation Reactions in Alkaline Media. *Advanced Functional Materials*. John Wiley and Sons Inc March 1, 2022. https://doi.org/10.1002/adfm.202106401.

[8] Han, X.; Sheng, H.; Yu, C.; Walker, T. W.; Huber, G. W.; Qiu, J.; Jin, S. Electrocatalytic Oxidation of Glycerol to Formic Acid by CuCo2O4Spinel Oxide Nanostructure Catalysts. *ACS Catal*, **2020**, *10* (12), 6741–6752. https://doi.org/10.1021/acscatal.0c01498.

[9] Rafaïdeen, T.; Neha, N.; Kouamé, B. R. S.; Baranton, S.; Coutanceau, C. Electroreforming of Glucose and Xylose in Alkaline Medium at Carbon Supported Alloyed Pd3Au7 Nanocatalysts: Effect of Aldose Concentration and Electrolysis Cell Voltage. *Clean Technologies*, **2020**, *2* (2), 184–203. https://doi.org/10.3390/cleantechnol2020013.

[10] Houache, M. S. E.; Hughes, K.; Ahmed, A.; Safari, R.; Liu, H.; Botton, G. A.; Baranova, E. A. Electrochemical Valorization of Glycerol on Ni-Rich Bimetallic NiPd Nanoparticles: Insight into Product Selectivity Using in Situ Polarization Modulation Infrared-Reflection Absorption Spectroscopy. *ACS Sustain Chem Eng*, **2019**, *7* (17), 14425–14434. https://doi.org/10.1021/acssuschemeng.9b01070.

[11] Houache, M. S. E.; Shubair, A.; Sandoval, M. G.; Safari, R.; Botton, G. A.; Jasen, P. V.; González, E. A.; Baranova, E. A. Influence of Pd and Au on Electrochemical Valorization of Glycerol over Ni-Rich Surfaces. *J Catal*, **2021**, *396*, 1–13. https://doi.org/10.1016/j.jcat.2021.02.008.

[12] Houache, M. S. E.; Safari, R.; Nwabara, U. O.; Rafaïdeen, T.; Botton, G. A.; Kenis, P. J. A.; Baranton, S.; Coutanceau, C.; Baranova, E. A. Selective Electrooxidation of Glycerol to Formic Acid over Carbon Supported Ni1- XMx(M = Bi, Pd, and Au) Nanocatalysts and Coelectrolysis of CO2. *ACS Appl Energy Mater*, **2020**, *3* (9), 8725–8738. https://doi.org/10.1021/acsaem.0c01282.

[13] Rizk, M. R.; Abd El-Moghny, M. G.; Abdelhady, H. H.; Ragheb, W. M.; Mohamed, A. H.; Fouad, H. F.; Mohsen, M.; Kamel, A. S.; El-Deab, M. S. Tailor-Designed Bimetallic Co/Ni Macroporous Electrocatalyst for Efficient Glycerol Oxidation and Water Electrolysis. *Int J Hydrogen Energy*, **2022**, *47* (75), 32145–32157. https://doi.org/10.1016/j.ijhydene.2022.07.129.

[14] Du, J.; Qin, Y.; Dou, T.; Ge, J.; Wang, Y.; Zhao, X.; Zhang, F.; Lei, X. Copper Nanoparticles Dotted on Copper Sulfide Nanosheets for Selective Electrocatalytic Oxidation of Glycerol to Formate. *ACS Appl Nano Mater*, **2022**. https://doi.org/10.1021/acsanm.2c00323.

[15] Vo, T. G.; Tran, G. S.; Chiang, C. L.; Lin, Y. G.; Chang, H. E.; Kuo, H. H.; Chiang, C. Y.; Hsu, Y. J. Au@NiSx Yolk@Shell Nanostructures as Dual-Functional Electrocatalysts for Concomitant Production of Value-Added Tartronic Acid and Hydrogen Fuel. *Adv Funct Mater*, **2023**, *33* (4). https://doi.org/10.1002/adfm.202209386.

[16] Xu, Y.; Liu, T.; Shi, K.; Yu, H.; Deng, K.; Wang, Z.; Li, X.; Wang, L.; Wang, H. Iridium-Incorporated Co3O4 with Lattice Expansion for Energy-Efficient Green Hydrogen Production Coupled with Glycerol Valorization. *Chemical Communications*, **2023**, *59* (13), 1817–1820. https://doi.org/10.1039/d2cc06931h.

[17] Liu, B.; Wang, G.; Feng, X.; Dai, L.; Wen, Z.; Ci, S. Energy-Saving H2 Production from a Hybrid Acid/Alkali Electrolyzer Assisted by Anodic Glycerol Oxidation. *Nanoscale*, **2022**, *14* (35), 12841–12848. https://doi.org/10.1039/d2nr02689a.

[18] Yan, S.; Zhong, M.; Zhu, W.; Li, W.; Chen, X.; Li, M.; Wang, C.; Lu, X. Controllable Fabrication of a Nickel-Iridium Alloy Network by Galvanic Replacement Engineering for High-Efficiency Electrocatalytic Water Splitting. *Inorg Chem Front*, **2022**, *9* (23), 6225–6236. https://doi.org/10.1039/d2qi01494g.

[19] Xu, Y.; Liu, T.; Shi, K.; Yu, H.; Deng, K.; Wang, X.; Wang, Z.; Wang, L.; Wang, H. Ru-Doping Induced Lattice Strain in Hetero-Phase Ni2P-Ni12P5 Arrays Enables Simultaneous Efficient Energy-Saving Hydrogen Generation and Formate Electrosynthesis. *J Mater Chem A Mater*, **2022**, *10* (38), 20365–20374. https://doi.org/10.1039/d2ta05151f.

[20] Yu, X.; dos Santos, E. C.; White, J.; Salazar-Alvarez, G.; Pettersson, L. G. M.; Cornell, A.; Johnsson, M. Electrocatalytic Glycerol Oxidation with Concurrent Hydrogen Evolution Utilizing an Efficient MoOx/Pt Catalyst. *Small*, **2021**, *17* (44). https://doi.org/10.1002/smll.202104288.

[21] White, J.; Peters, L.; Martín-Yerga, D.; Terekhina, I.; Anil, A.; Lundberg, H.; Johnsson, M.; Salazar-Alvarez, G.; Henriksson, G.; Cornell, A. Glycerol Electrooxidation at Industrially Relevant Current Densities Using Electrodeposited PdNi/Nifoam Catalysts in Aerated Alkaline Media. *J Electrochem Soc*, **2023**, *170* (8), 086504. https://doi.org/10.1149/1945-7111/acee27.

[22] Frutis-Murillo, M.; Velázquez-Hernández, I.; Esparza, R.; López-Meza, J. E.; Cayetano-Castro, N.; Rosas, G. Facile Synthesis of Gold Nanoflowers and Their Application in Glycerol Electro-Oxidation. *Appl Surf Sci*, **2024**, *642*. https://doi.org/10.1016/j.apsusc.2023.158628.

[23] Gördesel Yıldız, M.; Yörük, Ö.; Uysal, D.; Doğan, Ö. M.; Uysal, B. Z. Parametric Study on Electrochemical Reforming of Glycerol for Hydrogen Production. *Int J Hydrogen Energy*, **2022**, *47* (95), 40196–40203. https://doi.org/10.1016/j.ijhydene.2022.03.027.

[24] Xie, Y.; Sun, L.; Pan, X.; Zhou, Z.; Zheng, Y.; Yang, X.; Zhao, G. Carbon Paper Supported Gold Nanoflowers for Tunable Glycerol Electrooxidation Boosting Efficient Hydrogen Evolution. *Carbon N Y*, **2023**, *203*, 88–96. https://doi.org/10.1016/j.carbon.2022.11.067.

[25] Qiu, Z.; Martín-Yerga, D.; Lindén, P. A.; Henriksson, G.; Cornell, A. Green Hydrogen Production via Electrochemical Conversion of Components from Alkaline Carbohydrate Degradation. *Int J Hydrogen Energy*, **2022**, *47* (6), 3644–3654. https://doi.org/10.1016/j.ijhydene.2021.11.046.

[26] González-Cobos, J.; Baranton, S.; Coutanceau, C. Development of Bismuth-Modified PtPd Nanocatalysts for the Electrochemical Reforming of Polyols into Hydrogen and Value-Added Chemicals. *ChemElectroChem*, **2016**, *3* (10), 1694–1704. https://doi.org/10.1002/celc.201600147.

[27] Zhang, Z.; Xin, L.; Qi, J.; Chadderdon, D. J.; Li, W. Supported Pt, Pd and Au Nanoparticle Anode Catalysts for Anion-Exchange Membrane Fuel Cells with Glycerol and Crude Glycerol Fuels. *Appl Catal B*, **2013**, *136–137*, 29–39. https://doi.org/10.1016/j.apcatb.2013.01.045.

[28] Terekhina, I.; White, J.; Cornell, A.; Johnsson, M. Electrocatalytic Oxidation of Glycerol to Value-Added Compounds on Pd Nanocrystals. *ACS Appl Nano Mater*, **2023**, *6* (13), 11211–11220. https://doi.org/10.1021/acsanm.3c01236.

[29] Lazaridis, T.; Stühmeier, B. M.; Gasteiger, H. A.; El-Sayed, H. A. Capabilities and Limitations of Rotating Disk Electrodes versus Membrane Electrode Assemblies in the Investigation of Electrocatalysts. *Nat Catal*, **2022**, *5* (5), 363–373. https://doi.org/10.1038/s41929-022-00776-5.

[30] Zhang, J. H.; Liang, Y. J.; Li, N.; Li, Z. Y.; Xu, C. W.; Jiang, S. P. A Remarkable Activity of Glycerol Electrooxidation on Gold in Alkaline Medium. *Electrochim Acta*, **2012**, *59*, 156–159. https://doi.org/10.1016/j.electacta.2011.10.048.

[31] Habibi, B.; Delnavaz, N. Electrooxidation of Glycerol on Nickel and Nickel Alloy (Ni-Cu and Ni-Co) Nanoparticles in Alkaline Media. *RSC Adv*, **2016**, *6* (38), 31797–31806. https://doi.org/10.1039/c5ra26006j.

[32] Habibi, E.; Razmi, H. Glycerol Electrooxidation on Pd, Pt and Au Nanoparticles Supported on Carbon Ceramic Electrode in Alkaline Media. *Int J Hydrogen Energy*, **2012**, *37* (22), 16800–16809. https://doi.org/10.1016/j.ijhydene.2012.08.127.

[33] Shubair, A.; Houache, M. S. E.; Mousavi M, S. S.; Botton, G. A.; Baranova, E. A. Electrolysis of Glycerol to Value-Added Chemicals in Alkaline Media. *Journal of Chemical Technology and Biotechnology*, **2022**, *97* (8), 1950–1958. https://doi.org/10.1002/jctb.7088.

[34] Hausmann, J. N.; Traynor, B.; Myers, R. J.; Driess, M.; Menezes, P. W. The PH of Aqueous NaOH/KOH Solutions: A Critical and Non-Trivial Parameter for Electrocatalysis. *ACS Energy Letters*. American Chemical Society October 8, 2021, pp 3567–3571. https://doi.org/10.1021/acsenergylett.1c01693.

[35] de Paula, J.; Nascimento, D.; Linares, J. J. Influence of the Anolyte Feed Conditions on the Performance of an Alkaline Glycerol Electroreforming Reactor. *J Appl Electrochem*, **2015**, *45* (7), 689–700. https://doi.org/10.1007/s10800-015-0848-6.

[36] Simões, M.; Baranton, S.; Coutanceau, C. Electrochemical Valorisation of Glycerol. *ChemSusChem*. November 2012, pp 2106–2124. https://doi.org/10.1002/cssc.201200335.

[37] Yu, X.; dos Santos, E. C.; White, J.; Salazar-Alvarez, G.; Pettersson, L. G. M.; Cornell, A.; Johnsson, M. Electrocatalytic Glycerol Oxidation with Concurrent Hydrogen Evolution Utilizing an Efficient MoOx/Pt Catalyst. *Small*, **2021**, *17* (44). https://doi.org/10.1002/smll.202104288.

[38] Pham, T. H.; Lee, W. H.; Byun, J. H.; Kim, J. G. Improving the Performance of Primary Aluminum-Air Batteries through Suppressing Water Activity by Hydrogen Bond-Rich Glycerol Solvent Additive. *Energy Storage Mater*, **2023**, *55*, 406–416. https://doi.org/10.1016/j.ensm.2022.12.012.

[39] Stuart, J.; Wyithe, B.; Loeb, A. The Nature and Transport Mechanism of Hydrated Hydroxide Ions in Aqueous Solution. *Nature*, **2002**, *417* (6892), 923–925. https://doi.org/10.1038/nature00794.

[40] Long, Z.; Tuckerman, M. E. Hydroxide Diffusion in Functionalized Cylindrical Nanopores as Idealized Models of Anion Exchange Membrane Environments: An Ab Initio Molecular Dynamics Study. *Journal of Physical Chemistry C*, **2023**, *127* (6), 2792–2804. https://doi.org/10.1021/acs.jpcc.2c05747.

[41] Gong, Y.; Xu, Y.; Zhou, Y.; Li, C.; Liu, X.; Niu, L.; Huang, Y.; Zhang, X.; Sun, C. Q. Hydrogen Bond Network Relaxation Resolved by Alcohol Hydration (Methanol, Ethanol, and Glycerol). *Journal of Raman Spectroscopy*, **2017**, *48* (3), 393–398. https://doi.org/10.1002/jrs.5060.

[42] Saito, M.; Tsuzuki, S.; Hayamizu, K.; Okada, T. Alcohol and Proton Transport in Perfluorinated Ionomer Membranes for Fuel Cells. *Journal of Physical Chemistry B*, **2006**, *110* (48), 24410–24417. https://doi.org/10.1021/jp0643496.

[43] Affoune, A. M.; Yamada, A.; Umeda, M. Conductivity and Surface Morphology of Nafion Membrane in Water and Alcohol Environments. *J Power Sources*, **2005**, *148* (1–2), 9–17. https://doi.org/10.1016/j.jpowsour.2005.01.039.

[44] Cossar, E.; Houache, M. S. E.; Zhang, Z.; Baranova, E. A. Comparison of Electrochemical Active Surface Area Methods for Various Nickel Nanostructures. *Journal of Electroanalytical Chemistry*, **2020**, *870*. https://doi.org/10.1016/j.jelechem.2020.114246.

[45] Mohammed-Ibrahim, J.; Xiaoming, S. Recent Progress on Earth Abundant Electrocatalysts for Hydrogen Evolution Reaction (HER) in Alkaline Medium to Achieve Efficient Water Splitting – A Review. *Journal of Energy Chemistry*. Elsevier B.V. July 1, 2019, pp 111–160. https://doi.org/10.1016/j.jechem.2018.09.016.

[46] Du, N.; Roy, C.; Peach, R.; Turnbull, M.; Thiele, S.; Bock, C. Anion-Exchange Membrane Water Electrolyzers. *Chemical Reviews*. American Chemical Society July 13, 2022, pp 11830–11895. https://doi.org/10.1021/acs.chemrev.1c00854.

[47] Ge, Z.; Fu, B.; Zhao, J.; Li, X.; Ma, B.; Chen, Y. A Review of the Electrocatalysts on Hydrogen Evolution Reaction with an Emphasis on Fe, Co and Ni-Based Phosphides. *Journal of Materials Science*. Springer October 1, 2020, pp 14081–14104. https://doi.org/10.1007/s10853-020-05010-w.

[48] Lee, C. S.; Aroua, M. K.; Wan Daud, W. A.; Cognet, P.; Pérès, Y.; Ajeel, M. A. Selective Electrochemical Conversion of Glycerol to Glycolic Acid and Lactic Acid on a Mixed Carbon-Black Activated Carbon Electrode in a Single Compartment Electrochemical Cell. *Front Chem*, **2019**, *7* (MAR). https://doi.org/10.3389/fchem.2019.00110.

[49] Morales, D. M.; Jambrec, D.; Kazakova, M. A.; Braun, M.; Sikdar, N.; Koul, A.; Brix, A. C.; Seisel, S.; Andronescu, C.; Schuhmann, W. Electrocatalytic Conversion of Glycerol

to Oxalate on Ni Oxide Nanoparticles-Modified Oxidized Multiwalled Carbon Nanotubes. *ACS Catal*, **2022**, *12* (2), 982–992. https://doi.org/10.1021/acscatal.1c04150.

[50] Dong, L.; Chang, G.-R.; Feng, Y.; Yao, X.-Z.; Yu, X.-Y. Regulating Ni Site in NiV LDH for Efficient Electrocatalytic Production of Formate and Hydrogen by Glycerol Electrolysis. *Rare Metals*, *41*. https://doi.org/10.1007/s12598.

[51] Han, J.; Kim, Y.; Kim, H. W.; Jackson, D. H. K.; Lee, D.; Chang, H.; Chae, H. J.; Lee, K. Y.; Kim, H. J. Effect of Atomic-Layer-Deposited TiO2 on Carbon-Supported Ni Catalysts for Electrocatalytic Glycerol Oxidation in Alkaline Media. *Electrochem commun*, **2017**, *83*, 46–50. https://doi.org/10.1016/j.elecom.2017.08.023.

[52] Shilpa, N.; Pandikassala, A.; Krishnaraj, P.; Walko, P. S.; Devi, R. N.; Kurungot, S. Co-Ni Layered Double Hydroxide for the Electrocatalytic Oxidation of Organic Molecules: An Approach to Lowering the Overall Cell Voltage for the Water Splitting Process. *ACS Appl Mater Interfaces*, **2022**, *14* (14), 16222–16232. https://doi.org/10.1021/acsami.2c00982.

[53] Bagchi, J.; Bhattacharya, S. K. Studies of the Electrocatalytic Activity of Binary Palladium Ruthenium Anode Catalyst on Ni Support for Ethanol Alkaline Fuel Cells. *Transition Metal Chemistry*, **2008**, *33* (1), 113–120. https://doi.org/10.1007/s11243-007-9021-3.

[54] Wu, J.; Yang, X.; Gong, M. Recent Advances in Glycerol Valorization via Electrooxidation: Catalyst, Mechanism and Device. *Chinese Journal of Catalysis*. Science Press December 1, 2022, pp 2966–2986. https://doi.org/10.1016/S1872-2067(22)64121-4.

[55] Holade, Y.; Morais, C.; Servat, K.; Napporn, T. W.; Kokoh, K. B. Toward the Electrochemical Valorization of Glycerol: Fourier Transform Infrared Spectroscopic and Chromatographic Studies. *ACS Catal*, **2013**, *3* (10), 2403–2411. https://doi.org/10.1021/cs400559d.

[56] Oliveira, V. L.; Morais, C.; Servat, K.; Napporn, T. W.; Olivi, P.; Kokoh, K. B.; Tremiliosi-Filho, G. Kinetic Investigations of Glycerol Oxidation Reaction on Ni/C. *Electrocatalysis*, **2015**, *6* (5), 447–454. https://doi.org/10.1007/s12678-015-0261-2.

[57] Houache, M. S. E.; Sandoval, M. G.; Safari, R.; Gaztañaga, F.; Escudero, F.; Hernández-Laguna, A.; Sainz-Díaz, C. I.; Botton, G. A.; Jasen, P. V.; González, E. A.; et al. Morphology Alteration of Nickel Microstructures for Glycerol Electrooxidation. *J Catal*, **2021**, *404*, 348–361. https://doi.org/10.1016/j.jcat.2021.10.010.

[58] Pérez-Rodríguez, S.; Pastor, E.; Lázaro, M. J. *Electrochemical Behavior of the Carbon Black Vulcan XC-72R: Influence of the Surface Chemistry*.

[59] Mello, G. A. B.; Busó-Rogero, C.; Herrero, E.; Feliu, J. M. Glycerol Electrooxidation on Pd Modified Au Surfaces in Alkaline Media: Effect of the Deposition Method. *Journal of Chemical Physics*, **2019**, *150* (4). https://doi.org/10.1063/1.5048489.

[60] Zhang, Z.; Xin, L.; Li, W. Supported Gold Nanoparticles as Anode Catalyst for Anion-Exchange Membrane-Direct Glycerol Fuel Cell (AEM-DGFC). *Int J Hydrogen Energy*, **2012**, *37* (11), 9393–9401. https://doi.org/10.1016/j.ijhydene.2012.03.019.

[61] White, J.; Anil, A.; Martín-Yerga, D.; Salazar-Alvarez, G.; Henriksson, G.; Cornell, A. Electrodeposited PdNi on a Ni Rotating Disk Electrode Highly Active for Glycerol Electrooxidation in Alkaline Conditions. *Electrochim Acta*, **2022**, *403*. https://doi.org/10.1016/j.electacta.2021.139714.

[62] Luo, H.; Yukuhiro, V. Y.; Fernández, P. S.; Feng, J.; Thompson, P.; Rao, R. R.; Cai, R.; Favero, S.; Haigh, S. J.; Durrant, J. R.; et al. Role of Ni in PtNi Bimetallic Electrocatalysts for Hydrogen and Value-Added Chemicals Coproduction via Glycerol Electrooxidation. *ACS Catal*, **2022**, *12* (23), 14492–14506. https://doi.org/10.1021/acscatal.2c03907.

[63] Oh, L. S.; Park, M.; Park, Y. S.; Kim, Y.; Yoon, W.; Hwang, J.; Lim, E.; Park, J. H.; Choi, S. M.; Seo, M. H.; et al. How to Change the Reaction Chemistry on Nonprecious Metal Oxide Nanostructure Materials for Electrocatalytic Oxidation of Biomass-Derived Glycerol to Renewable Chemicals. *Advanced Materials*, **2023**, *35* (4). https://doi.org/10.1002/adma.202203285.

[64] Melle, G.; de Souza, M. B. C.; Santiago, P. V. B.; Corradini, P. G.; Mascaro, L. H.; Fernández, P. S.; Sitta, E. Glycerol Electro-Oxidation at Pt in Alkaline Media: Influence of Mass Transport and Cations. *Electrochim Acta*, **2021**, *398*. https://doi.org/10.1016/j.electacta.2021.139318.

[65] Lee, J. K.; Lee, C. H.; Fahy, K. F.; Zhao, B.; LaManna, J. M.; Baltic, E.; Jacobson, D. L.; Hussey, D. S.; Bazylak, A. Erratum: Critical Current Density as a Performance Indicator for Gas-Evolving Electrochemical Devices (Cell Reports Physical Science (2020) 1(8), (S266638642030151X), (10.1016/j.Xcrp.2020.100147)). *Cell Reports Physical Science*. Cell Press May 19, 2021. https://doi.org/10.1016/j.xcrp.2021.100440.

[66] Verma, A. M.; Laverdure, L.; Melander, M. M.; Honkala, K. Mechanistic Origins of the PH Dependency in Au-Catalyzed Glycerol Electro-Oxidation: Insight from First-Principles Calculations. *ACS Catal*, **2022**, *12* (1), 662–675. https://doi.org/10.1021/acscatal.1c03788.

[67] Del Colle, V.; Melle, G.; Previdello, B. A. F.; Feliu, J. M.; Varela, H.; Tremiliosi-Filho, G. The Effect of Pt Surface Orientation on the Oscillatory Electro-Oxidation of Glycerol. *Journal of Electroanalytical Chemistry*, **2022**, *926*. https://doi.org/10.1016/j.jelechem.2022.116934.

[68] Ferreira, R. S.; Janete Giz, M.; Camara, G. A. Influence of the Local PH on the Electrooxidation of Glycerol on Palladium-Rhodium Electrodeposits. *Journal of Electroanalytical Chemistry*, **2013**, *697*, 15–20. https://doi.org/10.1016/j.jelechem.2013.03.007.

[69] Melle, G. B.; Machado, E. G.; Mascaro, L. H.; Sitta, E. Eff Ect of Mass Transport on the Glycerol Electro-Oxidation. *Electrochim Acta*, **2019**, *296*, 972–979. https://doi.org/10.1016/j.electacta.2018.11.085.

[70] Yu, X.; Pickup, P. G. Deactivation/Reactivation of a Pd/C Catalyst in a Direct Formic Acid Fuel Cell (DFAFC): Use of Array Membrane Electrode Assemblies. *J Power Sources*, **2009**, *187* (2), 493–499. https://doi.org/10.1016/j.jpowsour.2008.11.014.

[71] Tian, M.; Conway, B. E. Phenomenology of Oscillatory Electro-Oxidation of Formic Acid at Pd: Role of Surface Oxide Films Studied by Voltammetry, Impedance Spectroscopy and Nanogravimetry. *Journal of Electroanalytical Chemistry*, **2005**, *581* (2), 176–189. https://doi.org/10.1016/j.jelechem.2004.12.029.

[72] Jeon, H.; Jeong, B.; Choun, M.; Lee, J. In-Situ Electrochemical Extended X-Ray Absorption Fine Structure Spectroscopy Study on the Reactivation of Pd Electrocatalyst in Formic Acid Oxidation. *Electrochim Acta*, **2014**, *140*, 525–528. https://doi.org/10.1016/j.electacta.2014.06.093.

[73] Technical Targets for Liquid Alkaline Electrolysis https://www.energy.gov/eere/fuelcells/technical-targets-liquid-alkaline-electrolysis (accessed Mar 3, 2024).

[74] Elgrishi, N.; Rountree, K. J.; McCarthy, B. D.; Rountree, E. S.; Eisenhart, T. T.; Dempsey, J. L. A Practical Beginner's Guide to Cyclic Voltammetry. *J Chem Educ*, **2018**, *95* (2), 197–206. https://doi.org/10.1021/acs.jchemed.7b00361.

[75] Oliveira, C. P.; Lussari, N. V.; Sitta, E.; Varela, H. Oscillatory Electro-Oxidation of Glycerol on Platinum. *Electrochim Acta*, **2012**, *85*, 674–679. https://doi.org/10.1016/j.electacta.2012.08.087.

[76] Gao, R.; Kodaimati, M. S.; Handy, K. M.; Root, S. E.; Whitesides, G. M. Generating Oscillatory Behavior by Applying a Magnetic Field during Electrocatalytic Oxidation of Glycerol. *Journal of Physical Chemistry C*, **2022**, *126* (42), 18159–18169. https://doi.org/10.1021/acs.jpcc.2c05145.

[77] Pérez-Martínez, L.; Balke, L.; Cuesta, A. Reactive and Inhibiting Species in the Electrocatalytic Oxidation of Glycerol on Gold. A Study Combining in-Situ Visible Reflectance and ATR-SEIRAS. *J Catal*, **2021**, *394*, 1–7. https://doi.org/10.1016/j.jcat.2020.12.010.

[78] Birss, V. I.; Chan, M.; Phan, T.; Vanysekb, P.; Zhang, A. *An Electrochemical Study of the Composition of Thin, Compact Pd Oxide Films*; 1996.

[79] Grdeń, M.; Łukaszewski, M.; Jerkiewicz, G.; Czerwiński, A. Electrochemical Behaviour of Palladium Electrode: Oxidation, Electrodissolution and Ionic Adsorption. *Electrochimica Acta*. November 1, 2008, pp 7583–7598. https://doi.org/10.1016/j.electacta.2008.05.046.

[80] Grdeń, M. Electrochemical Quartz Crystal Microbalance Studies of a Palladium Electrode Oxidation in a Basic Electrolyte Solution. *Electrochim Acta*, **2009**, *54* (3), 909–920. https://doi.org/10.1016/j.electacta.2008.08.021.

[81] Velázquez-Hernández, I.; Zamudio, E.; Rodríguez-Valadez, F. J.; García-Gómez, N. A.; Álvarez-Contreras, L.; Guerra-Balcázar, M.; Arjona, N. Electrochemical Valorization of Crude Glycerol in Alkaline Medium for Energy Conversion Using Pd, Au and PdAu Nanomaterials. *Fuel*, **2020**, *262*. https://doi.org/10.1016/j.fuel.2019.116556.

[82] Simões, M.; Baranton, S.; Coutanceau, C. Enhancement of Catalytic Properties for Glycerol Electrooxidation on Pt and Pd Nanoparticles Induced by Bi Surface Modification. *Appl Catal B*, **2011**, *110*, 40–49. https://doi.org/10.1016/j.apcatb.2011.08.020.

[83] Valter, M.; Busch, M.; Wickman, B.; Grönbeck, H.; Baltrusaitis, J.; Hellman, A. Electrooxidation of Glycerol on Gold in Acidic Medium: A Combined Experimental and DFT Study. *Journal of Physical Chemistry C*, **2018**, *122* (19), 10489–10494. https://doi.org/10.1021/acs.jpcc.8b02685.

[84] Su, G.; Yang, S.; Jiang, Y.; Li, J.; Li, S.; Ren, J. C.; Liu, W. Modeling Chemical Reactions on Surfaces: The Roles of Chemical Bonding and van Der Waals Interactions. *Progress in Surface Science*. Elsevier Ltd December 1, 2019. https://doi.org/10.1016/j.progsurf.2019.100561.

[85] Karim, N. A.; Alias, M. S.; Kamarudin, S. K. The Mechanism of the Water Dissociation and Dehydrogenation of Glycerol on Au (111) and PdAu Alloy Catalyst Surfaces. *Int J Hydrogen Energy*, **2021**, *46* (60), 30937–30947. https://doi.org/10.1016/j.ijhydene.2021.05.009.

[86] Delgado, J. M.; Blanco, R.; Orts, J. M.; Pérez, J. M.; Rodes, A. Glycolate Adsorption at Gold and Platinum Electrodes: A Theoretical and in Situ Spectroelectrochemical Study. *Electrochim Acta*, **2010**, *55* (6), 2055–2064. https://doi.org/10.1016/j.electacta.2009.11.034.

[87] Rodriguez-Reyes, J. C. F.; Siler, C. G. F.; Liu, W.; Tkatchenko, A.; Friend, C. M.; Madix, R. J. Van Der Waals Interactions Determine Selectivity in Catalysis by Metallic Gold. *J Am Chem Soc*, **2014**, *136* (38), 13333–13340. https://doi.org/10.1021/ja506447y.

[88] Muramoto, E.; Chen, W.; Jia, X.; Friend, C. M.; Sautet, P.; Madix, R. J. Toward Benchmarking Theoretical Computations of Elementary Rate Constants on Catalytic Surfaces: Formate Decomposition on Au and Cu. *Chem Sci*, **2022**, *13* (3), 804–815. https://doi.org/10.1039/d1sc05127j.

[89] O'Connor, C. R.; Hiebel, F.; Chen, W.; Kaxiras, E.; Madix, R. J.; Friend, C. M. Identifying Key Descriptors in Surface Binding: Interplay of Surface Anchoring and Intermolecular Interactions for Carboxylates on Au(110). *Chem Sci*, **2018**, *9* (15), 3759–3766. https://doi.org/10.1039/c7sc05313d.

[90] Ma, G.; Yang, N.; Zhou, G.; Wang, X. The Electrochemical Reforming of Glycerol at Pd Nanocrystals Modified Ultrathin NiO Nanoplates Hybrids: An Efficient System for Glyceraldehyde and Hydrogen Coproduction. *Nano Res*, **2022**, *15* (3), 1934–1941. https://doi.org/10.1007/s12274-021-3829-6.

[91] Holade, Y.; Morais, C.; Napporn, T. W.; Servat, K.; Kokoh, K. B. Electrochemical Behavior of Organics Oxidation on Palladium-Based Nanocatalysts Synthesized from Bromide Anion Exchange. *ECS Trans*, **2014**, *58* (46), 25–35. https://doi.org/10.1149/05846.0025ecst.

[92] Muramoto, E.; Patel, D. A.; Chen, W.; Sautet, P.; Sykes, E. C. H.; Madix, R. J. Direct Observation of Solvent-Reaction Intermediate Interactions in Heterogeneously Catalyzed Alcohol Coupling. *J Am Chem Soc*, **2022**, *144* (38), 17387–17398. https://doi.org/10.1021/jacs.2c02199.

[93] Bowker, M.; Morgan, C.; Couves, J. Acetic Acid Adsorption and Decomposition on Pd(1 1 0). *Surf Sci*, **2004**, *555* (1–3), 145–156. https://doi.org/10.1016/j.susc.2003.12.040.

[94] Hansen, E.; Neurock, M. First-Principles Based Kinetic Simulations of Acetic Acid Temperature Programmed Reaction on Pd(111). *Journal of Physical Chemistry B*, **2001**, *105* (38), 9218–9229. https://doi.org/10.1021/jp0103427.

[95] Carvalho, J. A.; Gaiotti, A. C.; Zanata, C. R.; Fonseca, S.; Giz, M. J.; Pinto, L. M. C.; Camara, G. A. How Does CO Co-Adsorption Affect Glycerol Electro-Oxidation on Polycrystalline Platinum? In Situ FTIR and DFT Approaches. *Electrochim Acta*, **2023**, *443*. https://doi.org/10.1016/j.electacta.2023.141978.

[96] Zalineeva, A.; Serov, A.; Padilla, M.; Martinez, U.; Artyushkova, K.; Baranton, S.; Coutanceau, C.; Atanassov, P. B. Self-Supported PdxBi Catalysts for the Electrooxidation of Glycerol in Alkaline Media. *J Am Chem Soc*, **2014**, *136* (10), 3937–3945. https://doi.org/10.1021/ja412429f.

[97] Hiltrop, D.; Cychy, S.; Elumeeva, K.; Schuhmann, W.; Muhler, M. Spectroelectrochemical Studies on the Effect of Cations in the Alkaline Glycerol Oxidation Reaction over Carbon Nanotube-Supported Pd Nanoparticles. *Beilstein Journal of Organic Chemistry*, **2018**, *14*, 1428–1435. https://doi.org/10.3762/bjoc.14.120.

[98] Wu, J.; Li, J.; Li, Y.; Ma, X. Y.; Zhang, W. Y.; Hao, Y.; Cai, W. Bin; Liu, Z. P.; Gong, M. Steering the Glycerol Electro-Reforming Selectivity via Cation–Intermediate Interactions. *Angewandte Chemie - International Edition*, **2022**, *61* (11). https://doi.org/10.1002/anie.202113362.

[99] Mathanker, A.; Yu, W.; Singh, N.; Goldsmith, B. R. Effects of Ions on Electrocatalytic Hydrogenation and Oxidation of Organics in Aqueous Phase. *Current Opinion in Electrochemistry*. Elsevier B.V. August 1, 2023. https://doi.org/10.1016/j.coelec.2023.101347.

[100] Lind, E.; White, J.; Anil, A.; Salazar-Alvarez, G.; Cornell, A. *Catalyst Layer Utilisation during Glycerol Electrooxidation in Alkaline Media with Electrodeposited Pd Catalysts at Different Thicknesses*.

[101] Ghosh, S.; Mondal, B.; Roy, S.; Shalom, M.; Sadan, M. B. Alcohol Oxidation with High Efficiency and Selectivity by Nickel Phosphide Phases. *J Mater Chem A Mater*, **2022**, *10* (15), 8238–8244. https://doi.org/10.1039/d2ta00863g.

[102] Kwon, Y.; Schouten, K. J. P.; Koper, M. T. M. Mechanism of the Catalytic Oxidation of Glycerol on Polycrystalline Gold and Platinum Electrodes. *ChemCatChem*, **2011**, *3* (7), 1176–1185. https://doi.org/10.1002/cctc.201100023.

[103] Gomes, J. F.; Tremiliosi-Filho, G. Spectroscopic Studies of the Glycerol Electro-Oxidation on Polycrystalline Au and Pt Surfaces in Acidic and Alkaline Media. *Electrocatalysis*, **2011**, *2* (2), 96–105. https://doi.org/10.1007/s12678-011-0039-0.

[104] Van Der Vliet, D. F.; Koper, M. T. M. Electrochemistry of Pt (100) in Alkaline Media: A Voltammetric Study. *Surf Sci*, **2010**, *604* (21–22), 1912–1918. https://doi.org/10.1016/j.susc.2010.07.027.

[105] Wang, C.; Gao, W.; Wan, X.; Yao, B.; Mu, W.; Gao, J.; Fu, Q.; Wen, D. In Situ Electrochemical Synthesis of Pd Aerogels as Highly Efficient Anodic Electrocatalysts for Alkaline Fuel Cells. *Chem Sci*, **2022**, *13* (46), 13956–13965. https://doi.org/10.1039/d2sc05425f.

[106] Berretti, E.; Giaccherini, A.; Montegrossi, G.; D'acapito, F.; Di Benedetto, F.; Zafferoni, C.; Puri, A.; Lepore, G. O.; Miller, H.; Giurlani, W.; et al. In-Situ Quantification of Nanoparticles Oxidation: A Fixed Energy X-Ray Absorption Approach. *Catalysts*, **2019**, *9* (8). https://doi.org/10.3390/catal9080659.

[107] Wang, L.; Lavacchi, A.; Bellini, M.; D'Acapito, F.; Benedetto, F. Di; Innocenti, M.; Miller, H. A.; Montegrossi, G.; Zafferoni, C.; Vizza, F. Deactivation of Palladium Electrocatalysts for Alcohols Oxidation in Basic Electrolytes. *Electrochim Acta*, **2015**, *177*, 100–106. https://doi.org/10.1016/j.electacta.2015.02.026.

[108] Macazo, F. C.; Hickey, D. P.; Abdellaoui, S.; -, al; Lamy, C.; Simoes, M. *Electrocatalytic Oxidation of Glycerol: I. Behavior of Palladium Electrode in Alkaline Medium You May Also like A Hybrid Multi-Catalyst Motif for Enhanced Electro-Oxidation of Glycerol The Electrocatalytic Oxidation of Glycerol in a Solid Alkaline Membrane Fuel Cell (SAMFC)*.

[109] Falase, A.; Main, M.; Garcia, K.; Serov, A.; Lau, C.; Atanassov, P. Electrooxidation of Ethylene Glycol and Glycerol by Platinum-Based Binary and Ternary Nano-Structured Catalysts. *Electrochim Acta*, **2012**, *66*, 295–301. https://doi.org/10.1016/j.electacta.2012.01.096.

[110] Nagao, R.; Sitta, E.; Varela, H. Stabilizing Nonstationary Electrochemical Time Series. *Journal of Physical Chemistry C*, **2010**, *114* (50), 22262–22268. https://doi.org/10.1021/jp109554r.

[111] Holade, Y.; Morais, C.; Arrii-Clacens, S.; Servat, K.; Napporn, T. W.; Kokoh, K. B. New Preparation of PdNi/C and PdAg/C Nanocatalysts for Glycerol Electrooxidation in Alkaline Medium. *Electrocatalysis*, **2013**, *4* (3), 167–178. https://doi.org/10.1007/s12678-013-0138-1.

[112] Ivanov, R.; Nakova, A.; Tsakova, V. Glycerol Oxidation at Pd Nanocatalysts Obtained through Spontaneous Metal Deposition on Carbon Substrates. *Electrochim Acta*, **2022**, *427*. https://doi.org/10.1016/j.electacta.2022.140871.

[113] Beden, B.; Kadirgan, F.; Lamy, C.; Leger, J. M. *OXIDATION OF METHANOL ON A PLATINUM ELECTRODE IN ALKALINE MEDIUM EFFECT OF METAL AD-ATOMS ON THE ELECTROCATALYTIC ACTIVITY*; Elsevier Sequoia S.A, 1982; Vol. 142.

[114] Vyas, A. N.; Ambekar, J. D.; Kale, B. B.; Sartale, S. D. Palladium Nanoparticles Grown by Using Successive Ionic Layer Adsorption and Reaction Method: Ethanol Electrooxidation and Electrochemical Quartz Crystal Microbalance Studies. *J Electrochem Soc*, **2023**, *170* (8), 084508. https://doi.org/10.1149/1945-7111/aceb92.

[115] Ipadeola, A. K.; Abdelgawad, A.; Salah, B.; Abdullah, A. M.; Eid, K. Interfacial Engineering of Porous Pd/M (M = Au, Cu, Mn) Sponge-like Nanocrystals with a Clean Surface for Enhanced Alkaline Electrochemical Oxidation of Ethanol. *Langmuir*, **2023**, *39* (39), 13830–13840. https://doi.org/10.1021/acs.langmuir.3c01285.

[116] Serov, A.; Asset, T.; Padilla, M.; Matanovic, I.; Martinez, U.; Roy, A.; Artyushkova, K.; Chatenet, M.; Maillard, F.; Bayer, D.; et al. Highly-Active Pd-Cu Electrocatalysts for Oxidation of Ubiquitous Oxygenated Fuels. *Appl Catal B*, **2016**, *191*, 76–85. https://doi.org/10.1016/j.apcatb.2016.03.016.

[117] Lović, J. D. Electrochemical Oxidation of Methanol and Ethanol on Electrodeposited Pd and PdNi-Coated Electrodes. *Russian Journal of Applied Chemistry*, **2017**, *90* (12), 2039–2045. https://doi.org/10.1134/S1070427217120229.

[118] Ruiz-López, E.; Diaz-Perez, M. A.; de Lucas-Consuegra, A.; Dorado, F.; Serrano-Ruiz, J. C. Membrane-Less Ethanol Electrooxidation over Pd-m (M: Sn, Mo and Re) Bimetallic Catalysts. *Catalysts*, **2021**, *11* (5). https://doi.org/10.3390/catal11050541.

[119] Zhang, S.; Liu, K.; Liu, Z.; Liu, M.; Zhang, Z.; Qiao, Z.; Ming, L.; Gao, C. Highly Strained Au-Ag-Pd Alloy Nanowires for Boosted Electrooxidation of Biomass-Derived Alcohols. *Nano Lett*, **2021**, *21* (2), 1074–1082. https://doi.org/10.1021/acs.nanolett.0c04395.

[120] Łukaszewski, M.; Czerwiński, A. Comparative EQCM Study on Electrooxidation of Carbon Oxides Adsorption Products on Noble Metals and Their Alloys. Polycrystalline

Pd-Based Systems. *Journal of Electroanalytical Chemistry*, **2007**, *606* (2), 117–133. https://doi.org/10.1016/j.jelechem.2007.06.002.

[121] Berretti, E.; Pagliaro, M. V.; Giaccherini, A.; Montegrossi, G.; Di Benedetto, F.; Lepore, G. O.; D'Acapito, F.; Vizza, F.; Lavacchi, A. Experimental Evidence of Palladium Dissolution in Anodes for Alkaline Direct Ethanol and Formate Fuel Cells. *Electrochim Acta*, **2022**, *418*. https://doi.org/10.1016/j.electacta.2022.140351.

[122] Bambagioni, V.; Bianchini, C.; Marchionni, A.; Filippi, J.; Vizza, F.; Teddy, J.; Serp, P.; Zhiani, M. Pd and Pt-Ru Anode Electrocatalysts Supported on Multi-Walled Carbon Nanotubes and Their Use in Passive and Active Direct Alcohol Fuel Cells with an Anion-Exchange Membrane (Alcohol = Methanol, Ethanol, Glycerol). *J Power Sources*, **2009**, *190* (2), 241–251. https://doi.org/10.1016/j.jpowsour.2009.01.044.

[123] Anil, A.; White, J.; Campos dos Santos, E.; Terekhina, I.; Johnsson, M.; Pettersson, L. G. M.; Cornell, A.; Salazar-Alvarez, G. Effect of Pore Mesostructure on the Electrooxidation of Glycerol on Pt Mesoporous Catalysts. *J Mater Chem A Mater*, **2023**, *11* (31), 16570–16577. https://doi.org/10.1039/d3ta01738a.

[124] Antolini, E. Glycerol Electro-Oxidation in Alkaline Media and Alkaline Direct Glycerol Fuel Cells. *Catalysts*, **2019**, *9* (12). https://doi.org/10.3390/catal9120980.

[125] Xia, S. J.; Birss, V. I. *A Multi-Technique Study of Compact and Hydrous Au Oxide Growth in 0.1 M Sulfuric Acid Solutions*; 2001; Vol. 500.

5.7 Supplementary

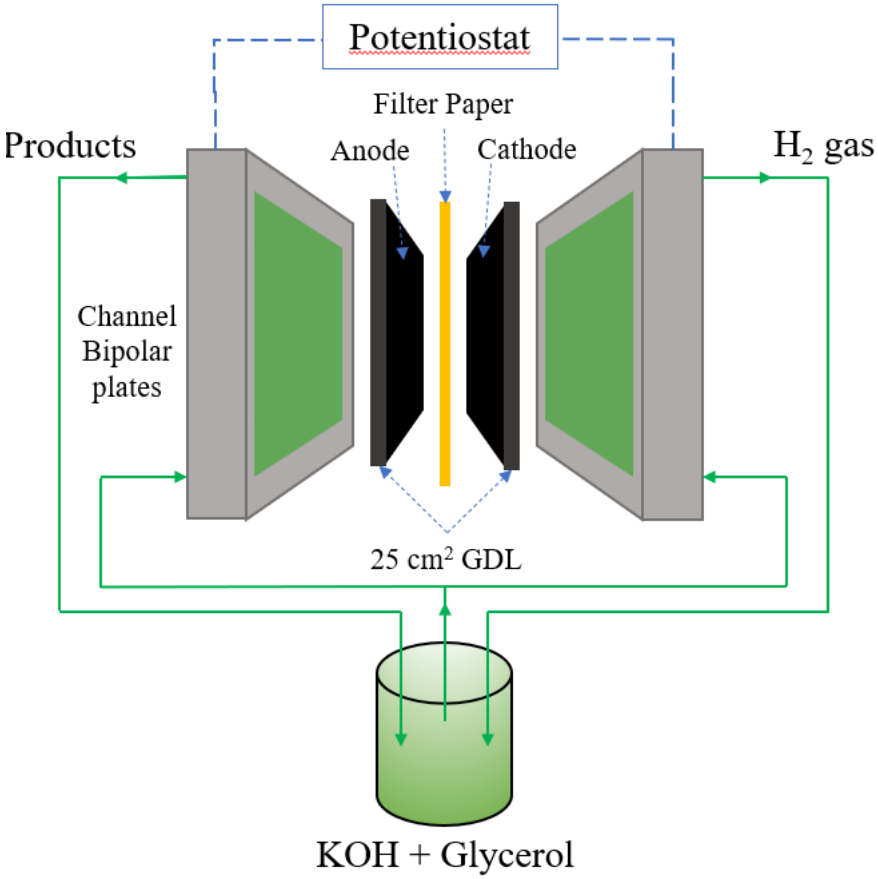

Figure 5.S1) Schematic illustration of the electrolyser setup. Gaskets are not shown but sandwiched between graphite plates.

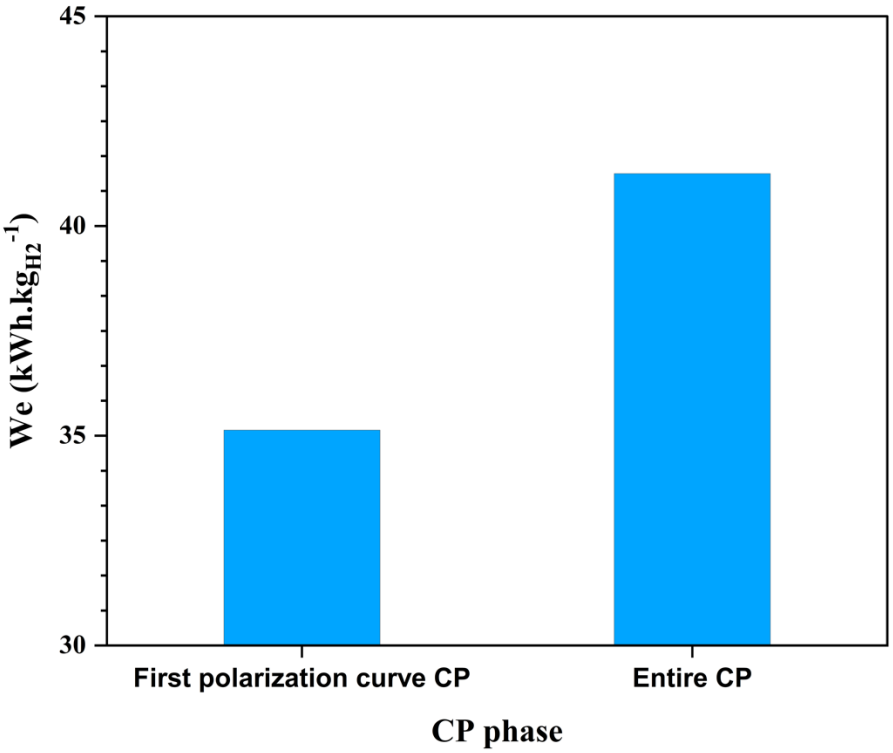

Figure 5.S2) A comparison of the W_e of the first low voltage polarization curve in the CP to the entire CP at 100 mA.cm^{-2} for the 1 mg.cm^{-2} $Ni_{80}Pd_{20}$/C anode and 2 mg.cm^{-2} $Ni_{80}Pd_{20}$/C cathode at 1M KOH and 1M glycerol flowing at 0.5 L.min^{-1} at 80^{o}C with a measured faradaic efficiency of 97%.

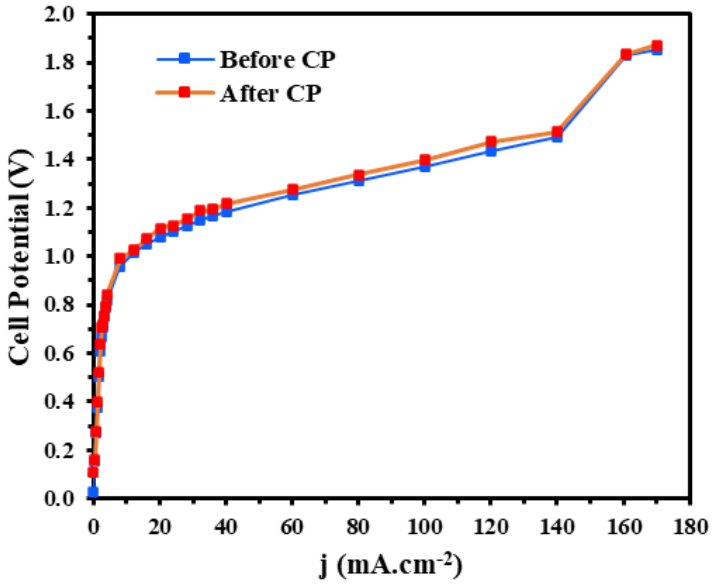

Figure 5.S3) Polarization curve of $Ni_{80}Au_{20}$/C anode (1 mg.cm^{-2}) and $Ni_{80}Pd_{20}$/C cathode (2 mg.cm^{-2}) before and after CP measurements in 0.1M glycerol and 1M KOH at 80^{o}C.

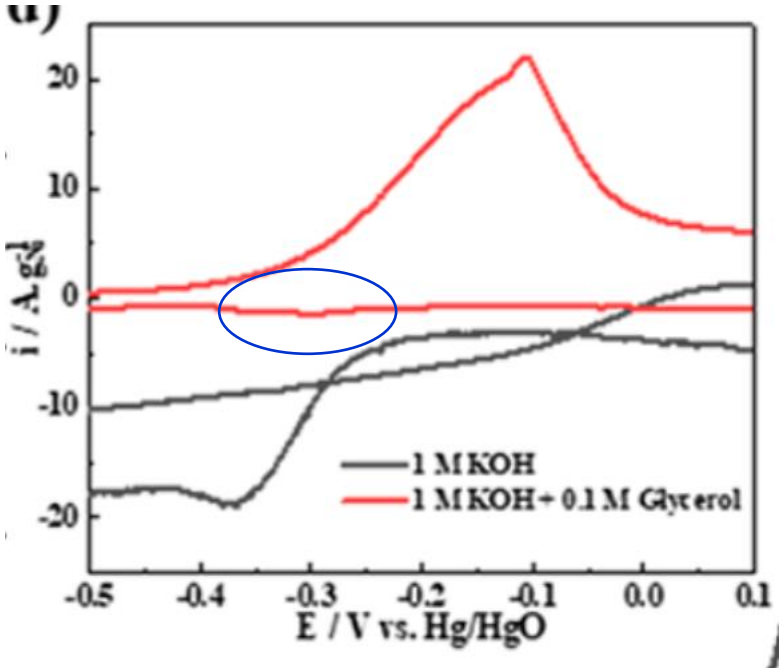

Figure 5.S4) Houache et al. 2021 figure 5.D inset demonstrating the CV $Ni_{80}Pd_{20}$ in 1M KOH and various glycerol concentrations at a scan rate of 50 $mV.s^{-1}$ [10]. Bleu circle represents the reduction peak prior to the reactivation peak.

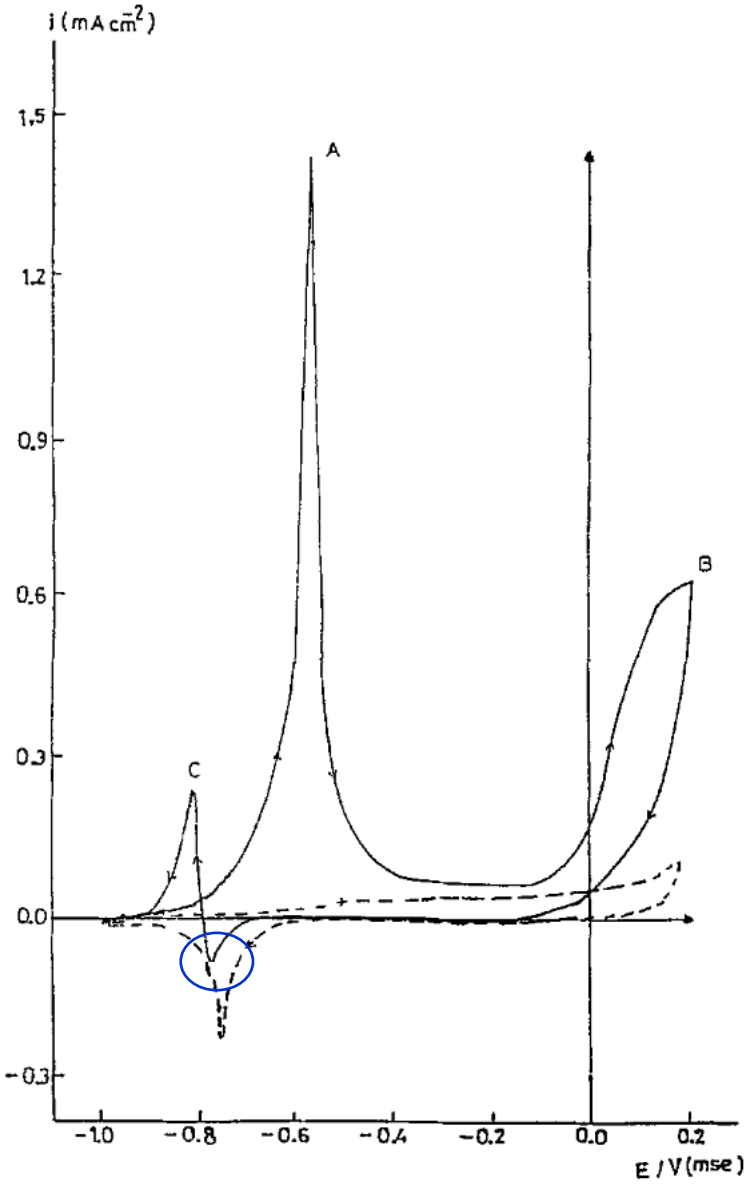

Fig. 2. Cyclic voltammograms of the palladium electrode in alkaline medium (25°C, 1*M* NaOH, v = 50 mV s^{-1}); (– – – –) without glycerol and (———) with 0.1*M* glycerol.

Figure 5.S5) Yildiz et al. 1994 figure 2 CV of Pd electrode in alkaline media (25°C, 1M NaOH, v = 50 $mV.s^{-1}$); Dashed line represents the CV without glycerol and the solid line represents the CV with 0.1M glycerol. Potential is reported in reference to MSE. [108] Bleu circle represents the reduction peak prior to the reactivation peak.

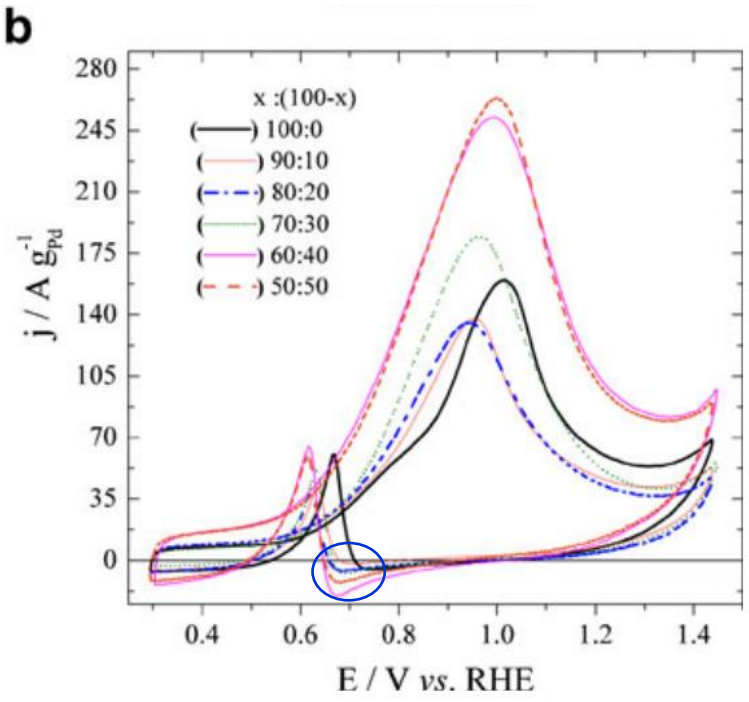

Fig. 8 CVs of **a** $Pd_xNi_{(100-x)}/C$ and **b** $Pd_xAg_{(100-x)}/C$ catalysts at 50 mV s^{-1} in 0.1 mol L^{-1} NaOH+0.1 mol L^{-1} glycerol

Figure 5.S6) Holade et al. 2013 figure 8B CVs of $Pd_xSg_{(100-x)}/C$ catalysts in 0.1M NaOH and 0.1M glycerol measured at a scan rate of 50 $mV.s^{-1}$ and at room temperature. [111] Bleu circle represents the reduction peak prior to the reactivation peak.

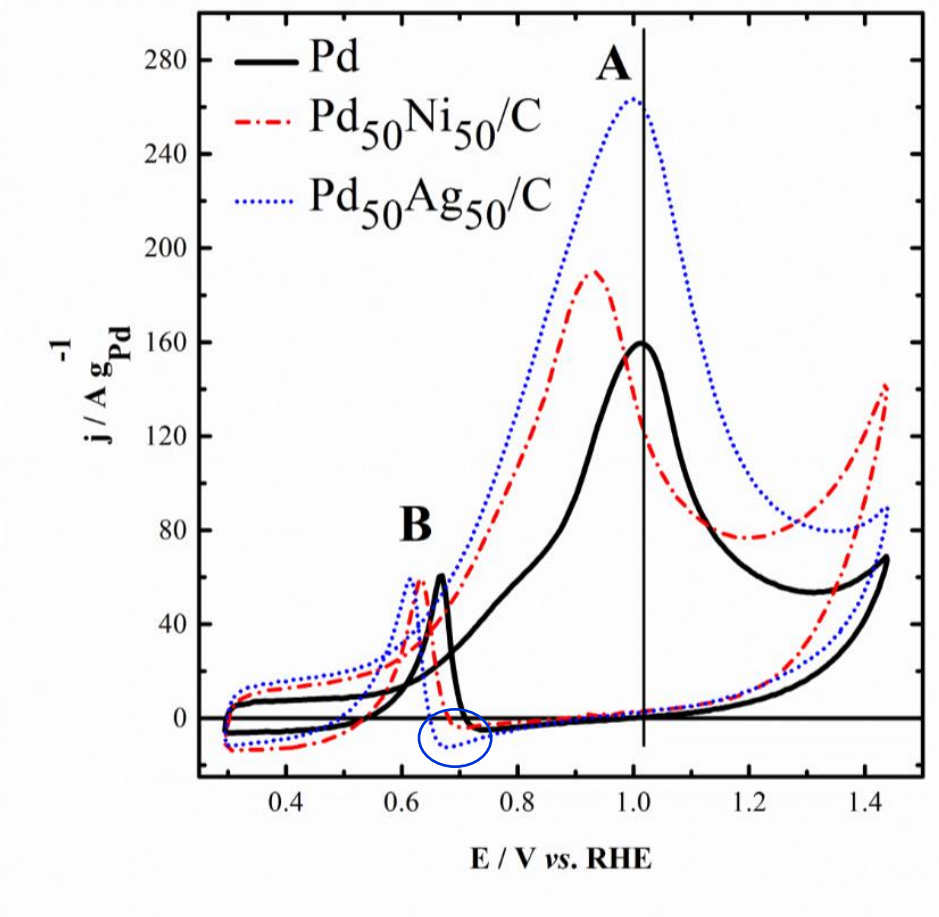

Figure 4. Steady-state cyclic voltammograms recorded in 0.1 mol L^{-1} NaOH in the presence of 0.1 mol L^{-1} Glycerol on 30 wt.% Pd-based electrodes at 50 mV s^{-1}.

Figure 5.S7) Holade et al. 2014 figure 4 CV of Pd, $Pd_{50}Ni_{50}$/C and $Pd_{50}Ag_{50}$/C catalysts measured in 0.1M NaOH and 0.1M glycerol at a scan rate of 50 $mV.s^{-1}$ and room temperature. [91] Bleu circle represents the reduction peak prior to the reactivation peak.

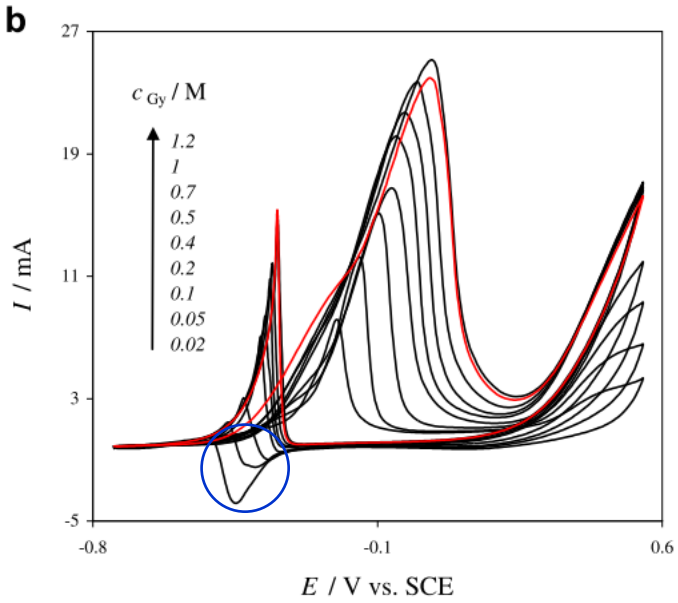

Figure 5.S8) Habibi et al. 2012 figure 4B CVs of Pd/CCE electrode in 0.5M KOH and various concentrations of glycerol scanned at 50 $mV.s^{-1}$ and room temperature. [32] Bleu circle represents the reduction peak prior to the reactivation peak.

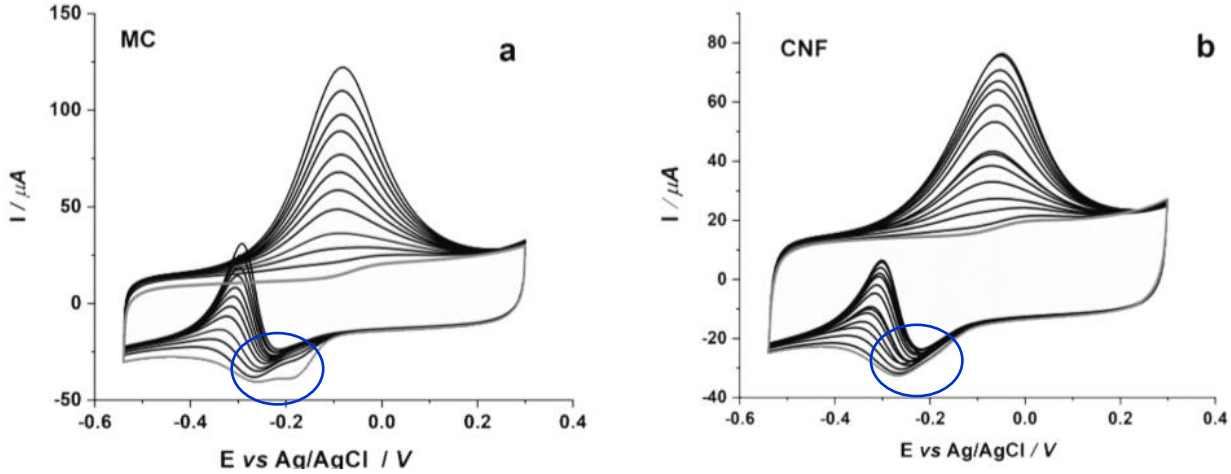

Figure 5.S9) Ivanov et al. 2022 figure 10 CVs of (A) Pd-MC and (B) Pd-CNF in 0.1M KOH and 0M glycerol (grey lines) or different concentrations of glycerol (0.2-15 mM; black lines) measured at a scan rate of 50 $mV.s^{-1}$ and room temperature. [112] Bleu circle represents the reduction peak prior to the reactivation peak.

Chapter 6: Thesis conclusion and recommendation

6.1 Conclusion

In chapter 3, a revision of Houache et al. 2020's $Ni_{90}Bi_{10}$ catalyst by varying reactive conditions have identified key promotional and inhibitory roles KOH and glycerol has to GEOR, identifying GEOR's indirect mechanism prevents the stable formation of surface β-NiOOH. This oxidation state on the surface is necessary for the bulk phase of the nanoparticle to achieve a Ni^{+3} oxidation state which has an improved conductivity. In addition, it is also retains a key role in promoting the de-intercalation of surface β-$Ni(OH)_2$ when it is regenerated. In turn, it is theorised that glycerol inhibits GEOR by preventing the bulk material from oxidising as well. In addition, concentration tests revealed glycerol has a capacity to adsorb over Ni^{+2}.

Upscaling the polarization curves to a 25 cm^2 electrolyser identified the presence of a possible novel Bi oxidation process which is rendered identifiable when the temperature is sufficiently elevated. Furthermore, the production of polarization curves also highlights a need to perform slow scan rate or constant CP polarization curves for several minutes to identify multiple polarization curves, representing different reaction processes which was shown invaluable for the 5th chapter of this work. Polarization curves were also key to identify a divergence between GEOR electrolyser designs to OER where catalyst underutilization is significant even at low loadings which are not easily observable on small 3-electrode cells. Overall, a $Ni_{90}Bi_{10}$ anode and Pt/C cathode cell achieved 37.9 $kWh.kg_{H2}^{-1}$ at 0.1M glycerol and 1M KOH and 80^{o}C at 4 $mA.cm^{-2}$. Due to the low current density, this energy consumption shouldn't be used lightly for comparison.

In chapter 4, the question on the influence of glycerol on HER over Ni/C, $Ni_{98}Bi_2$/C, $Ni_{80}Au_{20}$/C and $Ni_{80}Pd_{20}$/C was explored. While literature hypothesized the inhibitory influence of glycerol is caused by an increase in viscosity and loss of OH^- conduction in solution, results from this work shows glycerol has an inhibitory and promotional role depending on the catalyst material and the specific HER mechanism being operated. It also identified the majority of the observed resistances in the measurements do not originate from the bulk electrolyte solution but from the influence of glycerol on the Nafion® binder microphase structure, which is instrumental for OH^- conduction and H_2O replenishment. It should be highlighted this was not discovered in this work since this is

known in the fuel cell field. Overall, the primary influence of glycerol on HER is localised at the catalyst interface and not in the bulk electrolyte solution.

In chapter 5, the influence of KOH and glycerol was investigated over Ni/C, $Ni_{98}Bi_2$/C, $Ni_{80}Au_{20}$/C and $Ni_{80}Pd_{20}$/C during GEOR with a focus on electrolyser performance. Although the focus was originally intended to be on Ni based GEOR, it was identified $Ni_{80}Au_{20}$/C and $Ni_{80}Pd_{20}$/C presented polarization curves associated with Au and Pd instead of Ni. Based on the polarization curves, Au and Pd polarization behaviours showed key inconsistencies with current established theories of how GEOR is meant to occur over these different reactive metal phases. A key inconsistency was the deactivation mechanism which showed Au and Pd weren't deactivated from the formation of oxides but via a competitive inhibition with an unknown intermediate. This is supported based on the reverse polarization curve scans of the cells.

Furthermore, CP measurements highlight the observable effect of acidification of electrolyte from the net consumption of hydroxide which highlight the need for catalyst design to vary reactive conditions. This acidification can potentially be used as a method of further quantifying the amount of CO_3^- formed in combination with HPLC. In terms of power consumption, the Ni/C anode and Pt/C cathode reported the lowest power consumption at 42.1 $kWh.kg_{H2}^{-1}$ in 0.1M glycerol and 1M KOH at 200 $mA.cm^{-2}$. The lowest electrical power consuming symmetrical/asymmetrical Ni cell was 56.2 $kWh.kg_{H2}^{-1}$ in 0.1M glycerol and 1M KOH at 200 $mA.cm^{-2}$, which does not meet the D.O.E. energy target of 40 $kWh.kg_{H2}^{-1}$. That said, 400 mV of the symmetrical/asymmetrical Ni cells originated from the overpotential at the cathode. Through improved HER catalyst design, the electrical power can decrease significantly. In turn, while the Ni catalysts in this study did not meet the D.O.E. target, significant improvements remain which can meet this target.

6.2 Recommendations

- Determine the existence of a Bi based GEOR mechanism at elevated temperatures.
- Produce a proper Ni based GEOR model as a guide to understand the role of each reactant on the catalyst.
- Perform a more in-depth investigation of the influence of different OER electrolyser design parameters on GEOR.

- Perform a complete study on the electroreduction of glycerol and its oxidation products to assess the future potential of membrane-free GEOR systems.
- A physical characterisation study to validate the competitive nature of glycerol and OH^- on the bulk formation of Ni catalysts.
- Perform DFT and AIMD simulations to account for the influence alcohols have over HER.
- Investigate the nature of the different polarization curves over Au and Pd with physical characterisations.
- A critical study on the influence of different glycerol and product concentrations over various catalyst materials to observe the impact competitive adsorption on GEOR efficacy for larger systems.